Structural and biochemical insights into members of the kinesin and ubiquitin ligase families

Marta Klejnot (MSc)

Submitted to the University of Glasgow in fulfilment of the requirements for the Degree of Doctor of Philosophy

Beatson Institute for Cancer Research
Garscube Estate, Switchback Road
Glasgow, G61 1BD

September 2013

Abstract

The thesis focuses on characterisation of two different protein families, kinesins and ubiquitin ligases, that are involved in different biological processes. Kinesins constitute a superfamily of microtubule-based motor proteins, fulfilling important cellular functions, ranging from intracellular transport to cell division. They also play a role in primary cilia and Hedgehog signalling. Ubiquitin ligases are enzymes that catalyse the transfer of ubiquitin to the lysine residues of the substrate. Marking protein substrates with ubiquitin alters their functions and fates. With nearly 700 different ubiquitin ligases in humans, they control a vast array of cellular processes.

The first part of this thesis summarises results relating to kinesins. Protocols for creation of a panel of kinesin motor domains, a useful tool for anti-mitotic inhibitors specificity testing are presented. Furthermore, biochemical, kinetic and structural features of a poorly described kinesin motor protein — Kif15 are reported. Kif15's motor domain structure is described and compared to Eg5's catalytic core. Moreover, the influence of Eg5 inhibitors on Kif15 ATPase activity is investigated. Scouting for small molecules targeting Kif15 is also performed. Kif15 interaction with microtubules in various nucleotide-bound states is characterised. The possibility of a secondary microtubule binding site in the tail of Kif15 is examined. The binding of Kif15 with partner proteins is also investigated. Additionally the high-resolution structure of the human Kif7 motor domain is presented, providing the first step towards structural characterisation of this Kinesin-4 family member.

The second part of this thesis concerns a ubiquitin ligase, Trim28. Trim28 was first reported as a transcription corepressor, working by recruiting proteins that drive the heterochromatin state, whilst its mechanism of action as a ubiquitin ligase remains elusive. Attempts to crystallise and determine the three-dimensional structure of Trim28 are described. Additionally, Trim28 functioning as an E3 ubiquitin ligase, and its interactions with E2s, KRAB domains of various zinc finger proteins and with the Mage-C2 protein are investigated. The results provide the foundation for future studies on Trim28.

Contents

List of Tables

List of Figures

Preface

This thesis comprises two distinct parts. The first concerns molecular motors — kinesins and the second relates to the ubiquitination system and the E3 ligase — Trim28.

Because my first supervisor, Prof. Frank Kozielski, left the Beatson Institute, the kinesins project was stopped after two and a half years.

Thereafter a new project on the ubiquitin system in Dr. Danny Huang's group was undertaken and pursued for a year and a half.

Acknowledgements

First of all, I would like to thank my husband Błażej for his invincible support and encouragement.

I would like to express my gratitude to Dr. Danny Huang for being a wonderful mentor and for all his help with changing projects. I would like to thank Prof. Frank Kozielski for giving me a chance of pursuing a PhD in the Beatson Institute. I am also grateful to Dr. Chris Gray for all his advice and guidance.

I am obliged to Dr. Kristal Kaan for all her help at the beginning of my work in the Molecular Motors Lab, and to all members of R9 (Dr. Oliver Rath, Dr. Alexander Schuettelkopf, Dr. Sandeep Talapatra, Dr. James Good, Dr. Venkatasubramanian Ulaganathan) and R4 (Dr. Lori Buetow, Dr. Gary Sibbet, Hao Dao (Julia), Gabriele Marchiano) for being great colleagues.

I would like to express my appreciation to all the people that I had a chance to collaborate with during my time in the Institute: Dr. Elisabeth Black, Dr. Antonio Trinidad, Jennifer Cameron, Prof. Michael Olson and Dr. Mads Gabrielsen. It has been a great experience to work in such a vibrant scientific community.

I would like to thank Prof. Peter Bass, Dr. Aditi Falnikar and Prof. Robert Cross for their input into the Kif15 paper.

A great deal of appreciation goes to all Beatson services, particularly to central services for the preparation of media and reagents and for always keeping up with demand in our lab. Also thanks to the molecular technology service that makes our life so easy. I also thank proteomics group for all mass spectroscopy analysis.

Completion of this work would not be possible without beam time provided by European Synchrotron Radiation Facility and Diamond Light Source and all help received from local contacts on site.

Last but not least, I am thankful to Cancer Research UK for funding the research.

Author's Declaration

I declare that, except where explicit reference is made to the contribution of others, that this dissertation is the result of my own work and has not been submitted for any other degree at the University of Glasgow or any other institution.

Definitions / Abbreviations

Å	Ångström
ACES	N-(2-acetamido)-2-aminoethanesulphonic acid
ADP	Adenosine diphosphate
AMP-PNP	Adenyl imidodiphosphate
APS	Ammonium persulphate
ATP	Adenosine triphosphate
BRD	Bromo domain
cDNA	Complementary DNA
CENPE	Centromere associated protein E
Ci	Cubitus interruptus
CK1	Casein kinase 1
cm	Centimetre
Cos2	Costal2
Da	Dalton
DHh	Desert hedgehog
DMSO	Dimethyl sulfoxide
DTT	Dithiothreitol
EDTA	Ethylenediaminetetraacetic acid
EGTA	Ethylene glycol tetraacetic acid
ESRF	European Synchrotron Radiation Facility
FHA	Forkhead associated domain
GSKβ	Glycogen synthase kinase β
GST	Glutathione S-transferase
GTP	Guanosine triphosphate
h	Hour
HECT	Homologous to the E6-AP carboxyl terminus
Hh	Hedgehog
His-tag	Histidine tag
HRP	Horseradish peroxidase

IFT	Intraflagellar transport
IHh	Indian hedgehog
IMAC	Immobilized metal affinity chromatography
IPTG	Isopropyl β-D-1-thiogalactopyranoside
KAP1	KRAB-associated protein 1
k_{cat}	Catalytic rate
K_D	Dissociation constant
kDa	Kilodalton
KHC	Kinesin heavy chain
KLC	Kinesin light chain
Klp	Kinesin-like protein
KRAB	Krüppel-associated box
l	Litre
LB	Lysogeny broth
LDH	Lactate dehydrogenase
Mage	Melanoma-associated antigen
MAP	Microtubule-associated proteins
MBP	Maltose-binding protein
MD	Motor domain
MHG	Mage homology domain
min	Minute
ml	Millilitre
mM	Millimolar
MPD	2-methyl-2,4-pentanediol
MT	Microtubule
mV	Millivolts
NAD^+	Nicotinamide adenine dinucleotide (oxidised)
NADH	Nicotinamide adenine dinucleotide (reduced)
NEB	Nuclear envelope breakdown
nm	Nanometre
nM	Nanomolar
NMR	Nuclear magnetic resonance
OD_{600}	Optical density of a sample measured at 600 nm
PCR	Polymerase chain reaction
PDB	Protein Data Bank
PEP	Phosphoenolpyruvate
PEG	Polyethylene glycol
PEG MME	Polyethylene glycol monomethyl

PHD	Plant homeo domain
PIPES	Piperazine-N,N'-bis(2-ethanesulphonic acid)
PK	Pyruvate kinase
PKA	Protein kinase A
PMSF	Phenylmethanesulphonylfluoride
Ptch	Patched
RING	Really interesting new gene
rmsd	Root-mean-square deviation
SAXS	Small-angle X-ray scattering
SDS-PAGE	Sodium dodecyl sulphate-polyacrylamide gel electrophoresis
SERp	Surface entropy reduction prediction
SHh	Sonic hedgehog
Smo	Smoothened
SPR	Surface plasmon resonance
STLC	S-trityl-L-cysteine
SUMO	Small ubiquitin-like modifier
TB	Terrific broth
TBS-T	Tris-buffered saline and tween 20
TEMED	Tetramethylethylenediamine
TEV	Tobacco etch virus
TPX2	Targeting protein for Xklp2
Trim28	Tripartite motif-containing 28
Tris-HCl	Tris(hydroxymethyl)aminomethane hydrochloride
Trx	Thioredoxin
U	Enzyme unit, defined as the amount of the enzyme that catalyses the conversion of 1 micromole of substrate per minute at 25°C
Ubls	Ubiquitin-like modifiers
μg	Microgram
μl	Microlitre
μm	Micrometre
μM	Micromolar
WB	Western blot
V	Volt
Xklp2	Xenopus kinesin-like protein 2
ZFP	Zinc finger protein

Part I

Structural and biochemical insights into members of the kinesin superfamily

Chapter 1

Introduction

1.1 Kinesin superfamily overview

Movements within cells, including transport of cellular components, muscle contraction and cell division, are essential in eukaryotes. This is carried out by three families of molecular motors: myosins, dyneins and kinesins (Figure 1.1) (Mallik and Gross, 2004).

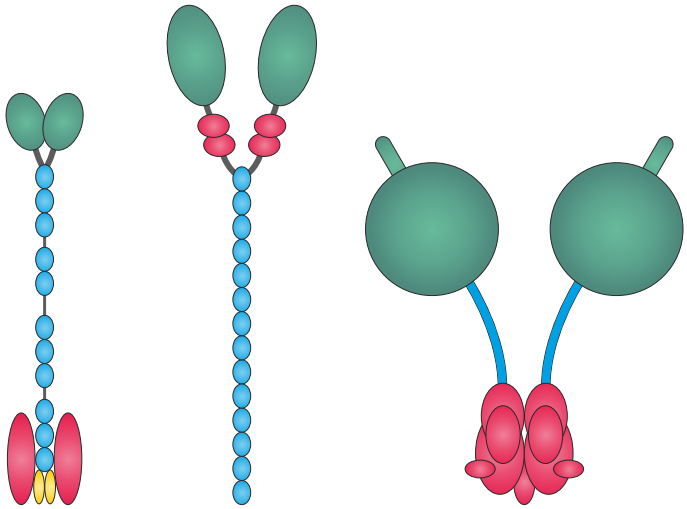

Figure 1.1: Overall architecture of three molecular motor types. From left: kinesin, myosin and dynein. All of them contain a catalytic site (green) followed by a stalk domain (blue). Protrusions emanating from the dynein head provide the microtubule binding site (in the case of the other motors, this is an integral part of the motor domain). The kinesin tail (yellow) and associated peptides (pink) are also presented. Figure adapted from Woehlke and Schliwa (2000).

In order to move, all cellular motors utilise specific cytoskeletal tracks — actin, in the case of myosins, and microtubules, used by dyneins and kinesins. Microtubules (MTs) are biopolymers of α and β-tubulin dimers, which exist in a state of "dynamic instability" — enabling

them to rapidly switch from growing to shrinking phase. Tubulin heterodimers form linear protofilaments in a GTP-dependent manner. In mammalian cells, thirteen protofilaments create a cylinder with a diameter of 24 nm (Figure 1.2). MTs are polar entities due to the "head to tail" tubulin dimer (α-β) linkage, and possess an α-monomer on the minus MT end (slow growing), and β-tubulin on the plus end (fast growing) (Conde and Caceres, 2009).

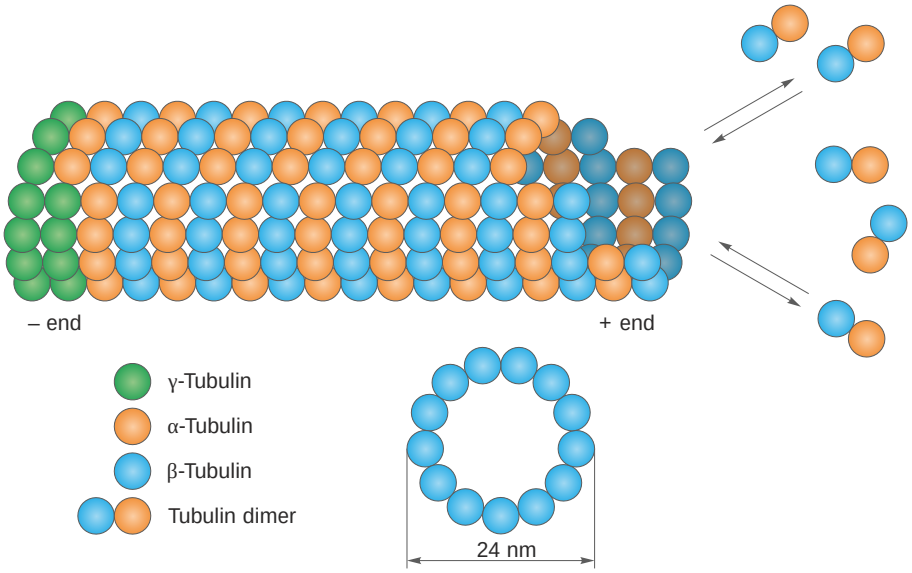

Figure 1.2: Structure of microtubules. Microtubules are polar biopolymers of α- and β-tubulin dimers. Figure adapted from Conde and Caceres (2009).

The discovery of the kinesin superfamily was initiated following the observation of cellular particle transport in the axoplasm extracted from the *Loligo pealei* squid (Allen et al., 1985). This movement along the MT filaments was detected for organelles, beads and MTs (Vale et al., 1985b). A 110–120 kDa translocation protein was identified and named kinesin, from the Greek *kinein* — to move (Brady, 1985; Vale et al., 1985a). It had the ability to associate with MTs in the presence of AMP-PNP, a non-hydrolysable ATP analogue. In addition it was detected in solution only when ATP was present in the experimental setup (Vale et al., 1985a).

Since conventional kinesin, the founding member of the kinesin superfamily was discovered, several other representatives have been described. Originally they were divided into 3 groups based on the position of the motor domain within their amino acid sequence. Kinesins with the motor domain at the N-terminus, middle or C-terminus of the protein were named KinN, KinI or KinC, respectively (Vale and Fletterick, 1997). The KinN family was then subdivided into 12 families (Kinesin-1 to Kinesin-12) while KinI was renamed as Kinesin-13 and KinC as Kinesin-14 family (Kinesin-14A and Kinesin-14B) (Figure 1.3) (Miki et al., 2005). These that could not be classified into any family (some nematode kinesin-like proteins) were categorised as orphan kinesins (Lawrence et al., 2004; Miki et al., 2001). A more robust analysis of kinesin

sequences was possible with growing availability of complete eukaryotic genomes. This led to identification of 17 kinesin families (Wickstead and Gull, 2006).

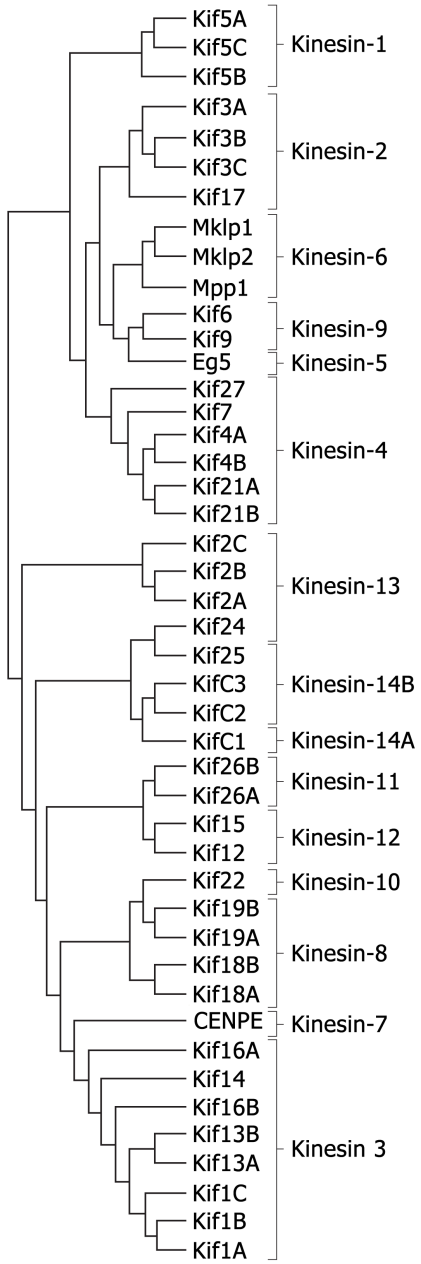

Figure 1.3: Phylogeny of human kinesins. Figure adapted from Hirokawa et al. (2009), Miki et al. (2001).

1.1.1 Organisation of the kinesin molecule

A conventional kinesin consists of a heavy chain (KHC) dimer and two associated kinesin light chains (KLC) that are involved in substrate recognition and binding. The heavy chain comprises an N-terminal motor domain (MD) followed by an elongated stalk and a small,

intrinsically disordered C-terminal tail domain (Figure 1.4) (Hirokawa et al., 1989; Seeger et al., 2012; Yang et al., 1989).

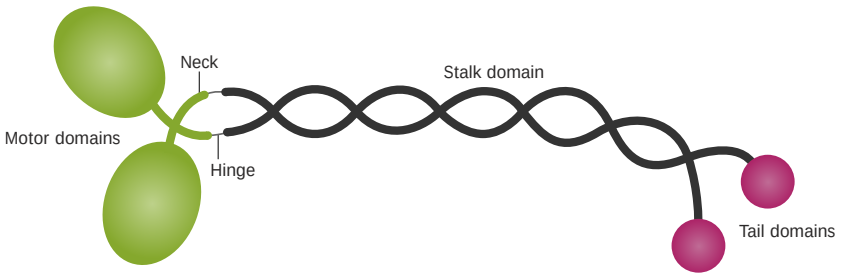

Figure 1.4: Overall structural design of conventional kinesin heavy chain. Figure adapted from Woehlke and Schliwa (2000).

The motor domain is the catalytic core of the kinesin, comprising the ATP binding pocket and the nucleotide-dependent MT binding site (Yang et al., 1989). This part is highly conserved among kinesins and to an even higher degree within any single kinesin family (Miki et al., 2005). Conservation of α and β secondary structure elements is prominent in motor domains, with loop regions providing the distinct features of each kinesin family (e.g. loop L5 in Eg5, K-loop in Kif1A) (Marx et al., 2009). The crystal structure of the human conventional kinesin, Kif5B (Figure 1.5), revealed the overall fold of the motor domain — eight-stranded β-sheet surrounded by six α-helices (Kull et al., 1996). This structural organisation strongly resembles the core region of the myosin head fold, despite lacking amino acid sequence conservation.

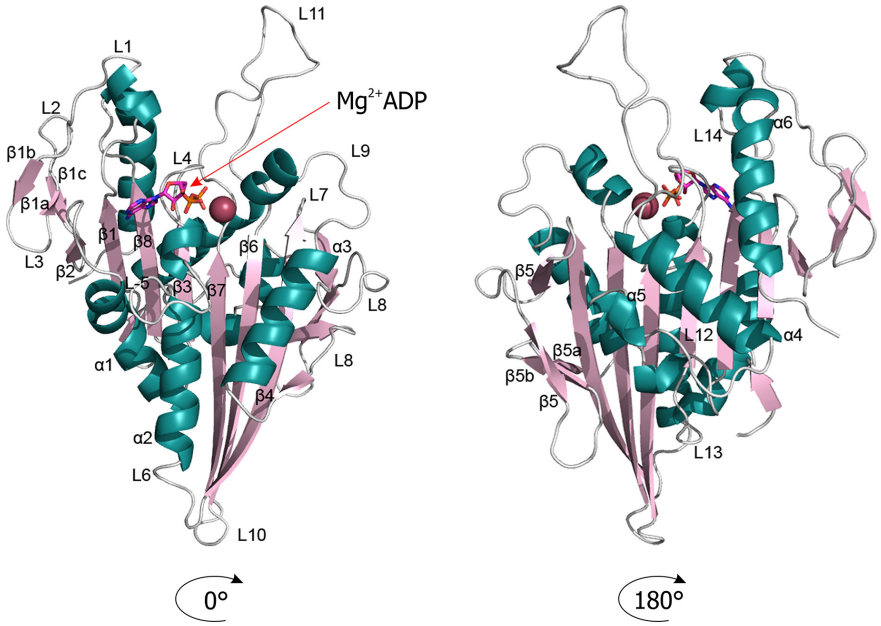

Figure 1.5: Conventional kinesin catalytic core fold. Architecture of the conventional kinesin catalytic core, presenting α-helices in teal, β-sheets in pink and loops in grey (PDB ID: 1BG2 (Kull et al., 1996)). Mg^{2+}ADP is shown as a ball and stick model. Secondary structure elements are labelled on the front or back-view of the motor domain.

The Kif5B structure contained Mg^{2+}ADP bound in the the P-loop (Walker motif (Walker et al., 1982)), the short loop between β3 and α2 (stabilising the α- and β-phosphate of ADP). The magnesium ion is vital for the stabilisation of the nucleotide and cannot be substituted by any other cation (Cross, 2004). The globular motor domain is followed by the neck region, containing a neck linker (two short β-strands) and a neck coiled-coil (Kozielski et al., 1997). This region is implicated in the process of motor domain dimerisation of conventional kinesin and is thought to play a key role in promoting kinesin movement and maintaining association with MT tracks (Case et al., 2000; Grummt et al., 1998; Romberg et al., 1998). The neck linker region is responsible for communicating subtle changes that occur in the motor domain (depending on its nucleotide bound state) to the rest of the kinesin molecule (Woehlke and Schliwa, 2000).

It has been noted that not all kinesins move in the same direction. Furthermore, this directionality is linked to the position of the motor domain in the primary sequence. Thus, kinesins have been subdivided into three groups (Figure 1.6), N-type kinesins (KinN, Kinesin-1 to Kinesin-12) that move in the plus-direction of the MTs and contain a motor domain at the amino-end of the molecule and C-type kinesins (KinC, Kinesin-14A and Kinesin-14B) moving towards the minus-end of the MTs, with a carboxy-terminal motor domain (Hirokawa et al., 2009; Woehlke and Schliwa, 2000). The third group, M-type kinesins (KinI, Kinesin-13), which unlike others, contain a motor in the middle of the polypeptide chain and do not move directionally along MT tracks, instead these kinesins can depolymerise and modulate the dynamics of MTs (Friel and Howard, 2011; Kobayashi et al., 2011).

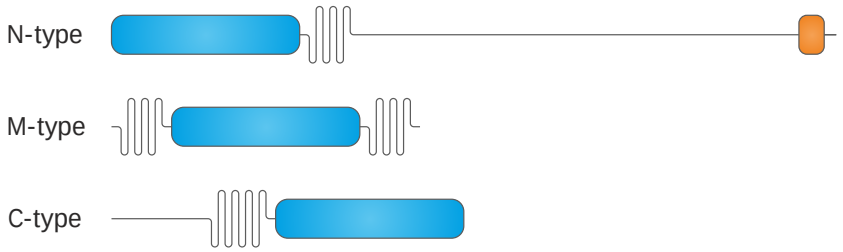

Figure 1.6: Kinesin classification due to the motor domain position. Position of the kinesin motor domain in its general architecture determines its mode of action and directionality. Figure adapted from Hirokawa et al. (2009).

The conventional kinesin and ncd motor domain share a typical fold of kinesin catalytic core (Figure 1.7). The structures of a dimeric conventional kinesin heavy chain (Kozielski et al., 1997) and a representative C-type kinesin, *Drosophila melanogaster* ncd (minus-end directed motor) (Figure 1.8) revealed differences in orientation of the neck linker of the conventional kinesin and neck region of ncd with respect to the motor domains. Plus-end directed motors dimerise through perpendicular positioned neck linkers. The ncd coiled-coil neck region stays in close contact and aligns with the globular motor domain (Sablin et al., 1996). Deletion

studies and investigation of chimeric constructs confirmed that the neck region is responsible for motor directionality and the mode of movement (Case et al., 2000; Grummt et al., 1998; Romberg et al., 1998).

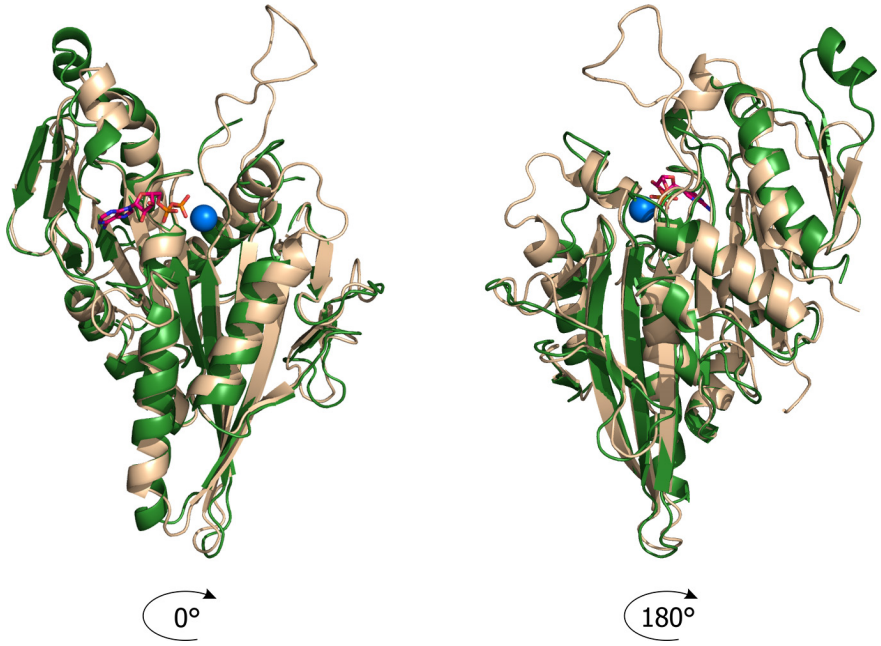

Figure 1.7: Structure overlay of Kif5B and ncd motor domain. Front and back view of overlaid Kif5B (beige) (PDB ID: 1BG2 (Kull et al., 1996)) and ncd (green) (PDB ID: 2NCD (Sablin et al., 1996)) reveals similarity of their catalytic cores. Mg^{2+}ADP is shown as a ball and stick model.

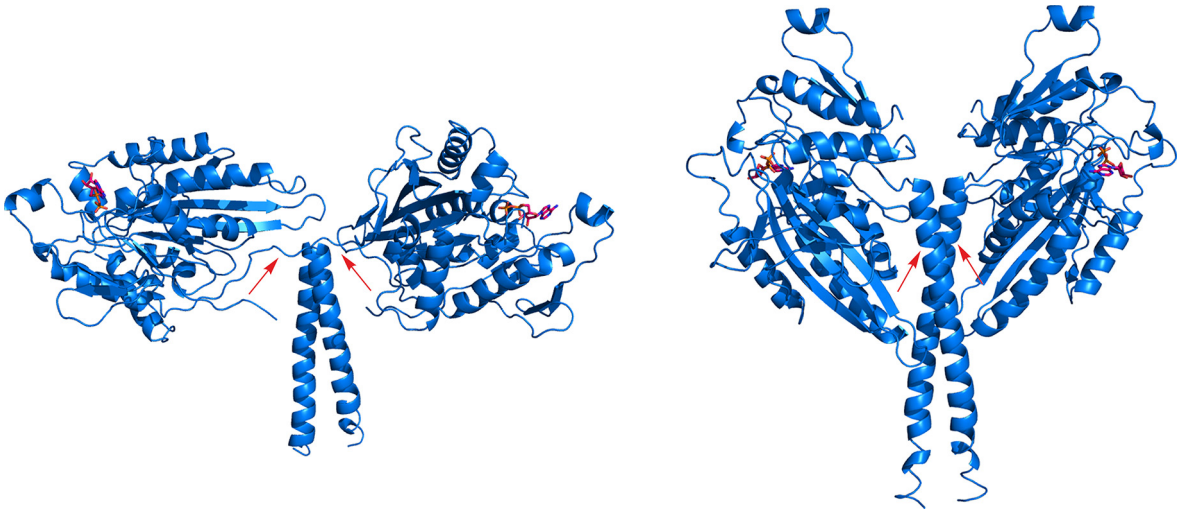

Figure 1.8: Influence of neck region orientation on kinesin directionality. Differently oriented neck region in the structures of rat conventional kinesin dimer (on the left) (PDB ID: 3KIN (Kozielski et al., 1997)) and in ncd C-type motor (on the right) (PDB ID: 2NCD (Sablin et al., 1996)). Neck linker of the conventional kinesin and neck region of ncd are highlighted with red arrows.

Sequence conservation is not retained outside of the catalytic core of the kinesins. After the

hinge region that connects the motor and neck linker with the rest of the kinesin body, there is an elongated stalk with one or more regions with the potential of coiled-coil structure creation that supports oligomerisation into dimers or higher oligomers. The conventional kinesin heavy chain ends with a small tail domain that facilitates binding to cargoes (Figure 1.4) (Yang et al., 1989).

Conventional kinesins perform their mode of action as tetramers with KHC and KLC homodimers. The Kinesin-2 family works as heterotrimers (two complementary motors and an auxiliary protein). Eg5, a member of Kinesin-5 family, has the ability to form homotetramers. A representative of the Kinesin-3 subfamily, Kif1A, utilises the specialised K-loop to perform movement as a monomeric motor (Okada and Hirokawa, 2000).

1.1.2 Mechanism of conventional kinesin movement

What makes kinesin not only an allosteric enzyme, but also a motor protein, is its processive movement. This feature allows conventional kinesin dimers to perform over a hundred steps before dissociating from MT. As kinesins are ATPases that convert the chemical energy of ATP hydrolysis into mechanical movement, their speed depends on the rates of their enzymatic turnover. The process of kinesin movement can be observed from two perspectives. First, by looking into chemical kinetic events driven by the enzyme, and secondly, by looking at structural changes occurring in the kinesin dimer, in relation to MTs, upon each of the enzymatic steps (Woehlke and Schliwa, 2000).

The state of the motor domain can be referred to as open, closed or trapped, depending on its nucleotide loading state. In the MT-free environment the majority of kinesins exist in the ADP-bound state (trapped state). The ADP release is a rate-limiting step in ATP turnover. ADP-bound kinesin motor domain possess low affinity for MTs. Binding to MTs changes the motor domain conformation to open, stimulating rapid ADP release. This nucleotide free state of kinesin (open) is stably bound to MTs. Once the nucleotide-binding site is free, ATP binding causes the motor domain conformation to change from open to closed. The kinetics of ADP and ATP binding is similar. The change from the open to closed state of the motor domain upon ATP binding leads to structural changes in the catalytic core active site. Two motor domain elements are rearranged when ATP is present in the active site: the switch I element (SSRSH) and switch II element (DLAGSE). In the closed conformation, they come together to create a salt bridge enabling γ-phosphate hydrolysis by positioning the water molecule, crucial for the process. This was shown by Parke et al. (2009), in their Eg5-AMPPNP structure. The γ-phosphate hydrolysis occurs in the closed state, with the kinesin head attached to the MT and does not result in any structural changes in the motor domain. However, γ-phosphate release returns the cycle to the open state. Kinesins can perform their

catalytic action both in the presence and absence of MTs, although their presence speeds up the process significantly (about 10^4 fold) (Cross, 2004). The cycle of kinesin enzymatic turnover is summarised in Figure 1.9.

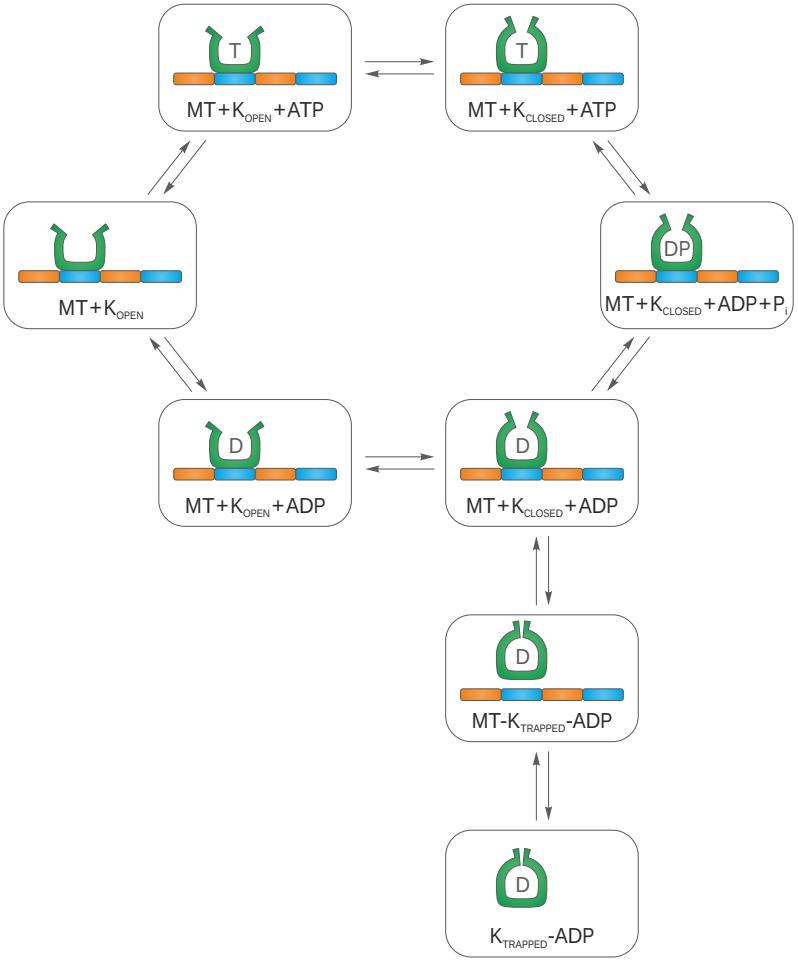

Figure 1.9: Influence of the nucleotide state of the motor domain on kinesin enzymatic turnover. Kinesin enzymatic turnover in the various nucleotide states (D-ADP, T-ATP, P_i) in the presence of MTs. Figure adapted from Cross (2004).

Kinesin movement cannot be considered independently of MTs. Although crystal structures of the motor domains allow a detailed insight into the catalytic core fold, they do not provide information about the mechanism of kinesin movement, parts of the motor contacting MTs and the secondary structure elements rearrangement during the enzymatic cycle. The visualisation of kinesins and their tracks was possible by applying cryo-electron microscopy (cryo-EM). The MT-interacting region of the kinesin is composed of helices α4, α5 and α6. All of these helices are placed on the same side of the eight-stranded β-sheet. On the opposite side, several loops (loop L7 — the P loop, loop 9 — switch I, loop 11 — switch II) create the nucleotide-binding site. Binding of the MTs and the nucleotide leads to conformational changes, which are further amplified and result in a neck linker movement. Once bound to MTs, switch II helix (α4) is extended by an ordered part of loop L11. The presence of ATP

causes helix α6 extension and consequently the neck linker docks onto the motor domain (Sindelar and Downing, 2007). A recent crystal structure report of a kinesin motor domain bound to tubulin dimer (Figure 1.10) stays in line with all cryo-EM data and allowed an additional, atomic level insight into the interaction between the kinesin and MTs (Gigant et al., 2013).

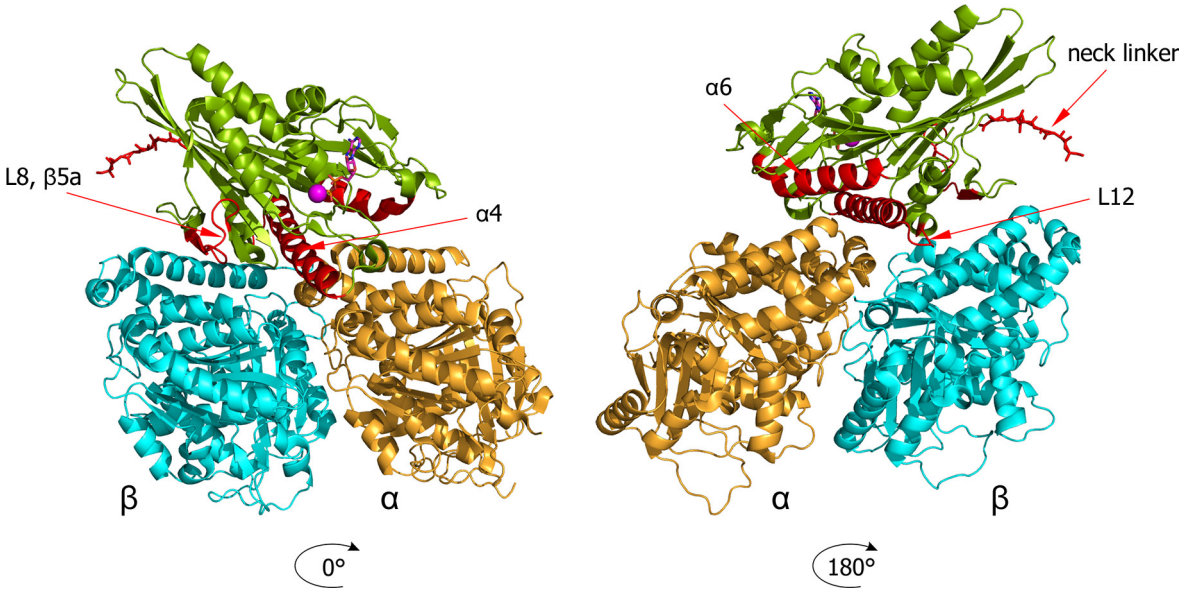

Figure 1.10: Overall structure of kinesin-tubulin complex (PDB ID: 4HNA (Gigant et al., 2013)). The tubulin heterodimer is coloured in orange for α- and blue for β-tubulin. The conventional kinesin is shown in green. Part of the motor involved in the tubulin-heterodimer binding (L8, β5a, α4, L12, α6) and the neck linker (ball and stick model) are coloured in red. Mg^{2+}ADP is shown in magenta as a ball and stick model.

The relative conformation between the motor domain and the neck linker can be linked with the nucleotide bound in the active site of the catalytic core. The ADP-bound state is associated with the neck linker in an undocked (disordered) position, whereas in the ATP-bound state the neck linker is docked (ordered) to the motor domain. The shift between these two locations creates a power stroke by switching from disordered to ordered conformation, causing the whole motor domain to exert force and move forward (Figure 1.11) (Woehlke and Schliwa, 2000). It is worth mentioning that the correlation between the neck linker position and bound nucleotide is genuine only in the presence of MTs (Sindelar et al., 2002).

Although the exact model of how conventional kinesins processively move along MTs is still not entirely understood, the asymmetric hand-over-hand is the most common and accepted one (Figure 1.12). In this model, each kinesin head undergoes a different conformational change as it moves forward and therefore the final motor domain conformation is different from the initial one. The active domains that create dimer through their neck regions alternately hydrolyse a single ATP molecule, causing one head to stay bound to the MT, and the other to dissociate (Asbury et al., 2003). The sequential ADP release occurring in both

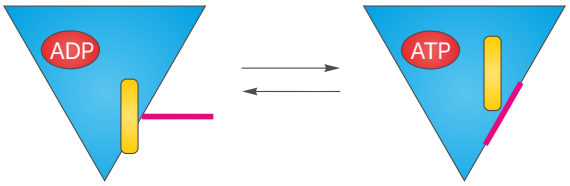

Figure 1.11: Diagram of differences in the kinesin motor domain in different nucleotide-bound states in the presence of MTs. The ADP-bound state is correlated with the switch II cluster (yellow) in the down position and an undocked neck linker (pink). ATP binding induces switch II cluster to move upwards and allows neck linker docking onto the motor domain.

kinesin heads produces a "stepping" type of kinesin movement (Hackney, 1994). This type of motion requires a head-to-head coordination, in order to keep the processivity, and this type of communication has been termed as a "gating mechanism", where the changes in one motor domain enable the occurrence of the catalytic steps in the partner head (Gennerich and Vale, 2009).

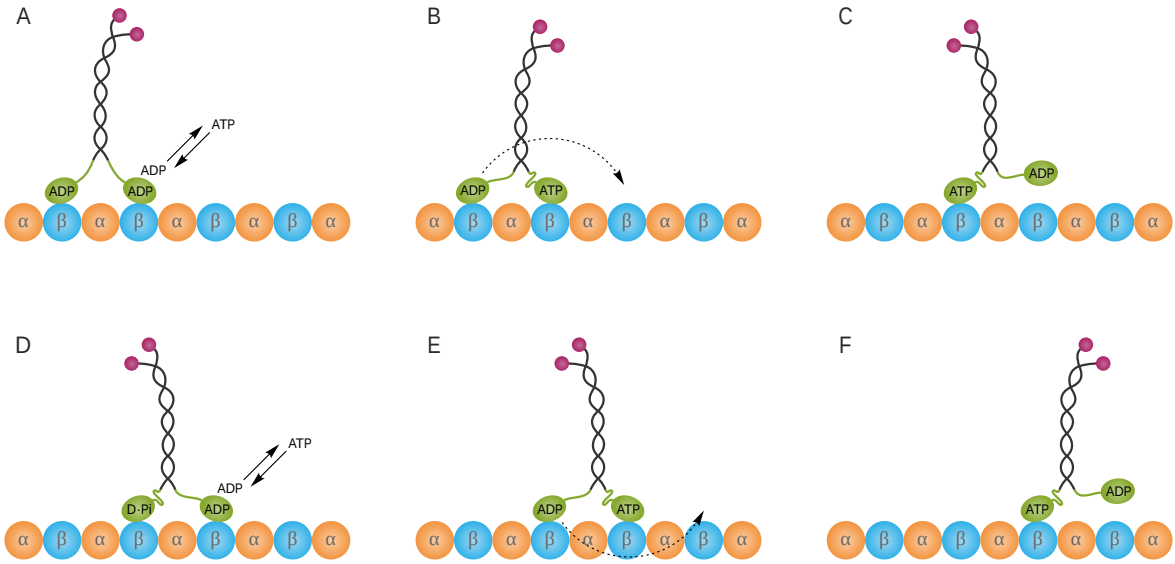

Figure 1.12: Illustration of the hand-over-hand kinesin mechanism of movement. (A) One of the kinesin dimer motor domains is stimulated by MTs, releases ADP, and binds ATP. (B) ATP binding causes docking of the neck linker to the catalytic core of the kinesin, neck docking generates the power stroke. (C) The ADP bound head is now presented in front of the ATP bound one. (D) ATP is hydrolysed, Pi released, the ADP bound head exchanges the nucleotide. (E) The second head undergoes a process analogous to the one described in point B, the neck linker docks, the power stroke occurs. (F) Kinesin performs a second step, analogous to the one in step C. Figure adapted from Toprak et al. (2009).

1.1.3 Functions of kinesins

Kinesins fulfil a variety of functions within eukaryotic cells (summarised in Table 1.1). They transport synaptic proteins, the Golgi apparatus, endoplasmic reticulum, endosomes, lysosomes and mitochondria, promote neuron polarity and elongation. They have also been shown to participate in axonal and dendritic transport (Hirokawa et al., 2009; Seog et al., 2004).

Kinesin family	Function
Kinesin-1	Transport of vesicles, organelles and mRNA
Kinesin-2	Transport of vesicles, melanosomes, intraflagellar transport
Kinesin-3	Transport of vesicles
Kinesin-4	Positioning of chromosomes, intraflagellar transport
Kinesin-5	Organisation and separation of mitotic spindle
Kinesin-6	Assembly of spindle midzone and cytokinesis
Kinesin-7	Attachment of chromosomes and kinetochore
Kinesin-8	Congression of chromosomes
Kinesin-9	Intraflagellar transport
Kinesin-10	Positioning of chromosomes
Kinesin-11	Function poorly understood
Kinesin-12	Organisation and maintenance of mitotic spindle
Kinesin-13	Correction of kinetochore-MT errors
Kinesin-14A	Organisation of spindle poles, transport
Kinesin-14B	Organisation of spindle poles, transport

Table 1.1: Kinesin families and their functions (Verhey and Hammond, 2009).

Another scenario where kinesin activity is crucial is cilia formation. Primary cilia are a place of various signalling events crucial for cellular homeostasis (Verhey et al., 2011). Proper execution of mitosis also relies on kinesin activity. To date, sixteen human kinesins have been implicated in various stages of cell division from bipolar spindle initiation, elongation and maintenance, MT dynamic modulation, accommodating MT and kinetochore interaction, regulating chromosome structure, dynamics and congression to cytokinesis (Rath and Kozielski, 2012). Figure 1.13 (top) depicts kinesin function in cellular division. Figure 1.13 (bottom) shows specific functions fulfilled by different motors. Frequently a single kinesin can perform multiple functions, e.g. in mitosis and in neuronal development or intracellular transport (Kif2A (Hirokawa et al., 2009; Ishikawa et al., 2008), Kif4A and Kif4B (Martinez et al., 2008; Zhu and Jiang, 2005), Eg5 (Blangy et al., 1995; Ferhat et al., 1998a), Kif15 (Boleti et al., 1996; Buster et al., 2003), Mklp1 (Ferhat et al., 1998b; Nislow et al., 1992)).

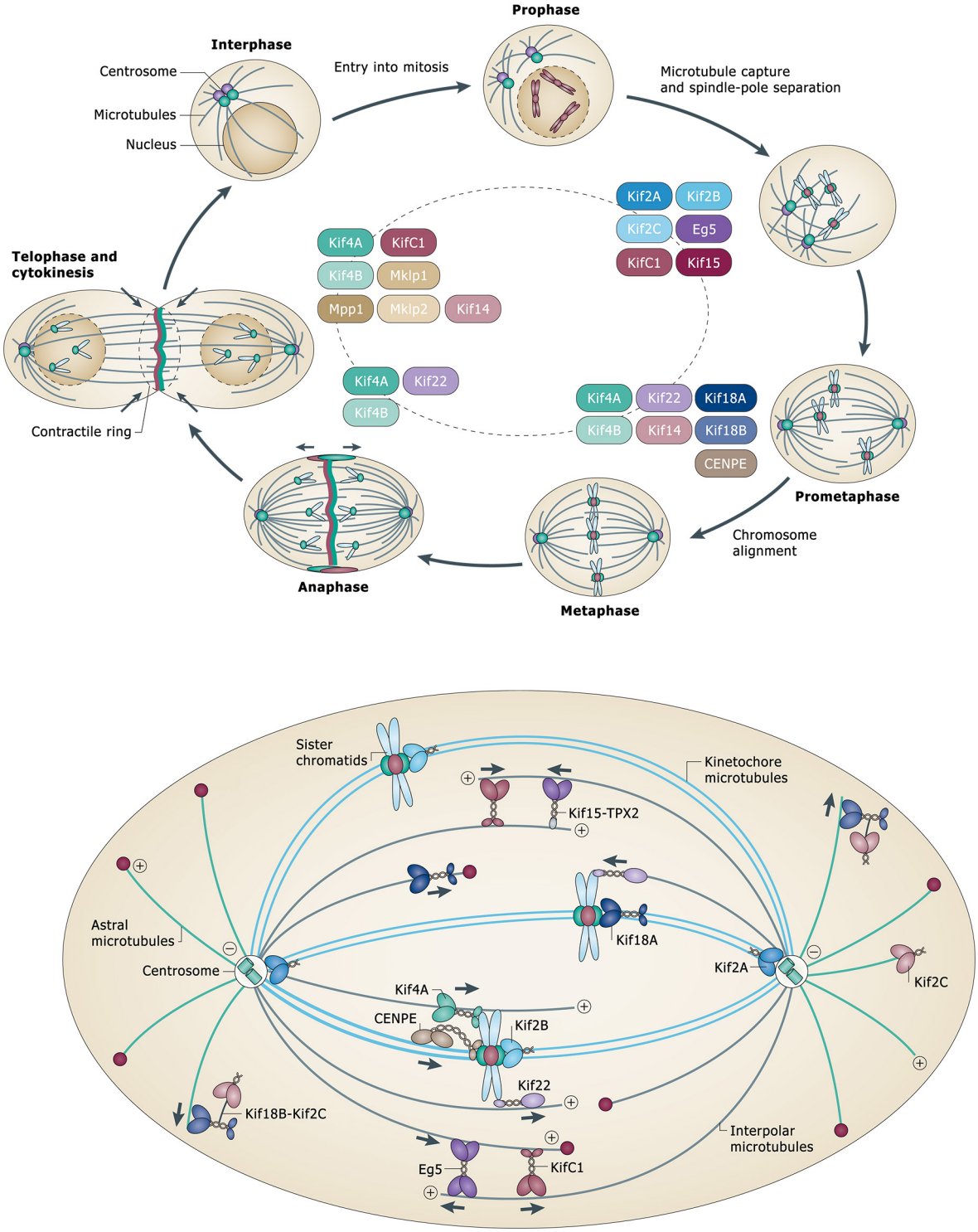

Figure 1.13: Kinesins in mitotic cell division. Top figure depicts kinesin functioning in cellular division. The bottom one shows specific functions fulfilled by different motors. Adapted by permission from Macmillan Publishers Ltd: [Marta Klejnot] (Rath and Kozielski, 2012), copyright (2012).

1.1.4 Regulation of kinesins

Kinesins possess control mechanisms allowing them to manage their activity and ensure energy efficiency. Although the process by which a kinesin switches on and off is not well characterised, it is believed that the presence / absence of cargo induces an active or inhibited state. Autoinhibition has been reported for Kinesin-1, Kinesin-2 and Kinesin-3 families (Verhey and Hammond, 2009). The structure of the autoinhibited *Drosophila melanogaster* Kinesin-1 dimer revealed a mechanism for this process, showing that a single tail peptide binds between two dimer heads, stabilising the ADP bound conformation, and precluding the advancement of the catalytic cycle (Kaan et al., 2011). The other question is how kinesins are targeted to their zone of action, for example the bipolar spindle in the case of mitosis. Phosphorylation has been implicated as a modification used in kinesin targeting (Verhey and Hammond, 2009).

1.1.5 Kinesins as targets in anti-mitotic therapies

In order to successfully divide, the genome of the dividing cell has to be properly segregated and separated. Since cancer cells divide rapidly, the mitotic spindle is an appealing drug target. Several anti-proliferative drugs targeting MTs have been developed, like taxanes (stabilising MTs) and vinca alkaloids (depolymerising MTs) (Rath and Kozielski, 2012). These agents, though effective, have several drawbacks, mostly because MT polymers are not exclusively vital in the process of cell division but also fulfil roles during neuronal transport and other non-neuronal transport events. This type of treatment may lead to acute side effects. Moreover, prolonged treatment leads to drug resistance (Miyamoto et al., 2003). The requirement for kinesin activity in mitosis makes them attractive candidates as drug targets that may circumvent problems associated with MT targeting drugs. The first selective kinesin inhibitor was discovered in a phenotype-based screen scouting for small molecules inhibiting the bipolar spindle assembly (Mayer et al., 1999). The identified compound did not affect MT stability, but it specifically targeted Eg5 and led to the formation of monoastral spindle (Figure 1.14). Based on this characteristic phenotype the compound was named monastrol. This small molecule was then commonly used in various biochemical, functional and mechanistic studies of Eg5 (Liu et al., 2011).

The 1.9 Å structure of Eg5-ADP plus monastrol complex provides insight into the inhibitor-binding pocket (Figure 1.15) (Yan et al., 2004). The inhibitor-binding pocket is restricted by helix $\alpha 3$, loop L5 and helix $\alpha 2$, with about 20 residues contributing to monastrol stabilisation. Since its binding pocket is placed 12 Å away from the nucleotide-binding site, monastrol is considered an ATP-noncompetitive inhibitor (Yan et al., 2004). The comparison of the

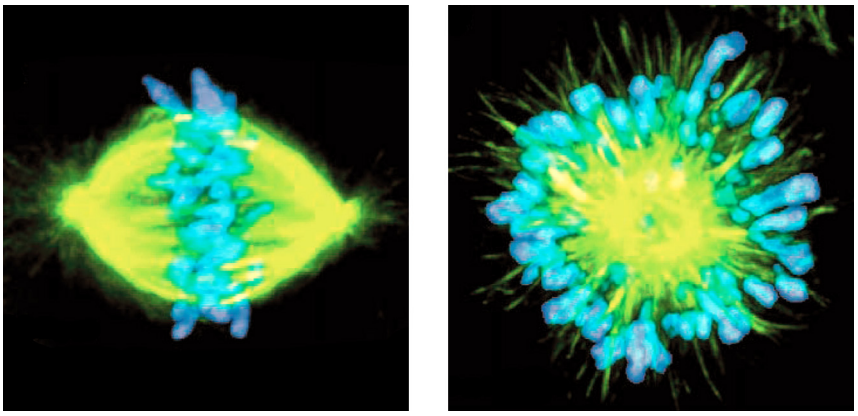

Figure 1.14: Monastrol leads to formation of monoastral spindles in dividing cells. Two pictures show the normal bipolar spindle of the control cells treated with DMSO (left) and the monastrol treated cells with a rosette-like spindle morphology (right). From Mayer et al. (1999). Reprinted with permission from AAAS.

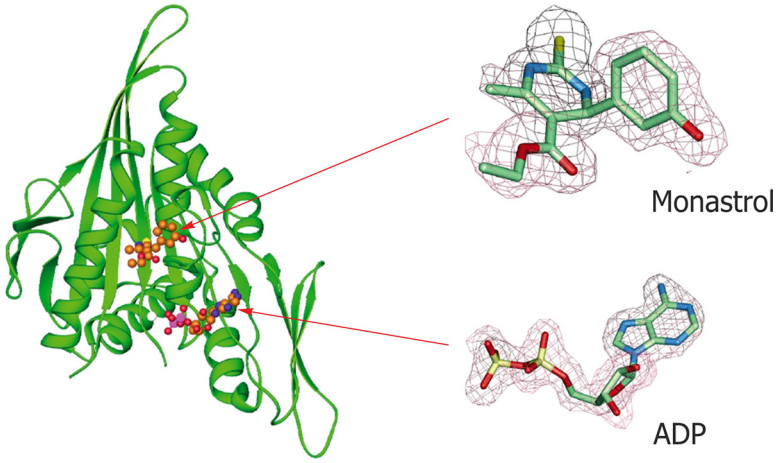

Figure 1.15: Eg5-ADP in a complex with monastrol. The overall Eg5 structure (green) with Mg^{2+} (white ball), ADP and monastrol (balls and sticks: C — orange, N — blue, S — yellow, O — red). The electron densities of ADP and monastrol are presented. Reprinted from Yan et al. (2004). Copyright (2014), with permission from Elsevier.

native and monastrol-bound structure (Turner et al., 2001), several conformational changes were detected. Starting from Arg112 (helix $\alpha 2$) and Tyr211 (helix $\alpha 3$) moving outwards, to Trp127 (loop L5) that swings down from the solvent-exposed area (7 Å) and forms a π-interaction with the Tyr211 ring (Figure 1.16). These changes in Eg5 conformation close the entrance of the induced-fit binding pocket (Yan et al., 2004). Additionally the γ-phosphate sensor (switch I) moves outward in the solvent exposed direction (6 Å). Changes occur around the inhibitor-binding pocket leading to the rearrangements of helix $\alpha 4$ and $\alpha 5$ (switch II, move upwards) and the neck linker (docked, aligned with the motor domain) (Figure 1.17) (Yan et al., 2004). The structural insight into the allosteric inhibitor-binding pocket of Eg5 enabled structure-based drug design and development of others potent Eg5 inhibitors. Another kinesin targeted in anti-mitotic therapies is CENPE. Several Eg5 and CENPE targeting drugs are

currently undergoing testing in multiple phase I and II clinical trials (Rath and Kozielski, 2012).

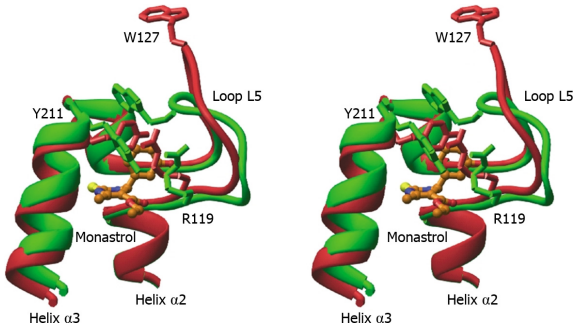

Figure 1.16: A stereo view of the monastrol-binding pocket, before (red) and after (green) monastrol binding to Eg5-ADP. Residues R119, W127 and Y211 are highlighted to emphasise their movement upon inhibitor binding. Reprinted from Yan et al. (2004). Copyright (2014), with permission from Elsevier.

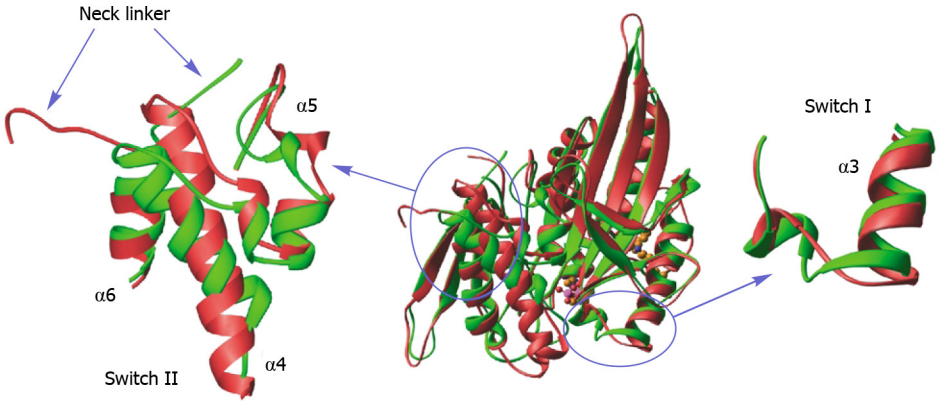

Figure 1.17: Differences in switch I, switch II and neck linker regions upon monastrol binding. Eg5 structures before and after inhibitor binding are coloured in red and green respectively. The circled parts of the structure are magnified. Reprinted from Yan et al. (2004), Copyright (2014), with permission from Elsevier.

1.2 Human mitotic kinesin — Kif15

Kif15 (KIF15, Hklp2, Kinesin-12 family) was first identified in the *Xenopus laevis* genome, along with three other kinesin-like proteins, and has been named Xklp2 — *Xenopus* kinesin-like protein 2 (Vernos et al., 1993). After Xklp2 was detected in the *Xenopus* system, homologous genes were detected in mice, though the architecture, or protein function was not assigned in this case (Nakagawa et al., 1997).

The elucidated gene encodes a 159 kDa protein, comprising an N-terminal motor domain, followed by a long stalk with several coiled-coil regions. The analysis of the Xklp2 sequence revealed unusual feature of its C-terminal tail, which consists of coiled-coil (Figure 1.18).

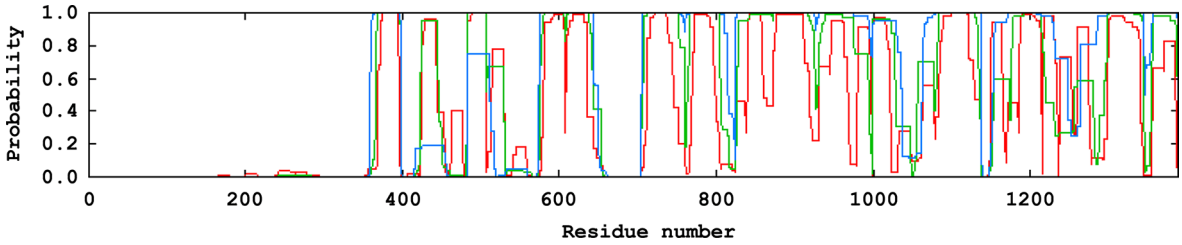

Figure 1.18: Probability of coiled-coil content in human Kif15 sequence. The plot was generated using COILS software. The program compares the query sequence with a database of reported coiled-coils and assigns a similarity factor, which is then compared to the distribution of scores in globular and coiled-coil proteins. Finally, the probability of coiled-coil formation is computed. Three lines correlate to the sequence fragment lengths that were used when scanning the database (green — 14, blue — 21, red — 28 residues) (Lupas et al., 1991).

This feature makes the overall protein design resemble the topography of myosin II, rather than that of a typical kinesin. It has also been pointed out that the stalk (500 amino acids) shares about 20% sequence identity with myosin (Boleti et al., 1996). A typical consensus phosphorylation site for Cdc2 in Xklp2 was found (Thr666), however unlike in other superfamily members, it is not located in the tail domain. Instead, it is situated in the stalk, in the region where the coiled-coil is interrupted (Boleti et al., 1996). Phosphorylation of this conserved motif in Eg5 (Thr927) is known to be responsible for its targeting to spindle MTs in the mitotic prophase, and a loss of this modification causes a failure of Eg5 localisation (Sawin and Mitchison, 1995). The role of this site in Kif15 has not been addressed yet, though it is possible that it is analogous to this feature of Eg5. The C-terminal tail domain was assigned as residues 1137–1387. Moreover the presence of a leucine zipper (four leucine residues with six amino acids separating each of them, a common structural protein motif, often involved in oligomerisation) was detected at the very end of the tail domain. Initial protein characterisation revealed that the protein moves along MTs in the plus-end direction with rather low velocity (3.2 ± 1.2 μm/min), therefore it is a slow kinesin (Boleti et al., 1996). In comparison, conventional kinesin, considered as a fast motor protein, moves 10 to 60 times faster (Woehlke and Schliwa, 2000).

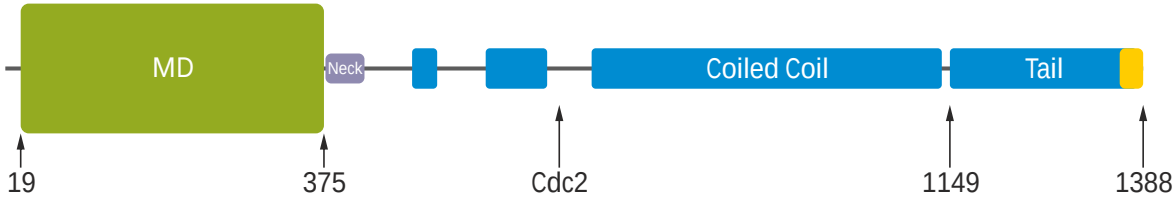

Figure 1.19: Overall Kif15 architecture. The motor domain (MD) shown in green is followed by a neck region and stalk domain with coiled-coil regions and a putative tail (blue). The leucine zipper is presented in yellow. Residue numbering relates to the human Kif15 representative.

```
Hklp2      MAPGCKTELRSVTNGQSNQPSNEGDAIKVFVRIRPPAERSGS-ADGEQNLCLSVLSSTSL 59
KIF15      MAPGCKSELRNVTNSHSNQPSNEDDAIKVFVRIRPAEEGARS-ADGEQSLCLSVLSQTAL 59
Xklp2      MPPGTKGDPSNVTQPLPCLPSAEEDAIKVFVRIRPPVEGTLTGVDGEQGLCLTALSSTTI 60
KRP-180    --------MSKKLKEQAANDASEGDAIKVFVRVRPSE---SHDADAAFGQCLEVRLPDTI 49
KLP-18     ----------------------MSQYIKCYGRVRPSAR------LGAPSESLFVG-GRVV 31

Hklp2      RLHSNPEPKTFTFDHVADVDTTQESVFATVAKSIVESCMSGYNGTIFAYGQTGSGKTFTM 119
KIF15      RLHSNPDPKTFVFDYVAGMDTTQESVFSTVAKSIVESCMSGYNGTIFAYGQTGSGKTFTM 119
Xklp2      RLHSKPEPKMFTFDHVANVDTNQESVFSSVAKNIVESCMNGYNGTIFAYGQTGSGKTFTM 120
KRP-180    IMHSKPEPKVFTYDHVTAANTTQESVFTAVGKRIIESCVGGFNGTIFAYGQTGSGKTFTM 109
KLP-18     TIETDNGSKRYELHHIFDSSSSQEDVFGTVAKKIVEDCVEGYNGTVFAYGQTGSGKTHTM 91

Hklp2      MGPSES-DNFSHNLRGVIPRSFEYLFSLIDREKEKAGAGKSFLCKCSFIEIYNEQIYDLL 178
KIF15      MGPSDS-DNFSHNLRGVIPRSFEYLFSLIDREKEKAGAGKSFLCKCSFIEVYNEQIYDLL 178
Xklp2      LGPSES-DNFTHNLRGVIPRSFEYLFFLINREKEKAGEGKSFLCKCSFIEIYNEQIFDLL 179
KRP-180    LGPCEDGDNFHHEMRGVIPRSFEYLFSLVNREREKHGDRYEFLCRCSFLEIYNEQIYDLL 169
KLP-18     LGPCDS--WTDQELMGLIPRSVEHVFQHLDT-KAKECQKLTFSVSVEFVELYNEVIYDLL 148

Hklp2      DSASAGLYLREHIKKGVFVVGAVEQVVTSAAEAYQVLSGGWRNRRVASTSMNRESSRSHA 238
KIF15      DSASVGLYLREHIKKGVFVVGAVEQVVASAAEAYQVLSRGWRNRRVASTSMNRESSRSHA 238
Xklp2      DSASAGLFLREHIKKGVFVVGAVEQVVTSAAEAYQVLSMGWRNRRVASTSMNRESSRSHA 239
KRP-180    DPASLGLHLRENMKKGVFVDGLIERAVASASEAYGVLQAGWHNRRVAATSMNRESSRSHA 229
KLP-18     N-AKNKVQLRDSGKD-IQLVGALSKNVDNPLDLMHLVQKGWQERSTGSTAMNAESSRSHA 206

Hklp2      VFTITIESMEKSNEIVNIRTSLLNLVDLAGSERQKDTHAEGMRLKEAGNINRSLSCLGQV 298
KIF15      VFTITIESMEKSSEAVNIRTSLLNLVDLAGSERQKDTHAEGMRLKEAGNINRSLSCLGQV 298
Xklp2      VFTVTIESMEKTNDLVNIRSSQLNLVDLAGSERQKDTQTEGVRLKEAGSINRSLSCLGQV 299
KRP-180    VFTVSIESKEKKAGVSNIRVSQLHLVDLAGSERQKDTKAIGVRLKEAGSINKSLSILGNV 289
KLP-18     LLIIRIKTQERTGELVKERSSILNLVDLAGSERQTHTKSSGDRLKEATNINSSLTVLGRC 266

Hklp2      ITALVDVGNGKQRHVCYRDSKLTFLLRDSLGGNAKTAIIANVHPGSRCFGETLSTLNFAQ 358
KIF15      ITALVDVGNGKQRHVCYRDSKLTFLLRDSLGGNAKTAIIANVHPGSRCFGETLSTLNFAQ 358
Xklp2      ITALVDVANGRQRHICYRDSKLTFLLRDSLGGNAKTFYIANVHPGSKCFGETLSTLQFAQ 359
KRP-180    IMALVDIAHGKQRHVPYRDSKLSFLLRDSLGGNAKTYIIANVHPDAKCFGETLSTLKFAR 349
KLP-18     IRLLADPSKAKG-HVPYRDSHLTHILKNSLGGNSKTAVIVNMHPDRDFAQESNSTLMFAQ 325

Hklp2      RAKLIKNKAVVNEDTQGN 376
KIF15      RAKLIKNKAVVNEDTQGN 376
Xklp2      RAKLIKNKAVVNEDTQGN 377
KRP-180    RAKMIKNRAVVNEDTQGN 367
KLP-18     SCTMIMNIATRNEVMTGD 343
```

Figure 1.20: Motor domain sequence alignment of Kif15 homologues. Human Hklp2 (Sueishi et al., 2000), rat KIF15 (Buster et al., 2003), *Xenopus laevis* Xklp2 (Vernos et al., 1993), sea urchin KRP180 (Rogers et al., 2000) and KLP-18 in *Caenorhabditis elegans* (Segbert et al., 2003). The alignment was generated using the ClustalW2 multiple alignment tool (Larkin et al., 2007). Small and hydrophobic residues are shown in red, acidic residues in blue and basic residues are shown in magenta. Glycine and residues containing hydroxyl, sulfhydryl or amine groups are shown in green.

In several proceeding studies, representatives of other Kif15 homologues have been described; KRP180 in sea urchin (Rogers et al., 2000), Hklp2 in human (Sueishi et al., 2000), KIF15 in rat (Buster et al., 2003) and KLP-18 in *Caenorhabditis elegans* (Segbert et al., 2003). All of these share high sequence homology within the motor domain (50–60%), and contain a rod-like stalk with a leucine zipper at the carboxy-terminus of the protein. The overall Kif15

architecture is presented in Figure 1.19. The sequence alignment of Kif15 motor domain homologues is shown in Figure 1.20.

The oligomeric state of the Kif15 protein was assessed by gel filtration and sucrose gradient centrifugation which indicated that it forms dimers (Wittmann et al., 1998). Moreover the experiments confirmed that the protein is asymmetric, as expected for such a long protein with a predominant rod-like shaped domain. The dimeric state of the protein was also established in case of KRP180 (Rogers et al., 2000) and rat KIF15 (Liu et al., 2011).

1.2.1 Kif15 cellular localisation, functions and partner proteins

In the original paper by Boleti et al. (1996) Xklp2 was implicated as a centrosome associated protein that was mainly detected in dividing cells. Immunofluorescent staining performed in the *Xenopus* egg extract revealed its centrosomal localisation, from prometaphase and throughout mitotic cell division. In addition, a fraction of the protein could be detected on the spindle MTs, especially in close proximity to spindle poles. A portion of the protein could also be visualised in the cytoplasm in interphase. The centrosomal staining could not be abolished upon MT depolymerisation: after nocodazole (a MT depolymerisation agent) treatment of the *Xenopus* egg extract, Xklp2 staining was still visible on the centrosomes. This led to the belief that Xklp2 can co-localise with centrosomes in a MT independent manner. The effort to establish which part of the protein is in fact crucial for Xklp2 targeting to MTs pointed to the critical role of the protein C-terminus. It has also been established that, in order to perform movement, Xklp2 requires both N-terminal motor and C-terminals tail domains. Protein localisation on the bipolar spindle was further investigated and Xklp2 was believed to be required for its formation and maintenance, as well as for initial centrosome separation (Boleti et al., 1996).

This range of functions is highly similar to the role played in mitosis by Eg5. This kinesin is able to link antiparallel MTs due to its homotetrameric structure, and by performing plus-end directed movement, to slide them apart, and in doing so, to separate sister chromatids (Saunders and Hoyt, 1992; Sawin et al., 1992). Obviously, Kif15 would have to employ a somewhat different mechanism to promote spindle separation, because it does not have the ability to form tetramers. The necessity of Kif15 activity for proper mitotic spindle assembly and maintenance was initially somewhat controversial, pointing to its role in spindle preservation and elongation rather than initiation (Walczak et al., 1998).

New light was shed on the mechanism of Xklp2 action when it was recognised that it does not associate with centrosomes, and the centrosomal staining was due to Xklp2 presence

on minus-end MTs. But how can a plus-end directed motor accumulate at the MT minus-end? It has been shown that a cytoplasmic motor — dynein — can take part in Xklp2 localisation, together with the dynactin complex. Inhibition of dynein function (antibody addition), caused Xklp2 dissociation from the MTs (Wittmann et al., 1998).

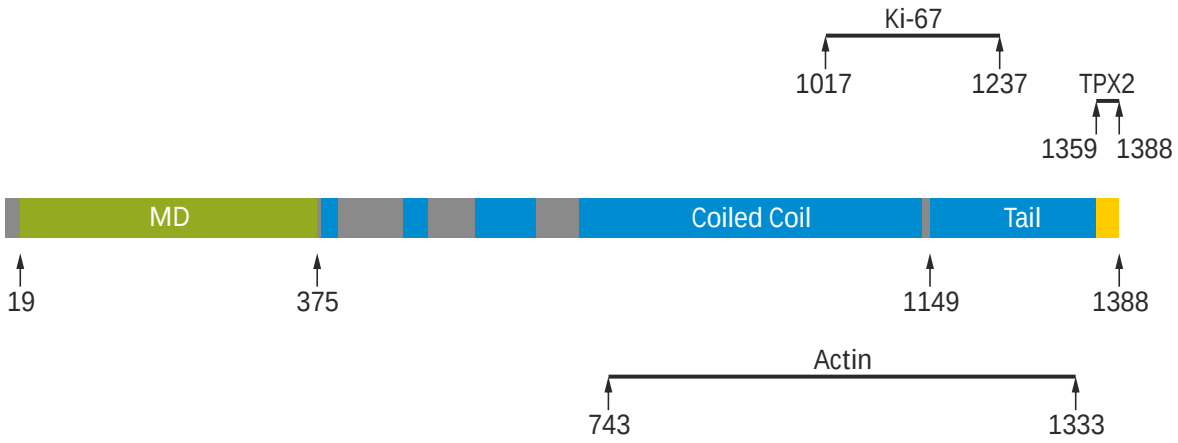

Figure 1.21: Bar diagram of Kif15 and its putative partner proteins. Black bars represent regions involved in the interactions. The numbering relates to human Kif15 residues. Colouring is as for Figure 1.19.

Furthermore a novel protein was identified — TPX2 (Targeting protein for Xklp2) that mediates the Xklp2 tail interaction with MTs. TPX2 is a highly basic 82.4 kDa MT-associated protein (MAP) that is located to the mitotic spindle after nuclear envelope breakdown (NEB) in a dynein-dynactin dependent manner (Wittmann et al., 2000). A human TPX2 homolog has also been described (Heidebrecht et al., 2003). The interaction between Xklp2 and TPX2 occurs through the Xklp2 leucine zipper (Figure 1.21), and even a single amino acid mutation in this region eradicates the ability of Xklp2 to bind MTs. Further analysis of the tail domain unveiled the function of the N-terminal tail part in supporting protein dimerisation. Occurrence of dimerisation seems to be important because of low endogenous Xklp2 affinity to MTs observed in *Xenopus* egg extract (Boleti et al., 1996), and it is possible that creation of a higher oligomeric state stabilises the interaction with MTs. Another interesting finding was the fact that the Xklp2 tail and TPX2 do not seem to bind at all when MTs are absent (Wittmann et al., 1998).

A similar cellular distribution could be observed for KRP180 in sea urchin, providing the first verification of Kif15 motor action *in vivo*. Moreover, the experiments in this setting further proved that KRP180 is not essential for primary events during mitosis, but it is crucial for maintenance and elongation of an already initiated spindle (Rogers et al., 2000). Additionally, a specific time point during mitosis has been pinpointed, when blocking KRP180 activity caused dramatic collapse of the spindles — just after NEB. This is in agreement with the notion that this class of proteins is targeted to MTs by TPX2, which co-localises with

MTs in NEB (Wittmann et al., 1998).

A separate study looked into KLP-18, a *C. elegans* homolog of Kif15, and its role in mitosis and meiosis. Its mitotic localisation resembled these described previously. In addition Kif15 was enriched in the interzone throughout late anaphase and telophase. *C. elegans* meiotic spindles lack centrosomes and KLP-18 was found to localise to the acentrosomal spindle. The protein was detected on disorganised MTs and remained on them upon spindle polarisation, concentrated mainly at the poles, but also between poles and chromosomes. Once cells entered anaphase, KLP-18 was concentrated in the interzone. It has been shown that KLP-18 activity is not essential in mitotic spindle centrosome dependent separation, but it is crucial for proper MT sorting and spindle assembly in the acentrosomal setting (Segbert et al., 2003).

Human Kif15 was detected in rather striking circumstances. Two-hybrid screening in yeast, utilising the forkhead-associated (FHA) domain of Ki-67 as bait, resulted in the pulling down of a novel human kinesin-like protein that shared 53% amino acid identity with Xklp2 (Sueishi et al., 2000).

Ki-67 is well known as a proliferation marker. It was first identified when Ki-67 antibody was generated by injecting mice with nuclei of Hodgkin lymphoma cells. Ki-67 is very effective as an indicator of cell division, because it is present during active stages of the cell cycle, but absent when cells are in the resting period. Although its existence has been known for 30 years, the exact function of Ki-67 is still not clear (Scholzen and Gerdes, 2000), though it has been implicated in the process of higher chromatin organisation and association with chromosomes (Takagi et al., 1999; Verheijen et al., 1989). The best-characterised part of Ki-67 is its N-terminal FHA domain. This is quite a common protein motif that has been shown to specifically recognise phosphorylated threonine residues, which often triggers assembly of protein complexes (Durocher and Jackson, 2002).

Interaction of Kif15 and Ki-67 led to the hypothesis that Kif15 can associate with chromosomes, through its interaction with the FHA domain. Regions required for interaction were further narrowed to residues 1–99 of Ki-67 and residues 1017–1237 of Kif15 (Figure 1.21). This interaction has been shown to occur both in yeast and *in vitro*, using recombinant protein expressed in *E. coli* (Sueishi et al., 2000).

Examination of the cellular distribution of Kif15 revealed its association with centrosomes at interphase, as shown in previous studies. In prometaphase and metaphase, Kif15 co-localises to the spindle. A novel observation was that a pool of Kif15 was detected in the equatorial region of the spindle. This localisation could not be abolished by depolymerisation of MTs, which resulted in the creation of a punctuate staining pattern of Kif15 bound to the chromosomes. These dots were in close proximity to centromeres although not centrally on them. Furthermore, it has been shown that mitotic full-length Kif15 presented a lower

electrophoresis velocity, than the one from interphase cells. It is tempting to assign this feature to protein phosphorylation, though it has never been tested. This hypothesis is appealing, as this could be a mechanism of protein modification that enables changes in its localisation during a cell cycle (Sueishi et al., 2000).

Another study looked at KIF15 from a different angle. Buster et al. (2003) reported expression of KIF15 in rat post-mitotic neurons and its effect on neuronal migration. The rat homologue of KIF15 shared all common features of this protein family, including N-terminal motor and a rod-shaped C-terminal domain. Their study emphasised the presence of a myosin tail homology domain in the stalk extending from amino acids 740 to 1333. Overall, the reported localisation in the mitotic cell for KIF15 stayed in line with all previous reports. A novel reported compartment of KIF15 association was suggested, located on the actomyosin ring upon cytokinesis and localisation with actin during interphase (Buster et al., 2003). A similar distribution was reported once before in sea urchin, but it has not been further investigated (Rogers et al., 2000). A closer look at the KIF15 mode of action in neurons showed that they perform an analogous function to that observed in mitosis, sorting and controlling MT movement (Buster et al., 2003). It has been further demonstrated that removing KIF15 activity makes axonal growth over two times faster and affects proper growth cone turning. Similar events occur after Eg5 depletion (Ferhat et al., 1998a). Nonetheless there were several differences in neuron phenotype upon deletion of these proteins. Lack of KIF15 caused a decrease in axonal branching while Eg5 activity elimination led to exactly the opposite effect. Co-immunoprecipitation of KIF15 with actin confirmed possibility of their co-localisation (Eg5 did not immunoprecipitate with actin) (Liu et al., 2011). Potentially, KIF15 could utilise its myosin tail homology domain located in the coiled-coil to associate with an actin-based motor and through this interaction contact actin (Figure 1.21), though this theory has not yet been diligently investigated.

1.2.2 Kif15 activity and possible clinical implications

Kif15 exerts only a fraction of the forces important for bipolar spindle vitality and its functioning is not necessary for spindle formation. Kif15 depleted cells can successfully execute mitotic division, although it has been noted that without its activity the assembled spindles are shorter (in comparison with control cells) (Vanneste et al., 2009). A different effect of Kif15 loss was observed when it was tested in cells treated with monastrol (an Eg5 inhibitor (Mayer et al., 1999)), in the context of inhibited Eg5 activity, where creation of monopolar spindles rose to 95% from 61% in control cells. Subsequent monastrol washout caused cells to recover 15% faster if Kif15 activity was present. The localisation of Kif15 and Eg5 during metaphase has also been shown to differ. Eg5 was visualised mostly on spindle MTs in

close proximity to the spindle poles, while Kif15 was enriched mostly in the central part of the spindle, close to chromosomes. Also, the time of their association to MTs was different, with Eg5 gathering around the centrosome at the origin of mitosis, and Kif15 appearing on spindles after NEB. Cells with fully assembled spindles, blocked in the metaphase, did not collapse upon Eg5 inhibition as long as Kif15 activity was retained. And when it was depleted, monopolar spindle percentage rose dramatically. Additionally, overexpression of Eg5 did not lead to any spindle defects, whilst Kif15 overexpression led to multipolar spindle formation and major MT formation abnormalities. All this strongly points to a role for Kif15 in spindle elongation and maintenance (Vanneste et al., 2009).

A distinct Kif15 quality is its chromosomal localisation via interaction with Ki-67. The interaction has been further supported by the observation that Ki-67 silenced cells did not disrupt Kif15 MT localisation but caused a chromosome association loss. Moreover, the spindles were about 12% longer than these in control cells, showing that once Kif15-chromosome interaction is blocked, it contributes more towards spindle elongation (Vanneste et al., 2009).

An independent study identified Kif15 as the motor protein responsible for the maintenance of the bipolar spindle in metaphase from the pool of all human kinesins, utilising a siRNA approach. This work led to conclusions similar to these of Vanneste et al. (2009), depicting Kif15 as crucial for rapid spindle elongation, but not for its assembly. Also, the interaction between TPX2 and Kif15 was verified in human cells. This study went one step further, showing that overexpression of Kif15 can rescue formation of the spindle when Eg5 activity is blocked by its inhibitor (Tanenbaum et al., 2009).

Overall, Kif15 and Eg5 seem to work together to assure bipolar spindle wellbeing. Co-inhibition of both of Kif15 andf Eg5, might be of value from a clinical point of view. Especially since it is suspected that Eg5 inhibition can be overcome by upregulating Kif15 expression levels. A patent for Kif15 inhibitors was deposited in 2004 (McDonald et al., 2004), although no biochemical or structural data were published since to validate these compounds as potent Kif15 targeting drugs. Until now, knowledge about Kif15 deregulation in cancer or other proliferative-related diseases is poor (Scanlan et al., 2001).

A more recent study showed that interfering with MT dynamics upon Eg5 inhibition enables Kif15 to bypass the role of Eg5 in initial centrosome separation, to establish the bipolar spindle, and progress successfully through mitosis (Florian and Mayer, 2011). This is interesting, particularly in the context of targeting Eg5 and MTs in cancer treatment that could be bypassed by employing an acentrosomal nucleation pathway (in a manner similar to the one described in *C. elegans* meiosis (Segbert et al., 2003)). It is worth noting that this effect varies depending on the MT-targeting drug deployed: it was observed when using vinblastine, but not paclitaxel. These results emphasise the need for careful consideration

when combining Eg5 and MT-targeting drugs (Florian and Mayer, 2011).

1.3 Kif7 and Kif27, Kinesin-4 family representatives

Human Kif7 and Kif27, members of the Kinesin-4 family (Katoh and Katoh, 2004a, b) are paralogues, presenting the typical kinesin fold. Overall, they share 44% sequence identity, and even more in the motor domains (61%).

1.3.1 Kif7 and Kif27 structural organisation

Kif7 and Kif27 possess an N-terminal, globular motor domain, containing a nucleotide binding and MT-interacting region, followed by a stalk domain predicted to form a discontinuous coiled-coil, and C-terminal tail domain (Figure 1.22).

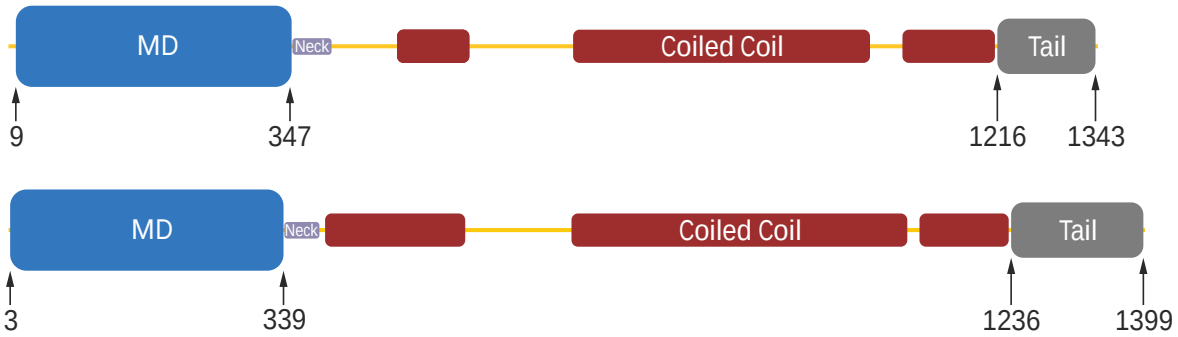

Figure 1.22: General architecture of Kif7 (top) and Kif27 (bottom). The globular motor domain (MD, blue) is followed by the neck linker (violet), a stalk predicted to form a discontinuous coiled-coil (red), followed by a C-terminal tail domain (grey).

Both proteins are orthologues of the *Drosophila melanogaster* kinesin-like protein called Costal-2 (Cos2) that plays a key role in Hedgehog (Hh) signalling. The Hh ligands (Sonic hedgehog — SHh, Indian hedgehog — IHh and Desert hedgehog — DHh) are glycoproteins that have a crucial role during embryogenesis (Bijlsma et al., 2004) and tumorigenesis (Pasca di Magliano and Hebrok, 2003). Their signals are transduced through the transmembrane proteins Patched 1 (Ptch 1), Patched 2 (Ptch 2) and Smoothened (Smo). In the absence of Hh proteins, Ptch family members suppress Smo activity, which becomes activated upon Hh ligand binding to the Ptch protein. These events lead to the activation of the transcription factors Gli 1, Gli 2 and Gli 3. The direct interaction of the MT-bound protein Cos2 with Cubitus interruptus (Ci) in the cytoplasm is believed to be essential for its sequential phosphorylation by three distinct kinases: Protein Kinase A (PKA), Glycogen Synthase Kinase β (GSKβ) and Casein Kinase 1 (CK1), and subsequent proteasome-dependent cleavage. The

generated fragment, CiR, diffuses into the nucleus, where it corepresses Hh target genes (Tay et al., 2005; Wang et al., 2000).

1.3.2 Kif7 and Kif27 role in primary cilia

Human Kif7 and Kif27 function in the primary cilium, a sensory organelle (Verhey et al., 2011), where they have been shown to interact with Gli transcription factors, and are believed to fulfil distinct functions in regulating Gli proteins. Kif7, a critical regulator of mammalian Hh signalling, acts as both positive and negative regulator in the Hh signalling pathway, but it performs this role differently from Cos2, as it does not interact with Smo or Fu (Endoh-Yamagami et al., 2009). The current hypothesis suggests that Kif7 is a plus-end directed motor, transporting Gli2 from the cilium, thus preventing its activation (Goetz and Anderson, 2012). In contrast, Kif27 interacts with Fu, which takes part in the construction of the primary cilium (Wilson et al., 2009). Kif7 and Kif27 seem to work together in vertebrates to fulfil the role of the single Cos2 gene in *D. melanogaster*. There are several reports describing Kif7 mutant alleles in mouse embryos and their characterisation has highlighted the critical role of Kif7 in primary cilium formation and Hh signalling (Cheung et al., 2009; Endoh-Yamagami et al., 2009; Liem et al., 2009). One of these alleles carried a L130P mutation, and caused the death of mouse embryos at the end of gestation.

1.3.3 Kif7 associated diseases

In humans, various Kif7 mutations have been linked to a range of neurodegenerative diseases including Joubert (Dafinger et al., 2011), Hydrolethalus and Acrocallosal syndromes (Putoux et al., 2011). In addition, since inappropriate activation of Hh signalling can lead to the formation of medulloblastomas, rhabdomyosarcomas, basal carcinomas and other tumour types (Goetz and Anderson, 2012), and given Kif7's role in human primary cilium formations and Hh signalling (Liem et al., 2009), Kif7 might also be linked to other diseases such as cancer.

1.4 Objectives

The objectives of this project were:
– to create a kinesin motor domain expression panel;
– to obtain biochemical, kinetic and structural insight into a poorly described motor — Kif15;
– to structurally characterise Kinesin-4 family members.

Chapter 2

Materials and methods

2.1 Materials

cDNAs, codon-optimised for expression in *E. coli*, were purchased from GenScript. DTT, glutathione, IPTG, imidazole, NaCl, Na-EGTA, $MgCl_2$, meso-erythtritol, methanol, PIPES, PMSF, primers for subcloning, taxol, TB medium, TBS-T, Tris-HCl and urea were bought from Sigma. All restriction enzymes and Quick Ligase were purchased from New England Biolabs. The accessories for the QiaCube robot, such as nickel columns and the HotStar HiFidelity PCR kit were obtained from Qiagen. 1 and 5 ml HisTrap FF, 1 and 5 ml HiTrapQ FF, 1 and 5 ml HiTrapSP FF, HiPrep 26/10 desalting, Superose 12, HiLoad Superdex S30, HiLoad Superdex S75, HiLoad Superdex S200 columns and nickel beads were purchased from GE Healthcare. A Vibra-Cell VCX 750 sonicator was purchased from Sonics & Materials, Inc. GS-800 Calibrated Densitometer was purchased from Bio-Rad. Amicon Ultra-15 centrifugal filter units were purchased from Millipore. Crystallisation screens were purchased from Qiagen and Hampton Research. Crystallisation reagents, additives, detergents, dialysis buttons and Fluorinert solution were purchased from Hampton Research. BL21(DE3)pLysS, Rosetta-gami(DE3)pLysS and Origami 2(DE3)pLysS cells, Bug Buster and Benzonase nuclease were bought from Novagen. NuPAGE system SDS-PAGE gels, WB membranes, running and transfer buffers were obtained from Invitrogen. QuikChange kit, BL21-CodonPlus(DE3)-RIPL and ArcticExpress cells were purchased from Agilent Technologies. 6xHis mAb-HRP conjugate was bought from Clontech and BM Chemiluminescence Western Blotting Substrate from Roche. All expression vectors were obtained from previous lab members. The proteins were purified utilising ÄKTA purification systems from GE Healthcare. Bovine brains were obtained from the University of Glasgow's School of Veterinary Medicine. The Beatson Proteomics group performed mass spectroscopy. Beatson Sequencing Services carried out DNA sequencing.

2.2 Kinesin expression panel methods

2.2.1 Subcloning into expression vectors

The protein sequences of the human kinesins were aligned with the motor domain sequence of human Kif5B, for which the crystal structure is known (PDB ID: 1BG2), to define the boundaries of the motor domain, using the ClustalW2 multiple alignment program from the European Bioinformatics Institute (Larkin et al., 2007). Figure 2.1 present an exemplary alignment of Kif5B, Kif6 and Kif9 motor domain sequences.

```
Kif5B    MADLAECN-IKVMCRFRPLNESE-------VNRGDKYIAKFQGED----TVVIASKPYAF 48
Kif3B    MSKLKSSESVRVVVRCRPMNGKEKAASYDKVVDVDVKLGQVSVKNP-KGTAHEMPKTFTF 59
Kif9     ---MGTRKKVQAFVRVRPTDDFAHEMIKYGEDNKSIDIHLKKDTRRGVVNNQQTDWSFKL 57

Kif5B    DRVFQSSTSQEQVYNDCAKKIVKDVLEGYNGTIFAYGQTSSGKTHTMEGKLHDPEGMGII 108
Kif3B    DAVYDWNAKQFELYDETFRPLVDSVLQGFNGTIFAYGQTGTGKTYTMEGIRGDPEKRGVI 119
Kif9     DGVLHN-ASQDLVYETVAKDAVSQALDGYNGTIMCYGQTGAGKTYTMTGATENYKHRGIL 116

Kif5B    PRIVQDIFNYIYSMDENLEFHIKVSYFEIYLDKIRDLLD----VSKTN-LSVHEDKNRVP 163
Kif3B    PNSFDHIFTHIS-RSQNQQYLVRASYLEIYQEEIRDLLS----KDQTKRLELKERPDTGV 174
Kif9     PRALQQVFRMIE-ERPTHAITVRVSYLEIYNENLFDLLSTLPYVGPSVTPMTIVENPQGI 175

Kif5B    YVKGCTERFVCSPDEVMDTIDEGKSNRHVAVTNMNEHSSRSHSIFLINVKQENTQTEQK- 222
Kif3B    YVKDLSSFVTKSVKEIEHVMNVGNQNRSVGATNMNEHSSRSHAIFVITIECSEVGLDGEN 234
Kif9     FIKGLSVHLTSQEEDAFSLLFEGETNRIIASHTMNKNSSRSHCIFTIYMEAHSRTLSDEK 235

Kif5B    --LSGKLYLVDLAGSEKVSKTGAEGAVLDEAKNINKSLSALGNVISALAEG-STYVPYRD 279
Kif3B    HIRVGKLNLVDLAGSERQAKTGAQGERLKEATKINLSLSALGNVISALVDGKSTHIPYRD 294
Kif9     -YITSKINLVDLAGSERLSKTGSEGRVLKEATYINKSLSFLEQAIIALGDQNRDHVPFRQ 294

Kif5B    SKMTRILQDSLGGNCRTTIVICCSPSSYNESETKSTLLFGQRAKTIKNTVCVNVELTA 337
Kif3B    SKLTRLLQDSLGGNAKTVMVANVGPASYNVEETLTTLRYANRAKNIKNKPRVNEDPKD 352
Kif9     SKLTHALKDSLGGNCNMVLVTNIYGEAAQLDETLSSLRFASRMKLVTTEPAINEKYDA 352
```

Figure 2.1: Alignment of Kif5B, Kif6 and Kif9 motor domain sequences. The alignment was generated using ClustalW2 multiple alignment tool (Larkin et al., 2007). Small and hydrophobic residues are shown in red, acidic residues in blue and basic residues are shown in magenta. Glycine and residues containing hydroxyl, sulfhydryl or amine groups are shown in green.

Codon-optimised cDNAs encoding human kinesin motor domains were purchased in vector pUC57 for the following kinesins: Kif1A$_{1-355}$ (coding for residues 1–355, naming system is kept for all constructs), Kif1B$_{1-354}$, Kif4B$_{1-337}$, Kif6$_{103-351}$, Kif7$_{8-361}$, Kif12$_{1-361}$, Kif13$_{1-353}$, Kif14$_{366-713}$, Kif15$_{19-375}$, Kif17$_{10-347}$, Kif24$_{216-546}$, Kif26A$_{386-737}$, Kif26B$_{462-813}$ and Kif27$_{1-341}$. Additional constructs were cloned from full-length DNA for a set of kinesins using the HotStar HiFidelity PCR kit. The primers were designed by introducing a required restriction site in the middle of the oligonucleotide, with an overhang of at least 9 nucleotides

on each site. Efforts were made to keep primer GC content above 50% and melting temperature above 75°C. The PCR reaction was conducted with following cycling parameters: initial denaturation — 95°C, 5 min; 45 extension cycles (95°C, 15 sec; 55°C, 1 min; 72°C, 1 min); final extension — 72°C, 10 min. The created constructs and used PCR primers are shown in Table 2.1.

Construct	Forward primer	Reverse primer
$Kif2B_{208-555}$	5' C AGC AAG ATC TCA GTC ATG AAG CCC CCG CAA GAA 3'	5' G TGC CTC ATG TCC CTC GAG ATA GTG GCC ACG ATG 3'
$Kif3A_{7-360}$	5' ATG CCG ATC ATC ATG ACA GAG AAG CCA GAA AGC 3'	5' CTG GAA CTG CTC GAG CAA AGC ATC CTT TGG ATC 3'
$Kif3B_{1-354}$	5' G ACT GGA TCA GAG TTC ATC ATG ACA AAG TTG AAA AGC TCA GAG 3'	5' TTC CTG GAA TTC TCG CTC GAG GGC ATC CTT 3'
$Kif5A_{1-339}$	5' CCG GCT ACC ATC ATG ACG GAG ACC AAC 3'	5' CTT CTC ATA TTT CTT CTT CCA CTG CTC GAG AGT CAA CTC CAA ATT 3'
$Kif5C_{1-339}$	5' CG GCC GTC ATG ACG GAT CCA GCC GAA 3'	5' CTC TTT TTC ATA TTT CTT CTT CTC GAG TTC TGC TGT CAG TTC TAG G 3'
$Kif9_{1-351}$	5' CTG GTG AAC GCT ACC ATG GGT ACT AGG AAA AAA GTT CAT GCA TTT 3'	5' CTC CAG GTT CTT GAC CAT TCT CTC GAG ATC ATA CTT TTC ATT GAT 3'

Table 2.1: Kinesins constructs cloned from the full-length DNA. The construct length, forward and reverse primers are presented.

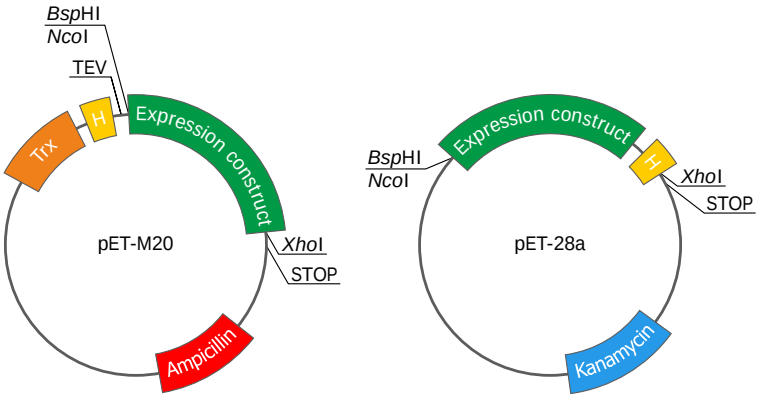

Figure 2.2: *E. coli* expression vectors used in the kinesin motor domain study. A modified pET-M20 possesses N-terminal Trx fusion protein, His-tag and TEV cleavage site. TEV cleaved kinesin construct carries additional glycine and alanine residues at the N-terminus. A pET-28a contains C-terminal uncleavable His-tag. The plasmid-mediated resistance and used restriction sites are indicated.

Subsequently, all amplified genes were double-restricted with *Nco*I or *Bsp*HI and *Xho*I and cloned into two *E. coli* expression vectors using standard methods: a modified pET-M20

(N-terminal Trx fusion protein (thioredoxin, 12 kDa fusion protein, promotes solubility and folding), His-tag and TEV cleavage site) and pET-28a (C-terminal His-tag) (Figure 2.2). Both vectors contain an engineered stop codon (pET-M20 after *Xho*I site, pET-28a after His-tag). After cloning into expression vectors, the sequence of the constructs was verified by DNA sequencing.

2.2.2 Small-scale expression and semi-automated purification

The kinesin motor domain constructs were transformed into the following *E. coli* expression strains: BL21-CodonPlus(DE3)-RIPL, BL21(DE3), BL21(DE3)pLysS (pLysS plasmid suppress pre-induction protein expression by producing inhibitor of T7 RNA polymerase (T7 lysozyme)), Origami 2(DE3)pLysS (strain carries mutations in the thioredoxin reductase and glutathione reductase genes, which enhance disulfide bond formation), Rosettagami(DE3)pLysS (strain contains codons rarely used in *E. coli*) and ArcticExpress (strain promotes soluble protein expression). All competent cells were thawed on ice. For each transformation 50 μl of cells were mixed with 1 μl of mini-prepped DNA and incubated on ice for 30 min. After incubation transformation reactions were incubated in a 42°C water bath for 30 sec, then cooled on ice for 5 min. Subsequently, the reactions were supplemented with 200 μl of LB medium (no antibiotic) and incubated for 1 h at 37°C. Then, about 100 μl of the resulting cultures were spread on LB plates (with appropriate antibiotic added, ampicillin for pET-M20 clones, or kanamycin for pET-28a). Plates were incubated overnight at 37°C. A single colony was picked from each plate for expression test. 20 ml cultures were grown in Falcon 50 ml tubes in TB medium at 37°C to an OD_{600} of approximately 0.7 and subsequently induced overnight with 0.5 mM IPTG at 18°C. The cultures were centrifuged (15 min, 4°C, 3300g), the pellets transferred into 2 ml QiaCube safe-lock tubes, frozen in liquid nitrogen and stored at −80°C. Small-scale purifications were performed using a QiaCube robot with the following buffers: 20 mM Tris-HCl, 300 mM NaCl, 1mM $MgCl_2$, containing 10 mM imidazole in the equilibration buffer, 50 mM in the washing buffer and 250 mM in the elution buffer. To assure protein solubility, the pH of the buffers was adjusted depending on the pI of the protein and kept by one pH unit away from the pI of the construct. QiaCube robot enables automated purification of 12 small-scale expressed samples, by utilising small immobilized metal afnity chromatography (IMAC) spin-columns. IMAC is a highly efficient method used for purification of polyhistidine-tagged (His-tagged) proteins. The divalent metal ions, for example nickel or cobalt, have propensity to bind histidine. The metals immobilized on the resin by chelation facilitate purification of the overexpressed protein from the crude *E. coli* lysate. Prior to purification buffers were kept at 4°C. The pI of prepped constructs are presented in Table 2.2 along with their systematic and trivial names, construct lengths, pH of the buffers used in the purifications and extinction coefficients.

Systematic name	Other names	Construct	pI of construct	pH of buffer	Extinction coeff. [$M^{-1}cm^{-1}$]
Kif1A	ATSV, MRD9	$Kif1A_{1-355}$	8.92	7.0	33600
Kif1B	KLP, CMT2	$Kif1B_{1-354}$	8.87	7.0	33725
Kif2B	FLJ53902	$Kif2B_{208-555}$	10.30	7.0	24005
Kif3A	KRP85, Klp64D	$Kif3A_{1-354}$	8.98	7.0	18130
Kif3B	KRP95, Klp68D	$Kif3B_{1-354}$	9.04	7.0	23505
Kif4B	Chromokinesin	$Kif4B_{1-337}$	6.85	7.9	13910
Kif5A	nKHC	$Kif5A_{1-339}$	6.33	7.5	16765
Kif5C	uKHC	$Kif5C_{1-339}$	6.38	7.5	15275
Kif6	C6orf102	$Kif6_{103-351}$	6.46	7.5	19620
Kif7	ACLS, HLS2	$Kif7_{8-361}$	5.98	7.0	16180
Kif9	MGC104186	$Kif9_{1-351}$	6.87	7.9	26610
Kif12	RP11-56P10.3	$Kif12_{1-361}$	9.60	7.0	20315
Kif13	GAKIN	$Kif13_{1-353}$	9.08	7.0	30620
Kif14	MGC142302	$Kif14_{366-713}$	6.40	7.5	36120
Kif15	Hklp2, Xklp2	$Kif15_{19-375}$	8.68	7.0	17608
Kif17	Kif17b	$Kif17_{10-347}$	8.19	7.0	23880
Kif24	C9orf48	$Kif24_{216-546}$	8.18	7.0	26275
Kif26A	FLJ22753	$Kif26A_{386-737}$	9.59	7.0	18048
Kif26B	FLJ10157	$Kif26B_{462-813}$	9.45	7.0	23545
Kif27	RP11-575L7.3	$Kif27_{1-341}$	6.85	7.9	13910

Table 2.2: Kinesins tested in a motor domain expression trial. Systematic and trivial names, construct lengths, pI of the constructs, pH of the buffers used in the purifications and extinction coefficients of twenty tested human kinesin motor domains.

Before purification, samples were re-suspended in 50 μl of 50% Bug Buster in equilibration buffer supplemented with 1 μl of Benzonase nuclease. Subsequently, cells were lysed by three cycles of freezing on dry ice and thawing at 25°C (six cycles for BL21-CodonPlus(DE3)-RIPL and ArcticExpress cells). Samples were purified using nickel pull down of His-tagged proteins and eluents were analysed by SDS-PAGE. Bands of the expected size were excised from the gel and analysed by mass spectrometry fingerprint analysis.

2.2.3 Western blot

Following small-scale purification, samples which did not reveal any significant protein over-expression by SDS-PAGE, were further examined by western blot. Supernatants and pellets were analysed separately. Supernatants were diluted 20-fold with equilibration buffer. 20 μl of pellet was re-suspended and boiled in 1 ml of 6 M urea and diluted 20-fold with equilibration buffer. SDS-PAGE was run with the following volumes: 10 μl of the sample, 8 μl loading buffer (4% SDS, 20% glycerol, 0.004% bromophenol blue, 0.125M Tris-HCl pH 7.0) and 2 μl reducing agent (10% 2-mercaptoethanol). Next, proteins were transferred onto a nitrocellulose membrane (30 V, 400 mA, 1 h 20 min) in transfer buffer supplemented with

20% methanol. Afterwards the membrane was blocked overnight at 4°C in a solution of 5% milk solution in TBS-T. After blocking, the membrane was incubated in 1% milk solution, containing the 6xHis mAb-HRP conjugate for 1 h at room temperature. After incubation the conjugate excess was removed by three washes with TBS-T (5 min each) and a final rinse (5 min) in water. Finally, the membrane was developed with BM Chemiluminescence Western Blotting Substrate.

2.2.4 Large-scale expression and purification

12 l of bacterial cultures were grown and harvested as described for the small-scale expression test and re-suspended in lysis buffer (affinity wash buffer supplemented with 1 mM PMSF, 0.1 mg/ml lysozyme, 50–60 ml). Cells were lysed by sonication (8 cycles of 8 sec on/off, 20 ml lysate fractions) and centrifuged (1 h, 4°C, 31,400g). Supernatants were pooled and proteins were purified by affinity chromatography (1 ml HisTrap FF; wash buffer: 50 mM PIPES, 250 mM NaCl, 2 mM $MgCl_2$, 40 mM imidazole; elution buffer: 50 mM PIPES, 250 mM NaCl, 2 mM $MgCl_2$, 500 mM imidazole). After elution, protein solutions were supplemented with 1 mM Mg^{2+}ATP (repeated after each purification step). Subsequently, they were cleaved overnight with His-tagged TEV protease (0.05 mg TEV / 1 mg protein). Before TEV cleavage, the buffer was exchanged to eliminate imidazole (HiPrep 26/10 desalting; 50 mM PIPES, 250 mM NaCl, 2 mM $MgCl_2$). Afterwards, His-tagged Trx and TEV were removed by a second run of the HisTrap column. The final purification step for all kinesins consisted of gel filtration chromatography (HiLoad Superdex S75) in gel filtration buffer (50 mM PIPES, 250 mM NaCl, 2 mM $MgCl_2$, 1 mM DTT).

2.2.5 Expression and purification of His-tagged TEV protease

The expression construct for TEV (Tobacco etch virus) protease consisted of full-length cDNA cloned into the pET-15b expression vector (C-terminal His-tag) with *Nco*I at the 5' and *Bam*HI at the 3' end. The plasmid was transformed into BL21(DE3)pLysS competent cells and bacteria were grown in 12 l of TB medium at 37°C, until an OD_{600} of 0.4, then temperature was reduced to 18°C. Once the temperature reached 18°C, and the OD_{600} was close to 0.6–0.8, the cultures were induced with 0.5 mM IPTG and grown for another 16 h. Cells were harvested and lysed by sonication as previously described. After centrifugation the supernatant was applied to an affinity column (1 ml HisTrap FF; wash buffer: 50 mM Tris-HCl pH 8.0, 250 mM NaCl, 40 mM imidazole; elution buffer: 50 mM Tris-HCl pH 8.0, 250 mM NaCl, 500 mM imidazole). The TEV protease was then applied to a HiPrep 26/10 desalting column equilibrated in 50 mM Tris-HCl pH 8.0, 250 mM NaCl and 10% sucrose (cryoprotectant). Finally, TEV was concentrated to 2 mg/ml (Amicon Ultra-15, 10 kDa),

aliquoted, frozen in liquid nitrogen and stored at −80°C. On average, 12 l of bacterial culture yielded 30–50 mg of 80–90% pure TEV. The identity of the protease was confirmed by mass spectrometry fingerprint with coverage of 75%.

2.2.6 Determination of protein concentration

Protein concentrations were determined using either the Beer-Lambert law, with absorbance measured under native conditions, taking bound ADP into consideration (extinction coefficient = 2500 $M^{-1}cm^{-1}$), or by employing the Bradford method. The extinction coefficient for each kinesin was calculated using the ProtParam software from the Bioinformatics Resource Portal (Wilkins et al., 1999). Both methods yielded similar protein concentrations with differences of 10–20% and the concentration obtained by applying the Beer-Lambert law was used in further calculations.

2.2.7 Analytical gel filtration

The oligomeric state of the proteins was determined using a Superose 12 10/300 GL analytic gel filtration column with a flow rate of 0.5 ml/min. This chromatographic method enables molecular weight estimation of a test protein by calibrating the column with proteins of known molecular weights. The major limitation of the method is that it works reliably only for compact and globular molecules. Kinesin motor domains are known to be globular making them ideal candidates for assigning molecular weight by analytical gel filtration. Prior to running test proteins, the column was calibrated with proteins of known molecular mass (ribonuclease A — 13.7 kDa, carbonic anhydrase — 29 kDa, ovalbumin — 43 kDa, conalbumin — 75 kDa) and dextran blue to determine the column void volume. The K_{av} values were calculated for the calibration proteins from the following equation:

$$K_{av} = \frac{V_e - V_0}{V_c - V_0}$$

(where V_e is the elution volume, V_0 is the void volume, V_c is the column volume), and plotted against the logarithm of the molecular weights of the standards. The molecular weight for each kinesin motor domain was calculated from the resulting equation.

2.2.8 Tubulin purification and polymerisation into MTs

Tubulin was purified from bovine brains, by a series of polymerisation and depolymerisation steps as described previously (Castoldi and Popov, 2003). Two fresh bovine brains were obtained on ice and homogenised in cold depolymerisation buffer (50 mM MES pH 6.8,

1 mM $CaCl_2$), then centrifuged at 29,000g, 4°C for 60 min. The pellet was discarded and the supernatant was supplemented with equal volumes of warm polymerisation buffer (1 M PIPES pH 6.9, 10 mM $MgCl_2$, 20 mM EGTA) and glycerol, 1.5 mM ATP (final) and 0.5 mM GTP (final). Tubulin was polymerised at 37°C for 60 min. Subsequently, the sample was centrifuged at 151,000g, 37°C for 30 min. The supernatant was discarded, the pellet was resuspended in 100 ml of cold depolymerisation buffer and incubated on ice for 30 min. Post incubation tubulin was centrifuged at 70,000g, 4°C for 30 min. The pellet was discarded, the supernatant was supplemented with an equal volume of warm polymerisation buffer and glycerol, 1.5 mM ATP and 0.5 mM GTP, incubated at 37°C for 60 min, then centrifuged at 151,000g, 37°C for 30 min. In the next step, the obtained MT-pellet was resuspended in 15 ml of cold BRB80 buffer (80 mM PIPES pH 6.8, 1 mM $MgCl_2$, 1 mM EGTA) and incubated on ice for 10 min. In a final step, tubulin was centrifuged at 104,000g, 4°C for 30 min. The pellet was discarded and the supernatant contained purified protein. The purity of the tubulin obtained is presented in Figure 2.3.

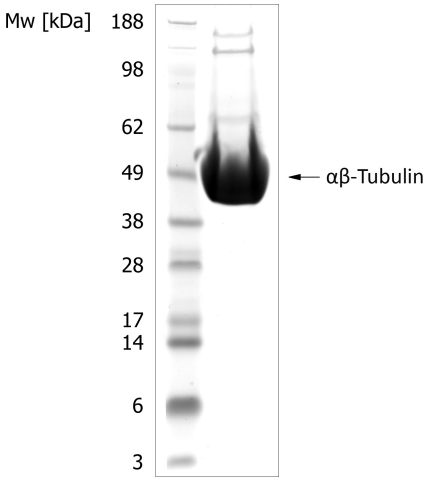

Figure 2.3: SDS-PAGE presenting purity of tubulin extracted from bovine brain.

Subsequently, tubulin was aliquoted at 18.5 mg/ml, snap frozen and stored in liquid nitrogen. MTs were prepared at 60 μM (heterodimer). Tubulin was gently mixed with pre-warmed (to 37°C) G-PEM buffer (100 mM PIPES pH 6.9, 1 mM EDTA, 1 mM $MgCl_2$, 1 mM GTP) supplemented with 20 μM of taxol. Polymerisation was carried out overnight at 37°C.

2.3 Kif15 methods

2.3.1 Kif15 cloning and expression

Several codon-optimised cDNAs ($Kif15_{19-375}$, $Kif15_{376-743}$, $Kif15_{744-1333}$, $Kif15_{1017-1237}$, $Kif15_{1149-1388}$), covering the entire length of Kif15, were cloned into expression vectors (a

modified pET-M20 and pET-28a) and screened for expression conditions in several *E. coli* strains (as described previously in Chapter 2.2.2). An additional construct — $Kif15_{1-375}$ was created, extending the $Kif15_{19-375}$ construct by PCR, with four forward primers (5' CA AAT GGT CAG TCT AAC CAG CCG AGC AAC GAA G 3', 5' GAG TTA CGC AGC GTG ACA AAT GGT CAG TCT AAC C 3', 5' GGC TGC AAA ACT GAG TTA CGC AGC GTG 3', 5' GAA CC ATG GCT CCT GGC TGC AAA ACT G 3'), and a single reverse primer (5' GAT CTC GAG TTA ACC CTG GGT ATC TTC ATT CAC AAC C 3'). When expression conditions for each of the constructs were established, large-scale purifications were performed in a manner analogous to these described in Chapter 2.2.4. The pI of constructs tested and pH of buffers used are presented in Table 2.3.

Construct	pI	pH of PIPES	Extinction coeff. $[M^{-1}cm^{-1}]$
$Kif15_{1-375}$	8.35	7.0	17670
$Kif15_{19-375}$	8.68	7.0	17608
$Kif15_{376-743}$	6.52	7.6	9002
$Kif15_{744-1333}$	4.76	7.0	23232
$Kif15_{1017-1237}$	5.09	7.0	10032
$Kif15_{1149-1388}$	5.39	7.0	10032

Table 2.3: Purification details for Kif15 construct expression trial. pI of constructs, pH of buffers used in the purifications and protein extinction coefficients.

2.3.2 Kif15 motor domain crystallisation

Purified $Kif15_{19-375}$ protein, concentrated to 10 mg/ml was used to set several crystallisation screens at 4 and 19°C, in the presence and absence of 1 mM Mg^{2+}ATP. The following crystallisation screens were used: ComPAS, JSCG+, PACT, ammonium sulphate grid screen, sodium malonate grid screen, MPD grid screen, Crystal screen HT, Crystal screen Lite, PEG Ion, PEG 6000 and PEG LiCl. The various commercially available crystal screens contain diverse precipitants, salts and buffers in a 96-well block format and allow high-throughput crystallisation screening.

2.3.3 Kif15 motor domain crystals optimisation

Numerous optimisation attempts for $Kif15_{19-375}$ crystals were tested. Various salts and PEGs were tried. Several trays were set to investigate the influence of pH (Tris-HCl pH 7.5–9.0), protein concentration (4–10 mg/ml), temperature (12 and 16°C), protein to well solution ratio (1:2, 2:1), seating versus hanging drop, micro-seeding, buffers (pH 7.0–9.0), additives and detergents.

2.3.4 X-ray crystallography

X-ray crystallography is an experimental technique exploiting the wave nature of X-rays to determine the three-dimensional structure of crystalline solids. It enables insight into the structure of biomolecules and facilitates the investigation of protein complexes. It is also a key tool in structure-based drug design.

2.3.4.1 X-rays and diffraction

X-rays are electromagnetic waves characterised by wavelength, amplitude and phase, just like visual light. The difference between them is the wavelength, much shorter for X-rays (0.02–100 Å) and their higher energy (inversely proportional to the wavelength). The range between 0.5 Å and 1.6 Å (similar to the size of atoms and bonds within biomolecules) is useful to provide high-resolution information about protein structures.

The determination of protein structure using X-rays requires obtaining a crystal, as diffraction from a single protein molecule would be too weak to be measurable. Moreover the X-ray beam is highly damaging to biological samples. In a single protein crystal the atoms are periodically and systematically organised to create a crystal lattice. There are seven crystal lattice systems (monoclinic, triclinic, orthorhombic, rhombohedral, tetragonal, hexagonal and cubic). Each of them is characterised by a unit cell — the smallest component of the crystal lattice determining the arrangement of atoms in a crystal and described by lattice parameters (cell edge length and angles between edges). The orientation of each plane within a lattice is uniquely identified by its Miller index.

Diffraction of an X-ray beam arises when the light interacts with the electron density surrounding the atoms within the crystal. The periodic arrangement within the crystal lends itself to a description in terms of series of equally separated planes. When X-ray beam hits

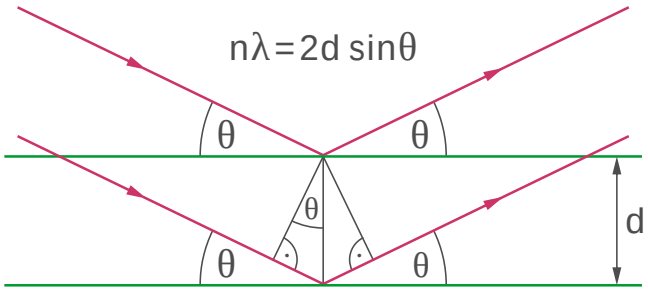

Figure 2.4: Bragg diffraction. X-ray beams hit a set of crystal planes separated by a distance d at an angle θ. For these two rays to produce a diffraction pattern, Bragg's law has to be satisfied.

a crystal at a specific angle (θ), a fraction of it will be diffracted from it at the same angle (Figure 2.4). The remaining beam penetrates the crystal and interacts with the second crystal plane. As they travel different lengths before diffracting, the X-ray waves are not all in the same phase and therefore some of them cancel each other out, while others add up. This phenomenon is described by the Bragg's law, which relates the distance between crystal planes and the X-ray diffraction angle. In order to produce a diffraction spot (reflection) the reflected waves need to be in phase (constructive interference) (Figure 2.4).

2.3.4.2 X-ray data processing

In order to gather enough data to solve the structure a crystal must be exposed to the X-ray radiation at various orientations. The amount of required data depends on the level of crystal symmetry. Data processing starts from indexing diffraction spots, identifying crystal lattice and unit cell dimensions. Once the crystal symmetry is identified the data are integrated into a single file containing the Miller index of each reflection from each diffraction image along with its intensity. Typically a data set contains several records of a single reflection and in the subsequent step these are identified, merged and scaled to ensure consistent intensity. The processed data quality is assessed by the R-factor that compares the crystallographic model and the experimental diffraction data.

Diffraction images (two-dimensional) from various crystal rotations are converted into an electron density model using the mathematical method of Fourier transform. To solve an X-ray structure, both amplitude and phase of the diffracted waves have to be known. The information about amplitude can be recovered due to its dependency on the diffraction intensity. The phase cannot be directly recorded during data collection but the information about it can be retrieved in several ways, for example by molecular replacement. If the structure of a homologous protein is known it can be used as a model to assign the orientation of the molecules in the unit cell and to generate a three-dimensional electron density model.

2.3.4.3 Kif15$_{19-375}$ data collection, processing and refinement

Data for optimised, cryo-protected (20% w/v meso-erythtritol) crystals were collected at the European Synchrotron Radiation Facility (ESRF) to a resolution of 2.7 Å. The structure was solved by molecular replacement with MOLREP (Vagin and Teplyakov, 2000) using the CENPE structure (PDB ID: 1T5C (Garcia-Saez et al., 2004)) as a search model. The model for molecular replacement was picked by comparison of the Kif15 motor domain sequence with the sequences of other kinesins for which X-ray structures were solved and deposited in the PDB. CENPE is the most similar (42% identity) one and was used as a model. The

asymmetric unit contains three copies of $Kif15_{19-375}$ with Mg^{2+}ATP bound in the catalytic site positioned with REFMAC5 (Vagin et al., 2004) by rigid body and restrained refinement. The structure model was improved using COOT (Emsley and Cowtan, 2004) and further refined using PHENIX (Afonine et al., 2012) with non-crystallographic symmetry restraints.

2.3.5 Kif15 basal and MT-stimulated steady state kinetics

Steady-state basal and MT-stimulated ATPase rates of activity were measured using the pyruvate kinase / lactate dehydrogenase linked assay (Hackney and Jiang, 2001). Kinetic measurements were performed at 25°C in 96-well micro-clear plates in a final volume of 100 μl using a 96-well Tecan Sunrise photometer. The following reaction buffer was used: 25 mM ACES, 2 mM Na-EGTA, 0.1 mM EDTA, 2 mM magnesium acetate, 1 mM 2-mercaptoethanol; supplemented with: 2 mM PEP, 0.25 mM NADH, 5 μg/ml PK and 3 μg/ml LDH. The reaction course is depicted in Figure 2.5.

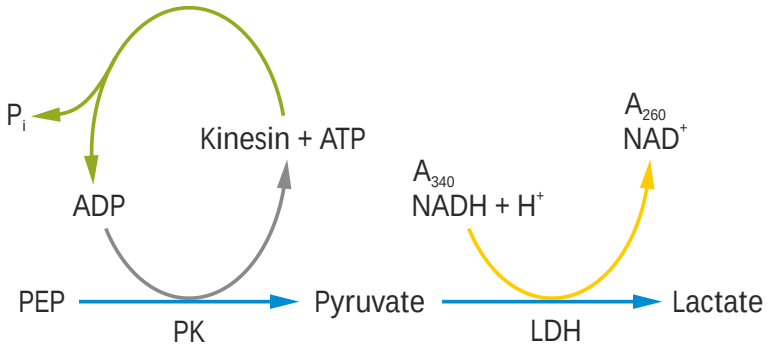

Figure 2.5: Course of coupled ATPase reaction. Pyruvate kinase (PK) catalyses transfer of a phosphate group from phosphoenolopyruvate (PEP) to ADP, yielding one molecule of pyruvate and one molecule of ATP. Lactate dehydrogenase (LDH) catalyses the interconversion of pyruvate and lactate with concomitant interconversion of NADH and NAD^+. In the assay absorbance at 340 nm is monitored, its decrease correlates with kinesin cycle progression.

Prior to the kinetic measurements, excess Mg^{2+}ATP was removed by gel filtration. All measurements were done at least in triplicate. The Michaelis-Menten curve was fitted using Kaleidagraph 4.0 using the least squares method. Rates of activity were calculated using the correlation between absorbance at 340 nm and kinesin activity (Hackney and Jiang, 2001) using following equation:

$$Rate = \frac{2 \cdot \Delta A_{340}/min}{\varepsilon_{NADH} \cdot 60 \cdot C_e}$$

where ε_{NADH} signifies the molar extinction coefficient of NADH [$M^{-1}cm^{-1}$], $\Delta A_{340}/min$ stands for the absorbance change per minute measured at 340 nm, C_e relates to the molar

concentration of the tested enzyme. The factor of 2 in the equation is a correction factor, normalising the optical path length in the 96-well Tecan plates to 1 cm. The salt dependence of the basal $Kif15_{19-375}$ and $Kif15_{1-375}$ ATPase activities was measured at NaCl concentrations from 0 to 275 mM in the presence of 0.59 μM $Kif15_{19-375}$ and 0.35 μM $Kif15_{1-375}$ and 1 mM Mg^{2+}ATP. To determine the basal ATPase activity of $Kif15_{19-375}$ and $Kif15_{1-375}$, their activities were examined at ATP concentrations from 0 to 2 mM in the presence of 0.35 μM $Kif15_{19-375}$ and 0.35 μM $Kif15_{1-375}$ as well as 75 mM NaCl for $Kif15_{19-375}$ and 50 mM NaCl for $Kif15_{1-375}$. The salt dependence of the MT-stimulated ATPase activity of $Kif15_{19-375}$ and $Kif15_{1-375}$ was determined by measuring rates of its activity at MT concentrations from 0 to 15 μM in the presence of 0.04 μM $Kif15_{19-375}$ and 0.08 μM $Kif15_{1-375}$. Finally, the MT-stimulated ATPase activity for both Kif15 constructs was measured in the presence of increasing ATP concentrations from 0 to 0.75 mM in the presence of 0.04 μM $Kif15_{19-375}$ and 0.04 μM $Kif15_{1-375}$, 3 mM MTs, in the absence of salt.

2.3.6 Kif15 inhibitor screening

$Kif15_{19-375}$ enzymatic activity was tested in presence of various small molecules by employing the *in vitro* coupled ATPase assay described in Chapter 2.3.5, using a 96-well Tecan Sunrise photometer. First, the influence of the Eg5 inhibitors STLC and monastrol (up to a concentration of 100 μM) was tested, both in the basal activity assay and in the presence of MTs. The IC_{50} data were fitted with the following equation:

$$\frac{v}{v_0} = 100 - A \cdot \frac{[I]}{[I] + IC_{50}}$$

where v is the reaction velocity at various inhibitor concentrations, v_0 is the control velocity in the absence of inhibitor (measured in the presensce of DMSO), A represents the amplitude, $[I]$ indicates the concentration of the inhibitor and IC_{50} indicates the median inhibitory concentration (Skoufias et al., 2006). Moreover, twenty one compounds described as Kif15 inhibitors (McDonald et al., 2004) were synthesised by Sai Advantium Pharma Ltd (India) and tested. Rates of ATPase activity were measured at 12 inhibitor concentrations from 0 to 200 μM. Since compounds were dissolved in DMSO, it was used as a control. The activity was tested both under basal (1 mM ATP, 75 mM NaCl, 0.25 μM $Kif15_{19-375}$) and under MT-stimulated conditions (1 μM MTs, 1 mM ATP, 0 mM NaCl, 0.015 μM $Kif15_{19-375}$). The compounds were also tested at a lower ATP concentration (100 μM ATP, 75 mM NaCl, 0.25 μM $Kif15_{19-375}$) to investigate the possibility of competitive inhibition.

In addition, other libraries were screened: 2452 small molecules from the National Cancer Institute (Natural Inhibitor Set, Approved Oncology Set, Mechanistic Set and Structural

Diversity Set), and 4000 natural product extracts (University of Strathclyde) were tested. All of the libraries were obtained in the 96-well plate format and were tested using 96-well micro-clear plates and a Tecan Sunrise photometer. Each compound was tested at a single concentration of 200 μM in the presence and absence of MTs.

2.3.7 Kif15 motor domain pelleting assays

Pelleting assays were performed in 50 mM PIPES pH 6.9, 20 mM NaCl, 2 mM $MgCl_2$ and 1 mM DTT. $Kif15_{19-375}$ (1–12 μM) was gently mixed with taxol-polymerised MTs (5 μM, prepared without GTP, 20 μM of taxol promotes MTs polymerisation) and supplemented with buffer to a final volume of 40 μl. Binding assays were performed in the presence of 2 mM Mg^{2+}ATP, 2 mM AMP-PNP or 4 mU of apyrase. Samples were incubated at room temperature for 10 min and centrifuged in a Beckman TL100 ultracentrifuge at 100,000g, 25°C for 20 min. Supernatants were removed from the pellets. The pellets were re-suspended in Laemmli reducing sample buffer (4% SDS, 20% glycerol, 0.004% bromophenol blue, 0.125 M Tris-HCl pH 7.0, 10% 2-mercaptoethanol). Supernatants and pellet samples were run on SDS-PAGE gels. On the gel for each experiment a standard of $Kif15_{19-375}$ was run: 1, 2, 4 and 8 μl of the Kif15 motor domain at 0.5 mg/ml, along with the empty lane (for the background correction). Gels were stained with Coomassie Brilliant Blue (Simply Blue Safe Stain) and scanned using a GS-800 Calibrated Densitometer. Data were analysed using ImageJ (Schneider et al., 2012), Microsoft Excel 2008 and Kaleidagraph 4.0. ImageJ software enables the analysis of gel bands intensity with background subtraction. Additionally, inclusion of a protein standard permits quantification of the proteins assayed. All assays were run in triplicate. To calculate the dissociation constant (K_D), the Michaelis-Menten representation was used as follows:

$$[MT \cdot Kif15_{19-375}] = \frac{B_{max} \cdot [Kif15_{19-375}]}{K_D \cdot [Kif15_{19-375}]}$$

with MT-bound $Kif15_{19-375}$ ($[MT \cdot Kif15_{19-375}]$) plotted as a function of free $Kif15_{19-375}$ ($[Kif15_{19-375}]$). B_{max} corresponds to the maximal number of interacting sites.

2.3.8 Kif15 actin binding assay

The assay was conducted in F-actin buffer (5 mM Tris-HCl pH 8.0, 0.2 mM $CaCl_2$, 50 mM KCl, 2 mM $MgCl_2$, 1 mM ATP) in a reaction volume of 50 μl. F-actin was prepared at a concentration of 18.4 μM by quickly thawing actin on ice and preparing G-actin at a concentration of 1 mg/ml in G-actin buffer (5 mM Tris-HCl pH 8.0, 0.2 mM $CaCl_2$). The G-actin

was polymerised to F-actin by adding polymerisation buffer (5 mM Tris-HCl pH 8.0, 0.2 mM $CaCl_2$, 50 mM KCl, 2 mM $MgCl_2$, 1 mM ATP) and incubation at room temperature for 1 h. The F-actin stock was stable for 1 h after preparation. Negative and positive controls were BSA (2 μM) and α-actinin (2 μM) (an actin-binding protein) respectively. Two constructs were used in this test: $Kif15_{740-1333}$, which contains a putative actin binding domain, and the Kif15 tail — $Kif15_{1149-1388}$. The proteins were purified and subsequently eluted in a buffer containing 50 mM PIPES pH 6.5, 20 mM NaCl, 2 mM $MgCl_2$ (also tested at pH 7.5) and used at 3 μM ($Kif15_{740-1333}$) and 5 μM ($Kif15_{1149-1388}$), respectively. All assays were performed in triplicate.

2.3.9 Purification of Kif15 partner proteins — FHA domain of Ki-67 and TPX2

cDNAs, codon optimised for *E. coli* expression for Ki-67 FHA domain and full-length TPX2 were purchased, cloned and screened for expression conditions (both expressed in modified pET-M20). The purification procedure for the FHA domain of Ki-67 (pI = 10.62) and TPX2 (pI = 9.77), followed that used for the kinesin motor domains purification protocol (Section 2.2.4), using PIPES pH 7.0 buffers.

2.3.10 Investigation of possibility of MT binding site in Kif15 tail domain

The possibility of an MT-binding site in the Kif15 tail was investigated *in vitro*. Direct binding of $Kif15_{1149-1388}$ with MTs was tested, with the procedure analogous to the pelleting assays for $Kif15_{19-375}$ with various nucleotides (Chapter 2.3.7). Increasing amounts of $Kif15_{1149-1388}$ (1–10 μM) were incubated with MTs (5 μM), supernatants and pellets were analysed by SDS-PAGE.

2.3.11 TPX2 interaction with MTs

Binding between TPX2 and MTs was tested using a pelleting assay (Chapter 2.3.7). The amounts used for the assay were 4 μM MTs and a gradient of TPX2 from 1 to 4 μM.

2.4 Kif7 and Kif27 methods

2.4.1 Kif7 and Kif27 cloning, protein expression and purification

Codon-optimised cDNAs of $Kif7_{8-361}$ and $Kif27_{1-341}$ were cloned previously (Chapter 2.2.1). Additional shorter constructs in a modified pET-M20 expression vector were created using the following primers. $Kif7_{8-347}$: 5' CGT GCC CAG *TAA* ATC CGC AAC CGC GCC AC 3'; $Kif27_{1-339}$: 5' GCG AAC CGC GCG CGT *TAG* ATT CTC GAG TAA TCG 3'; $Kif27_{6-341}$: 5' CT ATG GAA GCC ATG GCG GTG AAA GTT GCG 3', 5' GT GGT GCT CGA TTA CTC GAG AAT GTT ACG C 3'; $Kif27_{17-341}$: 5' GT ATT CGT CCC ATG GTG TGC AAA GAA GCG 3', 5' GT GGT GCT CGA TTA CTC GAG AAT GTT ACG C 3'. The Kif7 point mutation ($Kif7_{8-347}$ L130P) was introduced using a QuikChange kit with the following mutagenic primer: 5' C GAA GCC TTC AAA *CCG* ATC GAT GAA AAC GAC C 3'. The PCR reaction was conducted with the following cycling parameters: initial denaturation — 95°C, 30 sec; 18 extension cycles (95°C, 30 sec; 55°C, 1 min; 68°C, 2 min); final extension — 68°C, 5 min. After PCR the reaction was treated with *Dpn*I at 37°C for 30 min. Post digestion of template DNA, 10% of the reaction was used for a transformation into DH5α competent cells. All obtained proteins were expressed in *E. coli* BL21(DE3)pLysS expression cells. The purification procedure was analogous to the one for the originally created Kif7 and Kif27 constructs (Section 2.2.4).

2.4.2 Kif7 and Kif27 crystallisation

All Kif7 and Kif27 constructs described above were used for crystallisation trials at 10 mg/ml, at 4 and 19°C, in the presence and absence of 1 mM Mg^{2+}ATP. The set of crystallisation screens used for Kif15 crystallisation screening was employed (Chapter 2.3.2).

2.4.3 $Kif7_{8-347}$ data collection, structure determination and refinement

Data for $Kif7_{8-347}$ crystals were collected at beamline I04-1 at Diamond Light Source and processed with XDS (Kabsch, 2010) to 1.6 Å resolution. The structure was solved by molecular replacement with MOLREP (Vagin and Teplyakov, 2000) using the Kif3B structure as a search model (PDB ID: 3B6V) (39% identity with Kif7). The asymmetric unit contains one copy of $Kif7_{8-347}$ with bound Mg^{2+}ADP, positioned with REFMAC5 (Vagin et al., 2004) by rigid body and restrained refinement. The model was subsequently improved with COOT (Emsley and Cowtan, 2004) and further refined using PHENIX with TLS restraints (Afonine et al., 2012).

2.4.4 Kif7 and Kif27 oligomeric states

The oligomeric state of all constructs of Kif7 and Kif27 was determined as described in Chapter 2.2.7. The identities of the proteins were confirmed by mass spectroscopy finger print analyses.

2.4.5 $Kif7_{8-347}$ and $Kif7_{8-347}$ L130P western blot

One-litre cultures of native $Kif7_{8-347}$ and mutant $Kif7_{8-347}$ L130P were grown, harvested and lysed as described previously. Subsequently, a procedure described in Chapter 2.2.3 was performed to analyse their soluble and insoluble fractions.

Chapter 3

Results

3.1 Kinesin expression panel

Kinesins transport cellular cargoes and play key roles during cell division, in particular in mitosis and cytokinesis. Because of their implication in a broad range of cellular processes, they have been related to various diseases. The first CENPE inhibitor and a variety of Eg5 targeting agents are currently in phase I and multiple phase II clinical trials. In this chapter, in an effort to provide tools to test anti-mitotic inhibitor specificity, a description is given of the cloning motor domains of nearly half of the kinesin superfamily. Expression conditions were screened, the oligomeric state was established and purification procedures were developed.

3.1.1 Cloning, small-scale expression and purification

Twenty kinesin motor domains, from eleven different subfamilies (almost half of the forty-five kinesins identified in the human genome) were chosen as a first batch in the expression trial (it was planned to test expression of all family members). They were subcloned into two *E. coli* expression vectors: modified pET-M20 and pET-28a. The systematic and trivial names, lengths of the constructs, pI, pH of buffers used in the purification and the molar extinction coefficients are summarised in Table 2.2.

Six constructs were obtained by PCR (Chapter 2.2.1) and thirteen were purchased, as gene synthesised, codon-optimised cDNA fragments. Post cloning, expression constructs were sequenced, and two verified clones for each kinesin (in each expression vector) were transformed, into six different *E. coli* expression strains (Chapter 2.2.2). Subsequently, small-scale, semi-automated purifications were performed using a Qiacube robot. This established purification

conditions for nine different kinesin motor domains. The expected molecular weight is 52–55 kDa for the constructs expressed in modified pET-M20 (Trx-fused constructs) and 39–42 when using pET-28a. An example of SDS-PAGE after small-scale purification is shown in Figure 3.1. The summary of the expression trial is presented in Table 3.1. An average yield from 12 l culture for each of the expressed protein is shown in (Table 3.2).

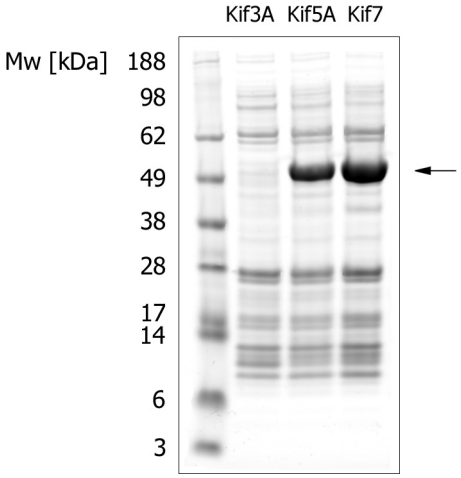

Figure 3.1: SDS-PAGE of small-scale purified kinesin motor domains, expressed in *E. coli* BL21(DE3)pLysS cells. Lane 1 shows molecular weight markers (in kDa). $Kif5A_{1-339}$ and $Kif7_{8-361}$ overexpressed in modified pET-M20 (with an N-terminal Trx fusion protein) are indicated with an arrow.

Construct	BL21(DE3) pLysS	BL21 (DE3)	BL21Codon Plus(DE3)	Arctic Express	Rosetta (DE3) pLysS	Origami2 (DE3) pLysS
$Kif3B_{1-354}$	pET-M20	pET-M20				
$Kif4B_{1-337}$	pET-M20					
$Kif5A_{1-339}$	pET-M20		pET-M20			
$Kif5C_{1-339}$	pET-M20		pET-M20			
$Kif7_{8-361}$	pET-M20	pET-M20	pET-M20		pET-M20	
$Kif9_{1-351}$	pET-M20	pET-M20	pET-M20	pET-M20	pET-M20	pET-M20
$Kif15_{19-375}$			pET-M20			
$Kif24_{216-546}$			pET-M20			
$Kif27_{1-341}$	pET-M20	pET-M20 pET-28a	pET-M20		pET-M20	pET-M20

Table 3.1: Summary of the human kinesin motor domain expression trial.

The identities of the kinesin motor domains were confirmed by mass spectroscopy fingerprint analyses (Table 3.2).

3.1.2 Determination of soluble kinesin oligomeric state and western blot analysis of the remaining constructs

The majority of positive results (protein expression) were obtained in the modified pET-M20 vector, indicating a significant role of the TEV-cleavable, Trx fusion protein, in improving protein solubility. This is in agreement with the performed western blot analysis on supernatants and pellets of samples, for which no soluble protein was obtained. The experiment, performed using pET-M20 constructs revealed, that the majority of constructs were in fact expressed, but insoluble (Figure 3.2). The only non-expressed proteins were: Kif12$_{1-361}$, Kif17$_{10-347}$, Kif26A$_{386-737}$ and Kif26B$_{462-813}$. These were crosschecked, by re-verifying the DNA sequence. All of the tested *E. coli* cultures grew to the comparable cell density.

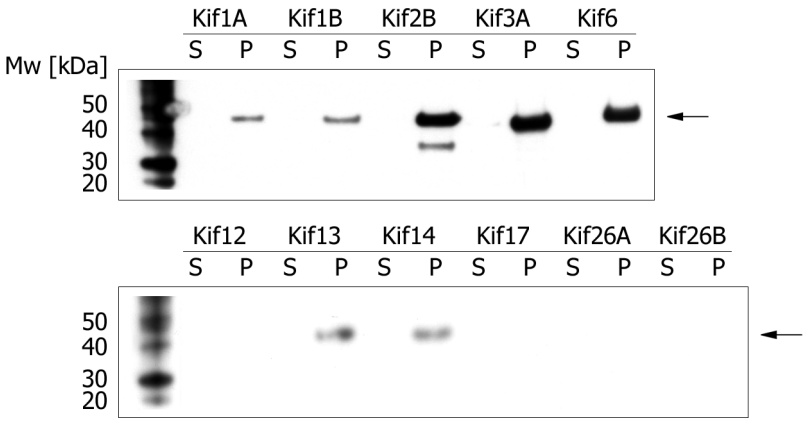

Figure 3.2: Western blot analysis of soluble (S, supernatant) and insoluble (P, pellet) fractions of kinesin cultures (pET-M20 constructs), that did not yield protein in the expression trial: Kif1A$_{1-355}$, Kif1B$_{1-354}$, Kif2B$_{208-555}$, Kif3A$_{1-354}$, Kif6$_{103-351}$, Kif12$_{1-361}$, Kif13$_{1-353}$, Kif14$_{366-713}$, Kif17$_{10-347}$, Kif26A$_{386-737}$ and Kif26B$_{462-813}$. The antibody for His-tagged proteins and His-tagged protein standard were used. The arrow points to the Trx-fused constructs (expected molecular weight: 52–55 kDa) visualised with His-tag antibody.

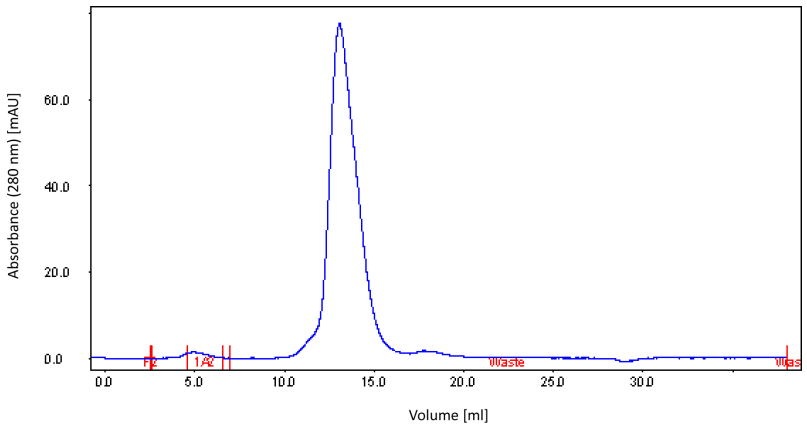

Figure 3.3: Analytical gel filtration profile of Kif15$_{19-375}$. The experiment was conducted using a Superose 12 10/300 GL column with a flow rate of 0.5 ml/min.

Soluble proteins were subjected to analytical gel filtration (Figure 3.3). As expected, all tested kinesin motor domains appear to be monomers in solution, as shown by their calculated and measured molecular weights (Table 3.2).

Construct	Sequence coverage [%]	Theoretical molecular weight [kDa]	Determined molecular weight [kDa]	Average yield from 12 l *E. coli* culture [mg]
$Kif3B_{1-354}$	57	39.2	35	18
$Kif4B_{1-337}$	55	37.0	40	12
$Kif5A_{1-339}$	62	37.8	38	35
$Kif5C_{1-339}$	71	37.7	38	32
$Kif7_{8-361}$	56	38.7	38	26
$Kif9_{1-351}$	80	39.5	36	24
$Kif15_{19-375}$	65	39.0	37	31
$Kif24_{216-546}$	59	37.7	39	15
$Kif27_{1-341}$	49	38.3	36	21

Table 3.2: Expressed kinesin mass spectroscopy fingerprint analysis, their theoretical and determined by analytical gel filtration molecular weights and an average yield from 12 l *E. coli* culture.

3.1.3 Large-scale protein production and purification

All soluble proteins were produced in large-scale (12 l) *E. coli* culture using the modified pET-M20 vector constructs and a three-step purification procedure (Chapter 2.2.4). An average yield from 12 l culture for each of the expressed proteins is shown in (Table 3.2). In the first step cell lysate was applied to a 1 ml HisTrap FF column equilibrated with

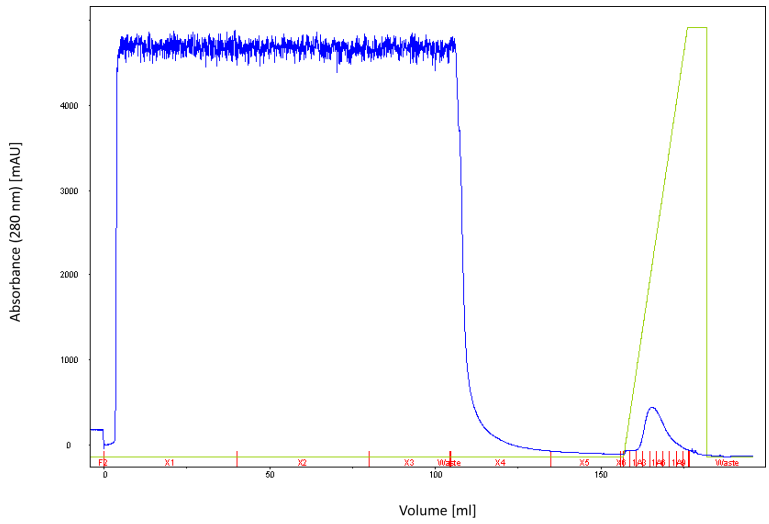

Figure 3.4: Purification of Trx-fused, His-tagged $Kif15_{19-375}$ using a 1 ml HisTrap FF column. Post binding and washing the protein was eluted with a gradient of imidazole (indicated by a green line).

wash buffer. Post binding, the column was washed with 50 ml of wash buffer and protein was eluted with a gradient of elution buffer (imidazole gradient, 40–500 mM) (Figure 3.4). After elution, protein sample was supplemented with 1 mM Mg^{2+}ATP (repeated after each purification step). The protein-containing fractions were pooled, buffer-exchanged on the desalting column and cleaved overnight with His-tagged TEV protease at 4°C (Figure 3.5). Subsequently, sample was subjected to the second run of the affinity purification. Untagged protein flowed through the nickel column, whereas His-tagged TEV and His-Trx remained bound to the resin (Figure 3.6).

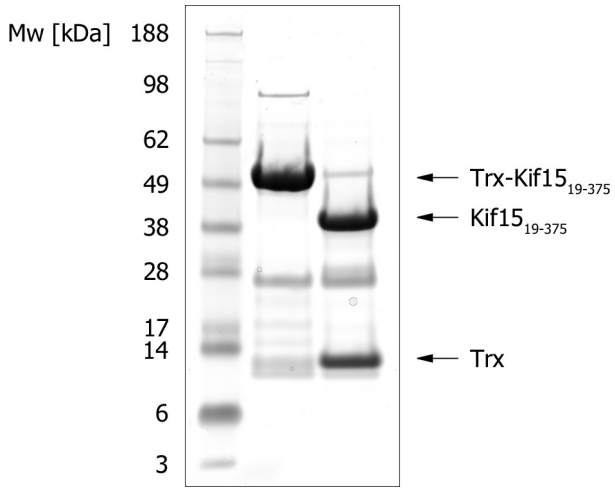

Figure 3.5: TEV cleavage of Trx-fused $Kif15_{19-375}$. The protein was cleaved overnight with His-tagged TEV protease. Lane 1 shows molecular weight markers (in kDa). Lane 2 shows Trx-fused $Kif15_{19-375}$ after affinity purification (theoretical molecular weight — 51 kDa). Lane 3 shows $Kif15_{19-375}$ (theoretical molecular weight — 39 kDa) and His-tagged Trx (theoretical molecular weight — 12 kDa) post TEV cleavage.

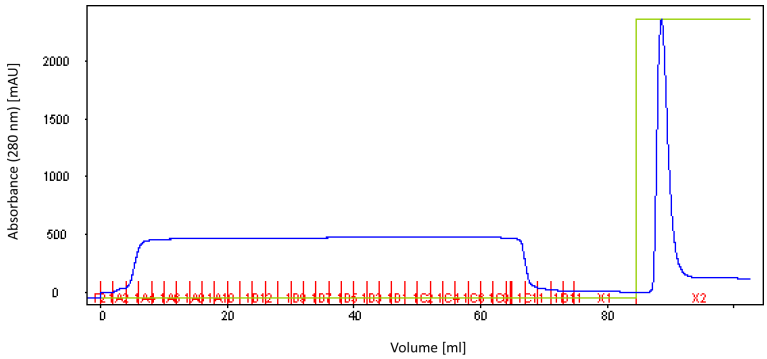

Figure 3.6: Chromatography profile of $Kif15_{19-375}$ second affinity purification. Post TEV cleavage, untagged $Kif15_{19-375}$ was flowed through a nickel column. His-tagged TEV and His-Trx bound to the column and were removed by washing the column with elution buffer (500 mM imidazole, indicated by a green line).

Once separated from His-tagged TEV and Trx, the protein sample was concentrated to 2.5 ml and applied to a HiLoad Superdex S75 gel filtration column (Figure 3.7). All large-scale produced kinesins were obtained with a purity close to 95% (Figure 3.8).

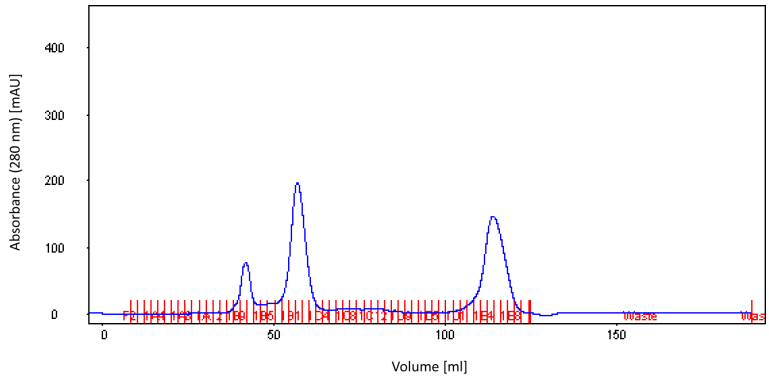

Figure 3.7: Gel filtration profile of $Kif15_{19-375}$. The final purification step, size exclusion chromatography was performed using a HiLoad Superdex S75 column. $Kif15_{19-375}$ eluted in fractions B2–C5 (second peak).

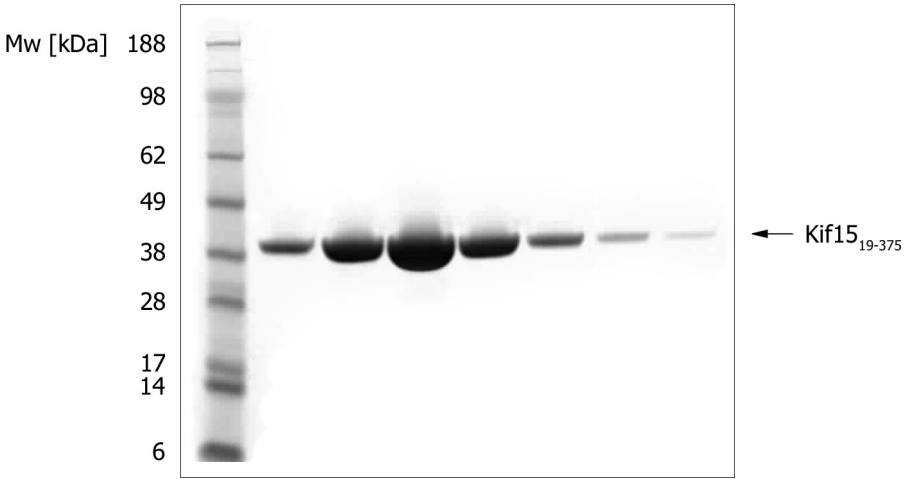

Figure 3.8: SDS-PAGE of $Kif15_{19-375}$ after the final purification step — size exclusion chromatography. Lane 1 shows molecular weight markers (in kDa). Subsequent lanes show fractions from the gel filtration purification (Figure 3.7, fractions B2–C5). The theoretical molecular weight of the construct is 39 kDa.

3.2 Kif15 characterisation

Kif15 functions in the early stages of mitosis, in the formation of the bipolar spindle, and it possess partially overlapping function with Eg5 — a well-characterised mitotic motor. Drugs targeting Eg5 have shown promise as anti-cancer agents. Kif15 has recently become interesting because it can substitute the functions of Eg5, and may itself have potential as a prospective drug target. In this chapter initial biochemical, kinetic and structural characterisation of Kif15 are presented and comparison to the functionally related motor — Eg5 is reported. Additionally, the interaction of Kif15 with MTs, and attempt to probe its interaction with other binding partners (actin, TPX2) are investigated.

3.2.1 Biophysical characterisation of mammalian Kif15

Several constructs covering the entire length of Kif15 (Figure 3.9) were created. After sequence verification, positive clones were tested for expression conditions in *E. coli*, as described previously (Chapters 2.2.1 and 2.2.2). The expression conditions were established for all of them, apart from $Kif15_{376-743}$. The summary of the expression trial is summarised in Table 3.3.

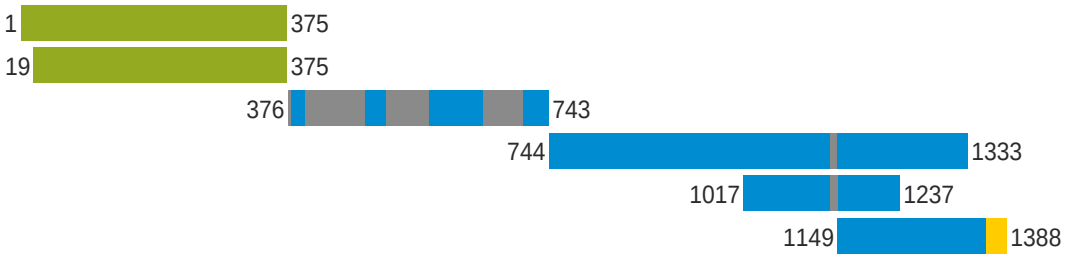

Figure 3.9: Bar diagram of cloned Kif15 constructs. Constructs presented in green cover the motor domain. The blue constructs depict the disrupted (grey) coiled-coil. The C-terminal leucine zipper is shown in yellow.

Construct	Expression vector	*E. coli* expression strain	Avg. yield from 12 l *E. coli* culture [mg]
$Kif15_{1-375}$	pET-M20	BL-21CodonPlus(DE3)-RIL	28
$Kif15_{19-375}$	pET-M20	BL-21CodonPlus(DE3)-RIL	31
$Kif15_{744-1333}$	pET-M20, pET-28a	BL21(DE3)pLysS	11
$Kif15_{1017-1237}$	pET-M20	BL-21CodonPlus(DE3)-RIL	22
$Kif15_{1149-1388}$	pET-M20	BL21(DE3)pLysS	18

Table 3.3: Results of the Kif15 construct expression trial.

The identity of the purified proteins was verified by mass spectrometry fingerprint analysis with a sequence coverage above 60% for all tested constructs. The molecular mass that were determined for both motor domain constructs by gel filtration was 39 kDa for $Kif15_{1-375}$ and 37 kDa for $Kif15_{19-375}$ (Figure 3.3), both close to their theoretical masses, indicating that the Kif15 motor domain is monomeric, in agreement with other kinesins. The gel filtration profiles for $Kif15_{744-1333}$, $Kif15_{1017-1237}$ and $Kif15_{1149-1388}$ were heterogeneous, indicating possible assembly into higher oligomers and/or partial aggregation. All Kif15 proteins were expressed in large-scale culture. The protocol for large-scale expression and purification consisted of nickel pull down of the His-tagged protein, buffer exchange to eliminate imidazole, overnight cleavage of the tag with TEV protease, a second affinity purification to remove the His-tagged protease and the cleaved tag, finally followed by gel filtration. The detailed procedure is described in Sections 2.2.4, 2.3.1 and 3.1.3.

3.2.2 Kif15 crystallisation and crystal optimisation

Crystallisation screening on the Kif15 motor domain ($Kif15_{19-375}$) was performed and a single crystallisation condition was identified. Crystals appeared after three days in the sitting drop set at 19°C in the presence of 1 mM Mg^{2+}ATP, 25% PEG 3350, 0.2 M $MgCl_2$ and 0.1 mM Tris-HCl pH 8.5. They were small and difficult to handle (Figure 3.10), as drops were covered with skin and precipitate. Additional difficulty arose from the fact that protein, snap-frozen in the liquid nitrogen, failed to form crystals. Therefore, each optimisation attempt required freshly purified protein (after purification, the protein stays soluble for up to 5–7 days at 4°C). Initial diffraction tests of small plate-shaped crystals revealed low crystal quality and poor diffraction (14–10 Å) (Figure 3.11). Several approaches to make the crystals bigger and more three-dimensional were tested. Reducing the protein concentration from 10 to 6–7 mg/ml and seeding promoted formation of larger and thicker crystals (Figure 3.10). Seeds were prepared from initially obtained crystals, by crushing them with a thin needle and diluting in 25% PEG 3350, 0.2 M $MgCl_2$ and 0.1 mM Tris-HCl pH 8.5. Seeding was performed using a cat whisker dipped into the seed stock and mixed into a freshly set crystallisation drop. The other challenge presented by the Kif15 motor domain crystals was their high radiation sensitivity, as the crystals decayed before a full data set could be collected. Radiation damage is caused by the interactions of X-ray beam photons with electrons and creating photoelectric electrons (primary radiation damage). This damage is proportional to the X-ray dose received by the crystal. The created photoelectric electrons cause further crystal decay by creating free radicals (secondary radiation damage). Their destructive influence can be reduced by cryocooling. Various cryoprotectants that protect crystals from freezing damage and prohibit ice formation were tested: meso-erythtritol, glycerol and ethylene glycol. Eventually several hundreds of crystals were screened to obtain a single, full data set reaching 2.7 Å. Figure 3.11 shows the diffraction quality of the Kif15 crystals before and after optimisation.

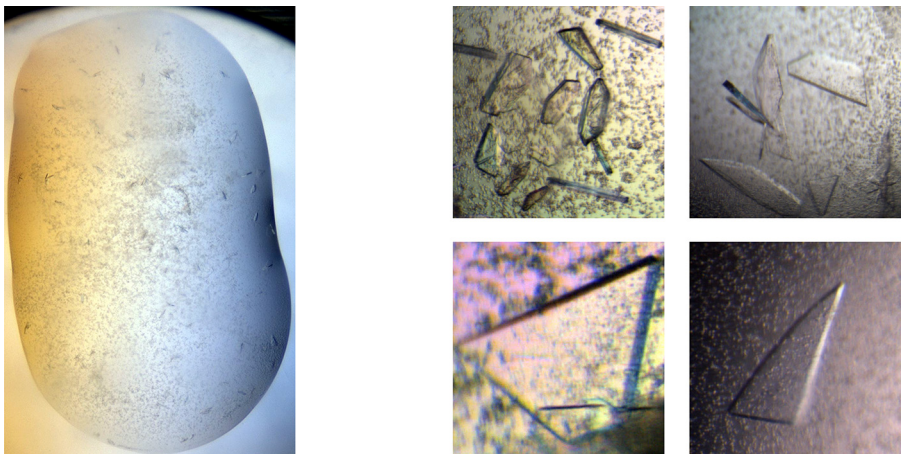

Figure 3.10: $Kif15_{19-375}$ crystals, pre- (left) and post- (right) optimisation.

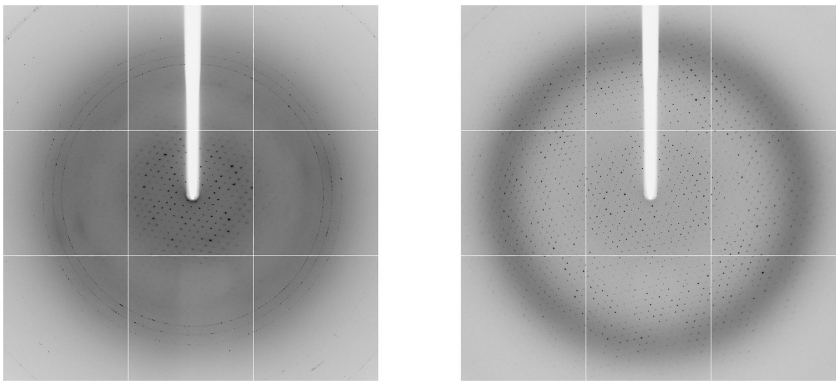

Figure 3.11: $Kif15_{19-375}$ crystals diffraction quality pre- (left) and post- (right) optimisation.

3.2.3 Crystal structure of the binary $Kif15_{19-375}$-Mg^{2+}ADP complex

The Kif15 motor domain structure was solved by molecular replacement and refined to a resolution of 2.7 Å. Data collection and refinement statistics are shown in Table 3.4. $Kif15_{19-375}$ crystallised in space group $P3_221$ with three molecules in the asymmetric unit. Crystals had a Matthews parameter of 2.4 and a solvent content of 49.1%. The rmsd from ideal geometry was 0.013 Å for bond lengths and 1.60° for bond angles. The final model contains residues 24–375 for molecules A and B and residues 24–372 for molecule C. Due to missing or non-interpretable electron density, several smaller loops that could not be built were deleted (loop L1: Gly27–Glu32, loop L6: Glu148–Ala142, loop L11: Gln258–Gly272), and these are absent

	$Kif15_{19-375}$-Mg^{2+}ADP
PDB ID	4BN2
Beamline / Detector	ID23-1 / Q315R
Resolution range [Å]	30–2.7
Space group	$P3_221$
Unit cell parameters [Å; °]	$a = b = 90.24$, $c = 251.39$
	$\alpha = \beta = 90$, $\gamma = 120$
Completeness [%]	89.7 (86.5)
R_{merge}	9.8 (37.8)
Multiplicity	3.7 (3.5)
Mean I/σ	8.6 (3.1)
No. of total / unique reflections	108223 / 29592
No. of copies per AU	3
R_{work} / R_{free} [%]	21.2 / 26.3
No. of Mg^{2+}ADP / water molecules	3 / 156
Bond length rmsd [Å]	0.013
Bond angle rmsd [°]	1.60

Table 3.4: Data collection and refinement statistics for $Kif15_{19-375}$-Mg^{2+}ADP complex. Values in parentheses are for the highest shell.

from the model. Side chains, for which no density was observed, were deleted from the Cβ position onwards. The Ramachandran plot shows that 94.3% of residues are in favoured regions, 5.5% are in additionally allowed regions and 0.2% of residues are outliers. Since molecule A presents better-defined electron density and a more complete model than molecules B and C, it was used for further discussion of the structure. An exemplary electron density map of Kif15 residues 89–96 is presented in Figure 3.12.

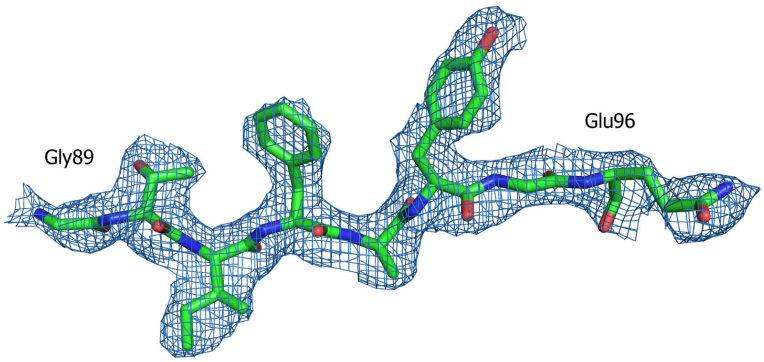

Figure 3.12: A model of Kif15$_{19-375}$ residues 89–96 (β3, part of loop L4). The electron density map (coloured in blue) is contoured at 1σ.

The Kif15 motor domain shows a typical kinesin fold with an 8-stranded β-sheet, surrounded by three major α-helices on each side (Figure 3.13). The crystallised Kif15 construct contains a neck linker, which aligns with the catalytic core, forming a small β-sheet. Although Mg^{2+}ADP is bound in the catalytic site, Kif15 is in the "ATP-like" conformation (see Figure 1.11). The switch II cluster (helix α4–loop L12–helix α5) is in the "upward" position allowing the neck linker to dock to the motor domain (Figure 3.13, Figure 3.15).

3.2.4 Comparison of the Kif15 motor domain to the functionally related motor Eg5

A comparison of the Kif15 motor domain to the functionally related motor Eg5 (Blangy et al., 1995; Turner et al., 2001) was performed, using the AMP-PNP-Eg5 complex, representing the "ATP-like" Eg5 state (PDB ID: 3HQD (Parke et al., 2009)). The sequence alignment of Kif15 and Eg5 (Figure 3.14) shows the high similarity inside their motor domains, with 41.8% identical, 15.5% strongly similar and 12.8% weakly similar residues, which is also reflected by their structures (Figure 3.15). Outside their motor domains, the primary sequence is at best only weakly conserved with 20.3% identical, 20.2% strongly similar and 9.8% weakly similar residues. The Kif15 motor domain, compared with the Eg5 catalytic core, has a deletion of two amino acids and a single insertion in the loop L1 region. Also, in the case of Eg5, loop L1 is interrupted by helix α0, while in Kif15, loop L1 is longer. Loop L1 is part of the L1-L3-L5 cluster that together with loop L9 mediates the entrance of the nucleotide (Song

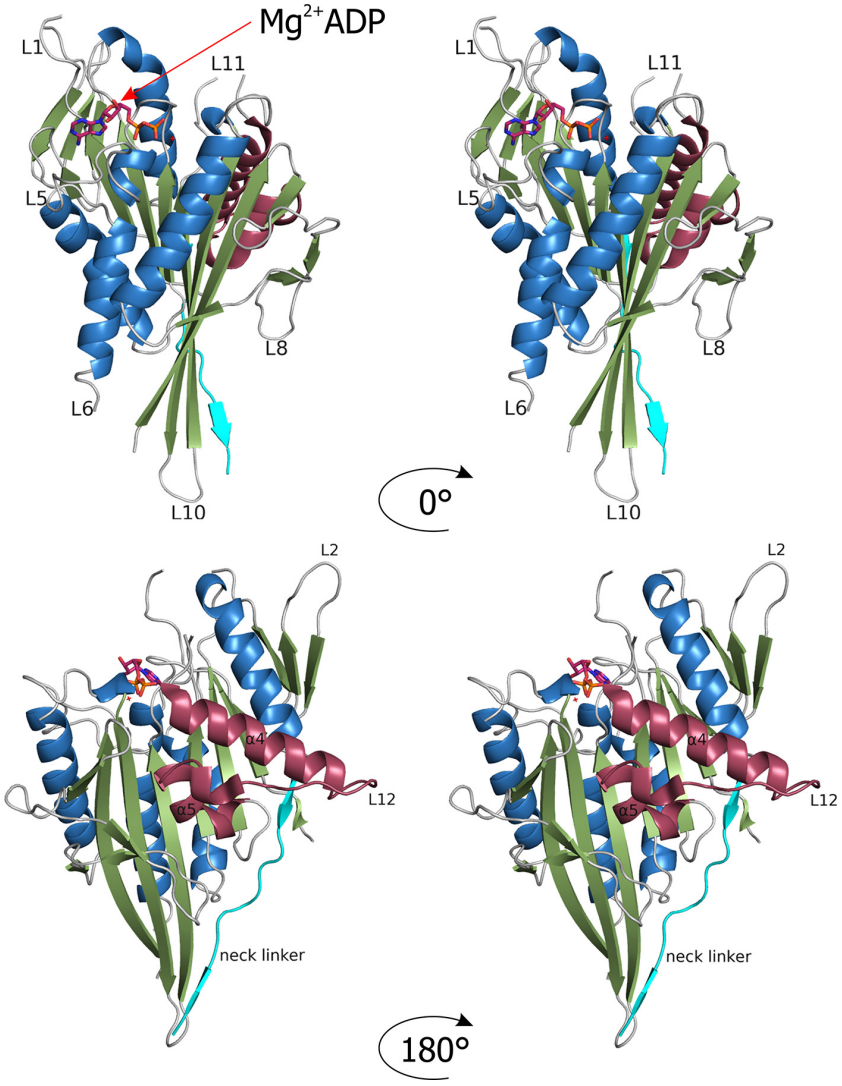

Figure 3.13: Stereo plots of the front and back view of the human Kif15$_{19-375}$-Mg^{2+}ADP complex. α-helices are coloured in blue, β-strands in green and loops / turns in grey. The switch II cluster (α4-L12-α5) is highlighted in claret. The neck linker, following the C-terminal helix α6 is shown in cyan. Mg^{2+}ADP is shown as a ball and stick model, indicated with an arrow.

et al., 2001). In contrast to Eg5, three residues are missing in the Kif15 loop L2 region. Four residues are missing in loop L5, five in loop L8 (loop L8 is implicated in MT-stimulated ADP release (Fourniol and Moores, 2010)) and a single residue is missing in the surface loop L10. There is a five-residue insertion in loop L6 of Kif15; this loop is believed to influence nucleotide affinity (Kollmar and Glockner, 2003). Loop L5 is known to be important for inhibitor binding in Eg5, in Kif15 this loop is shorter. In addition, several other key residues involved in inhibitor binding in Eg5 such as Glu116, Arg119, Trp127 and Ala216 (Yan et al., 2004) are not present in Kif15. All of these suggest that Kif15 could not be affected by Eg5 targeting drugs. Loop L11 is not visible in any of the three molecules of the asymmetric unit.

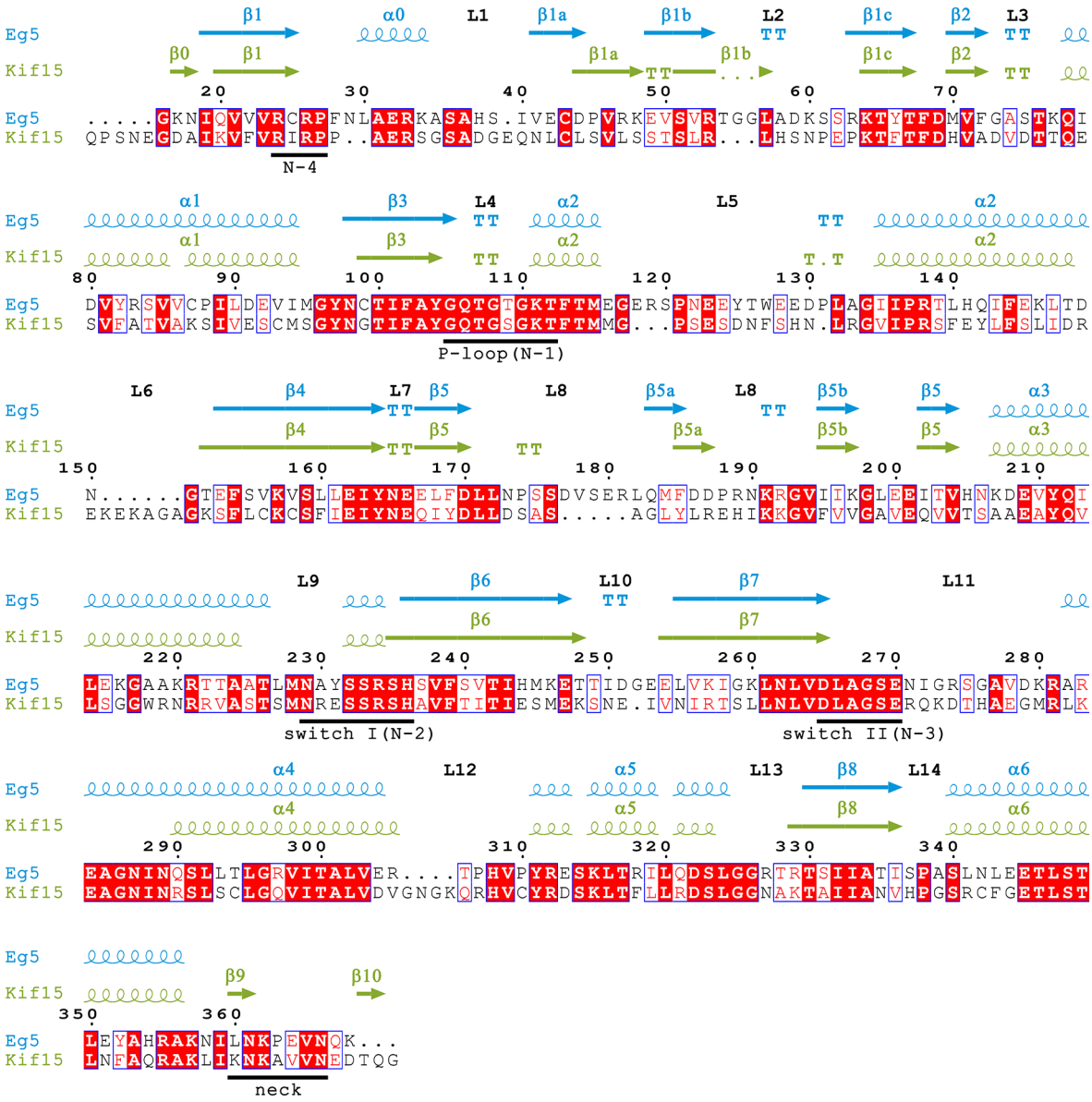

Figure 3.14: Comparison of sequences and secondary structures of Kif15 and Eg5 motor domains. Structural and sequence alignment of Eg5 (PDB ID: 3HQD (Parke et al., 2009)), and Kif15 motor domains. Residue 16 of Eg5 is aligned with residue 24 of Kif15. Identical residues are coloured in white on a red background and similar residues are shaded red. The position of the ATP-binding pocket (N1 to N4), the switch I and II regions and the position of the neck linker regions are underlined in black. The alignment was generated using ClustalW2 multiple alignment tool (Larkin et al., 2007). Figure was prepared using ESPript (Gouet et al., 2003).

3.2.5 Steady state ATPase activity

Kinetic parameters for $Kif15_{1-375}$ and $Kif15_{19-375}$ were measured (Table 3.5). To determine the optimal salt concentration, rates of the basal ATPase activity were measured using NaCl concentrations from 0 to 275 mM in buffer containing 1 mM ATP. The highest basal activity

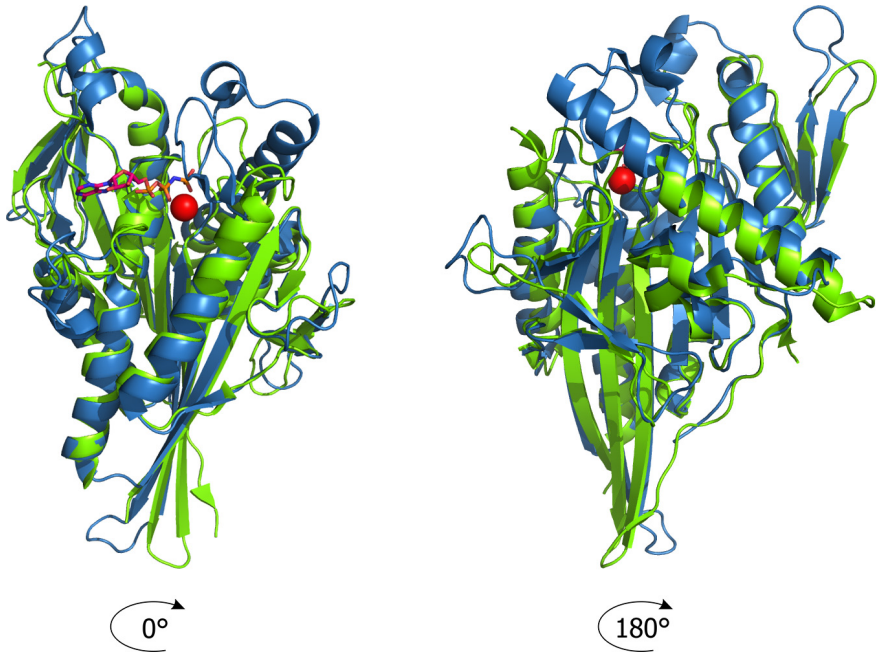

Figure 3.15: Structure overlay of Kif15 and Eg5-AMP-PNP complex. Front and back view of overlaid Kif15 (green) and Eg5 (blue) (PDB ID: 3HQD (Parke et al., 2009)) structures. Mg^{2+} and AMP-PNP are shown as a ball and stick model.

was registered at 50 mM NaCl for the longer Kif15 construct and 75 mM NaCl for $Kif15_{19-375}$ (Figure 3.16A). These salt concentrations were used in further basal activity tests. The differences in activity were rather minor and decreased only slowly at higher salt concentrations. The basal ATPase activity was measured using ATP concentrations from 0 to 2 mM. At 1 mM Mg^{2+}ATP the k_{cat} for the basal ATPase activity of $Kif15_{1-375}$ was 0.028 ± 0.0004 s^{-1} with a $K_{M,ATP}$ of 23.0 ± 2 μM. In contrast, the shorter construct was more active with a k_{cat} of 0.054 ± 0.001 s^{-1} and a $K_{M,ATP}$ of 40 ± 6 μM (Figure 3.16B). Subsequently, the salt dependence of the MT-stimulated ATPase activity of both constructs was determined, by performing the reactions at MT concentrations from 0 to 10 μM in the presence of 0 or

	Basal ATPase activity		MT-stimulated ATPase activity		
	k_{cat} [s^{-1}]	$K_{M,ATP}$ [μM]	k_{cat} [s^{-1}] (C_{KCl} [mM])	$K_{0.5,MT}$ [μM]	$K_{M,ATP}$ [μM]
$Kif15_{1-375}$	0.028 ± 0.0004	23 ± 2	2.1 ± 0.1 (0) 0.050 ± 0.005 (50)	3.1 ± 0.3	109 ± 20
$Kif15_{19-375}$	0.054 ± 0.001	40 ± 6	2.3 ± 0.1 (0) 0.50 ± 0.03 (50) 0.5 ± 0.1 (100) 0.4 ± 0.1 (150)	1.1 ± 0.1	33 ± 3

Table 3.5: Kinetic parameters determined for $Kif15_{1-375}$ and $Kif15_{19-375}$. Kinetic parameters were determined by fitting Michaelis-Menten curve by Kaleidagraph 4.0 using the least squares method. The errors represent the standard error values of the curve parameters.

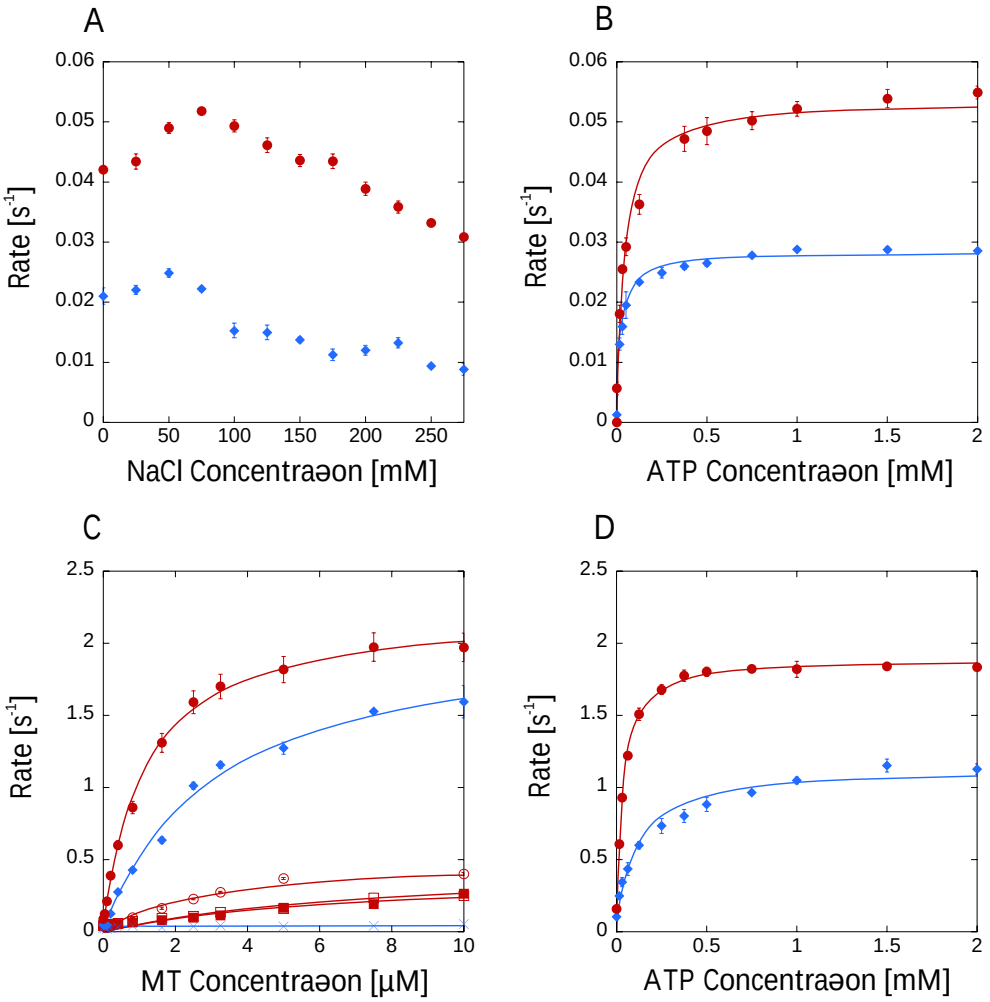

Figure 3.16: Characterisation of the basal and MT-stimulated ATPase activities of Kif15$_{1-375}$ and Kif15$_{19-375}$. (A) Influence of NaCl concentration on the basal ATPase activity of Kif15$_{1-375}$ (blue) and Kif15$_{19-375}$ (red), in the presence of 1 mM ATP. (B) Optimisation of the basal ATPase activity in the presence of increasing ATP concentrations measured at 50 mM NaCl for Kif15$_{1-375}$ (blue) and 75 mM NaCl for Kif15$_{19-375}$ (red). (C) Salt dependence of the MT-stimulated Kif15$_{1-375}$ (blue) ATPase activity in the presence of 0 (⬥) and 50 (×) mM KCl; salt dependence of the MT-stimulated Kif15$_{19-375}$ (red) ATPase activity in the presence of 0 (•), 50 (○), 100 (▫) and 150 (▪) mM KCl; all measured at 1 mM ATP. (D) Optimisation of the ATP concentration for the MT-stimulated ATPase activity of Kif15$_{1-375}$ (blue) and Kif15$_{19-375}$ (red), in the presence of increasing ATP concentrations, measured at 3 μM MT in the absence of salt. The Michaelis-Menten curve was fitted by Kaleidagraph 4.0 using the least squares method (Chapter 2.3.5). Rates of activity were calculated using the correlation between absorbance at 340 nm and kinesin activity. All measurements were done at least in triplicate, error bars are indicated.

50 mM KCl for Kif15$_{1-375}$, and 0, 50, 100 or 150 mM KCl for Kif15$_{19-375}$. With increasing salt concentrations MT-stimulated ATPase activity decreased significantly, especially for the Kif15$_{1-375}$ construct (Figure 3.16C). The k_{cat} for the MT-stimulated ATPase activity was 2.1 ± 0.1 s^{-1} with a K$_{0.5,MT}$ of 3.1 ± 0.1 μM for Kif15$_{1-375}$ and 2.3 ± 0.1 s^{-1} with a K$_{0.5,MT}$

of 1.1 ± 0.1 μM for $Kif15_{19-375}$. Finally, the MT-stimulated ATPase activity in the presence of increasing ATP concentrations (from 0 to 2 μM) was determined, establishing a $K_{M,ATP}$ of 109 ± 20 μM for $Kif15_{1-375}$ and a $K_{M,ATP}$ of 33 ± 3 μM for $Kif15_{19-375}$ (Figure 3.16D).

3.2.6 Kif15 inhibitor screening

Initially, the effect of two potent Eg5 inhibitors, monastrol and STLC, on Kif15 ATPase activity was checked, both in the presence and absence of MTs (Figure 3.17), the more active Kif15 construct was used ($Kif15_{19-375}$). As expected, Kif15 stayed fully active, even at the highest

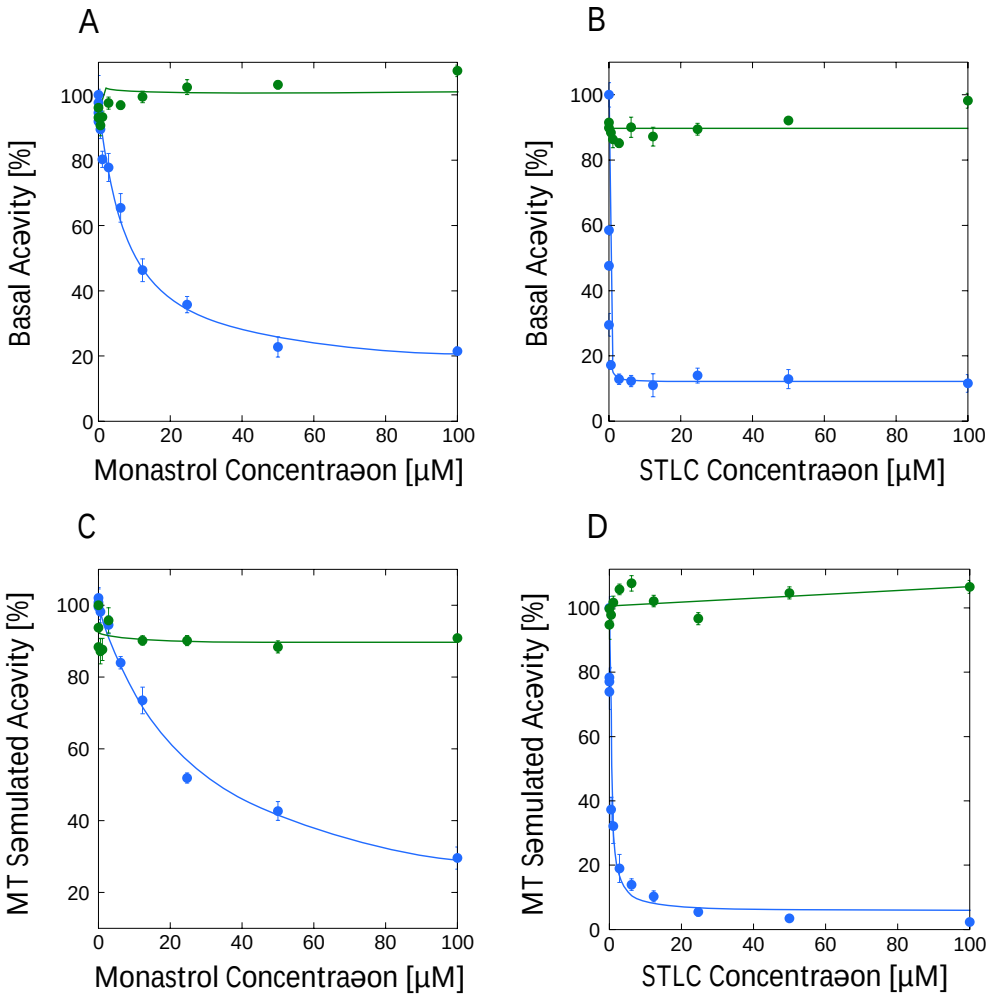

Figure 3.17: Inhibition of Kif15 (green) and Eg5 (blue) by monastrol and STLC. (A) Inhibition of the basal ATPase activity in the presence of increasing monastrol concentrations. (B) Inhibition of the MT-stimulated ATPase activity in the presence of increasing monastrol concentrations. (C) Inhibition of the basal ATPase activity in the presence of increasing STLC concentrations. (D) Inhibition of the MT-stimulated ATPase activity in the presence of increasing STLC concentrations. The IC_{50} curve was fitted using Kaleidagraph 4.0 using the least squares method (Chapter 2.3.6). All measurements were done at least in triplicate, error bars are indicated.

inhibitor concentration, up to 100 μM, while Eg5 was inhibited. In an effort to identify small molecules inhibiting Kif15 ATPase activity, nearly 2500 compounds and 4000 natural product

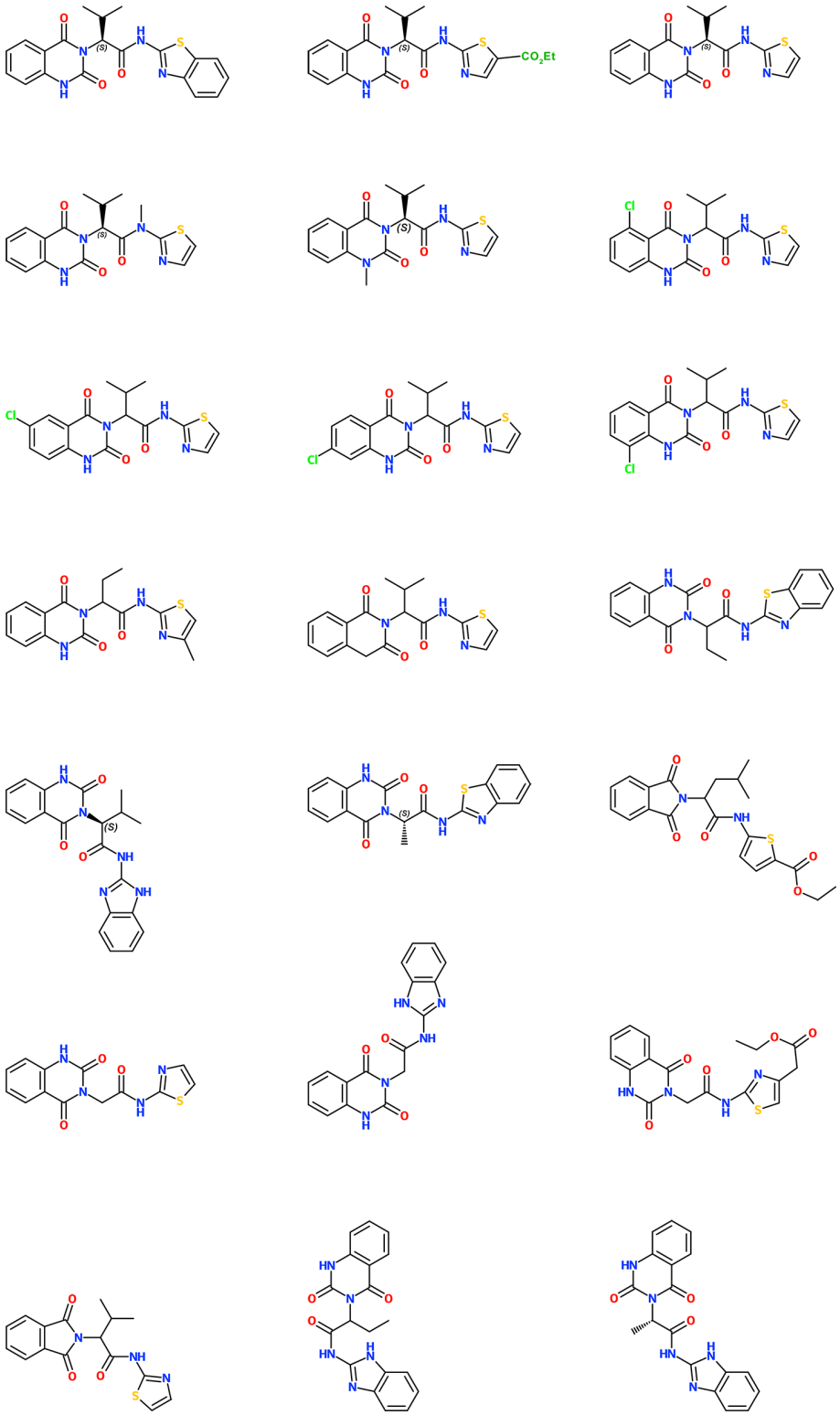

Figure 3.18: Structures of twenty-one small molecules from the Kif15 inhibitors patent (McDonald et al., 2004) tested in the Kif15 ATPase assay.

extracts were tested. The libraries were obtained in the 96-well plate format and were tested using 96-well micro-clear plates and a Tecan Sunrise photometer. Each compound was tested at a single concentration of 200 μM in the presence and absence of MTs. Unfortunately, none of them inhibited Kif15 activity. Upon encountering a patent for Kif15 inhibitors (McDonald et al., 2004), another approach to obtain a Kif15 inhibitor was undertaken. Twenty-one of the small molecules from the Kif15 inhibitors patent (Figure 3.18) were purchased and their influence on Kif15 activity, under basal and MT-stimulated conditions was tested. Additionally, the possibility of the competitive inhibition was investigated, by measuring rates of Kif15 activity at a low ATP concentration, up to 100 μM. In all of these conditions Kif15 activity was unaffected up to 200 μM of each compound. The patent does not provide any information about the mechanism of action of the described compounds (quinazolinedione derivatives), it only points to their inhibitory effect on Kif15 activity. Compounds were soluble in DMSO and prepared as described in Section 2.3.6. DMSO was used as a control and did not have any effect on Kif15 ATPase activity. In the used experimental setting (*in vitro* ATPase assay) the possibility of the compound binding to the protein could not be ruled out (this could possibly be investigated by NMR), but the possibility of inhibiting Kif15 enzymatic activity was eliminated. Due to limited information presented in the patent it is difficult to speculate as to why none of the inhibitors was effective.

3.2.7 Kif15 nucleotide-dependent MT-binding site

The affinity of $Kif15_{19-375}$ for MTs in the presence of 2 mM Mg^{2+}ATP, 2 mM AMP-PNP and 4 mU apyrase (thus establishing the "nucleotide-free" state) was determined, using the MT-pelleting assay. Increasing amounts of $Kif15_{19-375}$ (1–12 μM) were incubated with MTs (5 μM) and supplemented with nucleotide or apyrase. Post incubation and centrifugation samples of supernatants and pellets were analysed by SDS-PAGE. The results are shown in Figure 3.19. The K_D values, as well as the stoichiometry of binding of Kif15 to MTs, are summarised in Table 3.6. A portion of depolymerised MTs is visible in the supernatant. Although MTs were prepared in the presence of taxol, polymerisation was not complete and some of tubulin heterodimer is present in the soluble fraction of the sample. A comparable amount of unpolymerised tubulin heterodimer was recovered from the supernatant in the

	AMP-PNP	Apyrase
K_D [μM]	0.5 ± 0.2	0.4 ± 0.2
B_{max} [μM]	3.5 ± 0.2	3.2 ± 0.2
Stoichiometry ($Kif15_{19-375}$: MT)	1 : 1.1	1 : 1.3

Table 3.6: Dissociation constants, maximum binding capacity and the stoichiometry of binding of $Kif15_{19-375}$ to MTs measured in the presence of 2 mM AMP-PNP or 4 mU apyrase.

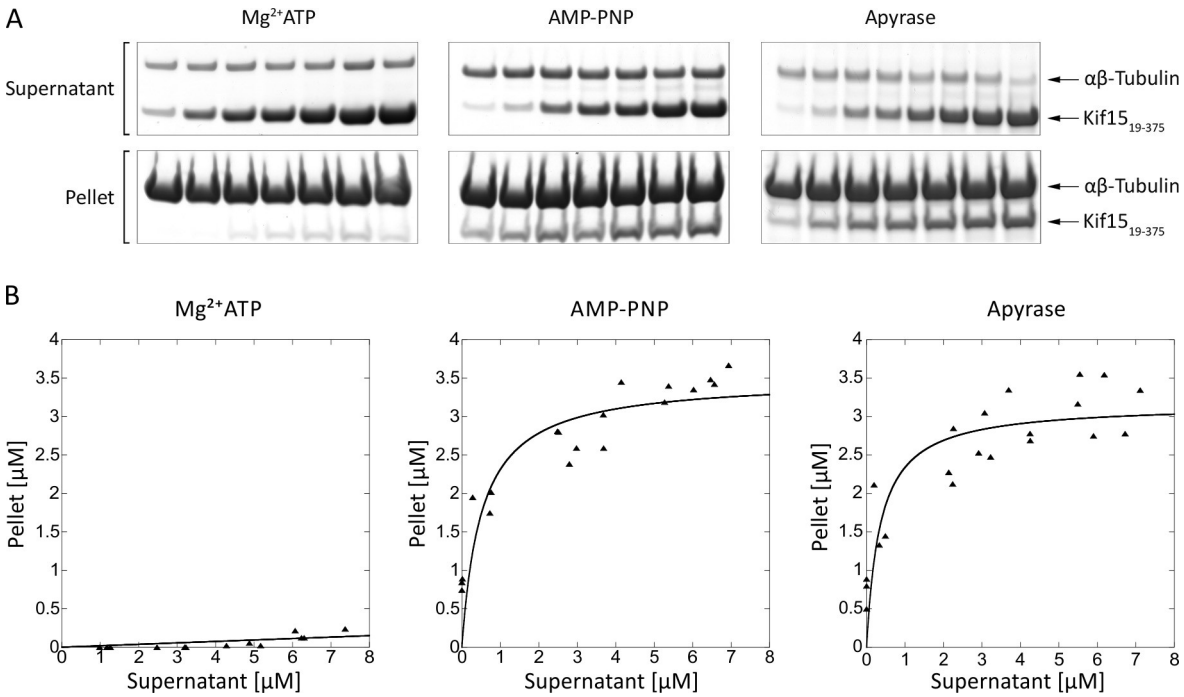

Figure 3.19: MT-pelleting assays in the presence of the Kif15 motor domain. (A) MT-pelleting assays of the Kif15 motor domain in the presence of various nucleotides. Increasing amounts of Kif15$_{19-375}$ (1–12 μM) were incubated with MTs (5 μM) in the presence of 2 mM Mg^{2+}ATP, 2 mM AMP-PNP or 4 mU apyrase. Samples of supernatants and pellets were analysed by SDS-PAGE. (B) MT-binding of Kif15$_{19-375}$ in the presence of 2 mM Mg^{2+}ATP, 2 mM AMP-PNP or 4 mU apyrase. The Michaelis-Menten curve was fitted by Kaleidagraph 4.0 using the least squares method.

control experiment, where no Kif15 was added. In the presence of the slowly-hydrolysable ATP analogue AMP-PNP or apyrase, Kif15$_{19-375}$ shows comparable affinities for MT with K_D values of 0.5 ± 0.2 and 0.4 ± 0.2 μM, respectively, with a stoichiometry (Kif15$_{19-375}$ to MTs) of close to one (1.1 and 1.3, respectively) indicating that one Kif15 motor domain binds to one $\alpha\beta$-tubulin heterodimer, in agreement with results reported for other kinesins. Under conditions tested, the Kif15 motor domain shows no affinity for MTs in the presence of Mg^{2+}ATP (in the presence of MTs, ATP is rapidly hydrolysed, the ADP-state is known to possess low affinity for MTs). In conclusion, human Kif15 contains a nucleotide-dependent MT binding region in its motor domain.

3.2.8 Investigation of the possibility of a second MT-binding site within the Kif15 tail domain

The possibility of a nucleotide-independent MT-binding region in the Kif15 tail domain was also investigated. A second MT-binding site has been identified in a variety of kinesin tail domains (Chandra et al., 1993; Echard et al., 1998; Germani et al., 2000; Karabay and

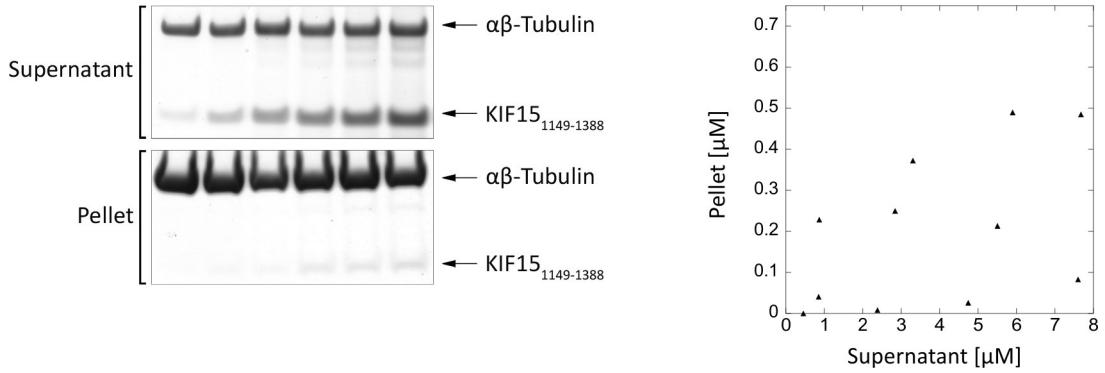

Figure 3.20: MT-pelleting assays for the Kif15 tail domain. Increasing amounts of $Kif15_{1149-1388}$ (1–10 μM) were incubated with MTs (5 μM). No nucleotide was added. Samples of supernatants and pellets were analysed by SDS-PAGE.

Walker, 1999; Kuriyama et al., 1994; Liao et al., 1994; Meluh and Rose, 1990; Narasimhulu and Reddy, 1998) and has been shown, in some cases, to be physiologically important for their biological function. The data for the Kif15 tail-MT interaction are shown in Figure 3.20. $Kif15_{1149-1388}$ did not bind to MTs in the pelleting assay, suggesting that the tail does not contain MT-binding site.

3.2.9 Kif15 and actin binding investigation

To investigate a possible, direct interaction between $Kif15_{740-1333}$ (the myosin homology domain) and actin *in vitro*, an actin-binding assay was performed (Figure 3.21). No binding was detected under conditions tested for Kif15, while the positive control (α-actinin, cytoskeletal actin-binding protein) co-pelleted with actin. Although this experiment did not reveal any interaction, it cannot be ruled out, because of the limitations of the used methodology. It

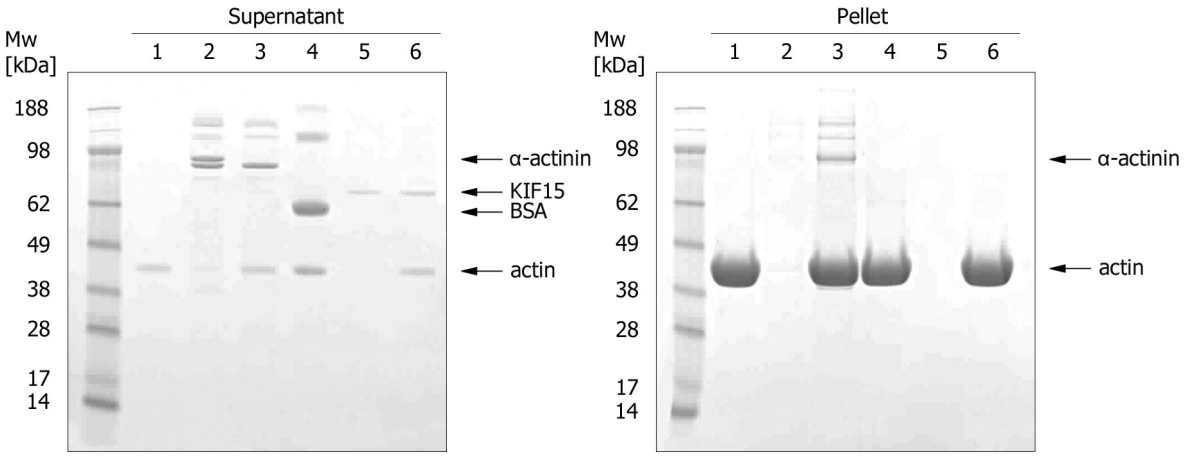

Figure 3.21: Actin-binding assay. Samples of supernatants and pellets were analysed by SDS-PAGE. Lane 1: F-actin alone. Lane 2: α-actinin alone. Lane 3: F-actin and α-actinin. Lane 4: F-actin and BSA. Lane 5: $Kif15_{740-1333}$ alone. Lane 6: F-actin and $Kif15_{740-1333}$.

is possible that designed construct was not sufficient for actin binding. Another possibility is that binding requires an additional molecule mediating the Kif15-actin interaction that was present in the *in vivo* scenario for which the binding was reported (Buster et al., 2003). Unfortunately no information about such a partner protein is available in the literature.

3.2.10 Kif15 partner protein investigation

In order to investigate interactions between Kif15 and its binding partners, full-length TPX2 and the FHA domain of Ki-67 were cloned and tested for expression, under a variety of conditions. Both were expressed in BL21(DE3)pLysS and purified from large-scale culture (Figure 3.22). Purified TPX2 was used to determine its affinity for MTs. The pelleting assay, in which increasing amounts of TPX2 (1–4 μM) was incubated with MTs (4 μM), revealed high TPX2 affinity for MTs (K_D = 50 nM). Results are presented in Figure 3.23.

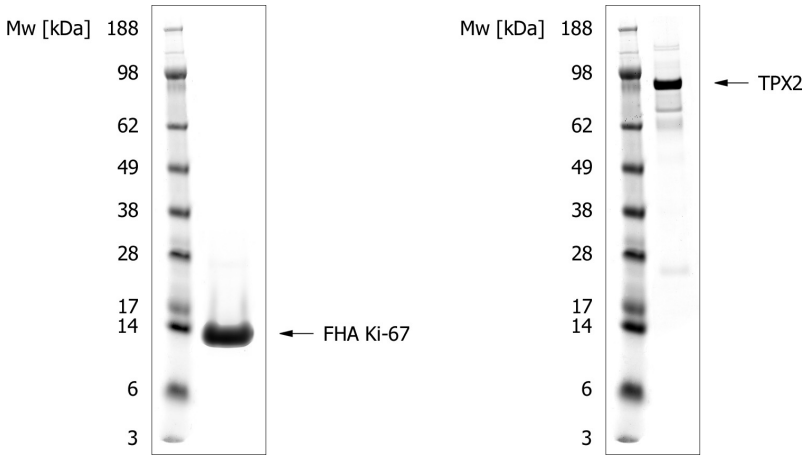

Figure 3.22: SDS-PAGE of purified Ki-67 FHA domain (left) and TPX2 (right). Lane 1 on each gel shows molecular weight markers (in kDa). The expected molecular weight of the proteins are 14 kDa for FHA domain and 86 kDa for TPX2.

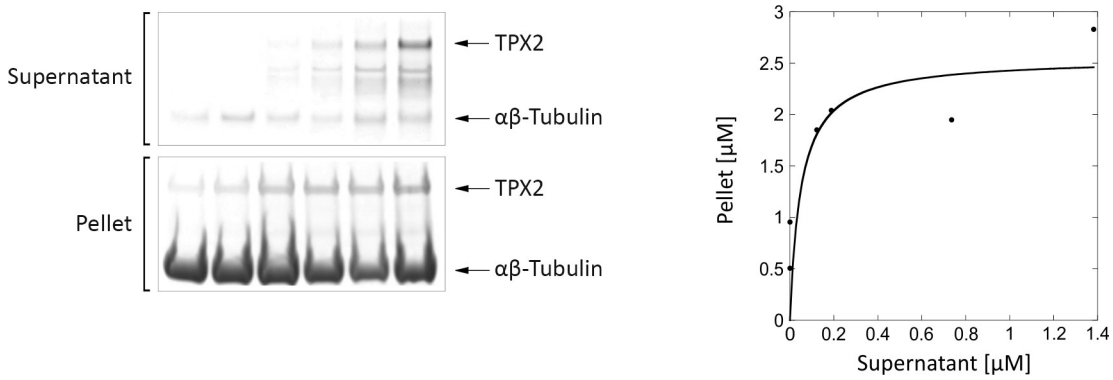

Figure 3.23: TPX2 MT-pelleting assays. Samples of supernatants and pellets were analysed by SDS-PAGE. Increasing amounts of TPX2 (1–4 μM) were incubated with MTs (4 μM).

3.3 Characterisation of Kif7 and Kif27, Kinesin-4 family members

Members of the Kinesin-4 superfamily are implicated in a variety of diseases, including Joubert, Hydrolethalus and Acrocallosal Syndromes. They also play a role in primary cilium formation and the Hedgehog signalling pathway. In this chapter, attempts to crystallise members of the Kinesin-4 family are reported. The obtained high-resolution structure of the human Kif7 motor domain is described and compared to conventional kinesin. In addition influence of one of the published Kif7 mutations is sampled.

3.3.1 Kif7 and Kif27 cloning, expression and purification

Following proteins were cloned, expressed and purified: $Kif7_{8-347}$, $Kif7_{8-361}$, $Kif27_{1-341}$, $Kif27_{1-339}$, $Kif27_{6-341}$, $Kif27_{17-341}$, as described in Sections 2.2.1–2.2.4 (cloning primers are

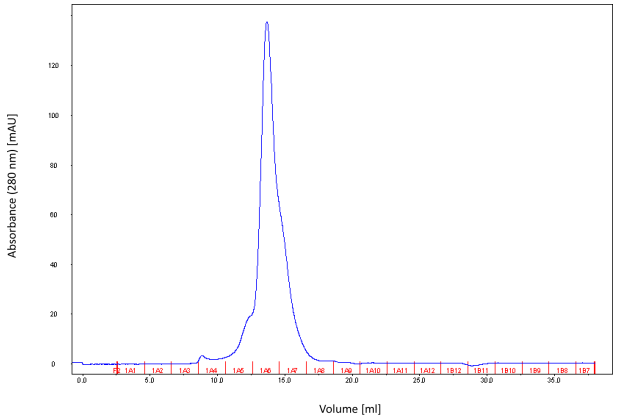

Figure 3.24: Analytical gel filtration profile of $Kif7_{8-347}$. The experiment was conducted a using Superose 12 10/300 GL column with a flow rate of 0.5 ml/min.

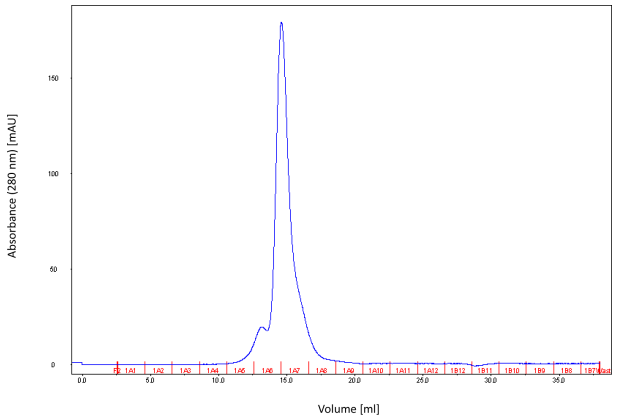

Figure 3.25: Analytical gel filtration profile of $Kif27_{1-341}$. The experiment was conducted using a Superose 12 10/300 GL column with a flow rate of 0.5 ml/min.

presented in Sections 2.2.1 and 2.4.1). Performed analytical gel filtration runs showed that all constructs were monomeric, as expected for kinesin motor domains. The exemplary gel filtration profiles are shown in Figure 3.24 and Figure 3.25. The proteins were 90–95% pure as judged by SDS-PAGE, presented in Figure 3.26.

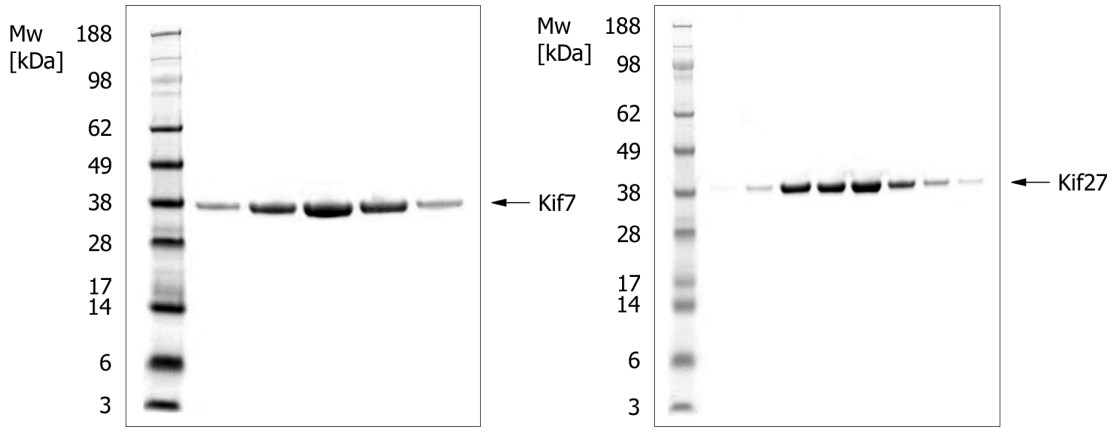

Figure 3.26: SDS-PAGE of fractions from gel filtration runs of $Kif7_{8-347}$ (left) and $Kif27_{1-341}$ (right). Lane 1 on each gel shows molecular weight markers (in kDa). The expected molecular weight of the proteins are 37 kDa for $Kif7_{8-347}$ motor domain and 38 kDa for $Kif27_{1-341}$.

3.3.2 Kif7 and Kif27 crystallisation

Of all Kif7 and Kif27 constructs used for crystallisation screening, only $Kif7_{8-347}$, which lacks the neck linker region, yielded crystals. None of the Kif27 constructs crystallised. $Kif7_{8-347}$ crystals grew in 20%PEG 3350, in the presence of one of various salts (0.2 M ammonium nitrate, 0.2 M lithium acetate, 0.1 M magnesium formate dihydrate, 0.2 M potassium sodium tartrate, 0.1 M sodium acetate, 0.2 M sodium nitrate), however, the best quality crystals were obtained in the presence of lithium acetate, and this condition was used to reproduce crystals at the micro-scale for X-ray diffraction data collection.

3.3.3 Kif7 motor domain structure

$Kif7_{8-347}$ crystallised with one molecule per asymmetric unit. Data were collected to 1.6 Å, thus Kif7 belongs to a small group of kinesin motor domains with X-ray structure solved to higher resolution. A higher resolution structure was reported for *Saccharomyces cerevisiae* Kar3 mutant motor domain (1.3 Å) (Yun et al., 2001). Figure 3.27 shows diffraction quality of the Kif7 crystals. An exemplary electron density map for Kif7 model is presented in Figure 3.32. Data collection and refinement statistics are summarised in Table 3.7. The final structure includes residues 12–347 (missing regions: 107–114, 207–211, 230–241, 260–273) with bound Mg^{2+}ADP (octahedrically coordinated) in the catalytic site, and 328 water

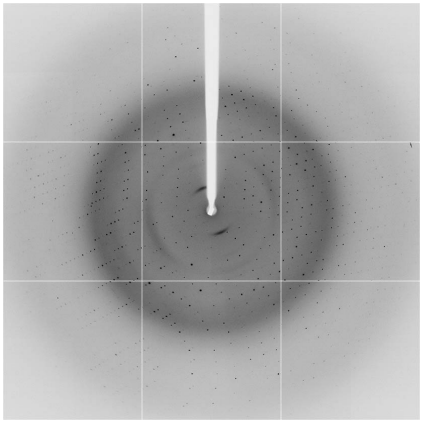

Figure 3.27: $Kif7_{8-347}$ crystal X-ray diffraction image.

molecules. The refined structure contains 98.7% of residues in the most favourable region, 1.3% in allowed regions and no outliers. Figure 3.28 presents the overall structure of the front and the back view of the Kif7 motor domain. Kif7 contains an 8-stranded β-sheet core with three solvent-exposed α-helices on each side, displaying the characteristic arrowhead-like structure, typical for all members of the kinesin superfamily solved so far (Kull et al., 1996).

Subsequently, Kif7 structure was compared to that of conventional kinesin, the founding member of the kinesin superfamily. The alignment of $Kif7_{8-347}$ with conventional kinesin (Kif5B) revealed their high structural similarity (Figure 3.29, Figure 3.30). The sequence identity between the Kif5B and Kif7 motor domains is 37%. There are two single insertions in Kif7 loop L2. The P-loop is conserved in both proteins. In both structures, helix α2

	$Kif7_{8-347}$-Mg^{2+}ADP
PDB ID	4A14
Beamline / Detector	I04-1 / Pilatus 2M
Resolution range [Å]	30–1.6
Space group	$P2_12_12_1$
Unit cell parameters [Å; °]	$a = 45.99$, $b = 79.80$, $c = 95.05$
	$\alpha = \beta = \gamma = 90$
Completeness [%]	99.9 (100)
R_{merge}	3.2 (43.1)
Multiplicity	7.5 (7.5)
Mean I/σ	30.1 (4.4)
No. of total / unique reflections	46998 / 6746
No. of copies per AU	1
R_{work} / R_{free} [%]	18.25 / 20.67
No. of Mg^{2+}ADP / water molecules	1 / 348
Bond length rmsd [Å]	0.011
Bond angle rmsd [°]	1.547

Table 3.7: Data collection and refinement statistics for $Kif7_{8-347}$-Mg^{2+}ADP complex. Values in parentheses are for the highest shell.

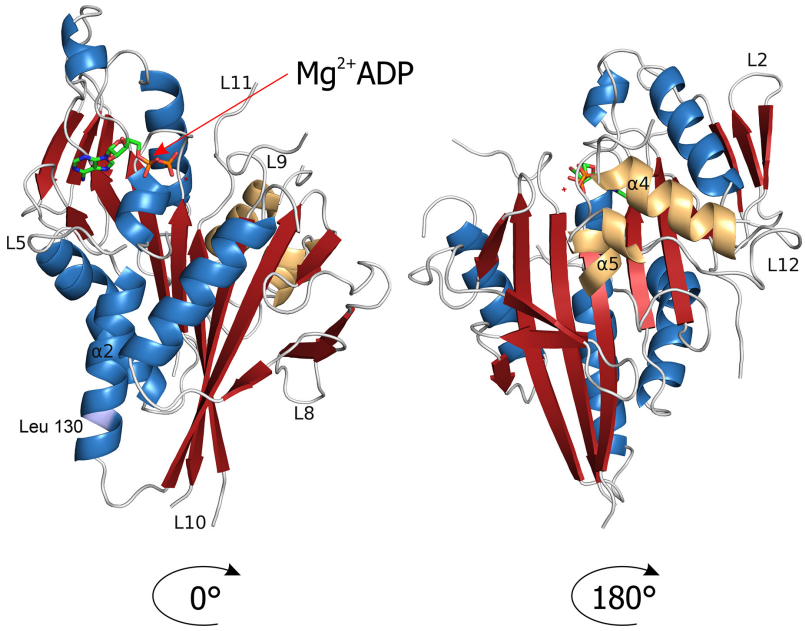

Figure 3.28: Overall structure of $Kif7_{8-347}$ in complex with Mg^{2+}ADP. α-helices are shown in blue, β-strands in red and loop regions are shaded in grey. The switch II cluster (α4-L12-α5) and the end of helix α6 preceding the neck-linker region (not visible in this structure) are coloured in orange. Mg^{2+}ADP is presented as a ball and stick model.

is interrupted by loop L5, Kif7 contains a three-residue insertion in this loop. Although some electron density was visible for loop L5, residues Ala107 to Glu114 are missing, due to its increased length and high flexibility. Several attempts were undertaken to build this

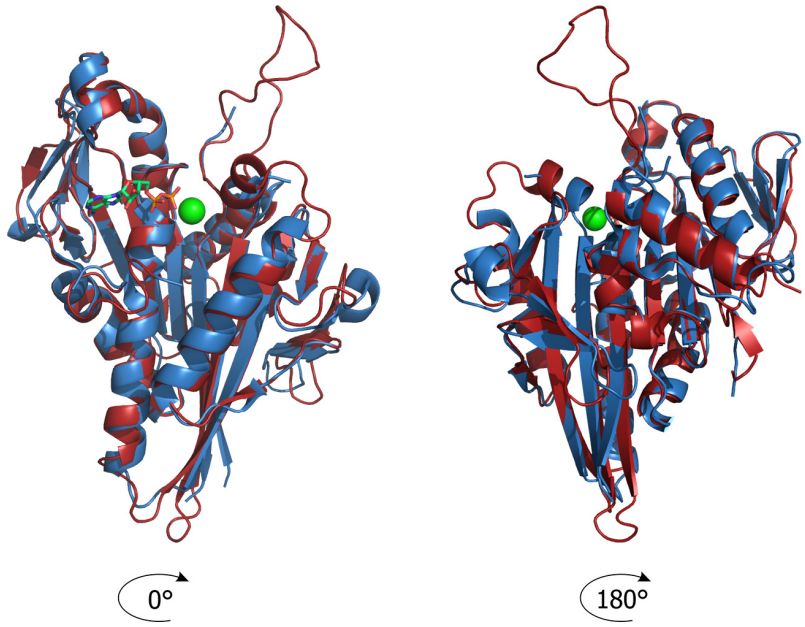

Figure 3.29: Structure overlay of Kif7 and Kif5B motor domain. Front and back view of overlaid Kif7 (blue) and Kif5B (red) (PDB ID: 1BG2 (Kull et al., 1996)) structures. Mg^{2+}ADP is shown as a ball and stick model.

region but each attempt caused appearance of negative electron density after refinement. Once this part of model was deleted, the structure was refined again and positive electron density appeared indicating that this region may possess a dual conformation. In Kif7, the end of the second part of helix $\alpha 2$ has a single residue deletion, compared with Kif5B. Another two-residue insertion in Kif7 occurs in the loop L8 region, which is fully visible in the structure. Only residues Val159–Thr161 have an unclear density, which may suggest a variable conformation of this part of the loop. In Kif5B, the switch I region (residues 199 to 205) consists of a small helix ($\alpha 3a$), whereas in Kif7 it forms a loop (L9). The remaining part of switch I region is highly conserved in both proteins. In Kif7, there is an eight-residue long insertion in loop L10, this region is disordered and not visible in the structure. Switch II

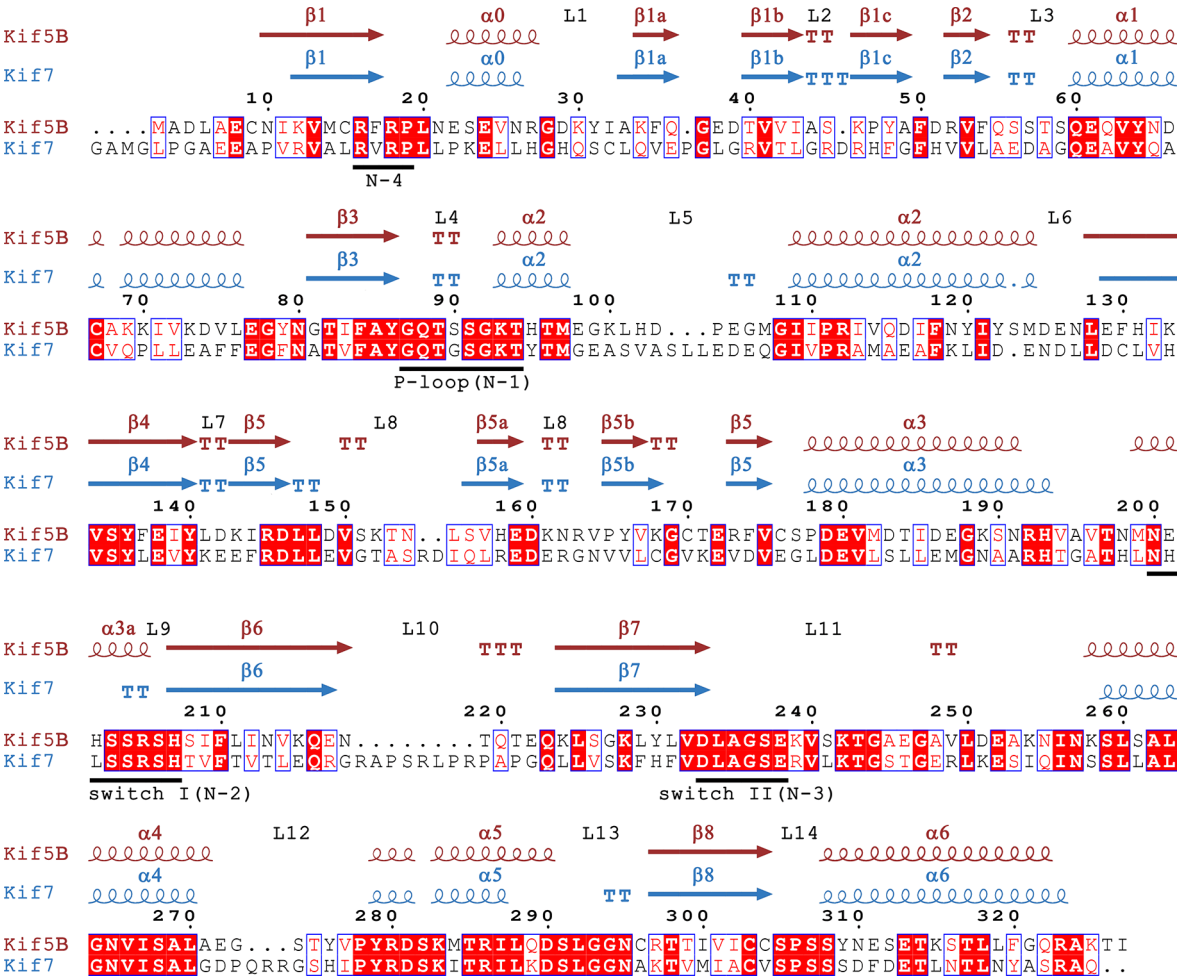

Figure 3.30: Sequence and secondary structure element alignment of Kif7 and Kif5B. Secondary structure elements derived from the crystal structures of the Kif5B (PDB ID: 1BG2 (Kull et al., 1996)) and Kif7 motor domains. Identical residues are coloured in white on a red background, similar residues are shaded in red. The ATP-binding pocket and the switch regions elements (N1 to N4) are underlined in black. The alignment was generated using ClustalW2 multiple alignment tool (Larkin et al., 2007). Figure was prepared using ESPript (Gouet et al., 2003).

(Asp251–Glu257), which is highly conserved in both proteins and typically disordered in kinesins, is not fully visible in the Kif7$_{8-347}$ structure. The switch II cluster (α4-L12-α5) is in the down position, and one would expect the neck linker (Arg350–Asn356) to be either unstructured, or structured, but in an undocked position with respect to the motor domain. However, the neck linker is not included in this structure, due to the short length of the crystallised Kif7 construct. Kif7$_{8-361}$ contained the neck linker region, but did not crystallise, whereas Kif7$_{8-347}$, lacking the neck linker, revealed that the C-terminal residue Gln347 shows crystal contacts, indicating that there would not be space for a neck linker in this crystal form. This might explain why the longer Kif7 construct did not yield crystals. The loop L11 region (Leu260–Ile273) is missing, as in most other kinesin structures. Kif7 contains a three-residue insertion in fully visible loop L12.

3.3.4 Influence of the L130P mutation on the Kif7 motor domain

In a mouse model, a single mutation in the Kif7 motor domain (L130P) caused early embryonic lethality. This mutation was introduced through N-ethyl-N-nitrosourea induction, in order to determine the impact on Hh signalling (Liem et al., 2009). To investigate how L130P mutation could influence the structure, the mutation was introduced into the expression construct of the motor domain (Kif7$_{8-347}$). Although the construct carrying the mutation was expressed in *E. coli*, the protein was insoluble (Figure 3.31).

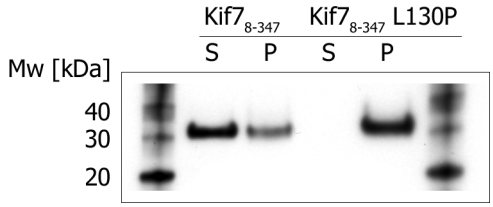

Figure 3.31: Western blot analysis of soluble (supernatant) and insoluble (pellet) fractions of Kif7$_{8-347}$ and Kif7$_{8-347}$ L130P. The antibody for His-tagged proteins and His-tagged protein standard were used. The expected molecular weight for Kif7$_{8-347}$ is 37.3 kDa

Nevertheless, the structure of native Kif7 reveals that the L130P mutation would be situated at the end of the second half of the interrupted helix α2 (Figure 3.32). It is possible that the mutation of leucine to proline, a known "helix breaker", could cause a significant change to the protein's secondary structure in this region. Also, there is one C-H-π interaction between Leu130 and Phe83 that is lost when leucine is mutated to proline.

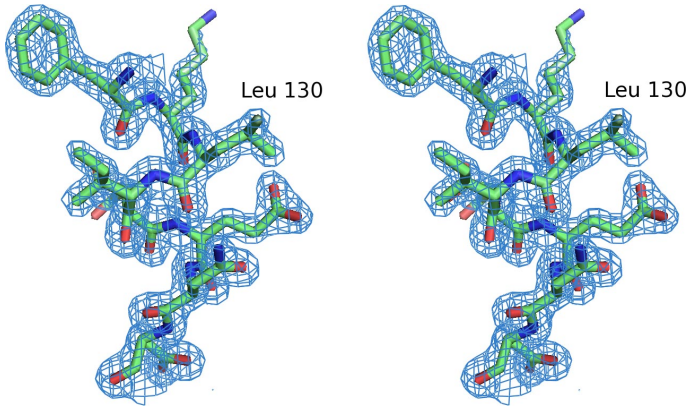

Figure 3.32: Stereo-plot of $Kif7_{8-347}$ helix $\alpha 2$ residues 128–132. The electron density map (coloured in blue) is contoured at 1 σ. A single mutation in this region (L130P) causes embryonic lethality.

Chapter 4

Discussion

4.1 Kinesin expression panel

Kinesins are known to perform a wide range of key cellular functions. Several human kinesins have been linked to various diseases (Mandelkow and Mandelkow, 2002). Certain mitotic kinesins, like CENPE and Eg5, are potential targets for drug development in cancer chemotherapy (Huszar et al., 2009). Therefore, it is desirable to establish protocol for kinesin expression conditions for at least one representative of each subfamily, to test the selectivity of specific kinesin inhibitors, or to facilitate inhibitor screening for these, which are potential targets. Last but not least, it is important to investigate kinesins from different subfamilies to correlate cellular functions with activity data. As the *E. coli* expression system is the most accessible, fast and cheap for *in vitro* protein expression, and it is employed in many laboratories, it would be most advantageous to use it for future studies on kinesins.

Kinesin panels play an important role in elucidating the specificity of kinesin inhibitors for drug discovery and for chemical genetics (a method of using small molecules as tools for basic biological research, analogous to classical genetics, it requires a library of compounds (equivalent to a mutation in classical genetics) and an assay to screen for a phenotype change). In particular, for chemical genetics it is crucial to know how specific the inhibitors are. Small subfamily-specific panels have been reported for Eg5 and CENPE (Rath and Kozielski, 2012) and larger multi-species panels have been reported (DeBonis et al., 2004). Lately, several kinesin panels of different size have been reported for the development of kinesin-targeting drugs for cancer chemotherapy (Sakowicz et al., 2004; Skoufias et al., 2006). A range of GST-tagged kinesins from different species are commercially available (Cytoskeleton, USA). A common feature of most of these panels is that the exact conditions (construct length, expression *E. coli* strain and strategy, purification protocol) used to obtain active kinesins

are not given.

In this study, motor domain expression of almost half of human kinesins was investigated. Of these, nine could be expressed and purified. In addition there are a few other human kinesin motor domain which have been previously investigated. These include as yet unpublished crystal structures submitted to the PDB by the Canadian Structural Genomics Consortium: Kif2A (PDB ID: 2GRY), Kif2C (PDB ID: 2HEH), Kif3B (PDB ID: 3B6U), Kif3C (PDB ID: 3B6V), Kif13B (PDB ID: 3GBJ), Kif22 (PDB ID: 3BFN), KifC1 (PDB ID: 2REP) and KifC3 (PDB ID: 2H58). Other groups published structures of Kif5B (PDB ID: 1BG2 (Kull et al., 1996)), CENPE (PDB ID: 1T5C Garcia-Saez et al., 2004)) and Eg5 (PDB ID: 1II6 (Turner et al., 2001)). The structure of human Kif18A has also been solved (PDB ID: 3LRE (Peters et al., 2010)). There is also reported expression for Kif1C and Kif14 (Tcherniuk et al., 2010). Other lab members have successfully expressed motor domains of three Kinesin-6 family representatives (Mklp1, Mklp2 and Mpp1). Taken together with kinesins tested in this study, twenty-four out of forty-five of the human kinesin motor domains can be produced in *E. coli*, although final statistics can only be provided once the other untested kinesins have been subjected to the screening procedure. The other approach that may increase the success

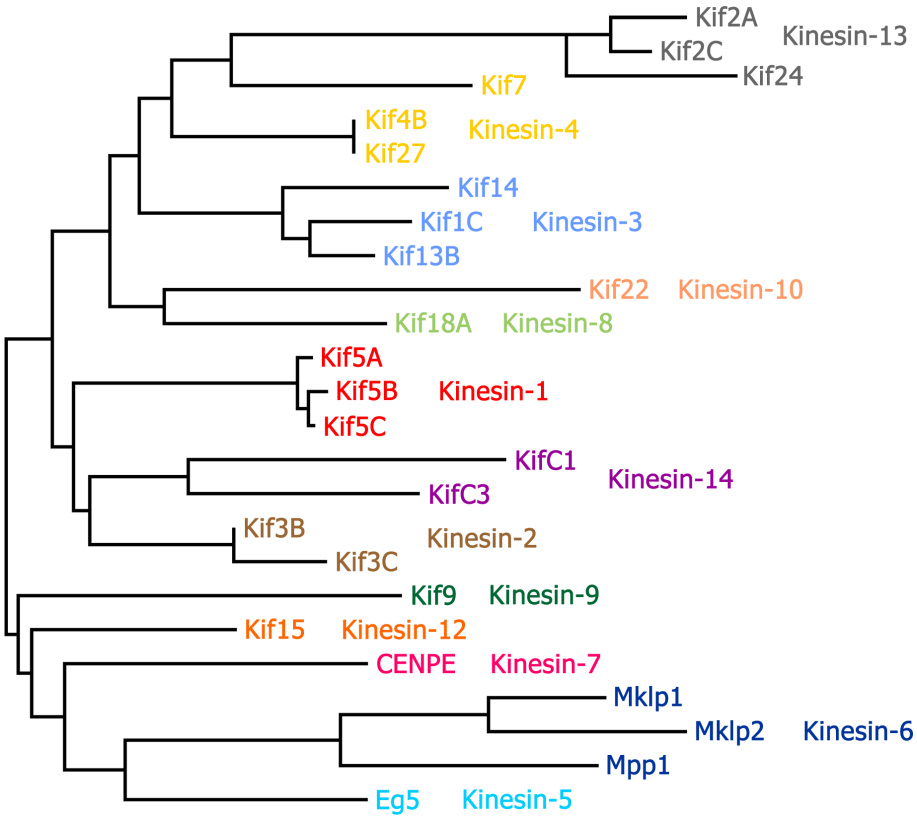

Figure 4.1: Phylogenetic analysis (Dereeper et al., 2008) of human kinesin motor domains, expressed and purified in *E. coli* in this study, and from a literature survey. The following kinesin motor domains were expressed in this study: Kif3B, Kif4B, Kif5A, Kif5C, Kif7, Kif9, Kif15, Kif24 and Kif27.

rate in the expression trial is usage of other fusion proteins (MBP, SUMO, GST), as solubility is clearly an issue for this family representatives. A simplified phylogenetic tree (Figure 4.1) reveals that kinesins from thirteen out of fourteen subfamilies can be expressed, purified and investigated. The only family with no reported *E. coli* expression is Kinesin-11, members of this family (Kif26A, Kif26B) are rather atypical kinesins. Although they possess a motor domain and bind to MTs, they lack ATPase activity. Kinesin-11 family members play a role in neuronal development (Zhou et al., 2009). In summary, this work provides information about expression conditions for a panel of human kinesins, which can be useful for kinetic characterisation of medically relevant motors, and for specificity assays on small molecules targeting medically relevant kinesins.

4.2 Kif15 and Eg5 fulfil overlapping roles in a distinct manner

The role of Kif15 role during bipolar spindle elongation and maintenance reveals that it may be, under certain conditions, a functional homologue of Eg5, a protein crucial for bipolar spindle initiation and separation. Although their mechanism of action is clearly different, both proteins are able to work redundantly to fulfil similar roles. Homotetrameric Eg5 performs its function because of its unique quaternary structure, allowing it to crosslink antiparallel MTs, and with its plus-ended directed motility, slides them apart, to form the bipolar spindle. In

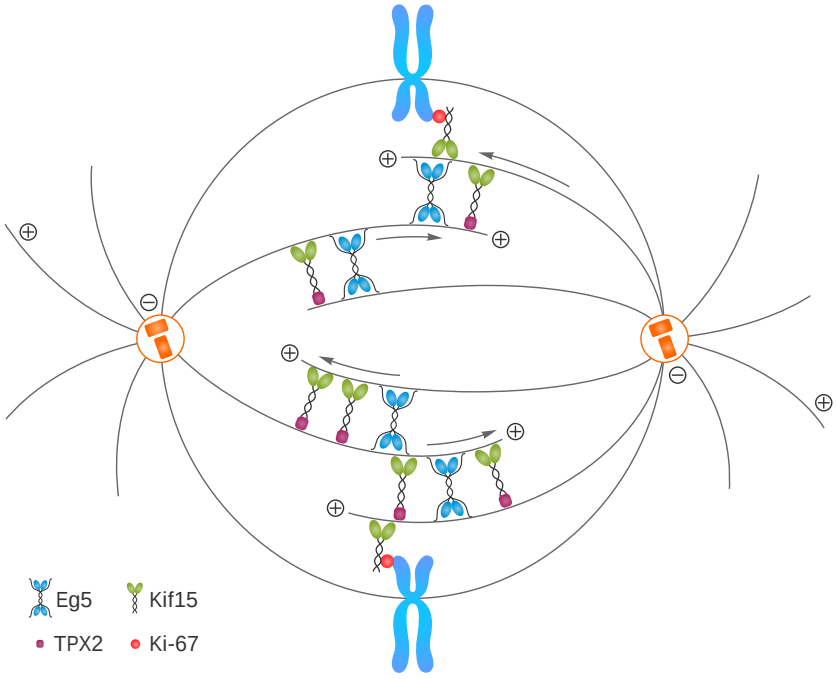

Figure 4.2: Model of Kif15 and Eg5 mode of action during bipolar spindle formation. Tetrameric Eg5 binds and slides MT poles apart. Kif15 associates with MTs via TPX2 or to chromosomes through its interaction with the FHA domain of Ki-67.

contrast, Kif15 works as a dimer (Wittmann et al., 1998) and, as demonstrated in this study, it does not contain a MT-binding site within its tail domain. The function of the MT-linker is carried out by TPX2 through the Kif15 C-terminal leucine zipper region (Wittmann et al., 2000) (Figure 4.2).

4.2.1 Kif15 enzymatic activity

Kif15 ATPase activity characterisation provided initial insight into its enzymatic mode of action. A specific Kif15 feature is its low affinity for MTs (compared with that of a conventional kinesin), in the case of both of the motor domain constructs tested. $Kif15_{1-375}$ construct possesses the first 18 residues that are thought to include the cover strand, a short nine-residue N-terminal region shown to interact with the C-terminal neck linker in the case of several other kinesin family members. These two regions have been shown to fold into the so-called neck-cover bundle by forming a small β-sheet and creating a force generating element in several members of the kinesin superfamily (Hwang et al., 2008; Khalil et al., 2008). In the case of Kif15 ATPase activity, with the exception of a threefold difference in the $K_{M,ATP}$ and $K_{0.5,MT}$ values there was no significant difference between $Kif15_{1-375}$ and $Kif15_{19-375}$, indicating that the presence or absence of the cover strand does not significantly change its ATPase characteristics.

4.2.2 Kif15 and partner proteins

Two reported partner proteins of Kif15 were cloned, expressed and purified — TPX2 and the FHA domain of Ki-67. Due to project termination, only initial characterisation was performed, confirming tight binding of TPX2 to MTs. The resultant production protocol for both protein production will be useful for further studies.

4.2.3 Kif15 function and clinical implications

Due to their similar functions, Kif15 may be able to take over the role played by Eg5, following anti-Eg5 chemotherapy, by simply up-regulating protein expression levels, at least in cell culture (Tanenbaum et al., 2009). Such an interchange of abilities of the two motors is supported by observations in neuronal cells (Liu et al., 2011), which are non-mitotic, suggesting a broadly applicable theme, by which two structurally different motors can share a function but not a mechanism of action. If this scenario of a possible resistance mechanism were true for certain tumours, co-inhibition of both motors, Eg5 and Kif15, could be a vital therapeutic approach. In light of recent studies it is apparent that Kif15 can overcome Eg5

inhibition after nuclear envelope breakdown (the initial events of mitotic division), after the centrosome separation is bypassed by nuclear envelope dynein (Raaijmakers et al., 2012; Tanenbaum and Medema, 2010). The crystal structure of human Kif15 obtained in this work will be a valuable asset for structure-guided drug design. The comparison of both of motors revealed that despite overall similarity, Kif15 and Eg5 have important differences allowing Kif15 to be impervious to Eg5 targeting drugs.

4.3 Kinesin-4 family members

The primary cilium, made of non-motile MTs, is a Hedgehog signalling transduction centre in vertebrate cells, where Kif7 plays a significant role in Gli protein trafficking (Figure 4.3). The Kif7 motor domain structure provides a first insight into Kinesin-4 family member structure. During investigation of the family representatives, several attempts to measure kinetic parameters of Kif7 and Kif27 constructs were undertaken, yet none of these was successful due to abnormal protein behaviour during the ATPase assay. Each attempt to measure the activity resulted in random data with no obvious trend and the attempts to fit the Michaelis-Menten curve were unsuccessful. The solved structure of Kif7 motor domain did not reveal

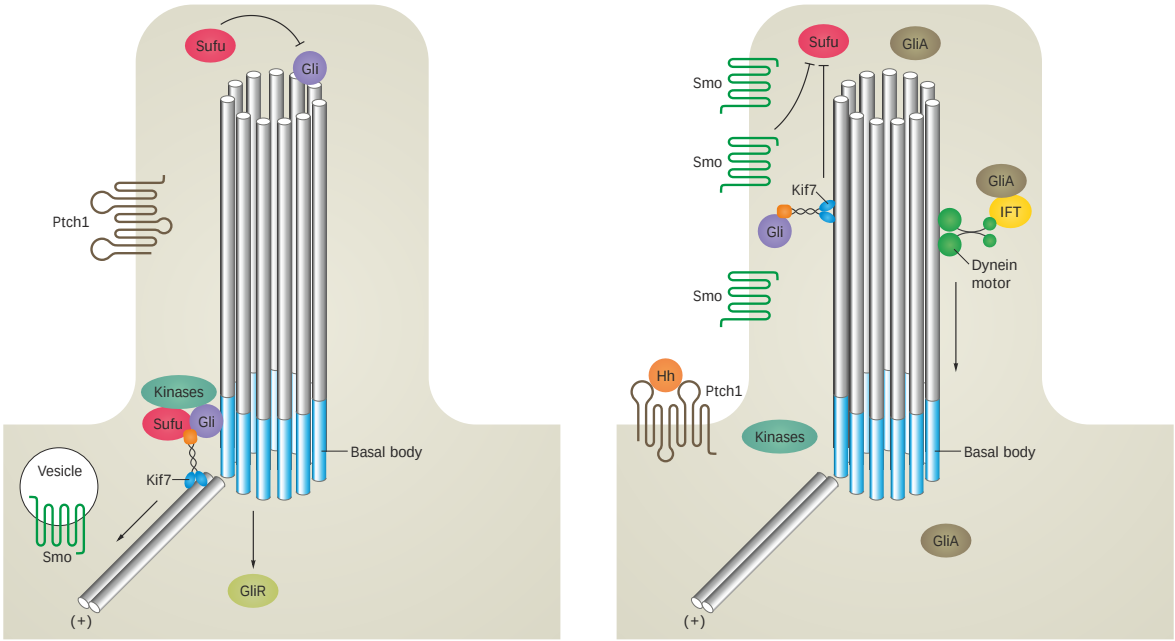

Figure 4.3: The Hedgehog signalling pathway in the primary cilium. (Left) When ligand is not present, Ptch1 is localised to the cilium, inhibiting membrane internalising of Smo. Kif7 prevents Gli enrichment. (Right) Upon ligand binding, Smo localises to the membrane, Kif7 moves onto cilium MTs, therefore promoting Gli accumulation at the cilium tip. Additionally, Kif7 can block Sufu activity. The reverse transport is accommodated by dynein and intraflagellar transport (IFT) elements. Figure adapted from Goetz and Anderson (2012).

any abnormal features of Kif7 catalytic core. On the contrary it shows its high similarity to the conventional kinesin motor. Even though the purified protein seems pure as judged by SDS-PAGE (Figure 3.26), it is possible that a minor contaminant is impeding the ATPase assay. Although some information is available about the involvement of kinesins in the vertebrate signalling centre, it still is vague and requires further investigation. The question regarding Kif7 regulation is still open. Is there an autoinhibitory mechanism that the protein undergoes? Does it require conformational change? How is its localisation regulated? From available studies, it is justified to assume that Kif7 motoric activity is crucial for early stages of development, and its lack or malfunction can lead to a set of neurodegenerative diseases and cancers (Dafinger et al., 2011; Putoux et al., 2011). In the future, it will be interesting to determine whether Kif7 and its closely related paralogue Kif27 are proteins worth targeting in the Hedgehog signalling pathway (Sarangi et al., 2009).

Part II

Structural and biochemical insights into members of the ubiquitin ligase family

Chapter 5

Introduction

5.1 Ubiquitin and ubiquitin-like proteins

Ubiquitin is an 8.5 kDa protein known for its ability to covalently modify other proteins (either as monoubiquitin or polyubiquitin chain), and in so doing, changing their fate. This protein is a prototype of ubiquitin-like modifiers (Ubls) family. The family members possess a common globular fold with one α-helix and four major β-strands (Schwartz and Hochstrasser, 2003). An other typical quality of the mature form of Ubls is the possession of diglycine at their flexible, carboxy-terminal end. Surprisingly, regardless of their high structural homology, no apparent sequence similarity is observed. The presence of the diglycine motif at their C-terminus is essential for their activation and subsequent formation of an isopeptide linkage between the Ubl's C-terminal carboxyl group and the amino group of the lysine side chain of the substrate (see Section 5.2). The process of utilising a covalently bound protein as a signalling event is unique for eukaryotes, although there are prokaryotic proteins exhibiting a ubiquitin-like fold (probably due to a shared ancestor) (Dye and Schulman, 2007). The Ubl family includes the following members: SUMO (three types in higher eukaryotes), which

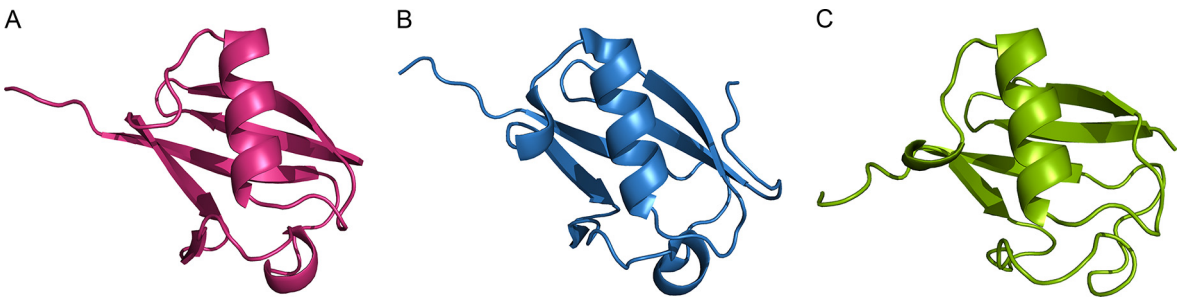

Figure 5.1: Typical fold of ubiquitin-like modifiers. The overall structure is presented for ubiquitin (A) (PDB ID: 1UBQ, (Vijay-Kumar et al., 1987)), SUMO-1 (B) (PDB ID: 1Y8R, (Lois and Lima, 2005)) and NEDD8 (C) (PDB ID: 1NDD, (Whitby et al., 1998)).

plays roles in DNA repair and transcription modification, nucleoplasmic transport and signal transduction (Johnson, 2004); NEDD8, involved in cell cycle progression, cytoskeletal regulation and signalling (Pan et al., 2004); ATG8 and ATG12, controlling autophagy by membrane modulation (Geng and Klionsky, 2008). Examples of ubiquitin-like proteins structures are presented in Figure 5.1.

Due to the presence of seven lysine residues (K6, K11, K27, K29, K33, K48 and K63) within the ubiquitin sequence, different types of chains can be created. This is achieved via the formation of an isopeptide linkage between the C-terminus of incoming ubiquitin and the lysine side chain of the growing ubiquitin chain. Different types of ubiquitin chain can lead to distinct cellular signals (Pickart and Eddins, 2004). The best-studied K48-linked chain targets protein for degradation by the proteasome (Finley et al., 1994), whereas the K63-linked chain is associated with DNA repair and protein trafficking (Zhao and Ulrich, 2010). In addition, substrates can also be monoubiquitinated or monoubiquitinated at multiple lysine sites. This type of modification has been implicated in histone modification, subcellular localisation and lysosome-dependent degradation (Pickart and Eddins, 2004). Creation of chains has been reported in the case of SUMO as well, although its role is not clear (Bylebyl et al., 2003).

5.2 Ubiquitin conjugation cascade

The process of ubiquitin attachment to the target protein can be summarised as conjugation of the C-terminal glycine to the amino-group, usually supplied by lysine (or the protein N-terminus) through formation of an isopeptide bond. This process is driven in a cascade-like manner and coordinated by a set of enzymes: E1 — activating enzyme, E2 — conjugating enzyme and E3 — ligase (Dye and Schulman, 2007). The ubiquitination pathway is summarised in Figure 5.2.

The first step in the ubiquitination pathway is driven by E1. The process of activation comprises two steps. The mature form of ubiquitin, with its C-terminal diglycine motif, is activated by ubiquitin-specific E1 in the presence of Mg^{2+}ATP, by forming an acyl-phosphate linkage with AMP (E1 is known to have a low affinity for ubiquitin in the absence of ATP). Subsequent attack by the E1 catalytic cysteine on the ubiquitin-AMP complex leads to the formation of a thioester linkage and AMP release. Each of the ubiquitin-like proteins possesses a dedicated E1 enzyme. E1 contains three distinct domains: an adenylation domain, a catalytic cysteine-containing domain and the ubiquitin-fold domain involved in E2 binding (Huang et al., 2004).

Ubiquitin is transferred from E1 onto E2, the conjugating enzyme, through a transthioesterification reaction to the E2 catalytic cysteine forming an E2∼ubiquitin conjugate (∼ indicates

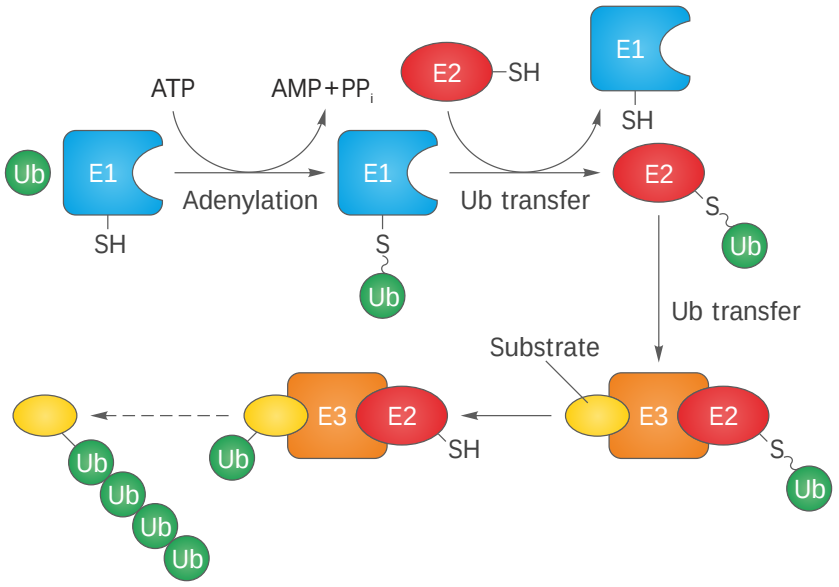

Figure 5.2: The ubiquitination pathway. E1 activates ubiquitin in an ATP dependent manner. Post-activation, ubiquitin is linked with the catalytic cysteine on E1, which in the next step is transferred onto the catalytic cysteine of E2. Further ubiquitin is passed onto the specific E3 ligase and finally onto the substrate. Figure adapted from Nakayama and Nakayama (2006).

a thioester bond). Single E2s exist for SUMO (Ubc9) and NEDD8 (Ubc12). Ubiquitin possesses a large family of E2 enzymes (about 40 in humans). E2s provide an additional step of ubiquitination control and their variety facilitates interactions with an even more abundant group of E3 ligases. All E2s contain a globular domain with a typical fold (∼17 kDa), possessing a catalytic cysteine positioned in the conserved sequence presented on the E2 surface (Pickart, 2001).

E3 ligases generally contain two domains: an E2 binding domain and a substrate recognition domain. E3 functions by recruiting E2∼ubiquitin and its specific substrate and promoting ubiquitin transfer from E2 to the lysine or N-terminus of the substrate (Dye and Schulman, 2007). Hundreds of E3s present in the human genome confer distinct substrate specificity and regulate diverse cellular processes (Peng et al., 2003). The ubiquitination system also employs deubiquitinating enzymes that deconjugate ubiquitin, thereby fulfilling regulatory functions (Reyes-Turcu et al., 2009).

The complexity of the system arises from the presence of two E1s, tens of E2 enzymes that can contact hundreds of E3s, which then pass the ubiquitin chain onto thousands of substrates (Hershko and Ciechanover, 1998). This setup is further complicated by the possibility of a single substrate binding to various E3s (Figure 5.3).

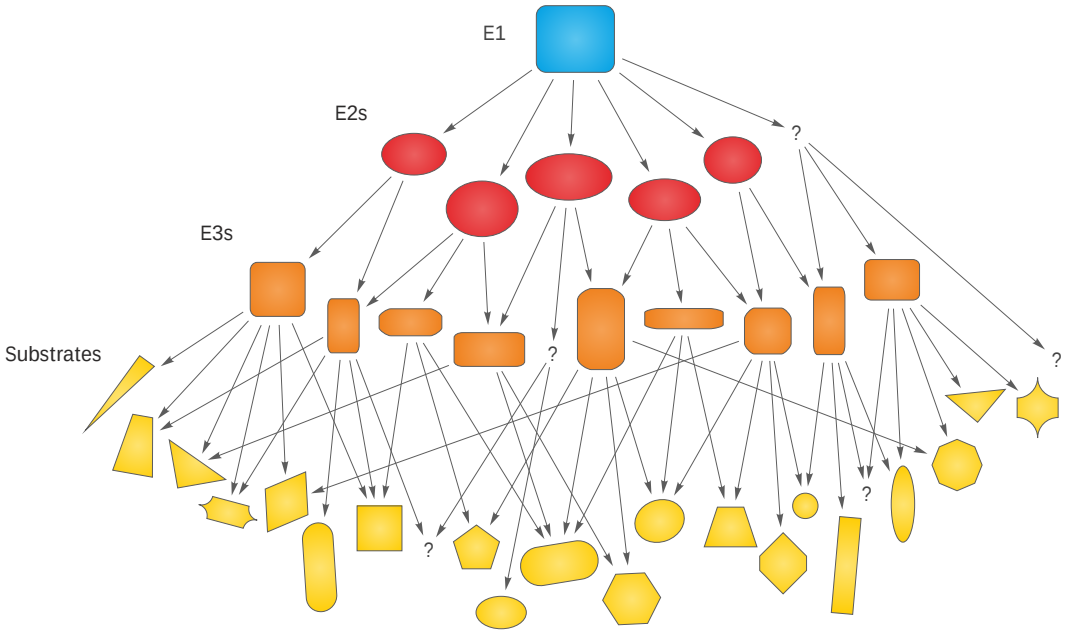

Figure 5.3: The E1-E2-E3 system and its complexity. A single E1 activating enzyme passes ubiquitin to tens of E2 enzymes and further via hundreds of E3s to thousands of substrates. Figure adapted from Nalepa et al. (2006).

5.3 Ubiquitin ligase family

The large family of ubiquitin ligases is divided into three groups (according to their E2∼Ubl binding domains): HECT (Homologous of E6AP Carboxy Terminus), RING (Really interesting new gene) and those that could not be classified into either group (Deshaies, 1999; Metzger et al., 2012). RING E3s are the largest family with approximately 600–700 members in the human genome (Dye and Schulman, 2007). RING E3s generally bind to the E2∼ubiquitin complex via their RING domain and are responsible for activation of the E2∼ubiquitin thioester linkage to facilitate discharge onto the substrate. By forming different E2-E3 pairs, both mono and polyubiquitination of different linkage types can be assembled. Unlike HECT E3s, RING ligases do not involve an intermediate state of thioester bound E3∼ubiquitin (Deshaies and Joazeiro, 2009). Differences between HECT and RING ligase modes of action are presented in Figure 5.4.

The RING domains are characterised by two zinc ligands with each coordinated by four cysteine / histidine residues. The unique zinc ligand configurations create a platform for E2∼ubiquitin binding (Deshaies and Joazeiro, 2009). Often the RING domains dimerise, thereby creating either homodimers (for examples RNF4 and BIRC7) or heterodimers (for example Mdm2-MdmX). Some RING E3s function in a higher oligomeric state (for example the Prp19 tetramer), while others form multi-subunit complexes such as the cullin RING ligases. Very few function as monomers (e.g. Mindbomb) (Metzger et al., 2013).

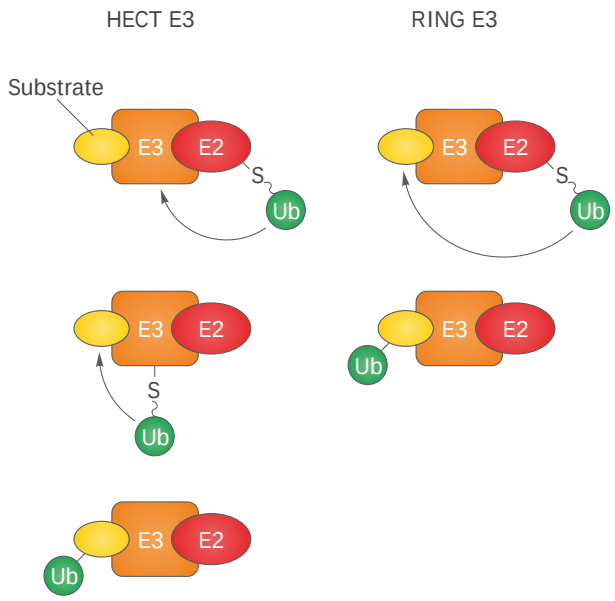

Figure 5.4: Differences in the course of action of two classes of E3 ligases, HECT and RING. RING E3s transfer ubiquitin directly onto the substrate, whereas HECT E3s form an E3∼ubiquitin thioester intermediate via their conserved cysteine residues. Figure adapted from Deshaies and Joazeiro (2009).

E3s are regulated, often-involving posttranslational modifications, for example phosphorylation (Metzger et al., 2013). The complexity of the system where most E2-E3 pairs are not known, where one E3 can modify several substrates and a single substrate may be the target of a number of E3s, is tremendous and not well ascertained (Metzger et al., 2013).

5.4 Significance of ubiquitination

It has been reported that mutations within RING E3s are associated with various diseases, by impairing their ability to control DNA repair, malignancy and tumour suppression (Lipkowitz and Weissman, 2011; Metzger et al., 2013; Nakayama and Nakayama, 2006). The importance of ubiquitination is not limited to the maintenance of genomic stability. It is also important for successful cell cycle progression, subcellular localisation and signal transduction (Lipkowitz and Weissman, 2011). Due to the significance of implicit ubiquitin ligases in cancer formation and malignancy, the ubiquitin system has become a drug target. Approaches to targeting varies. Some strategies are concentrated on specific E3s, others target the proteosome. Bortezomib also known as Velcade is the first inhibitor of the 26S proteasome used in cancer therapy (Adams and Kauffman, 2004; Bonvini et al., 2007). It is a dipeptide and comprises of pyrazinoic acid, phenylalanine and leucine with a boronic acid instead of a carboxylic acid. The boron atom of the peptide specifically binds to the proteasome with a high affinity. Bortezomib is successfully used in the clinic, predominantly in the treatment of

patients with multiple myeloma. Major treatment associated side effects are peripheral neuropathy, neutropenia and thrombocytopenia (Field-Smith et al., 2006). Therapies targeting specific E3 ligases are more challenging (Garber, 2005). Although one could speculate that targeting a particular E3 ligase would allow high specificity, it is important to keep in mind that many substrates of each E3 ligase are unknown and it is difficult to anticipate possible side effects. Nonetheless E3 ligases are extensively studied and several reports have been published focused on ubiquitin ligase targeting, either by precluding protein-protein interaction like nutlins (cis-imidazoline analogues) in case of MDM2-p53 interaction (Vassilev, 2004), or by allosteric inhibition as in a case of SCF ubiquitin ligase (Orlicky et al., 2010).

5.5 Trim28 — characteristic and architecture

Trim28 — tripartite motif-containing 28 (other names include KAP1 and TIF1β), a member of the Trim family of proteins, is involved in various cellular processes such as cell growth, differentiation and development. KAP1 (Krüppel-associated protein 1) was first described due to its interaction with KRAB domains (Krüppel-associated box) of the zinc finger proteins (ZFP), the largest family of transcriptional factors (Friedman et al., 1996). Trim28 is a corepressor of zinc fingers, and is targeted to DNA by interacting with them. In doing so, Trim28 creates a scaffold for chromatin modifiers. Trim28 possesses an N-terminal RING domain, followed by two B-box domains (zinc finger domains) and a coiled-coil region. This fragment is often termed RBCC, and is a hallmark of the Trim family of proteins. In RBCC motif all of the components work together in order to oligomerise or bind to the ligand. KRAB domains interact with the Trim28 RBCC with high affinity in a 1:3 ratio (KRAB to RBCC). Furthermore, the protein contains a C-terminal PHD domain (resembles the RING mechanism of metal binding) with an adjacent Bromo domain (BRD, which recognises acetylated lysine residues) (Friedman et al., 1996; Peng et al., 2007; Zeng et al., 2008). The Trim28 domain layout is depicted in Figure 5.5.

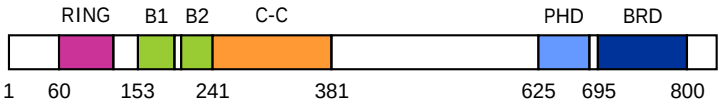

Figure 5.5: Schematic representation of Trim28 and its domains. N-terminal RING, two B-box domains and coiled-coil create RBCC motif. Protein terminates with PHD-BRD tandem. Figure adapted from Zeng et al. (2008).

5.5.1 Trim28 as a transcription corepressor

Trim28 is best characterised in the context of its function in gene silencing. The N-terminal RBCC motif interacts with zinc finger KRAB domains enabling Trim28 to be presented in

close proximity to DNA. The PHD and BRD domains are typical attributes found in chromatin associated proteins, both of them have been shown to be able to recognise histone tails, in addition they have the ability to cooperate and recruit binding partners. The Trim28 PHD-BRD tandem has been shown to influence chromatin state by engaging histone deacetylase and methylase. Deacetylation and methylation lead to transcription repression (Figure 5.6).

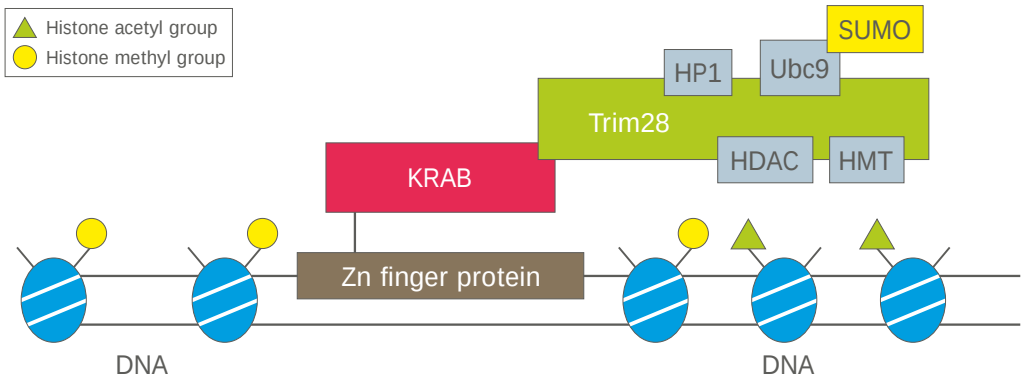

Figure 5.6: Scheme of Trim28 action mode in gene silencing. Trim28 binds to KRAB domains of the zinc finger proteins and recruits deacetylation and methylation machineries. It also recruits HP1 proteins. The process of gene silencing is controlled by sumoylation of the BRD domain mediated by the PHD motif. The PHD domain acts as a SUMO E3 ligase. Figure adapted from Friedman et al. (1996).

It has been reported that the ability of Trim28 to act as a scaffold for the binding of other proteins is controlled by sumoylation. The PHD domain serves as an intramolecular SUMO E3 ligase and recruits SUMO E2 — Ubc9 to modify the adjacent BRD domain (Peng and Wysocka, 2008). The addition of SUMO serves as a signal for the recruitment of deacetylation and methylation machineries. Although sumoylation has been detected on multiple sites within the Trim28 sequence, the majority of the modifications were present on the Lys779 and Lys804 of the BRD domain (Ivanov et al., 2007). The NMR spectroscopy structure of the Trim28 PHD-BRD domain provided an insight into their overall fold (Figure 5.7) (Zeng et al., 2008). Like the RING domain, the PHD domain binds to two zinc ligands coordinated by four cysteine / histidine residues. The zinc ligand binding supports a globular fold of the domain.

Intriguingly, other posttranslational modification such as phosphorylation on the unique Ser824 residue, by nuclear ATM protein kinase, in response to DNA damage, inhibits Trim28 sumoylation and prevents gene silencing (Li et al., 2007). Ser824 phosphorylation has also been shown to promote chromatin relaxation (Ziv et al., 2006). Trim28 deficient cells have been shown to by highly sensitivity to radiation (Ivanov et al., 2007).

Trim28 has also been shown to recruit HP1 protein family members (non-histone, heterochromatin-associated protein with a function in gene silencing) while being associated with KRAB domains. The region of the direct interaction has been assigned to involve residues

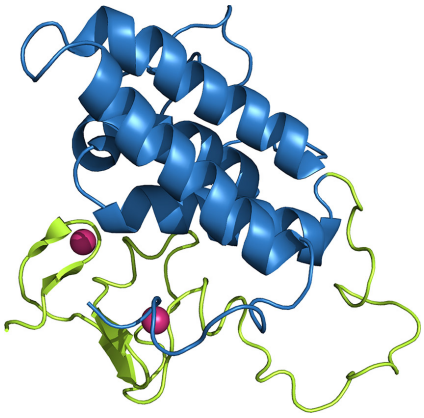

Figure 5.7: Overall fold of the Trim28 carboxy-terminal fragment. The PHD-BRD tandem, with the PHD domain (lime) and BRD domain (blue). Zinc ions are depicted as pink spheres (PDB ID: 2RO1) (Zeng et al., 2008).

located between coiled-coil and PHD domains. Existence of such an interaction pointed to the possibility of a more elaborate Trim28 function in chromatin organisation, beyond the histone tail modifications (Ryan et al., 1999). Furthermore, a study showed that Trim28 interacts with the acidic domain of Mdm2 via its coiled-coil region. This interaction promotes p53 ubiquitination and degradation (Wang et al., 2005).

5.5.2 Trim28 as a RING E3 ligase

Although Trim28 contains an N-terminal RING domain, its ubiquitin ligase activity remains elusive. A recent study investigated the ubiquitin ligase activity of Trim28. It was shown that Trim28 does not function efficiently as a ubiquitin ligase on its own. A Mage-C2 protein has been identified as a partner protein that enhances the Trim28 ligase activity (Doyle et al., 2010). Mage family members were initially considered as tumour-specific antigens. They possess a conserved MHG (Mage homology) domain and are involved in the interaction with RING E3s, though the interaction itself does not occur via the RING domain. How Mage-C2

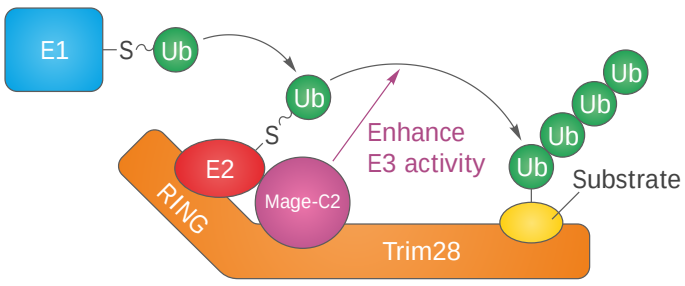

Figure 5.8: A model of Mage-C2 interactions with the Trim28 RING and an E2 enzyme. This protein-protein interactions were reported to promote the ligase activity of Trim28. Figure adapted from Espantman and O'Shea (2010).

stimulates Trim28 ubiquitin ligase activity is not clear (Figure 5.8) (Doyle et al., 2010; Feng et al., 2011).

5.5.3 Trim28 and diseases

Trim28 is overexpressed in many cancers and contributes to p53 inactivation. Its upregulation has been linked to poor prognosis for patients with gastric cancers (Hatakeyama, 2011; Iyengar et al., 2011). Trim28 has also been shown to highly express in the central nervous system and its loss is linked to anxiety-like behaviour in mice, consistent with a role in chromatin regulation during brain development (Alter and Hen, 2008).

5.6 Objectives

The objectives of this project were:
– to obtain structural information about Trim28;
– to elucidate how Trim28 functions as an E3 ligase;
– to investigate the interactions of Trim28 with partner proteins.

Chapter 6

Materials and methods

The majority of materials and methods used in the Trim28 study were equivalent to those described in the first part of the thesis. All additional techniques and reagents are described below.

6.1 Materials

cDNAs were purchased from Life Sciences. GSH-Sepharose resin and glutathione were purchased from GE Healthcare. Platinum Taq DNA polymerase was bought from Invitrogen. A 10 ml SourceQ and a 10 ml SourceS columns were prepared by Dr. Danny Huang using GE Healthcare resin. Dr. Gary Sibbet generated DH5α and BL21(DE3) competent cells. All produced proteins were expressed using BL21(DE3) *E. coli* strain. All expression vectors were obtained from previous lab members. Dr. Gary Sibbet performed all SPR experiments.

6.2 Methods

6.2.1 Trim28 cloning, expression and purification

Two constructs were obtained from Dr. Danny Huang — full-length Trim28 and Trim28_{33-412}, both in pGEX-4T1-TEV (N-terminal GST fusion protein, TEV cleavage site) (Figure 6.1). The constructs carry GST-fusion protein. GST — glutathione S-transferase is a 26 kDa protein which has a potential to improve the solubility of the expressed protein. Additionally once fused to a protein of interest, it can be used to pull-down from a lysate as GST has a strong binding affinity for GSH. Once bound to the resin the protein is washed and then eluted with free GSH excess.

Thereafter additional constructs were created using Platinum Taq DNA polymerase. Designed primers included STOP codon. The PCR reaction was conducted with following cycling parameters: initial denaturation — 94°C, 2 min; 35 extension cycles (94°C, 30 sec; 55°C, 30 sec; 68°C, 1 min); final extension — 68°C, 10 min. The PCR primers are shown in Table 6.1. PCR products were restricted with *Bam*HI or *Bgl*II and *Eco*RI and ligated with Quick Ligase into modified pGEX vector — pGEX-4T1-His-TEV (His-tag followed by a GST and TEV cleavage site, engineered by Dr. Lori Buetow) (Figure 6.1). Verified clones were transformed into BL21(DE3) cells.

Construct	Forward primer	Reverse primer
$Trim28_{61-241}$	5' CCG GGA TCC ATG CTG CTG GAG CAC TGC 3'	5' GGG GAA TTC TTA CTG GTG GTC CTT GTG GGC 3'
$Trim28_{33-149}$	5' CG AGA TCT TCC ACC GCC CCT TCG GC 3'	5' CG GAA TTC TTA CGC ATC CTG GGC GTC GG 3'
$Trim28_{625-685}$	5' CCG GGA TCC ATG GCC ACC ATT TGC CG 3'	5' GGG GAA TTC TTA ATC CAG GCT GAG GCT GCC ATC C 3'
$Trim28_{695-801}$	5' CCG GGA TCC AAG CTC TCA CCA GCC AAC CAG 3'	5' GGG GAA TTC TTA ACC GAA GGC CTC GTT CAT GCT 3'
$Trim28_{625-801}$	5' CCG GGA TCC ATG GCC ACC ATT TGC CG 3'	5' GGG GAA TTC TTA ACC GAA GGC CTC GTT CAT GCT 3'

Table 6.1: Trim28 constructs cloned from the full-length DNA. The construct boundaries, forward and reverse primers are presented.

12 l cultures in LB media were grown, harvested and lysed as described before (Section 2.2.4). The purification protocol consisted of a GST pull-down on a 10 ml GSH-Sepharose column at 4°C (wash buffer: 150 mM NaCl, 50 mM Tris-HCl pH 7.6, 1 mM DTT; elution buffer: 150 mM NaCl, 50 mM Tris-HCl pH 7.6, 5 mM DTT, 10 mM glutathione). After applying lysate through the column, resin was washed with 5 ml of wash buffer for each 1 ml of the lysate. Once eluted proteins were desalted (150 mM NaCl, 50 mM Tris-HCl pH 7.6) and cleaved with TEV overnight at 4°C (0.05 mg TEV / 1 mg protein). Post cleavage proteins were applied back through a 10 ml GSH-Sepharose or 5 ml HisTrap FF for proteins bearing His-tag to remove GST (or His-GST). Afterwards samples were diluted with 50 mM Tris-HCl pH 7.6 to reduce salt (NaCl) concentration in the sample to 20 mM and applied to ion exchange column — a 10 ml SourceQ column (anion exchange). Only $Trim28_{33-412}$ was applied to the 10 ml SourceS (cation exchange), due to its basic pI. Following buffers were used: wash buffer: 10 mM NaCl, 50 mM Tris-HCl pH 8.6 (Q column)/ MES pH 6.0 (S column), 1 mM DTT; elution buffer: 500 mM NaCl, 50 mM Tris-HCl pH 8.6 (Q column) / MES pH 6.0 (S column), 1 mM DTT. Ion exchange chromatography enables proteins separation according to their charge (affinity to the ion exchanger). Changing the pH of the buffer changes the net charge of the protein and its ability to bind to the ion-exchanger. For cation exchangers (S), a buffer must have a pH at least 1 pH unit below the pI of protein

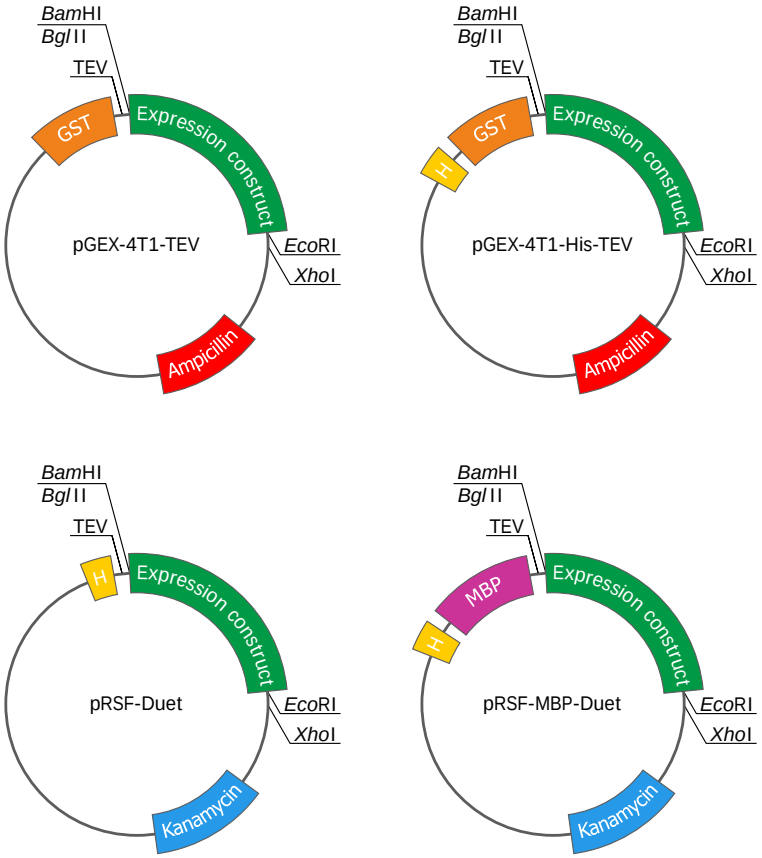

Figure 6.1: *E. coli* expression vectors used in the Trim28 study. A pGEX-4T1-TEV possesses N-terminal GST fusion protein and TEV cleavage site. A pGEX-4T1-His-TEV possesses N-terminal His-tag followed by a GST and TEV cleavage site. A pRSF-Duet possesses N-terminal His-tag followed by TEV cleavage site. A pRSF-MBP-Duet possesses N-terminal His-tag followed by an MBP fusion protein and TEV cleavage site. Post TEV cleavage all constructs carry additional glycine and alanine residues on the N-terminus. The plasmid-mediated resistance and used restriction sites are indicated.

to be bound and for anion exchangers (Q), at least 1 pH unit above the pI of protein to be bound. Proteins were eluted with a salt gradient (ionic strength). The final step involved size exclusion (150 mM NaCl, 50 mM Tris-HCl pH 7.6, 1 mM DTT) on a HiLoad Superdex S200 for full length Trim28 and Trim28_{33-412}, and a HiLoad Superdex S75 for the rest of the proteins. Pure proteins were concentrated using an Amicon system.

6.2.2 Trim28 crystallisation, crystal optimisation and testing

Purified proteins were used for crystallisation screening (Trim28, Trim28_{33-412}, Trim28_{33-149}, Trim28_{61-241} — 6 mg/ml; $\text{Trim28}_{625-685}$ — 8 mg/ml; $\text{Trim28}_{625-801}$ — 11 mg/ml), using screens specified in Section 2.3.2. Crystals were obtained in the first instance for the full-length protein (19°C; 1.2 M ammonium sulphate, 0.1 M Hepes pH 7.0). Optimisation attempts were undertaken to improve the initial crystal form. Besides those described in

Section 2.3.3, other approaches were applied, like growing crystals on top of Fluorinert solution (used for floating crystallisation, has viscosity similar to water and 75% greater density, not miscible with most crystallisation reagents, crystals grown using Fluorinert do not stick to the crystallisation plate), addition of 0.1% high purity agarose (crystallisation in agarose gel, reduce nucleation) and utilising dialysis buttons (crystallisation by dialysis). The second crystallised construct was $Trim28_{33-412}$ (19°C; 1.1 M ammonium tartrate dibasic pH 7.0; 5% Tacsimate pH 7.0, 0.1 M Hepes pH 7.0, 10% PEG MME). $Trim28_{33-412}$ crystals were improved by addition of detergents and additives (10% TRITON X-100, 10% CYMAL-1) in the crystallisation solution. Various cryoprotectants were tested: 10–20% glycerol, 10–20% ethylene glycol, 10–20% MPD, all of them protected crystals from freezing damage equally well. The $Trim28_{33-412}$ protein sequence was analysed using the UCLA MBI-SERp Server (Goldschmidt et al., 2007) (which predicts mutation clusters with a potential of enhancing crystallisation / changing crystal contacts). One of the mutants $Trim28_{33-412}$ K365A, K366A was created using a QuikChange kit (5' GCC CTT TTG CTT TCT *GCG GCG* TTG ATC TAC TTC CAG C 3'). The PCR reaction was conducted with following cycling parameters: initial denaturation — 95°C, 30 sec; 18 extension cycles (95°C, 30 sec; 55°C, 1 min; 68°C, 2 min); final extension — 68°C, 5 min. After PCR the reaction was treated with *Dpn*I at 37°C for 30 min. Post digestion of template DNA 10% of the reaction was used for a transformation into DH5α competent cells. Plasmid DNA was miniprep-purified and sequenced. A verified clone was transformed, expressed, purified and screened for crystallisation conditions as described previously.

6.2.3 E2 enzymes expression and purification

cDNA from three representatives of the UbcH2 family: *H. sapiens* UbcE2A, *M. musculus* UbcE2B, *S. cerevisiae* Rad6, and SUMO E2 enzyme — Ubc9, were obtained from Dr. Danny Huang, all in a pRSF-Duet vector (N-terminal His-tag) (Figure 6.1). Proteins were produced as described for Trim28 constructs (Section 6.2.1). A 10 ml SourceQ column (anion exchange) was used in the ion exchange step of the purification. Sixteen additional expression constructs generated by Dr. Huang were expressed and purified in a small-scale: UbcH5A, UbcH5B, UbcH5C, UbcH6, $UbcH6_{43-C}$, $UbcH4/5_{45-C}$, UbcH7, UbcH8, UbcH10, UbcE2Z, CDC34, UbcH2gI, UbcH2C, UbcH2-25k, UbcH2W, UbcH2T (pGEX-4T1-TEV, Figure 6.1). 1 l *E. coli* culture was grown, harvested and re-suspended in lysis buffer (affinity wash buffer supplemented with 1 mM PMSF, 0.1 mg/ml lysozyme). Cells were lysed by sonication (8 cycles of 8 sec on/off) and centrifuged (1 h, 4°C, 31,400g). The lysate was incubated (rocked at 4°C) with 0.5 ml of GSH-Sepharose beads for 2 h. Subsequently beads were washed 5 times with 10 ml of wash buffer. Proteins were cleaved on the beads (0.05 mg TEV / 1 mg protein) at 4°C. The cleaved proteins were eluted, while tag (GST) remained bound to the resin.

6.2.4 KRAB domain of zinc finger protein cloning, expression and purification

cDNAs for five zinc finger proteins were purchased and several constructs of KRAB domains were created using primers specified in Table 6.2 utilising Platinum Taq DNA polymerase. Designed primers included STOP codon. The PCR reaction was conducted with following cycling parameters: initial denaturation — 94°C, 2 min; 35 extension cycles (94°C, 30 sec; 55°C, 30 sec; 68°C, 30 sec); final extension — 68°C, 10 min.

Construct	Forward primer	Reverse primer
$ZnF320_{8-47}$	5' CG GGA TCC CTG ACA TTC AGG GAT GTG 3'	5' CG CTC GAG TTA CAG GGA GAC CAG GTT CCT ATA ATT CTC C 3'
$ZnF320_{8-80}$	5' CG GGA TCC CTG ACA TTC AGG GAT GTG 3'	5' CG CTC GAG TTA ATA ACT TGC TTG TCT CTG CAA TGT CC 3'
$ZnF10KOX_{14-53}$	5' CG GGA TCC GTG ACC TTC AAG GAT GTA TTT GTG G 3'	5' CG CTC GAG TTA CAA GGA AAC CAG GTT CTT ATA GTT CTC CAG CAT C 3'
$ZnF10KOX_{14-85}$	5' CG GGA TCC GTG ACC TTC AAG GAT GTA TTT GTG G 3'	5' CG CTC GAG TTA AGG ATG GGT CTC TTG GTG AAT TTC TCT C 3'
$MmZnF119_{4-43}$	5' CG AGA TCT GTG ACC TAT GAG GAT GTG CAT GTG AAC TTC 3'	5' CG CTC GAG TTA TAT ACA AGT AAG GTT CCA GTA GGT TTC CAG CAT CAC ATC 3'
$MmZnF119_{4-76}$	5' CG AGA TCT GTG ACC TAT GAG GAT GTG CAT GTG AAC TTC 3'	5' CG CTC GAG TTA CTG CTT CTT TCC ATA TGC AGA GGG ACA G 3'
$ZnF274_{14-53}$	5' CG GGA TCC GTG ACC TTT GAA GAT GTA ACA CTG GG 3'	5' CG CTC GAG TTA CAC TGA GAC CAG GTT CCT GTA GTT CTC C 3'
$ZnF274_{14-85}$	5' CG GGA TCC GTG ACC TTT GAA GAT GTA ACA CTG GG 3'	5' CG CTC GAG TTA TGG AAT GGT GTC TTG AGG AAT TCC TC 3'
$ZnF354C_{12-51}$	5' CG AGA TCT GTG ACA TTC AGG GAT GTG GCC G 3'	5' CG CTC GAG TTA CAG TGA GAC CAG GCT GCT GTA GTT CTC 3'
$ZnF354C_{12-83}$	5' CG AGA TCT GTG ACA TTC AGG GAT GTG GCC G 3'	5' CG CTC GAG TTA TAG ACG GGT ATC TGA AGG GAC TTC TCT TTC C 3'

Table 6.2: KRAB domain constructs of zinc finger proteins cloned from the full-length DNA. The construct length, forward and reverse primers are presented.

Double restricted DNA (*Bam*HI or *Bgl*II and *Xho*I) was ligated into three expression vectors: pGEX-4T1-His-TEV, pRSF-Duet and pRSF-MBP-Duet (N-terminal His-tag followed by an MBP fusion protein and TEV cleavage site) (Figure 6.1). MBP — maltose-binding

protein is a 43 kDa protein used to increase recombinant protein solubility. Expression conditions were established after small-scale tests (proteins pooled from 1 l cultures, using 200 μl nickel beads, the protocol for small-scale purification described in Section 6.2.3 was followed). Proteins were then produced in large-scale using pRSF-MBP-Duet constructs. 12 l of bacterial cultures were grown, harvested and re-suspended in lysis buffer (affinity wash buffer supplemented with 1 mM PMSF, 0.1 mg/ml lysozyme). Cells were lysed by sonication (8 cycles of 8 sec on/off, 20 ml lysate fractions) and centrifuged (1 h, 4°C, 31,400g). Supernatants were pooled and proteins were purified by affinity chromatography (5 ml HisTrap FF; wash buffer: 50 mM Tris-HCl pH 7.6, 150 mM NaCl, 20 mM imidazole; elution buffer: 50 mM Tris-HCl pH 7.6, 150 mM NaCl, 500 mM imidazole). After elution the buffer was exchanged to eliminate imidazole (HiPrep 26/10 desalting; Tris-HCl pH 7.6, 250 mM NaCl). Subsequently, proteins were cleaved overnight with His-tagged TEV protease (0.05 mg TEV / 1 mg protein). Afterwards, His-MBP and His-tagged TEV were removed by a second run of the HisTrap column. The final purification step for all KRAB domains consisted of gel filtration chromatography (HiLoad Superdex S30) in gel filtration buffer (50 mM Tris-HCl pH 7.6, 150 mM NaCl, 1 mM DTT). Proteins were concentrated using Amicon spin filters.

6.2.5 Native gel shift

4.5% native polyacrylamide gels were poured. Samples were prepared to a final volume of 5 μl and supplemented with 5% glycerol, loaded on a gel and run for 1.5 h at 130 V in a Tris-base boric acid pH 9.0 at 4°C. The assay enables detection of protein-protein interactions by comparing electrophoretic velocity of the individual proteins with the migration speed of the protein mixture. Small and negatively charged proteins migrate fast in the gel, while large and basic proteins move more slowly. Proteins separate in the native gel according to relation between their pI and the pH of the buffer used. In order to enter into the gel the protein pI needs to be lower than the pH of the buffer. No molecular weight markers were used for native gels.

6.2.6 Trim28 co-crystallisation attempts with partner proteins

Crystallisation trials were conducted for Trim28_{33-412} (7 mg/ml, 180 μM) with several partner proteins: HsE2A, MmE2B, Rad6, HsE2A_{C88A}∼ubiquitin, Rad6_{C88A}∼ubiquitin (ubiquitin conjugated E2 enzymes were generated by Dr. Danny Huang), ZnF320_{8-80}, ZnF274_{14-85}, ZnF10KOX_{14-85}, MmZnF119_{4-76}, ZnF354C_{12-83}. All complexes with E2s and E2∼ubiquitin conjugates were prepared by mixing proteins in the following ratio: for 1 μM of Trim28_{33-412}, 1.2 μM of E2s or E2∼ubiquitin was added. The complexes with KRAB domains were prepared by mixing proteins in the following ratio: for 1 μM of Trim28_{33-412}, 0.4 μM of KRAB

domain was added. All complexes were screened for crystallisation using screens specified in Section 2.3.2 at 4 and 19°C. Crystallisation drops were set immediately after proteins were mixed.

6.2.7 Ubiquitination assay

Ubiquitination assays were performed at 37°C in buffer containing 500 mM Tris-HCl pH 7.6, 5 mM $MgCl_2$ and 5 mM ATP. Each reaction contained 100 nM MmE1 (mice E1 ubiquitin-activating enzyme, purified by Dr. Danny Huang), 20 μM E2, 40 μM ubiquitin (non-labelled, or γ-^{32}P labelled) and 1 μM $Trim28_{33-412}$. Reactions were stopped by mixing with SDS loading dye. In the ubiquitination assay the ability of Trim28 to function as an E3 ligase was probed in the presence of various E2 conjugating enzymes. The course of the ubiquitination assay is depicted in Figure 6.2.

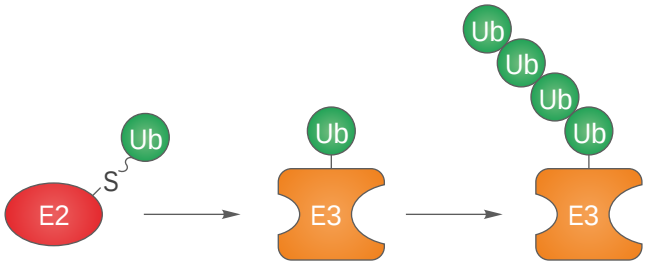

Figure 6.2: Ubiquitination assay. If an E3 is catalytically competent in the presence of a specific E2 enzyme (activated by an E1 ubiquitin-activating enzyme), it will autoubiquinate itself attaching first a single ubiquitin and subsequently additional ubiquitin moieties, creating a poly-ubiquitin chain.

6.2.8 Mage-C2 cloning, expression and purification

Three constructs were created from Mage-C2 cDNA utilising Platinum Taq DNA polymerase. The PCR reaction was conducted with following cycling parameters: initial denaturation —

Construct	Forward primer	Reverse primer
Mage-C2	5' CC GGA TCC ATG CCT CCC GTT CCA GG 3'	5' CG CTC GAG TCA CTC AGA AAA GGA GAC GTT GCT GG 3'
Mage-$C2_{131-C}$	5' CC GGA TCC ATG CCT CCC GTT CCA GG 3'	5' CG GGA TCC CCA GAC AGT GAG TCC TCT TTC ACA TAT ACA CTA GAT G 3'
Mage-$C2_{135-C}$	5' CC GGA TCC ATG CCT CCC GTT CCA GG 3'	5' CG GGA TCC TCC TCT TTC ACA TAT ACA CTA GAT GAA AAG GTG GCC G 3'

Table 6.3: Mage-C2 constructs cloned from full-length DNA. The construct boundaries, forward and reverse primers are presented.

94°C, 2 min; 35 extension cycles (94°C, 30 sec; 55°C, 30 sec; 68°C, 30 sec); final extension — 68°C, 10 min. The PCR primers are shown in Table 6.3 (included STOP codon). Expression constructs, created in pGEX-4T1-His-TEV and pRSF-Duet (Figure 6.1), were tested for expression conditions, expressed and purified as described in Sections 6.2.1 and 6.2.4.

6.2.9 Surface plasmon resonance

Binding between Trim28 and Ubc9 was assessed using Biacore. Biacore uses SPR (surface plasmon resonance), a method of probing biomolecular interactions (protein-protein, protein-ligand, DNA-protein, etc.) in real time, without labelling any of the assay components (Quinn et al., 2000). SPR is the electron oscillation that occurrs when light is reflected from a conducting film at the interface between two media of different refractive index. When using Biacore system, these two media are: the test sample and the surface of the used sensor chip. A thin layer of gold on the chip facilitates conductivity. SPR causes a reduction in the intensity of reflected light at a specific angle of reflection. The angle is determined by the mass of surface material, therefore it signals when biomolecules bind to the surface and change the mass of the surface layer (Figure 6.3). In the performed experiments GST-tagged Trim28 was immobilised on the chip surface, subsequently Ubc9 was injected across the chip surface. The experiments were performed by Dr. Gary Sibbet.

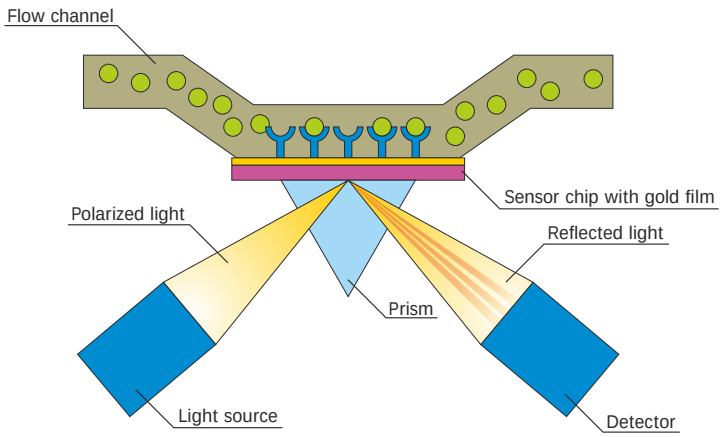

Figure 6.3: Experimental set-up of an SPR experiment. SPR detects variations of the refractive index in the near proximity of the sensor chip surface. It is observed as a sharp shadow in the light reflected from the surface. The angle change is determined by the mass of surface material, therefore it signals when biomolecules bind to the surface and change its mass. Figure adapted from Cooper (2002).

Chapter 7

Results

Trim28 is best characterised as a transcription corepressor, but how it functions as an ubiquitin ligase remains elusive. In this chapter, attempts to crystallise Trim28 to determine its three-dimensional structure are described. A description is given of a Trim28 autoubiquitination assay to identify its E2 partner. Additionally investigation of Trim28 interactions with Mage-C2 protein and KRAB domain-containing proteins is described.

7.1 Expression and purification of Trim28 constructs

Two constructs obtained from Dr. Danny Huang were tested for expression in BL21(DE3) cells (see Section 2.2.2). Both constructs yielded soluble, stable proteins in a small-scale expression test. Trim28 and Trim28_{33-412} were expressed and purified in a large-scale and concentrated to 7 mg/ml for the full-length protein, and to 10 mg/ml for the construct containing the RING domain, two B-box domains and a coiled-coil (RBCC, Trim28_{33-412}). The final purity of the proteins was higher for the shorter construct (Figure 7.1).

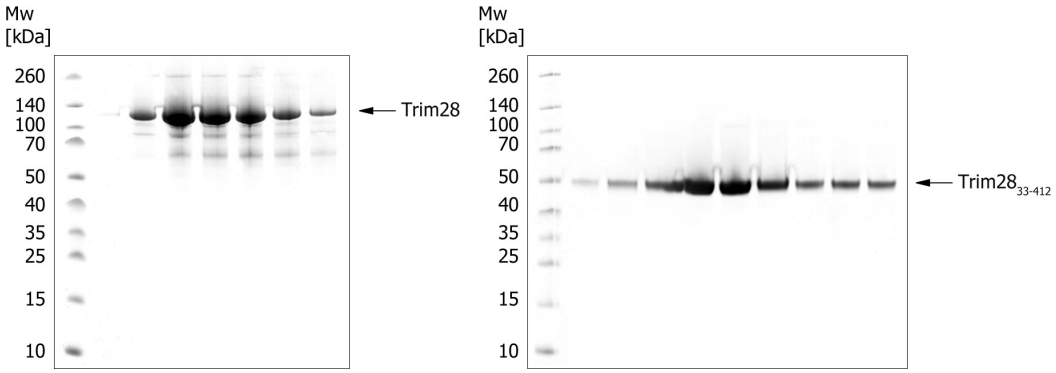

Figure 7.1: SDS-PAGE of purified full-length Trim28 (left) and Trim28_{33-412} (right). Lane 1 shows molecular weight markers (in kDa).

Then additional constructs were created: $Trim28_{33-149}$ — the RING domain, $Trim28_{61-241}$ — containing the RING domain and the two B-box domains, $Trim28_{625-685}$ — the PHD domain, $Trim28_{695-801}$ — BRD, $Trim28_{625-801}$ — covering both PHD and BRD tandem. All of the prepared constructs were expressed and purified from 12–24 l of *E. coli* culture. Obtained pure proteins were concentrated to 6–10 mg/ml using Amicon system. The cloning primers and purification details are described in Section 6.2.1. Trim28 constructs are depicted in Figure 7.2. Their theoretical molecular weights, extinction coefficients, pI of the constructs and an average yield from 12 l *E. coli* culture are presented in Table 7.1.

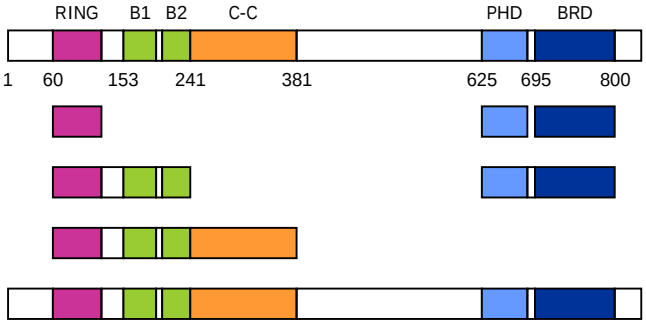

Figure 7.2: Cloned, expressed and purified Trim28 constructs: $Trim28_{33-149}$ (RING), $Trim28_{625-685}$ (PHD), $Trim28_{695-801}$ (BRD), $Trim28_{61-241}$ (RING-B-box), $Trim28_{625-801}$ (PHD-BRD), $Trim28_{33-412}$ (RBCC) and the full-lenght Trim28.

Construct	Theoretical molecular weight [kDa]	Extinction coeff. [$M^{-1}cm^{-1}$]	pI	Average yield from 12 l *E. coli* culture [mg]
Trim28	89	42400	6.2	5.4
$Trim28_{33-412}$	42	30940	8.4	6.5
$Trim28_{61-241}$	19.7	5960	5.6	6
$Trim28_{33-149}$	11.6	1490	4.8	5.8
$Trim28_{625-685}$	6.8	5500	4.3	16
$Trim28_{695-801}$	12.2	1490	7.9	20
$Trim28_{625-801}$	19.8	6990	5.1	22

Table 7.1: Expressed Trim28 constructs, their theoretical molecular weights, extinction coefficients, pI of the constructs and an average yield from 12 l *E. coli* culture.

7.2 Trim28 crystallisation attempts

Pure proteins were screened for crystallisation conditions as described in Section 6.2.2. The first one to crystallise was the full-length construct, the crystals appeared in drops set at 19°C in the presence of 1.2 M ammonium sulphate and 0.1 M Hepes pH 7.0 after 13 days. They were small and spindle-shape (Figure 7.3). The initial harvesting attempts revealed an unusual feature — they grew as a part of skin that covered the entire drop, making them extremely difficult to manipulate and isolate. Moreover, upon attempts to crush, they did not

shatter, as one would expect if they were protein crystals, instead, they presented "skin like" behaviour. The series of attempts to optimise these crystals (additives, detergents, growing with agarose, using dialysis buttons, Fluorinert reagent) did not improve their quality. Several crystals tested in the Diamond Light Source synchrotron diffracted only to ~20 Å.

The next one to crystallise was the $Trim28_{33-412}$ construct. Crystals appeared in the conditions similar to those that produced full-length Trim28 crystals (19°C; 1.1 M ammonium tartrate dibasic pH 7.0; 5% Tacsimate pH 7.0, 0.1 M Hepes pH 7.0, 10% PEG MME) after 3 days. They had a shape similar to the full-length crystals, but unlike the full-length crystals, they were easy to handle. However, they seemed unusually insensitive to poking or crushing. Once poked, they broke into a few large pieces and did not shatter into fine pieces, as would a typical protein crystal. Although early crystals were as small as full-length protein crystals, growing in the presence of various detergents (10% TRITON X-100, 10% CYMAL-1) made them grow bigger (Figure 7.3). Several crystals tested at the Diamond Light Source, diffracted only to 15 Å. Moreover, diffraction patterns were smeary (Figure 7.5), indicating poor crystal quality and therefore it was not possible to assign a space group or gain any additional information from these crystals.

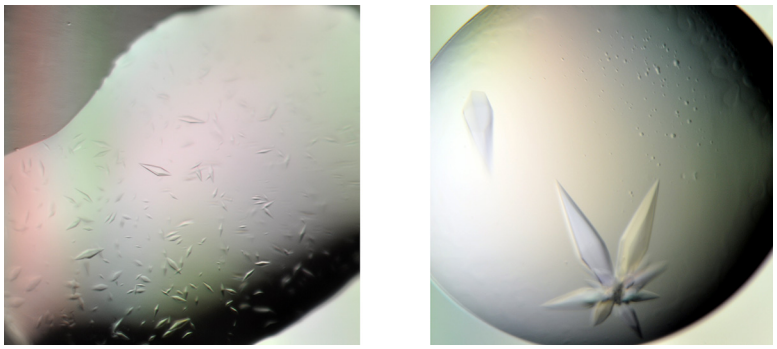

Figure 7.3: Crystals of full-length Trim28 (left) and optimised $Trim28_{33-412}$ crystals (right).

In an effort to further optimise $Trim28_{33-412}$ crystals the protein sequence was analysed using the UCLA MBI — Surface Entropy Reduction prediction Server (SERp). The SERp approach has been developed for the prediction of sites on a protein construct that are most suitable for mutation to enhance crystallisability (Goldschmidt et al., 2007). Three mutation clusters with the potential of enhancing crystallisation / changing crystal contacts were identified. The predicted mutant — $Trim28_{33-412}$ K365A, K366A, containing two mutations in the coiled-coil region was cloned, expressed and purified as the native protein. The protein expression level was lower compared with the wild type. In addition, the mutant was unstable in 150 mM NaCl, and successful purification required instead 300 mM NaCl in all buffers. Once purified and concentrated to 6 mg/ml, the protein was used for crystallisation screening. The screen yielded two new crystallisation conditions at 19°C: 20% ethanol, 0.1 M Tris-HCl pH 8.5 and 10% MPD, 0.1 M Tris-HCl pH 8.0. The mutant crystals had a rod-like shape that resembled

the native crystals (Figure 7.4). New hits were optimised by changing the pH and precipitant concentration and obtained bigger crystals with classic protein crystal-type behaviour.

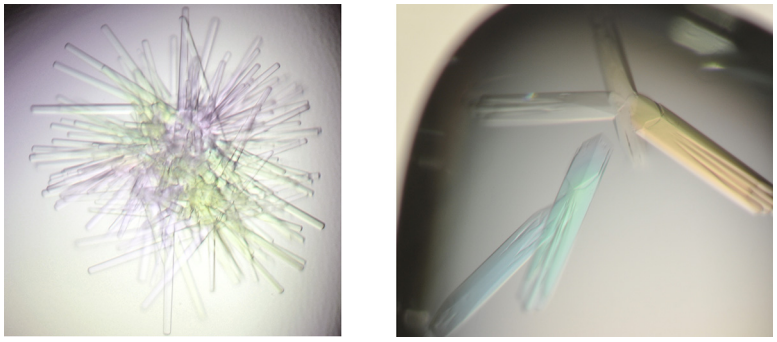

Figure 7.4: Crystals of $Trim28_{33-412}$ K365A, K366A. Crystals on the left grew in the presence of 10% MPD and 0.1 M Tris-HCl pH 8.5, on the right in the presence of 6% MPD and 0.1 M Tris-HCl pH 7.5.

Although these crystals yielded a protein-like diffraction pattern with properly separated diffraction spots (Figure 7.5), they did not diffract beyond 9 Å. Additional optimisation attempts, including crystal dehydration, did not improve diffraction quality. Nonetheless, those crystals provided better quality data, and several of them were indexed using XDS (Kabsch, 2010) giving invariably a P3 space group, with the following unit cell dimensions: $a = b = 310$ Å, $c = 240$ Å, $\alpha = \beta = 90°$, $\gamma = 120°$.

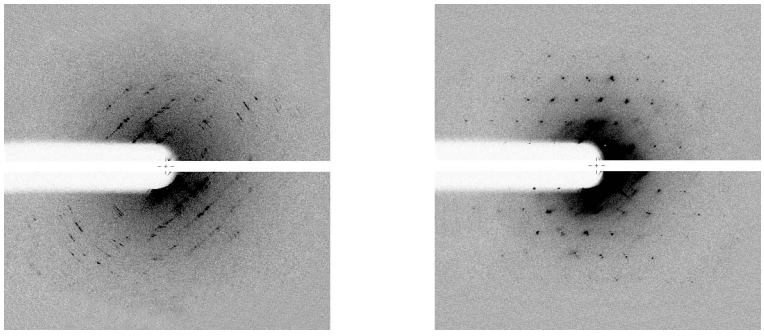

Figure 7.5: Trim28 crystal diffraction quality. On the left an X-ray diffraction image of a $Trim28_{33-412}$ crystal is shown, on the right a typical, higher quality $Trim28_{33-412}$ K365A, K366A crystal diffraction pattern is presented.

7.3 Identification of Trim28 E2 conjugating enzyme

Trim28 contains a RING domain at the N-terminus and a PHD domain at the C-terminus. The RING domain is known for its ability to interact with an E2 ubiquitin conjugating enzyme, though it is not clear whether the Trim28 RING domain has any ligase activity. Interestingly, the Trim28 PHD domain has been reported to interact with the E2 SUMO conjugating enzyme, Ubc9 (Peng and Wysocka, 2008). It is noteworthy that this is the only

report that described the PHD domain interaction with an E2. It is still debatable whether this interaction is real, since several other groups that studied SUMO E2 did not observe this interaction. To investigate whether Trim28 and Ubc9 form a stable complex, a native gel shift assay was performed at pH 9.0 by titrating full-length Trim28 (pI = 6.2), RING ($Trim28_{33-149}$, pI = 6.4) and PHD ($Trim28_{625-685}$, pI = 4.3) domains with Ubc9 (pI = 9.4). In the native gel, proteins are separated according to their molecular weight and charge. The separation depends on the pI of the protein and the charge of the protein in the running buffer. Negatively charged protein will enter the gel. In order to achieve this, the pI of the protein needs to be lower than the pH of the running buffer. Small and negatively charged proteins migrate fast in the gel, while large and basic proteins have lower electrophoretic velocity. Formation of a protein complex can be monitored by comparing migration velocity of the individual protein with that of the protein mixture. Unfortunately Ubc9 did not cause any band shift when mixed with Trim28 constructs (Figure 7.6). Ubc9 did not enter the gel because its pI is above the pH of the gel and running buffer. Due to the lack of a clear shift, SPR (surface plasmon resonance) was used to investigate the binding (Section 6.2.9). GST-tagged Trim28 was immobilised on the chip surface and Ubc9 (12 mg/ml) was injected across the chip surface. Likewise, SPR experiments did not detect any binding.

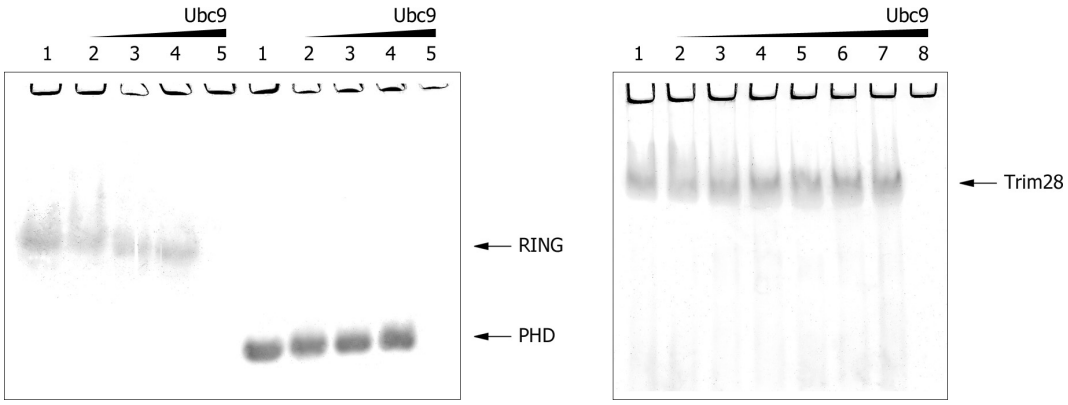

Figure 7.6: Native gel shift of Trim28 constructs titrated with Ubc9. The gel on the left shows the RING domain ($Trim28_{33-149}$) titrated with Ubc9 (micromolar ratio: 1:0, 1:1, 1:2, 1:3, 0:3) and PHD domain ($Trim28_{625-685}$) titrated with Ubc9 (micromolar ratio: 1:0, 1:1, 1:2, 1:3, 0:3). The gel on the right shows full-length Trim28 titrated with Ubc9 (micromolar ratio: 1:0, 1:0.5, 1:1, 1:1.5, 1:2, 1:3, 1:4, 0:4).

In an effort to identify an E2 enzyme that functions with Trim28, a panel of nineteen E2 proteins was expressed and purified. The following E2s were used: UbcH5A, UbcH5B, UbcH5C, UbcH6, $UbcH6_{43-C}$, $UbcH4/5_{45-C}$, UbcH7, UbcH8, UbcH10, MmUbcE2B, Rad6, UbcE2Z, UbcH2-25k, UbcH2gI, UbcH2C, CDC34, UbcE2A, UbcH2W, UbcH2T. All of the pure conjugating enzymes (3–6 mg protein obtained from 1 l culture) were used at 20 μM in the *in vitro* autoubiquitination assay (Dou et al., 2012) with $Trim28_{33-412}$. In the assay an ability of the $Trim28_{33-412}$ to function as an E3 ligase was probed (Figure 6.2). If an E3 is catalytically

competent in the presence of a specific E2 enzyme (activated by an E1 ubiquitin-activating enzyme), it will autoubiquinate itself attaching first a single ubiquitin and subsequently additional ubiquitin moieties, creating a poly-ubiquitin chain. Surprisingly only UbcH2 family members (Rad6, MmUbcE2B) displayed ubiquitination activity with Trim28. However, the activity was rather low, with a single band corresponding to the $Trim28_{33-412}$ modified with a single ubiquitin molecule (Figure 7.7). Additionally, the reaction was performed at 37°C for 1 h. Usually under these conditions, one would expect to see a smeary band at the top of the gel indicating poly-ubiquitinated products. A positive control was run using an E3 enzyme purified by Dr. Danny Huang — Ubr1. This enzyme is known to bind to Rad6 and was poly-ubiquitinated under test conditions. All these factors suggested that Trim28 is not an efficient ligase.

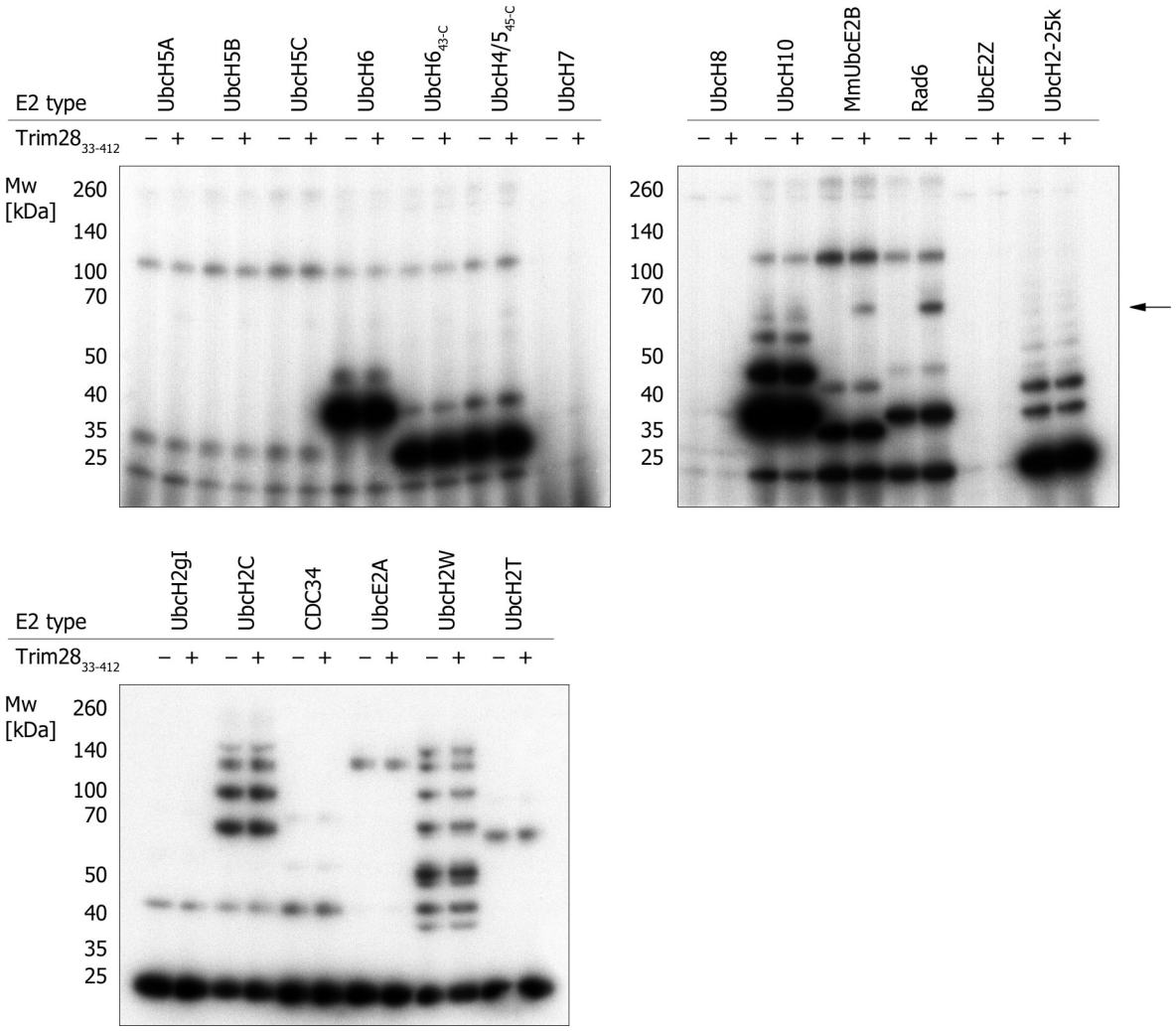

Figure 7.7: Ubiquitination assay of $Trim28_{33-412}$ by various E2 conjugating enzymes. Radiograms present results of the ubiquitination assay run for 1 h at 37°C with 40 μM γ-^{32}P radiolabelled ubiquitin, 100 nM MmE1, 5 mM $MgCl_2$, 5 mM ATP, testing 19 E2 (20 μM) conjugating enzymes. For each of the E2s, a control with no E3 enzyme was run. The arrow points to bands corresponding to $Trim28_{33-412}$ modified with a single ubiquitin molecule.

In order to validate the result, another assay using non-labelled ubiquitin was performed and analysed by SDS-PAGE (Figure 7.8). In this case a faint ladder could be observed, predominantly when the assay was run in the presence of Rad6 conjugating enzyme. Bands of the ladder were analysed by mass spectroscopy. It was confirmed that Trim28 is ubiquitinated at various lysine sites and, additionally, that ubiquitin also is conjugated to another ubiquitin, suggesting the formation of poly-ubiquitin chain.

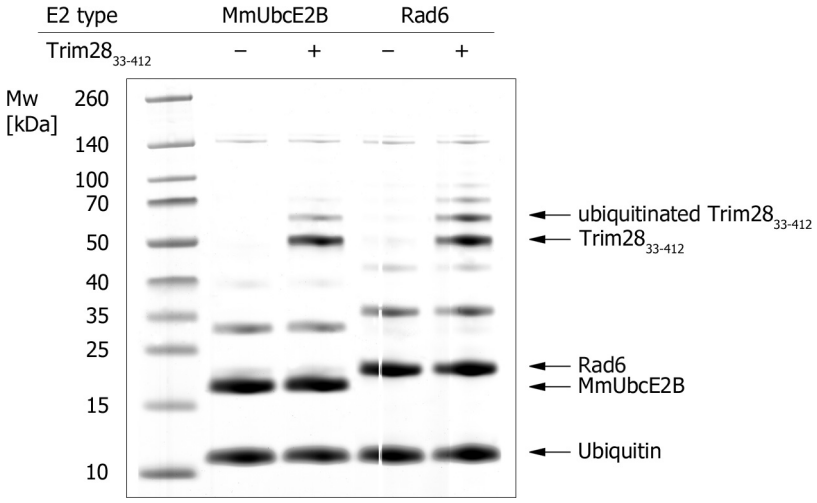

Figure 7.8: Ubiquitination assay of $Trim28_{33-412}$ by MmUbcE2B and by Rad6 conjugating enzymes. The ubiquitination assay was run for 1 h at 37°C with 40 μM ubiquitin, 100 nM MmE1, 5 mM $MgCl_2$, 5 mM ATP and 20 μM E2, and analysed by SDS-PAGE. Lane 1 shows molecular weight markers (in kDa).

To determine whether $Trim28_{33-412}$ interacts with Rad6, a native gel shift assay was performed. The experiment was run at pH 9.0. $Trim28_{33-412}$ was titrated with Rad6, and a stable conjugate of Rad6∼ubiquitin, prepared by Dr. Danny Huang. $Trim28_{33-412}$ has a pI

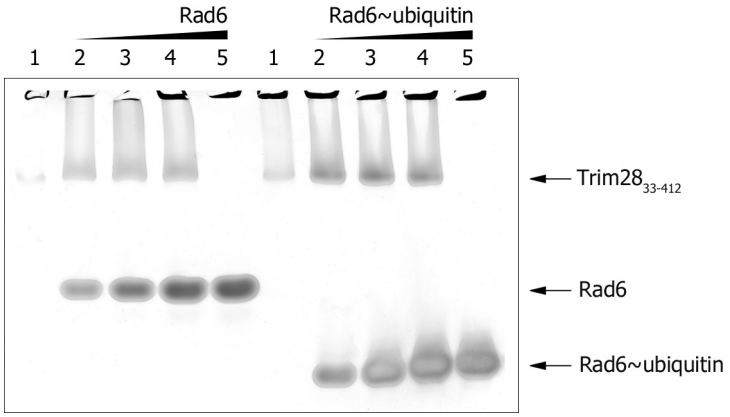

Figure 7.9: Native gel shift of $Trim28_{33-412}$ titrated with Rad6 and Rad6∼ubiquitin. The left part of the gel shows $Trim28_{33-412}$ titrated with Rad6 (micromolar ratio: 1:0, 1:1, 1:2, 1:3, 0:3), the right part shows $Trim28_{33-412}$ titrated with Rad6∼ubiquitin (micromolar ratio: 1:0, 1:1, 1:2, 1:3, 0:3).

of 8.4 and only slightly enters the gel. Both Rad6 (pI = 4.0) and Rad6∼ubiquitin conjugate (pI = 4.3) enter the gel due to their highly acidic pIs. As shown in Figure 7.9, the band corresponding to Trim28 (top) becomes more prominent with increasing amounts of Rad6 or Rad6∼ubiquitin, indicative of binding between Trim28 and Rad6.

7.4 Interaction of Trim28 and Mage-C2

Doyle et al. (2010) showed that in order for Trim28 to function efficiently as an E3 ligase, it requires a partner protein, Mage-C2. Mage-C2 massively stimulated Trim28 ubiquitin ligase activity with E2B by converting its ubiquitination pattern from mono-ubiquitinated product to explicit poly-ubiquitin chain formation. In order to reproduce this result, Mage-C2 was cloned, expressed and purified from the cDNA, according to procedures described before. Three constructs were created based on data presented in Doyle et al. (2010) paper: the full length Mage-C2 (pI = 4.1), Mage-C2$_{131-C}$ (pI = 4.4) and Mage-C2$_{135-C}$ (pI = 4.5). All three proteins could be expressed both in the GST-bearing construct and in the pRSF-Duet vector, resulting in His-tagged proteins. His-tagged constructs were selected for large-scale expression and purification and pure proteins were produced, concentrated up to 10 mg/ml for the truncated constructs, and 8 mg/ml for the full-length protein. An average yield from 12 l *E. coli* culture using pRSF-Duet construct was 3 mg for the full-length protein and 7–8 mg for truncated constructs. Then a native gel shift assay was performed to verify binding between purified Mage-C2 proteins and Trim28$_{33-412}$ (Figure 7.10). The experiments were performed similarly to the one described for the titration of Trim28$_{33-412}$ with Rad6 and Rad6∼ubiquitin (Section 7.3). All of the tested constructs caused Trim28$_{33-412}$ to migrate faster into the

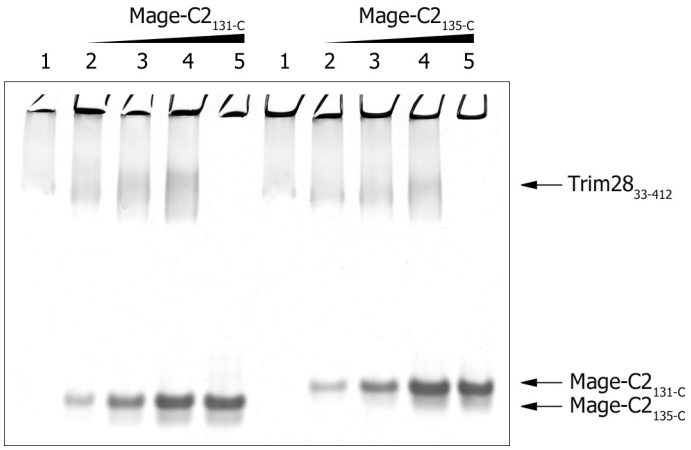

Figure 7.10: Native gel shift of Trim28$_{33-412}$ titrated with Mage-C2$_{131-C}$ and Mage-C2$_{135-C}$. The left part of the gel shows Trim28$_{33-412}$ titrated with Mage-C2$_{131-C}$ (micromolar ratio: 1:0, 1:0.5, 1:1, 1:2, 0:2), the right part Trim28$_{33-412}$ titrated with Mage-C2$_{135-C}$ (micromolar ratio: 1:0, 1:0.5, 1:1, 1:2, 0:2).

gel, indicating interactions between Mage-C2 and $Trim28_{33-412}$. After confirming binding between Trim28 and Mage-C2, all three constructs were used in the ubiquitination assay at concentration of 50 μM, as used in Doyle et al. (2010). The rest of the assay components were used as described in Section 7.3. Experiments performed using unlabelled ubiquitin or γ-^{32}P-labelled ubiquitin did not reveal stimulation of Trim28 ligase activity. Reanalysis of the Doyle et al. data led to the conclusion that the only difference between their reaction setup and the performed reaction was the protein expression strategy. In their study, Trim28 and Mage-C2 were co-expressed in *E. coli* rather than purified separately, as in this study. Thereupon, Trim28 and Mage-C2 were co-expressed using the GST-tagged $Trim28_{33-412}$ and each of the His-tagged Mage-C2 constructs, in the same manner as Doyle et al. (2010). All of the complexes could be expressed and purified, and were used in the ubiquitination assay (Figure 7.11). Unfortunately this approach did not cause any change in the Trim28 ubiquitination. Addition of Mage-C2 did not stimulate Trim28 ligase activity.

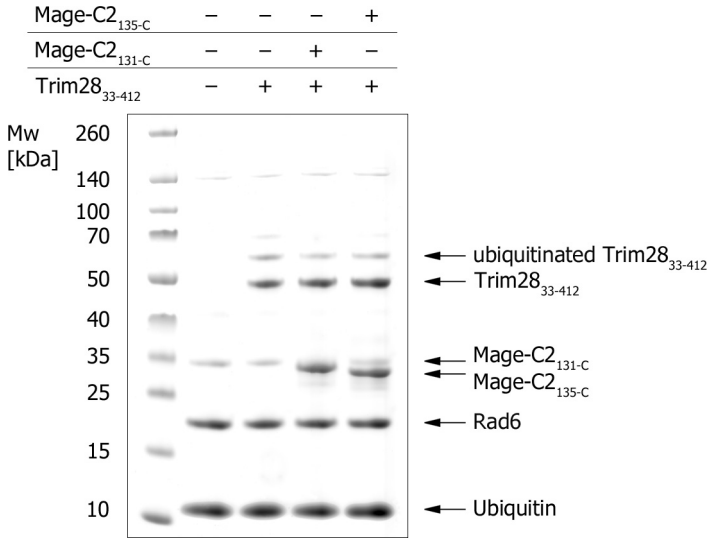

Figure 7.11: Ubiquitination assay of $Trim28_{33-412}$ by Rad6 conjugating enzyme in the presence of Mage-C2. The ubiquitination assay was run for 1 h at 37°C with 40 μM ubiquitin, 100 nM MmE1, 50 μM Mage-$C2_{131-C}$ or Mage-$C2_{135-C}$, 5 mM $MgCl_2$, 5 mM ATP and 20 μM E2, and analysed by SDS-PAGE. Lane 1 shows molecular weight markers (in kDa).

7.5 Interaction with zinc finger KRAB domains

Trim28 was first identified due to its interaction with the KRAB domains of zinc finger proteins. The KRAB domain is a transcriptional repression domain present in approximately 400 human zinc finger transcription factors (KRAB zinc finger proteins). They consist of about 75 amino acids and are made of two modules: A (highly conserved) and B (more diverse). The KRAB domain is followed by a zinc finger region, a small protein motif that binds DNA (Figure 7.12). In order to investigate the interactions between Trim28 and the

Figure 7.12: Schematic representation of KRAB zinc finger protein. The KRAB domain made of A and B modules is followed by a zinc finger motif.

KRAB domains, and to check whether addition of the KRAB domain may alter Trim28 crystal packing thereby yielding crystals with improved diffraction quality, five representatives of the ZnF family were selected and two KRAB domain constructs for each ZnF protein were generated. All of them were cloned into three expression vectors (pGEX-4T1-His-TEV, pRSF-Duet, pRSF-MBP-Duet) and tested for expression conditions (Section 6.4) The summary of the expression trial is presented in Table 7.2.

Construct	pGEX-4T1-His-TEV	pRSF-Duet	pRSF-MBP-Duet	Average yield from 12 l *E. coli* culture [mg]
$ZnF320_{8-47}$	−	−	+	2
$ZnF320_{8-80}$	−	−	+	1.5
$ZnF10KOX_{14-53}$	−	+	+	6
$ZnF10KOX_{14-85}$	+	+	+	4
$MmZnF119_{4-43}$	−	−	+	3
$MmZnF119_{4-76}$	−	−	+	1
$ZnF274_{14-53}$	−	−	+	5
$ZnF274_{14-85}$	+	+	+	4
$ZnF354C_{12-51}$	−	−	+	2
$ZnF354C_{12-83}$	−	−	+	2

Table 7.2: Results of the KRAB domains expression trial. An average yield from 12 l *E. coli* culture using pRSF-MBP-Duet constructs is presented.

These proteins have been previously shown to bind Trim28 (Peng et al., 2007). All constructs could be expressed as MBP fusion proteins. Additionally, $ZnF10KOX_{14-85}$ and $ZnF274_{14-85}$ also expressed in a GST-tagged version while $ZnF10KOX_{14-53}$, $ZnF10KOX_{14-85}$ and $ZnF274_{14-85}$ also expressed in the pRSF-Duet vector. All proteins were produced in a large-scale culture using pRSF-MBP-Duet constructs, purified and concentrated up to 3–4 mg/ml. Then a native gel shift assay was performed to investigate interactions between $Trim28_{33-412}$ and various KRAB domains (Figure 7.13). All KRAB domains caused $Trim28_{33-412}$ to migrate into the gel. According to the literature data (Friedman et al., 1996), three $Trim28_{33-412}$ molecules bind one zinc finger KRAB domain. To investigate the stoichiometry, a native gel shift assay with a finer titration of $Trim28_{33-412}$ with $ZnF274_{14-85}$ was performed (Figure 7.14). At a 1:0.4 ratio, all $Trim28_{33-412}$ migrated into the gel. This is indicated by the intensity of the $Trim28_{33-412}$ band, which remained unchanged with increasing $ZnF274_{14-85}$ concentration (Figure 7.14, lanes 2–8, upper band). This result is in agreement with published data, and suggests that a single KRAB domain binds to 3 $Trim28_{33-412}$ molecules.

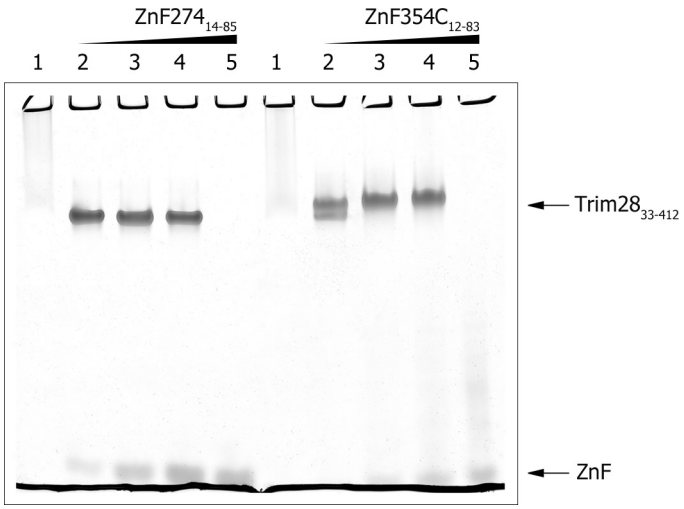

Figure 7.13: Native gel shift of $Trim28_{33-412}$ titrated with $ZnF274_{14-85}$ (pI = 4.2) and $ZnF354C_{12-83}$ (pI = 4.6). The left part of the gel shows $Trim28_{33-412}$ titrated with $ZnF274_{14-85}$ (micromolar ratio: 1:0, 1:1, 1:2, 1:3, 0:3), the right part $Trim28_{33-412}$ titrated with $ZnF354C_{12-83}$ (micromolar ratio: 1:0, 1:1, 1:2, 1:3, 0:3).

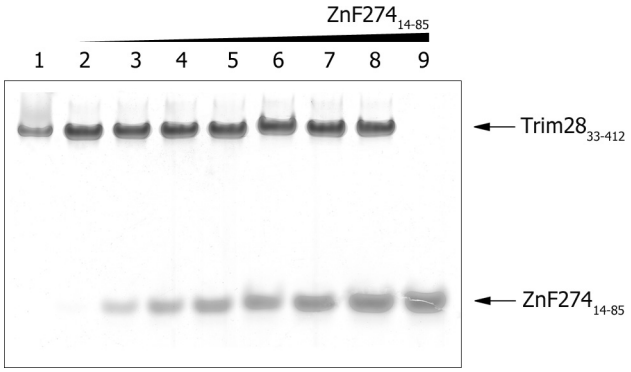

Figure 7.14: Native gel shift of $Trim28_{33-412}$ titrated with $ZnF274_{14-85}$ (left-to-right, micromolar ratio: 1:0.25, 1:0.4, 1:1, 1:1.5, 1:2, 1:2.5, 1:3, 1:4, 0:4).

7.6 Co-crystallisation of $Trim28_{33-412}$ with binding proteins

Various $Trim28_{33-412}$-KRAB domain complexes were assembled and crystallisation trials on a nanoscale were set up as described in Section 6.2.6. Of the screened complexes, only $Trim28_{33-412}$-$ZnF274_{14-85}$ crystallised (Figure 7.15). The complex crystallised in two conditions (1.6 M Na/K hydrogen phosphate; 1 M lithium sulphate, 0.1 M MES pH 6.5) at 19°C. These crystals were optimised and their diffraction was tested at the Diamond Light Source synchrotron. Unfortunately they did not diffract.

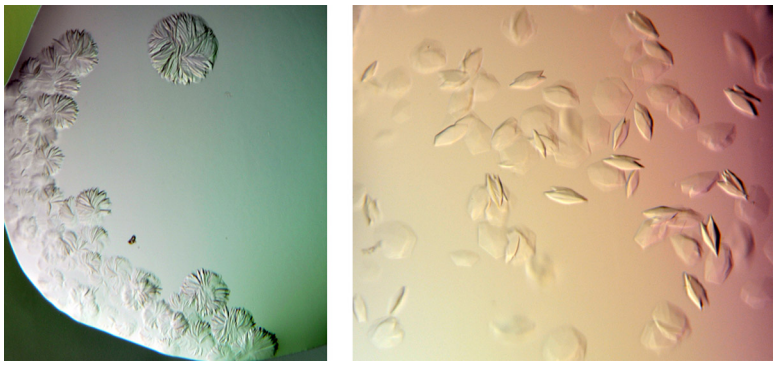

Figure 7.15: Crystals obtained for the Trim28$_{33-412}$-ZnF274$_{14-85}$ complex. On the left in 1.6 M Na/K hydrogen phosphate, on the right in 1 M lithium sulphate, 0.1 M MES pH 6.5.

Chapter 8

Discussion

8.1 Trim28 structure

Trim28 protein crystallised but the crystals diffracted poorly. Several approaches were used to optimise Trim28 crystals, but all failed to produce a useful dataset. The SERp approach yielded crystals with low diffracting resolution but with a nice diffracting pattern that allowed data indexing with the P3 space group.

The poor data quality may result from high oligomer formation, as Trim28 oligomerisation has been reported (Friedman et al., 1996). It could be observed when purifying full-length Trim28 and the N-terminal RBCC cluster. During size exclusion chromatography, both proteins eluted much faster than indicated by their theoretical molecular weights, suggesting protein oligomerisation. Additionally, high solvent content may impair diffraction quality.

It is possible that other Trim28 constructs or optimisation strategies may lead to further refining of the crystal packing and diffraction. A vital optimisation approach may involve more extreme dehydration methods (Hagelueken et al., 2012), or other mutation clusters that may promote other crystal forms (Goldschmidt et al., 2007). Trim28 is known to have multiple binding partners, for example the KRAB domains of various zinc finger proteins. Addition of different binding partners may disrupt Trim28 oligomerisation and promote formation of different crystal forms. Alternatively, inclusion of a fusion protein such as T4 lysozyme, may facilitate crystallisation. Fusion of T4 lysozyme at the N-terminus of a G-coupled protein receptor has been shown to facilitate crystallisation and to promote alternative crystal packing (Zou et al., 2012).

Ultimately other approach could be used to obtain an insight into the structure of the Trim28 N-terminus, for example NMR spectroscopy. This method was used to determine RING

domain structures of other members of the Trim protein family: Trim31 (PDB ID: 2YSJ), Trim32 (PDB ID: 2CT2) and Trim39 (PDB ID: 2ECJ) for which coordinates were submitted to PDB by the RIKEN Structural Genomics/Proteomics Initiative (Japan).

Information about the overall shape of the protein could be assessed by SAXS (Small-angle X-ray scattering). SAXS uses soluble protein samples and therefore does not require protein crystals. This method is useful in the characterisation of large and partially disordered proteins. Although SAXS resolution (1-3 nm) is much lower than that of X-ray crystallography it can provide information about the size and shape of a molecule (Lipfert and Doniach, 2007).

8.2 Trim28 ligase activity

Accessing Trim28 ligase activity and E2 interactions proved to be challenging. Despite literature reports pointing to interaction between the PHD domain and Ubc9 (Peng and Wysocka, 2008), the interaction was not detected in this study using a native gel shift assay or SPR analysis. Although autoubiquitination of $Trim28_{33-412}$ in the presence of Rad6 and MmUbcE2B was detected, the reaction was very inefficient, yielding only mono-ubiquitinated form of Trim28. Addition of Mage-C2 did not stimulate Trim28 ligase activity, as reported previously (Doyle et al., 2010). The remaining possibility is that the difference in the system used for protein co-expression may affect the assay outcome. In the published work proteins were produced using a single bicistronic expression vector, while in this study they were expressed using individual plasmids. It is possible that simultaneous expression of two proteins separately but from the same RNA transcript may influence their folding, hence affect the activity of Trim28. It is possible that other crucial detail in the experimental procedure was overlooked, though it was impossible to identify it from the published report. Moreover, it is possible that Trim28 does not prefer to autoubiquitinate itself like other E3s and it becomes catalytically competent only in the presence of a true substrate.

8.3 Trim28 and its binding partners

The ability of Trim28 to bind KRAB domains of various zinc finger proteins was confirmed. Also it binds of Mage-C2 and two E2 conjugating enzymes (Rad6 and MmUbcE2B) both without and with conjugated ubiquitin. From the native gel shift assays it appears that KRAB domains are the strongest binding partners, nonetheless ascertaining this requires using a more quantitative experimental method such as SPR.

Bibliography

Adams, J., and Kauffman, M. (2004). Development of the proteasome inhibitor Velcade (Bortezomib). Cancer Invest 22, 304-311.

Afonine, P.V., Grosse-Kunstleve, R.W., Echols, N., Headd, J.J., Moriarty, N.W., Mustyakimov, M., Terwilliger, T.C., Urzhumtsev, A., Zwart, P.H., and Adams, P.D. (2012). Towards automated crystallographic structure refinement with phenix.refine. Acta Crystallogr D Biol Crystallogr 68, 352-367.

Allen, R.D., Weiss, D.G., Hayden, J.H., Brown, D.T., Fujiwake, H., and Simpson, M. (1985). Gliding movement of and bidirectional transport along single native microtubules from squid axoplasm: evidence for an active role of microtubules in cytoplasmic transport. J Cell Biol 100, 1736-1752.

Alter, M.D., and Hen, R. (2008). Putting a KAP on transcription and stress. Neuron 60, 733-735.

Asbury, C.L., Fehr, A.N., and Block, S.M. (2003). Kinesin moves by an asymmetric hand-over-hand mechanism. Science 302, 2130-2134.

Bijlsma, M.F., Spek, C.A., and Peppelenbosch, M.P. (2004). Hedgehog: an unusual signal transducer. Bioessays 26, 387-394.

Blangy, A., Lane, H.A., d'Herin, P., Harper, M., Kress, M., and Nigg, E.A. (1995). Phosphorylation by p34cdc2 regulates spindle association of human Eg5, a kinesin-related motor essential for bipolar spindle formation in vivo. Cell 83, 1159-1169.

Boleti, H., Karsenti, E., and Vernos, I. (1996). Xklp2, a novel *Xenopus* centrosomal kinesin-like protein required for centrosome separation during mitosis. Cell 84, 49-59.

Bonvini, P., Zorzi, E., Basso, G., and Rosolen, A. (2007). Bortezomib-mediated 26S proteasome inhibition causes cell-cycle arrest and induces apoptosis in CD-30+ anaplastic large cell lymphoma. Leukemia 21, 838-842.

Brady, S.T. (1985). A novel brain ATPase with properties expected for the fast axonal transport motor. Nature 317, 73-75.

Buster, D.W., Baird, D.H., Yu, W., Solowska, J.M., Chauviere, M., Mazurek, A., Kress, M., and Baas, P.W. (2003). Expression of the mitotic kinesin Kif15 in postmitotic neurons: implications for neuronal migration and development. J Neurocytol 32, 79-96.

Bylebyl, G.R., Belichenko, I., and Johnson, E.S. (2003). The SUMO isopeptidase Ulp2 prevents accumulation of SUMO chains in yeast. J Biol Chem 278, 44113-44120.

Case, R.B., Rice, S., Hart, C.L., Ly, B., and Vale, R.D. (2000). Role of the kinesin neck linker and catalytic core in microtubule-based motility. Current Biology 10, 157-160.

Castoldi, M., and Popov, A.V. (2003). Purification of brain tubulin through two cycles of polymerization-depolymerization in a high-molarity buffer. Protein Expr Purif 32, 83-88.

Chandra, R., Endow, S.A., and Salmon, E.D. (1993). An N-terminal truncation of the ncd motor protein supports diffusional movement of microtubules in motility assays. J Cell Sci 104 (Pt 3), 899-906.

Cheung, H.O., Zhang, X., Ribeiro, A., Mo, R., Makino, S., Puviindran, V., Law, K.K., Briscoe, J., and Hui, C.C. (2009). The kinesin protein Kif7 is a critical regulator of Gli transcription factors in mammalian hedgehog signaling. Sci Signal 2, ra29.

Cochran, J.C., Gatial, J.E., 3rd, Kapoor, T.M., and Gilbert, S.P. (2005). Monastrol inhibition of the mitotic kinesin Eg5. J Biol Chem 280, 12658-12667.

Conde, C., and Caceres, A. (2009). Microtubule assembly, organization and dynamics in axons and dendrites. Nat Rev Neurosci 10, 319-332.

Cooper, M.A. (2002). Optical biosensors in drug discovery. Nat Rev Drug Discov 1, 515-528.

Cross, R.A. (2004). The kinetic mechanism of kinesin. Trends Biochem Sci 29, 301-309.

Cytoskeleton. http://www.cytoskeleton.com/

Dafinger, C., Liebau, M.C., Elsayed, S.M., Hellenbroich, Y., Boltshauser, E., Korenke, G.C., Fabretti, F., Janecke, A.R., Ebermann, I., Nurnberg, G., et al. (2011). Mutations in KIF7 link Joubert syndrome with Sonic Hedgehog signaling and microtubule dynamics. J Clin Invest 121, 2662-2667.

DeBonis, S., Skoufias, D.A., Lebeau, L., Lopez, R., Robin, G., Margolis, R.L., Wade, R.H., and Kozielski, F. (2004). In vitro screening for inhibitors of the human mitotic kinesin Eg5 with antimitotic and antitumor activities. Mol Cancer Ther 3, 1079-1090.

Dereeper, A., Guignon, V., Blanc, G., Audic, S., Buffet, S., Chevenet, F., Dufayard, J.F., Guindon, S., Lefort, V., Lescot, M., et al. (2008). Phylogeny.fr: robust phylogenetic analysis for the non-specialist. Nucleic Acids Res 36, W465-469.

Deshaies, R.J. (1999). SCF and Cullin/Ring H2-based ubiquitin ligases. Annu Rev Cell Dev Biol 15, 435-467.

Deshaies, R.J., and Joazeiro, C.A. (2009). RING domain E3 ubiquitin ligases. Annu Rev Biochem 78, 399-434.

Dou, H., Buetow, L., Hock, A., Sibbet, G.J., Vousden, K.H., and Huang, D.T. (2012). Structural basis for autoinhibition and phosphorylation-dependent activation of c-Cbl. Nat Struct Mol Biol 19, 184-192.

Doyle, J.M., Gao, J., Wang, J., Yang, M., and Potts, P.R. (2010). MAGE-RING protein complexes comprise a family of E3 ubiquitin ligases. Mol Cell 39, 963-974.

Durocher, D., and Jackson, S.P. (2002). The FHA domain. FEBS Lett 513, 58-66.

Dye, B.T., and Schulman, B.A. (2007). Structural mechanisms underlying posttranslational modification by ubiquitin-like proteins. Annu Rev Biophys Biomol Struct 36, 131-150.

Echard, A., Jollivet, F., Martinez, O., Lacapere, J.J., Rousselet, A., Janoueix-Lerosey, I., and Goud, B. (1998). Interaction of a Golgi-associated kinesin-like protein with Rab6. Science 279, 580-585.

Emsley, P., and Cowtan, K. (2004). Coot: model-building tools for molecular graphics. Acta Crystallogr D Biol Crystallogr 60, 2126-2132.

Endoh-Yamagami, S., Evangelista, M., Wilson, D., Wen, X., Theunissen, J.W., Phamluong, K., Davis, M., Scales, S.J., Solloway, M.J., de Sauvage, F.J., and Peterson, A.S. (2009). The mammalian Cos2 homolog Kif7 plays an essential role in modulating Hh signal transduction during development. Curr Biol 19, 1320-1326.

Espantman, K.C., and O'Shea, C.C. (2010). aMAGEing new players enter the RING to promote ubiquitylation. Mol Cell 39, 835-837.

Feng, Y., Gao, J., and Yang, M. (2011). When MAGE meets RING: insights into biological functions of MAGE proteins. Protein Cell 2, 7-12.

Ferhat, L., Cook, C., Chauviere, M., Harper, M., Kress, M., Lyons, G.E., and Baas, P.W. (1998a). Expression of the mitotic motor protein Eg5 in postmitotic neurons: implications for neuronal development. J Neurosci 18, 7822-7835.

Ferhat, L., Kuriyama, R., Lyons, G.E., Micales, B., and Baas, P.W. (1998b). Expression of the mitotic motor protein CHO1/MKLP1 in postmitotic neurons. Eur J Neurosci 10, 1383-1393.

Field-Smith, A., Morgan, G.J., and Davies, F.E. (2006). Bortezomib (Velcade) in the Treatment of Multiple Myeloma. Ther Clin Risk Manag 2, 271-279.

Finley, D., Sadis, S., Monia, B.P., Boucher, P., Ecker, D.J., Crooke, S.T., and Chau, V. (1994). Inhibition of proteolysis and cell cycle progression in a multiubiquitination-deficient yeast mutant. Mol Cell Biol 14, 5501-5509.

Florian, S., and Mayer, T.U. (2011). Modulated microtubule dynamics enable Hklp2/Kif15 to assemble bipolar spindles. Cell Cycle 10, 3533-3544.

Fourniol, F., and Moores, C.A. (2010). Kinesin motor activation: microtubules pull the switches. Proc Natl Acad Sci USA 107, 3949-3950.

Friedman, J.R., Fredericks, W.J., Jensen, D.E., Speicher, D.W., Huang, X.P., Neilson, E.G., and Rauscher, F.J., 3rd (1996). KAP-1, a novel corepressor for the highly conserved KRAB repression domain. Genes Dev 10, 2067-2078.

Friel, C.T., and Howard, J. (2011). The kinesin-13 MCAK has an unconventional ATPase cycle adapted for microtubule depolymerization. EMBO J 30, 3928-3939.

Garber, K. (2005). Missing the target: ubiquitin ligase drugs stall. J Natl Cancer Inst 97, 166-167.

Garcia-Saez, I., Yen, T., Wade, R.H., and Kozielski, F. (2004). Crystal structure of the motor domain of the human kinetochore protein CENP-E. J Mol Biol 340, 1107-1116.

Geng, J., and Klionsky, D.J. (2008). The Atg8 and Atg12 ubiquitin-like conjugation systems in macroautophagy. 'Protein modifications: beyond the usual suspects' review series. EMBO Rep 9, 859-864.

Gennerich, A., and Vale, R.D. (2009). Walking the walk: how kinesin and dynein coordinate their steps. Curr Opin Cell Biol 21, 59-67.

Germani, A., Bruzzoni-Giovanelli, H., Fellous, A., Gisselbrecht, S., Varin-Blank, N., and Calvo, F. (2000). SIAH-1 interacts with alpha-tubulin and degrades the kinesin Kid by the proteasome pathway during mitosis. Oncogene 19, 5997-6006.

Gigant, B., Wang, W., Dreier, B., Jiang, Q., Pecqueur, L., Pluckthun, A., Wang, C., and Knossow, M. (2013). Structure of a kinesin-tubulin complex and implications for kinesin motility. Nat Struct Mol Biol 20, 1001-1007.

Goetz, S.C., and Anderson, K.V. (2012). The primary cilium: a signalling centre during vertebrate development. Nat Rev Genet 11, 331-344.

Goldschmidt, L., Cooper, D.R., Derewenda, Z.S., and Eisenberg, D. (2007). Toward rational protein crystallization: A Web server for the design of crystallizable protein variants. Protein Sci 16, 1569-1576.

Gouet, P., Robert, X., and Courcelle, E. (2003). ESPript/ENDscript: extracting and rendering sequence and 3D information from atomic structures of proteins. Nucleic Acids Research 31, 3320-3323.

Grummt, M., Woehlke, G., Henningsen, U., Fuchs, S., Schleicher, M., and Schliwa, M. (1998). Importance of a flexible hinge near the motor domain in kinesin-driven motility. EMBO J 17, 5536-5542.

Hackney, D.D. (1994). Evidence for alternating head catalysis by kinesin during microtubule-stimulated ATP hydrolysis. Proc Natl Acad Sci USA 91, 6865-6869.

Hackney, D.D., and Jiang, W. (2001). Assays for kinesin microtubule-stimulated ATPase activity. Methods Mol Biol 164, 65-71.

Hagelueken, G., Huang, H., Harlos, K., Clarke, B.R., Whitfield, C., and Naismith, J.H. (2012). Crystallization, dehydration and experimental phasing of WbdD, a bifunctional kinase and methyltransferase from *Escherichia coli* O9a. Acta Crystallogr D Biol Crystallogr 68, 1371-1379.

Hatakeyama, S. (2011). TRIM proteins and cancer. Nat Rev Cancer 11, 792-804.

Heidebrecht, H.J., Adam-Klages, S., Szczepanowski, M., Pollmann, M., Buck, F., Endl, E., Kruse, M.L., Rudolph, P., and Parwaresch, R. (2003). repp86: A human protein associated in the progression of mitosis. Mol Cancer Res 1, 271-279.

Hershko, A., and Ciechanover, A. (1998). The ubiquitin system. Annu Rev Biochem 67, 425-479.

Hirokawa, N., Pfister, K.K., Yorifuji, H., Wagner, M.C., Brady, S.T., and Bloom, G.S. (1989). Submolecular domains of bovine brain kinesin identified by electron microscopy and monoclonal antibody decoration. Cell 56, 867-878.

Hirokawa, N., Noda, Y., Tanaka, Y., and Niwa, S. (2009). Kinesin superfamily motor proteins and intracellular transport. Nat Rev Mol Cell Biol 10, 682-696.

Huang, D.T., Walden, H., Duda, D., and Schulman, B.A. (2004). Ubiquitin-like protein activation. Oncogene 23, 1958-1971.

Huszar, D., Theoclitou, M.E., Skolnik, J., and Herbst, R. (2009). Kinesin motor proteins as targets for cancer therapy. Cancer Metastasis Rev 28, 197-208.

Hwang, W., Lang, M.J., and Karplus, M. (2008). Force generation in kinesin hinges on cover-neck bundle formation. Structure 16, 62-71.

Ishikawa, K., Kamohara, Y., Tanaka, F., Haraguchi, N., Mimori, K., Inoue, H., and Mori, M. (2008). Mitotic centromere-associated kinesin is a novel marker for prognosis and lymph node metastasis in colorectal cancer. Br J Cancer 98, 1824-1829.

Ivanov, A.V., Peng, H., Yurchenko, V., Yap, K.L., Negorev, D.G., Schultz, D.C., Psulkowski, E., Fredericks, W.J., White, D.E., Maul, G.G., et al. (2007). PHD domain-mediated E3 ligase activity directs intramolecular sumoylation of an adjacent bromodomain required for gene silencing. Mol Cell 28, 823-837.

Iyengar, S., Ivanov, A.V., Jin, V.X., Rauscher, F.J., 3rd, and Farnham, P.J. (2011). Functional analysis of KAP1 genomic recruitment. Mol Cell Biol 31, 1833-1847.

Johnson, E.S. (2004). Protein modification by SUMO. Annu Rev Biochem 73, 355-382.

Kaan, H.Y., Hackney, D.D., and Kozielski, F. (2011). The structure of the kinesin-1 motor-tail complex reveals the mechanism of autoinhibition. Science 333, 883-885.

Kabsch, W. (2010). Xds. Acta Crystallogr D Biol Crystallogr 66, 125-132.

Karabay, A., and Walker, R.A. (1999). Identification of microtubule binding sites in the Ncd tail domain. Biochemistry 38, 1838-1849.

Katoh, Y., and Katoh, M. (2004a). Characterization of KIF7 gene in silico. Int J Oncol 25, 1881-1886.

Katoh, Y., and Katoh, M. (2004b). KIF27 is one of orthologs for *Drosophila* Costal-2. Int J Oncol 25, 1875-1880.

Khalil, A.S., Appleyard, D.C., Labno, A.K., Georges, A., Karplus, M., Belcher, A.M., Hwang, W., and Lang, M.J. (2008). Kinesin's cover-neck bundle folds forward to generate force. Proceedings of the National Academy of Sciences of the United States of America 105, 19247-19252.

Kikkawa, M., Sablin, E.P., Okada, Y., Yajima, H., Fletterick, R.J., and Hirokawa, N. (2001). Switch-based mechanism of kinesin motors. Nature 411, 439-445.

Kobayashi, T., Tsang, W.Y., Li, J., Lane, W., and Dynlacht, B.D. (2011). Centriolar kinesin Kif24 interacts with CP110 to remodel microtubules and regulate ciliogenesis. Cell 145, 914-925.

Kollmar, M., and Glockner, G. (2003). Identification and phylogenetic analysis of *Dictyostelium discoideum* kinesin proteins. BMC Genomics 4, 47.

Kozielski, F., Sack, S., Marx, A., Thormahlen, M., Schonbrunn, E., Biou, V., Thompson, A., Mandelkow, E.M., and Mandelkow, E. (1997). The crystal structure of dimeric kinesin and implications for microtubule-dependent motility. Cell 91, 985-994.

Kull, F.J., Sablin, E.P., Lau, R., Fletterick, R.J., and Vale, R.D. (1996). Crystal structure of the kinesin motor domain reveals a structural similarity to myosin. Nature 380, 550-555.

Kuriyama, R., Dragas-Granoic, S., Maekawa, T., Vassilev, A., Khodjakov, A., and Kobayashi, H. (1994). Heterogeneity and microtubule interaction of the CHO1 antigen, a mitosis-specific kinesin-like protein. Analysis of subdomains expressed in insect sf9 cells. J Cell Sci 107 (Pt 12), 3485-3499.

Larkin, M.A., Blackshields, G., Brown, N.P., Chenna, R., McGettigan, P.A., McWilliam, H., Valentin, F., Wallace, I.M., Wilm, A., Lopez, R., et al. (2007). Clustal W and Clustal X version 2.0. Bioinformatics 23, 2947-2948.

Lawrence, C.J., Dawe, R.K., Christie, K.R., Cleveland, D.W., Dawson, S.C., Endow, S.A., Goldstein, L.S., Goodson, H.V., Hirokawa, N., Howard, J., et al. (2004). A standardized kinesin nomenclature. J Cell Biol 167, 19-22.

Li, X., Lee, Y.K., Jeng, J.C., Yen, Y., Schultz, D.C., Shih, H.M., and Ann, D.K. (2007). Role for KAP1 serine 824 phosphorylation and sumoylation/desumoylation switch in regulating KAP1-mediated transcriptional repression. J Biol Chem 282, 36177-36189.

Liao, H., Li, G., and Yen, T.J. (1994). Mitotic regulation of microtubule cross-linking activity of CENP-E kinetochore protein. Science 265, 394-398.

Liem, K.F., Jr., He, M., Ocbina, P.J., and Anderson, K.V. (2009). Mouse Kif7/Costal2 is a cilia-associated protein that regulates Sonic hedgehog signaling. Proc Natl Acad Sci USA 106, 13377-13382.

Lipfert, J., and Doniach, S. (2007). Small-angle X-ray scattering from RNA, proteins, and protein complexes. Annu Rev Biophys Biomol Struct 36, 307-327.

Lipkowitz, S., and Weissman, A.M. (2011). RINGs of good and evil: RING finger ubiquitin ligases at the crossroads of tumour suppression and oncogenesis. Nat Rev Cancer 11, 629-643.

Liu, M., Nadar, V.C., Kozielski, F., Kozlowska, M., Yu, W., and Baas, P.W. (2011). Kinesin-12, a mitotic microtubule-associated motor protein, impacts axonal growth, navigation, and branching. J Neurosci 30, 14896-14906.

Lois, L.M., and Lima, C.D. (2005). Structures of the SUMO E1 provide mechanistic insights into SUMO activation and E2 recruitment to E1. EMBO J 24, 439-451.

Lupas, A., Van Dyke, M., and Stock, J. (1991). Predicting coiled coils from protein sequences. Science 252, 1162-1164.

Mallik, R., and Gross, S.P. (2004). Molecular motors: strategies to get along. Curr Biol 14, R971-982.

Mandelkow, E., and Mandelkow, E.M. (2002). Kinesin motors and disease. Trends Cell Biol 12, 585-591.

Martinez, N.W., Xue, X., Berro, R.G., Kreitzer, G., and Resh, M.D. (2008). Kinesin KIF4 regulates intracellular trafficking and stability of the human immunodeficiency virus type 1 Gag polyprotein. J Virol 82, 9937-9950.

Marx, A., Hoenger, A., and Mandelkow, E. (2009). Structures of kinesin motor proteins. Cell Motil Cytoskeleton 66, 958-966.

Mayer, T.U., Kapoor, T.M., Haggarty, S.J., King, R.W., Schreiber, S.L., and Mitchison, T.J. (1999). Small molecule inhibitor of mitotic spindle bipolarity identified in a phenotype-based screen. Science 286, 971-974.

McDonald, A., Bergnes, G., and Morgans, D. (2004). US20040053948 A1. Cytokinetics, (USA).

Meluh, P.B., and Rose, M.D. (1990). KAR3, a kinesin-related gene required for yeast nuclear fusion. Cell 60, 1029-1041.

Metzger, M.B., Hristova, V.A., and Weissman, A.M. (2012). HECT and RING finger families of E3 ubiquitin ligases at a glance. J Cell Sci 125, 531-537.

Metzger, M.B., Pruneda, J.N., Klevit, R.E., and Weissman, A.M. (2013). RING-type E3 ligases: Master manipulators of E2 ubiquitin-conjugating enzymes and ubiquitination. Biochim Biophys Acta.

Miki, H., Setou, M., Kaneshiro, K., and Hirokawa, N. (2001). All kinesin superfamily protein, KIF, genes in mouse and human. Proc Natl Acad Sci USA 98, 7004-7011.

Miki, H., Okada, Y., and Hirokawa, N. (2005). Analysis of the kinesin superfamily: insights into structure and function. Trends Cell Biol 15, 467-476.

Miyamoto, D.T., Perlman, Z.E., Mitchison, T.J., and Shirasu-Hiza, M. (2003). Dynamics of the mitotic spindle–potential therapeutic targets. Prog Cell Cycle Res 5, 349-360.

Nakagawa, T., Tanaka, Y., Matsuoka, E., Kondo, S., Okada, Y., Noda, Y., Kanai, Y., and Hirokawa, N. (1997). Identification and classification of 16 new kinesin superfamily (KIF) proteins in mouse genome. Proc Natl Acad Sci USA 94, 9654-9659.

Nakayama, K.I., and Nakayama, K. (2006). Ubiquitin ligases: cell-cycle control and cancer. Nat Rev Cancer 6, 369-381.

Nalepa, G., Rolfe, M., and Harper, J.W. (2006). Drug discovery in the ubiquitin-proteasome system. Nat Rev Drug Discov 5, 596-613.

Narasimhulu, S.B., and Reddy, A.S. (1998). Characterization of microtubule binding domains in the *Arabidopsis* kinesin-like calmodulin binding protein. Plant Cell 10, 957-965.

Nislow, C., Lombillo, V.A., Kuriyama, R., and McIntosh, J.R. (1992). A plus-end-directed motor enzyme that moves antiparallel microtubules in vitro localizes to the interzone of mitotic spindles. Nature 359, 543-547.

Okada, Y., and Hirokawa, N. (2000). Mechanism of the single-headed processivity: diffusional anchoring between the K-loop of kinesin and the C terminus of tubulin. Proc Natl Acad Sci U S A 97, 640-645.

Orlicky, S., Tang, X., Neduva, V., Elowe, N., Brown, E.D., Sicheri, F., and Tyers, M. (2010). An allosteric inhibitor of substrate recognition by the SCF(Cdc4) ubiquitin ligase. Nat Biotechnol 28, 733-737.

Pan, Z.Q., Kentsis, A., Dias, D.C., Yamoah, K., and Wu, K. (2004). Nedd8 on cullin: building an expressway to protein destruction. Oncogene 23, 1985-1997.

Parke, C.L., Wojcik, E.J., Kim, S., and Worthylake, D.K. (2009). ATP hydrolysis in Eg5 kinesin involves a catalytic two-water mechanism. J Biol Chem 285, 5859-5867.

Pasca di Magliano, M., and Hebrok, M. (2003). Hedgehog signalling in cancer formation and maintenance. Nat Rev Cancer 3, 903-911.

Peng, J., Schwartz, D., Elias, J.E., Thoreen, C.C., Cheng, D., Marsischky, G., Roelofs, J., Finley, D., and Gygi, S.P. (2003). A proteomics approach to understanding protein ubiquitination. Nat Biotechnol 21, 921-926.

Peng, H., Gibson, L.C., Capili, A.D., Borden, K.L., Osborne, M.J., Harper, S.L., Speicher, D.W., Zhao, K., Marmorstein, R., Rock, T.A., and Rauscher, F.J., 3rd (2007). The structurally disordered KRAB repression domain is incorporated into a protease resistant core upon binding to KAP-1-RBCC domain. J Mol Biol 370, 269-289.

Peng, J., and Wysocka, J. (2008). It takes a PHD to SUMO. Trends Biochem Sci 33, 191-194.

Peters, C., Brejc, K., Belmont, L., Bodey, A.J., Lee, Y., Yu, M., Guo, J., Sakowicz, R., Hartman, J., and Moores, C.A. (2010). Insight into the molecular mechanism of the multitasking kinesin-8 motor. Embo Journal 29, 3437-3447.

Pickart, C.M. (2001). Mechanisms underlying ubiquitination. Annu Rev Biochem 70, 503-533.

Pickart, C.M., and Eddins, M.J. (2004). Ubiquitin: structures, functions, mechanisms. Biochim Biophys Acta 1695, 55-72.

Putoux, A., Thomas, S., Coene, K.L., Davis, E.E., Alanay, Y., Ogur, G., Uz, E., Buzas, D., Gomes, C., Patrier, S., et al. (2011). KIF7 mutations cause fetal hydrolethalus and acrocallosal syndromes. Nat Genet 43, 601-606.

Quinn, J.G., O'Neill, S., Doyle, A., McAtamney, C., Diamond, D., MacCraith, B.D., and O'Kennedy, R. (2000). Development and application of surface plasmon resonance-based biosensors for the detection of cell-ligand interactions. Anal Biochem 281, 135-143.

Raaijmakers, J.A., van Heesbeen, R.G., Meaders, J.L., Geers, E.F., Fernandez-Garcia, B., Medema, R.H., and Tanenbaum, M.E. (2012). Nuclear envelope-associated dynein drives prophase centrosome separation and enables Eg5-independent bipolar spindle formation. EMBO J 31, 4179-4190.

Rath, O., and Kozielski, F. (2012). Kinesins and cancer. Nat Rev Cancer 12, 527-539.

Reyes-Turcu, F.E., Ventii, K.H., and Wilkinson, K.D. (2009). Regulation and cellular roles of ubiquitin-specific deubiquitinating enzymes. Annu Rev Biochem 78, 363-397.

Rogers, G.C., Chui, K.K., Lee, E.W., Wedaman, K.P., Sharp, D.J., Holland, G., Morris, R.L., and Scholey, J.M. (2000). A kinesin-related protein, KRP(180), positions prometaphase spindle poles during early sea urchin embryonic cell division. J Cell Biol 150, 499-512.

Romberg, L., Pierce, D.W., and Vale, R.D. (1998). Role of the kinesin neck region in processive microtubule-based motility. J Cell Biol 140, 1407-1416.

Rupp, B. (2010). Biomolecular Crystallography: Principles, Practice, and Application to Structural Biology.

Ryan, R.F., Schultz, D.C., Ayyanathan, K., Singh, P.B., Friedman, J.R., Fredericks, W.J., and Rauscher, F.J., 3rd (1999). KAP-1 corepressor protein interacts and colocalizes with heterochromatic and euchromatic HP1 proteins: a potential role for Kruppel-associated box-zinc finger proteins in heterochromatin-mediated gene silencing. Mol Cell Biol 19, 4366-4378.

Sablin, E.P., Kull, F.J., Cooke, R., Vale, R.D., and Fletterick, R.J. (1996). Crystal structure of the motor domain of the kinesin-related motor ncd. Nature 380, 555-559.

Sakowicz, R., Finer, J.T., Beraud, C., Crompton, A., Lewis, E., Fritsch, A., Lee, Y., Mak, J., Moody, R., Turincio, R., et al. (2004). Antitumor activity of a kinesin inhibitor. Cancer Res 64, 3276-3280.

Sarangi, A., Valadez, J.G., Rush, S., Abel, T.W., Thompson, R.C., and Cooper, M.K. (2009). Targeted inhibition of the Hedgehog pathway in established malignant glioma xenografts enhances survival. Oncogene 28, 3468-3476.

Saunders, W.S., and Hoyt, M.A. (1992). Kinesin-related proteins required for structural integrity of the mitotic spindle. Cell 70, 451-458.

Sawin, K.E., LeGuellec, K., Philippe, M., and Mitchison, T.J. (1992). Mitotic spindle organization by a plus-end-directed microtubule motor. Nature 359, 540-543.

Sawin, K.E., and Mitchison, T.J. (1995). Mutations in the kinesin-like protein Eg5 disrupting localization to the mitotic spindle. Proc Natl Acad Sci USA 92, 4289-4293.

Scanlan, M.J., Gout, I., Gordon, C.M., Williamson, B., Stockert, E., Gure, A.O., Jager, D., Chen, Y.T., Mackay, A., O'Hare, M.J., and Old, L.J. (2001). Humoral immunity to human breast cancer: antigen definition and quantitative analysis of mRNA expression. Cancer Immun 1, 4.

Schneider, C.A., Rasband, W.S., and Eliceiri, K.W. (2012). NIH Image to ImageJ: 25 years of image analysis. Nat Methods 9, 671-675.

Scholzen, T., and Gerdes, J. (2000). The Ki-67 protein: from the known and the unknown. J Cell Physiol 182, 311-322.

Schwartz, D.C., and Hochstrasser, M. (2003). A superfamily of protein tags: ubiquitin, SUMO and related modifiers. Trends Biochem Sci 28, 321-328.

Seeger, M.A., Zhang, Y., and Rice, S.E. (2012). Kinesin tail domains are intrinsically disordered. Proteins 80, 2437-2446.

Segbert, C., Barkus, R., Powers, J., Strome, S., Saxton, W.M., and Bossinger, O. (2003). KLP-18, a Klp2 kinesin, is required for assembly of acentrosomal meiotic spindles in *Caenorhabditis elegans*. Mol Biol Cell 14, 4458-4469.

Seog, D.H., Lee, D.H., and Lee, S.K. (2004). Molecular motor proteins of the kinesin superfamily proteins (KIFs): structure, cargo and disease. J Korean Med Sci 19, 1-7.

Sindelar, C.V., Budny, M.J., Rice, S., Naber, N., Fletterick, R., and Cooke, R. (2002). Two conformations in the human kinesin power stroke defined by X-ray crystallography and EPR spectroscopy. Nat Struct Biol 9, 844-848.

Sindelar, C.V., and Downing, K.H. (2007). The beginning of kinesin's force-generating cycle visualized at 9-A resolution. J Cell Biol 177, 377-385.

Skoufias, D.A., DeBonis, S., Saoudi, Y., Lebeau, L., Crevel, I., Cross, R., Wade, R.H., Hackney, D., and Kozielski, F. (2006). S-trityl-L-cysteine is a reversible, tight binding inhibitor of the human kinesin Eg5 that specifically blocks mitotic progression. J Biol Chem 281, 17559-17569.

Song, Y.H., Marx, A., Muller, J., Woehlke, G., Schliwa, M., Krebs, A., Hoenger, A., and Mandelkow, E. (2001). Structure of a fast kinesin: implications for ATPase mechanism and interactions with microtubules. EMBO J 20, 6213-6225.

Sueishi, M., Takagi, M., and Yoneda, Y. (2000). The forkhead-associated domain of Ki-67 antigen interacts with the novel kinesin-like protein Hklp2. J Biol Chem 275, 28888-28892.

Takagi, M., Matsuoka, Y., Kurihara, T., and Yoneda, Y. (1999). Chmadrin: a novel Ki-67 antigen-related perichromosomal protein possibly implicated in higher order chromatin structure. J Cell Sci 112, 2463-2472.

Tanenbaum, M.E., Macurek, L., Janssen, A., Geers, E.F., Alvarez-Fernandez, M., and Medema, R.H. (2009). Kif15 cooperates with eg5 to promote bipolar spindle assembly. Curr Biol 19, 1703-1711.

Tanenbaum, M.E., and Medema, R.H. (2010). Mechanisms of centrosome separation and bipolar spindle assembly. Dev Cell 19, 797-806.

Tay, S.Y., Ingham, P.W., and Roy, S. (2005). A homologue of the *Drosophila* kinesin-like protein Costal2 regulates Hedgehog signal transduction in the vertebrate embryo. Development 132, 625-634.

Tcherniuk, S., Skoufias, D.A., Labriere, C., Rath, O., Gueritte, F., Guillou, C., and Kozielski, F. (2010). Relocation of Aurora B and survivin from centromeres to the central spindle impaired by a kinesin-specific MKLP-2 inhibitor. Angew Chem Int Ed Engl 49, 8228-8231.

Toprak, E., Yildiz, A., Hoffman, M.T., Rosenfeld, S.S., and Selvin, P.R. (2009). Why kinesin is so processive. Proc Natl Acad Sci USA 106, 12717-12722.

Turner, J., Anderson, R., Guo, J., Beraud, C., Fletterick, R., and Sakowicz, R. (2001). Crystal structure of the mitotic spindle kinesin Eg5 reveals a novel conformation of the neck-linker. J Biol Chem 276, 25496-25502.

Vagin, A., and Teplyakov, A. (2000). An approach to multi-copy search in molecular replacement. Acta Crystallogr D Biol Crystallogr 56, 1622-1624.

Vagin, A.A., Steiner, R.A., Lebedev, A.A., Potterton, L., McNicholas, S., Long, F., and Murshudov, G.N. (2004). REFMAC5 dictionary: organization of prior chemical knowledge and guidelines for its use. Acta Crystallogr D Biol Crystallogr 60, 2184-2195.

Vale, R.D., Reese, T.S., and Sheetz, M.P. (1985a). Identification of a novel force-generating protein, kinesin, involved in microtubule-based motility. Cell 42, 39-50.

Vale, R.D., Schnapp, B.J., Reese, T.S., and Sheetz, M.P. (1985b). Organelle, bead, and microtubule translocations promoted by soluble factors from the squid giant axon. Cell 40, 559-569.

Vale, R.D., and Fletterick, R.J. (1997). The design plan of kinesin motors. Annu Rev Cell Dev Biol 13, 745-777.

Vanneste, D., Takagi, M., Imamoto, N., and Vernos, I. (2009). The role of Hklp2 in the stabilization and maintenance of spindle bipolarity. Curr Biol 19, 1712-1717.

Vassilev, L.T. (2004). Small-molecule antagonists of p53-MDM2 binding: research tools and potential therapeutics. Cell Cycle 3, 419-421.

Verheijen, R., Kuijpers, H.J., van Driel, R., Beck, J.L., van Dierendonck, J.H., Brakenhoff, G.J., and Ramaekers, F.C. (1989). Ki-67 detects a nuclear matrix-associated proliferation-related antigen. II. Localization in mitotic cells and association with chromosomes. J Cell Sci 92, 531-540.

Verhey, K.J., and Hammond, J.W. (2009). Traffic control: regulation of kinesin motors. Nat Rev Mol Cell Biol 10, 765-777.

Verhey, K.J., Dishinger, J., and Kee, H.L. (2011). Kinesin motors and primary cilia. Biochem Soc Trans 39, 1120-1125.

Vernos, I., Heasman, J., and Wylie, C. (1993). Multiple kinesin-like transcripts in *Xenopus* oocytes. Dev Biol 157, 232-239.

Vijay-Kumar, S., Bugg, C.E., and Cook, W.J. (1987). Structure of ubiquitin refined at 1.8 A resolution. J Mol Biol 194, 531-544.

Walczak, C.E., Vernos, I., Mitchison, T.J., Karsenti, E., and Heald, R. (1998). A model for the proposed roles of different microtubule-based motor proteins in establishing spindle bipolarity. Curr Biol 8, 903-913.

Walker, J.E., Saraste, M., Runswick, M.J., and Gay, N.J. (1982). Distantly related sequences in the alpha- and beta-subunits of ATP synthase, myosin, kinases and other ATP-requiring enzymes and a common nucleotide binding fold. EMBO J 1, 945-951.

Wang, C., Ivanov, A., Chen, L., Fredericks, W.J., Seto, E., Rauscher, F.J., 3rd, and Chen, J. (2005). MDM2 interaction with nuclear corepressor KAP1 contributes to p53 inactivation. EMBO J 24, 3279-3290.

Wang, G., Amanai, K., Wang, B., and Jiang, J. (2000). Interactions with Costal2 and suppressor of fused regulate nuclear translocation and activity of cubitus interruptus. Genes Dev 14, 2893-2905.

Whitby, F.G., Xia, G., Pickart, C.M., and Hill, C.P. (1998). Crystal structure of the human ubiquitin-like protein NEDD8 and interactions with ubiquitin pathway enzymes. J Biol Chem 273, 34983-34991.

Wickstead, B., and Gull, K. (2006). A "holistic" kinesin phylogeny reveals new kinesin families and predicts protein functions. Mol Biol Cell 17, 1734-1743.

Wilkins, M.R., Gasteiger, E., Bairoch, A., Sanchez, J.C., Williams, K.L., Appel, R.D., and Hochstrasser, D.F. (1999). Protein identification and analysis tools in the ExPASy server. Methods Mol Biol 112, 531-552.

Wilson, C.W., Nguyen, C.T., Chen, M.H., Yang, J.H., Gacayan, R., Huang, J., Chen, J.N., and Chuang, P.T. (2009). Fused has evolved divergent roles in vertebrate Hedgehog signalling and motile ciliogenesis. Nature 459, 98-102.

Wittmann, T., Boleti, H., Antony, C., Karsenti, E., and Vernos, I. (1998). Localization of the kinesin-like protein Xklp2 to spindle poles requires a leucine zipper, a microtubule-associated protein, and dynein. J Cell Biol 143, 673-685.

Wittmann, T., Wilm, M., Karsenti, E., and Vernos, I. (2000). TPX2, A novel *Xenopus* MAP involved in spindle pole organization. J Cell Biol 149, 1405-1418.

Woehlke, G., and Schliwa, M. (2000). Walking on two heads: the many talents of kinesin. Nat Rev Mol Cell Biol 1, 50-58.

Yan, Y., Sardana, V., Xu, B., Homnick, C., Halczenko, W., Buser, C.A., Schaber, M., Hartman, G.D., Huber, H.E., and Kuo, L.C. (2004). Inhibition of a mitotic motor protein: where, how, and conformational consequences. J Mol Biol 335, 547-554.

Yang, J.T., Laymon, R.A., and Goldstein, L.S. (1989). A three-domain structure of kinesin heavy chain revealed by DNA sequence and microtubule binding analyses. Cell 56, 879-889.

Yun, M.Y., Zhang, X.H., Park, C.G., Park, H.W., and Endow, S.A. (2001). A structural pathway for activation of the kinesin motor ATPase. Embo Journal 20, 2611-2618.

Zeng, L., Yap, K.L., Ivanov, A.V., Wang, X., Mujtaba, S., Plotnikova, O., Rauscher, F.J., 3rd, and Zhou, M.M. (2008). Structural insights into human KAP1 PHD finger-bromodomain and its role in gene silencing. Nat Struct Mol Biol 15, 626-633.

Zhao, S., and Ulrich, H.D. (2010). Distinct consequences of posttranslational modification by linear versus K63-linked polyubiquitin chains. Proc Natl Acad Sci U S A 107, 7704-7709.

Zhou, R.Y., Niwa, S., Homma, N., Takei, Y., and Hirokawa, N. (2009). KIF26A Is an Unconventional Kinesin and Regulates GDNF-Ret Signaling in Enteric Neuronal Development. Cell 139, 802-813.

Zhu, C., and Jiang, W. (2005). Cell cycle-dependent translocation of PRC1 on the spindle by Kif4 is essential for midzone formation and cytokinesis. Proc Natl Acad Sci U S A 102, 343-348.

Ziv, Y., Bielopolski, D., Galanty, Y., Lukas, C., Taya, Y., Schultz, D.C., Lukas, J., Bekker-Jensen, S., Bartek, J., and Shiloh, Y. (2006). Chromatin relaxation in response to DNA double-strand breaks is modulated by a novel ATM- and KAP-1 dependent pathway. Nat Cell Biol 8, 870-876.

Zou, Y., Weis, W.I., and Kobilka, B.K. (2012). N-terminal T4 lysozyme fusion facilitates crystallization of a G protein coupled receptor. Plos One 7, e46039.

Manuscripts

Klejnot, M., Falnikar, A., Ulaganathan, V., Cross, R., Baas, P.W., and Kozielski, F. (2014). The crystal structure and biochemical characterization of Kif15: a bifunctional molecular motor involved in bipolar spindle formation and neuronal development. Acta Crystallogr D Biol Crystallogr 70, 123-133.

Klejnot, M., and Kozielski, F. (2012). Structural insights into human Kif7, a kinesin involved in Hedgehog signalling. Acta Crystallogr D Biol Crystallogr 68, 154-159.

Liu, M., Nadar, V.C., Kozielski, F., Klejnot, M., Yu, W., and Baas, P.W. (2010). Kinesin-12, a mitotic microtubule-associated motor protein, impacts axonal growth, navigation, and branching. J Neurosci 30, 14896-14906.

Klejnot, M., Talapatra, S.K., Kozielski, F. Expression analysis of human kinesins provides a tool to test the specificity of kinesin-based antimitotic inhibitors. Manuscript to be submitted.

Acta Crystallographica Section D
Biological Crystallography
ISSN 1399-0047

The crystal structure and biochemical characterization of Kif15: a bifunctional molecular motor involved in bipolar spindle formation and neuronal development

Marta Klejnot,[a]* Aditi Falnikar,[b] Venkatasubramanian Ulaganathan,[a]‡ Robert A. Cross,[c] Peter W. Baas[b] and Frank Kozielski[d]*

[a]The Beatson Institute for Cancer Research, Garscube Estate, Switchback Road, Glasgow G61 1BD, Scotland, [b]Department of Neurobiology and Anatomy, Drexel University College of Medicine, 2900 Queen Lane, Philadelphia, PA 19129, USA, [c]Warwick Medical School, University of Warwick, Coventry CV4 7AL, England, and [d]School of Pharmacy, University College London, 29–39 Brunswick Square, London WC1N 1AX, England

‡ Present address: School of Chemical and Biotechnology, SASTRA University, Tirumalaisamudram, Thanjavur 613 401, Tamilnadu, India

Correspondence e-mail: m.klejnot@beatson.gla.ac.uk, f.kozielski@ucl.ac.uk

Received 4 July 2013
Accepted 18 October 2013

PDB reference: Kif15$_{19–375}$, 4bn2

Kinesins constitute a superfamily of microtubule-based motor proteins with important cellular functions ranging from intracellular transport to cell division. Some kinesin family members function during the mitotic phase of the eukaryotic cell cycle and are crucial for the successful progression of cell division. In the early stages of mitosis, during prometaphase, certain kinesins are required for the formation of the bipolar spindle, such as Eg5 and Kif15, which seem to possess partially overlapping functions. Because kinesins transform the chemical energy from ATP hydrolysis into mechanical work, inhibition of their function is a tractable approach for drug development. Drugs targeting Eg5 have shown promise as anticancer agents. Kif15 has recently come to the fore because it can substitute the functions of Eg5, and may itself have potential as a prospective drug target. Here, the initial biochemical, kinetic and structural characterization of Kif15 is reported and it is compared with the functionally related motor Eg5. Although Kif15 contains ADP in the catalytic site, its motor-domain structure was captured in the 'ATP-like' configuration, with the neck linker docked to the catalytic core. The interaction of Kif15 with microtubules was also investigated and structural differences between these two motors were elucidated which indicate profound differences in their mode of action, in agreement with current models of microtubule cross-linking and sliding.

1. Introduction

Kinesins form a superfamily of proteins that play important roles in eukaryotic intracellular trafficking and cell division (Hirokawa *et al.*, 2009). The genomes of higher vertebrates contain as many as 45 genes coding for different kinesins. The majority of these molecular machines are implicated in intracellular transport, whereas a third of the superfamily members plays key roles in different stages of mitosis and cytokinesis (Wordeman, 2010). Some kinesins fulfill dual functions in both transport and cell division, such as Eg5 (KSP, Kif11, kinesin-5 family; Ferhat, Cook *et al.*, 1998), Kif15 (Hklp2, Xklp2, KRP180, KLP-18, kinesin-12 family; Buster *et al.*, 2003; Liu *et al.*, 2010), Kif2A (kinesin-13 family; Ganem & Compton, 2004; Zhu *et al.*, 2005), MKLP-1 (kinesin-6 family; Zhu *et al.*, 2005) and Kif4A/Kif4B (kinesin-4 family; Mazumdar *et al.*, 2004; Zhu *et al.*, 2005; Zhu & Jiang, 2005). A few kinesins are involved in the assembly and/or maintenance of the bipolar spindle (Tanenbaum & Medema, 2010), namely the two N-terminal plus-end-directed motors Eg5 (Blangy *et al.*, 1995) and Kif15, as well as the C-terminal minus-end-

directed kinesin KifC1 (HSET, kinesin-13 family) and dynein, which belongs to another class of microtubule (MT)-based motor proteins (Vaisberg *et al.*, 1993).

Kif15 has been identified in a variety of eukaryotes, including *Xenopus* (Boleti *et al.*, 1996), human (Sueishi *et al.*, 2000), sea urchin (Rogers *et al.*, 2000), *Caenorhabditis elegans* (Segbert *et al.*, 2003) and rodents (Buster *et al.*, 2003). Although Kif15 and Eg5 appear to share some functional similarities during bipolar spindle formation, they seem to work through distinct mechanisms, adopting rather diverse quaternary structures (Vanneste *et al.*, 2009).

The involvement of Eg5 in the separation of the duplicated centrosomes (Blangy *et al.*, 1995) has made it a potential target for drug development in cancer chemotherapy, with several kinesin-5-specific inhibitors in multiple Phase I and II clinical trials (Huszar *et al.*, 2009; Rath & Kozielski, 2012). Interestingly, Kif15 overexpression has been shown to be able to restore functions of Eg5 under certain conditions, for example when Eg5 is depleted (Tanenbaum *et al.*, 2009). Subsequently, it has been hypothesized (although not yet proven) that tumours treated with Eg5-targeting drugs might acquire resistance to these inhibitors by simply up-regulating Kif15. This interesting hypothesis and the involvement of Kif15 in bipolar spindle assembly makes it a potential target for drug development in cancer chemotherapy, and the first inhibitor scaffolds targeting Kif15 have been reported in the patent literature (McDonald *et al.*, 2004).

Although the role of Kif15 in bipolar spindle formation has been investigated in a variety of organisms (Boleti *et al.*, 1996; Rogers *et al.*, 2000; Segbert *et al.*, 2003; Sueishi *et al.*, 2000) and has been compared with that of Eg5 in cellular assays, much less is known about its biochemical, mechanochemical and structural properties or its interactions with binding partners. The recombinant expression of human Kif15 for inhibitor screening, and the structure determination of its motor domain for structure-based design, would be highly desirable to facilitate the drug-development process. Here, we provide the initial biochemical characterization of human Kif15 and compare its properties with those of its functionally related partner Eg5. We reveal that Kif15, in contrast to Eg5, does not have a second nucleotide-independent MT-binding site in its C-terminal tail domain. Furthermore, we determine the crystal structure of the binary Kif15–ADP complex captured in the 'ATP-like' state adopted by the switch II cluster and neck-linker region.

2. Materials and methods

2.1. Cloning, expression and purification of mammalian Kif15 proteins

The *Homo sapiens* Kif15 motor domain and neck-linker region (named $Kif15_{19–375}$ throughout this manuscript) was cloned, expressed and purified as described previously (Liu *et al.*, 2010). A longer construct including the first 19 residues that contains the cover strand (named $Kif15_{1–375}$) was cloned by extending the $Kif15_{19–375}$ construct by PCR with four forward primers (P1_F, 5′-CA AAT GGT CAG TCT AAC CAG CCG AGC AAC GAA G-3′; P2_F, 5′-GAG TTA CGC AGC GTG ACA AAT GGT CAG TCT AAC C-3′; P3_F, 5′-GGC TGC AAA ACT GAG TTA CGC AGC GTG-3′; P4_F, 5′-GAA **CC ATG G**CT CCT GGC TGC AAA ACT G-3′) and a single reverse primer (5′-GAT **CTC GAG** TTA ACC CTG GGT ATC TTC ATT CAC AAC C-3′). $Kif15_{1–375}$ was expressed and purified as described for the shorter construct. The Kif15 tail construct from *Rattus norvegicus* ($Kif15_{1149–1388}$) was cloned, expressed and purified as $Kif15_{19–375}$.

2.2. Determination of protein concentrations

Protein concentrations were determined either by using the Lambert–Beer law measured under native conditions [for the motor-domain constructs bound ADP was taken into account ($2500\ M^{-1}\ cm^{-1}$)] or by applying the Bradford method. The extinction coefficients for each Kif15 construct were calculated ($Kif15_{1–375}$, $17\,670\ M^{-1}\ cm^{-1}$; $Kif15_{19–375}$, $17\,608\ M^{-1}\ cm^{-1}$; $Kif15_{1149–1388}$, $10\,033\ M^{-1}\ cm^{-1}$) using *ProtParam* from the Bioinformatics Resource Portal (Wilkins *et al.*, 1999).

2.3. Analytical gel filtration

Analytical gel filtrations were performed on a Superose 12 10/300 GL column (GE Healthcare). Experiments were conducted at a flow rate of 0.5 ml min^{-1} (50 m*M* PIPES pH 6.8, 250 m*M* NaCl, 2 m*M* $MgCl_2$, 1 m*M* DTT; all from Sigma) using an injection volume of 200 µl. Prior to running Kif15 expression constructs, the column was calibrated with proteins of known molecular mass (ribonuclease A, 13.7 kDa; carbonic anhydrase, 29 kDa; ovalbumin, 43 kDa; conalbumin, 75 kDa) and blue dextran. The K_{av} values were calculated for the calibration proteins $[(V_e - V_0)/(V_c - V_0)$, where V_e is the elution volume, V_0 is the void volume and V_c is the column volume] and were plotted against the log of the molecular masses of the standards. The molecular masses were calculated from the resulting equation.

2.4. Steady-state enzyme kinetics

Steady-state basal and MT-stimulated activities were determined using the pyruvate kinase/lactate dehydrogenase coupled assay described previously (Hackney & Jiang, 2001). All measurements were carried out at 25°C using a 96-well Sunrise photometer (Tecan) in a final reaction volume of 100 µl at least in triplicate. Data were analysed using *Microsoft Excel* 2008 and *KaleidaGraph* 4.0 (Synergy Software). The salt dependence of the basal $Kif15_{19–375}$ and $Kif15_{1–375}$ ATPase activities was measured at NaCl concentrations from 0 to 275 m*M* in the presence of 0.59 µ*M* $Kif15_{19–375}$ and 0.35 µ*M* $Kif15_{1–375}$ and 1 m*M* Mg^{2+}-ATP. To determine the basal ATPase activity of $Kif15_{19–375}$ and $Kif15_{1–375}$, their activities were examined at ATP concentrations from 0 to 2 m*M* in the presence of 0.35 µ*M* $Kif15_{19–375}$ and 0.75 µ*M* $Kif15_{1–375}$ as well as 75 m*M* NaCl for $Kif15_{19–375}$ and 50 m*M* NaCl for $Kif15_{1–375}$. The salt dependence of the MT-stimulated ATPase activity of $Kif15_{19–375}$ and $Kif15_{1–375}$ was determined by measuring their

rates of activity at MT concentrations from 0 to 10 μ*M* in the presence of 0.04 μ*M* $Kif15_{19–375}$ and 0.08 μ*M* $Kif15_{1–375}$ (in the presence of 0, 50, 100 and 150 m*M* KCl for $Kif15_{19–375}$ and in the presence of 0 and 50 m*M* KCl for $Kif15_{1–375}$). Finally, the MT-stimulated ATPase activity for both Kif15 constructs was measured in the presence of increasing ATP concentrations from 0 to 2 m*M* in the presence of 0.04 μ*M* $Kif15_{19–375}$ and 0.04 μ*M* $Kif15_{1–375}$, 3 μ*M* MTs in the absence of salt.

2.5. Transient-state enzyme kinetics

Slow Mant-ATP [2′/3′-*O*-(*N*-methylanthraniloyl)adenosine-5′-triphosphate] turnovers were performed by making manual additions to a 100 µl cuvette in a modified Cary Eclipse fluorescence spectrophotometer at 25°C. Reactions were started by adding the motor to a 5 μ*M* solution of Mant-ATP (Jena Bioscience) in BRB80 (80 m*M* PIPES–KOH pH 6.9, 1 m*M* $MgCl_2$, 1 m*M* EGTA) to a final active-site concentration of 3.4 μ*M*. After the plateau of fluorescence had been reached, a 2.5 µl chase of unlabelled 100 m*M* Mg^{2+}-ATP was added. Mant fluorescence was excited at 350 nm and emission was monitored at 450 nm. Stopped-flow experiments were performed at 25°C using a TgK SF-61DX2 stopped-flow spectrofluorimeter. Syringe 1 contained the $Kif15_{19–375}$ or $Kif15_{1–375}$ single head–Mant-ADP complex, which was formed by adding stock 5 m*M* Mant-ATP to 2 μ*M* Kif15 in BRB80 buffer with rapid mixing and incubating on ice for 30 min. Syringe 2 contained MTs at various concentrations plus 2 m*M* Mg^{2+}-ATP chasing nucleotide. MTs for these experiments were assembled from pig brain tubulin in BRB80, stabilized using 20 μ*M* taxol and supplemented with 2 m*M* Mg^{2+}-ATP immediately prior to use. Tubulin was dissolved in BRB80 without nucleotide or taxol. Mant fluorescence was excited at 350 nm and emission was monitored at 450 nm. Data were fitted to single exponentials to yield an apparent rate of Mant-ADP release (k_{off} in s^{-1}) and an amplitude. Collected data for MT activation and tubulin activation of Mant-ADP release were fitted to rectangular hyperbolas using *KaleidaGraph*. Data points represent the averages of at least three pushes on at least two separate occasions.

2.6. Tubulin purification and polymerization into MTs

Tubulin was purified from bovine brain by cycles of polymerization and depolymerization as described previously (Castoldi & Popov, 2003). Subsequently, tubulin was aliquoted at 18.5 mg ml^{-1}, snap-frozen and stored in liquid nitrogen. MTs were prepared at 60 μ*M*. The MT concentration was calculated as the heterodimer concentration (110 kDa), assuming that all of the tubulin polymerized. Tubulin was gently mixed with pre-warmed G-PEM buffer (100 m*M* PIPES pH 6.9, 1 m*M* EDTA, 1 m*M* $MgCl_2$, 1 m*M* GTP; all from Sigma) supplemented with 20 μ*M* taxol. Polymerization was carried out overnight at 37°C. For nucleotide binding and ATPase assays MTs were used in the taxol-polymerized form prepared without GTP.

2.7. Pelleting assays

Pelleting assays were performed in 50 m*M* PIPES pH 6.9, 20 m*M* NaCl, 2 m*M* $MgCl_2$, 1 m*M* DTT. $Kif15_{19–375}$ (1–12 μ*M*) was gently mixed with taxol-polymerized MTs (5 μ*M*) and supplemented with buffer to a final volume of 40 µl. Binding assays were performed in the presence of 2 m*M* Mg^{2+}-ATP, 2 m*M* AMP-PNP or 4 mU apyrase. Samples were incubated at room temperature for 10 min and centrifuged in a Beckman TL100 ultracentrifuge at 100 000*g* and 25°C for 20 min. Supernatants were removed from the pellets. The pellet was resuspended in Laemmli reducing sample buffer. Supernatants and pellet samples were run on gradient SDS–PAGE gels (4–12%). All measurements were performed in triplicate. Data were analyzed using *ImageJ* 143.u, *Microsoft Excel* 2008 and *KaleidaGraph* 4.0. To calculate the dissociation constant (K_d), the Michaelis–Menten representation was used, with MT-bound $Kif15_{19–375}$ ([MT·$Kif15_{19–375}$]) plotted as a function of free $Kif15_{19–375}$ ([$Kif15_{19–375}$]),

$$[\mathrm{MT}\cdot\mathrm{Kif15}_{19-375}] = \frac{B_{\max}\cdot[\mathrm{Kif15}_{19-375}]}{K_d + [\mathrm{Kif15}_{19-375}]}. \quad (1)$$

B_{max} corresponds to the maximal number of interacting sites.

2.8. Protein crystallization, data collection, processing and refinement

Initial nanodrop screening was performed with purified $Kif15_{19–375}$ at 10 mg ml^{-1} in the presence and absence of Mg^{2+}-ATP at 4 and 19°C. The protein crystallized at 19°C in the presence of nucleotide and 200 m*M* $MgCl_2$, 25% PEG 3350, 100 m*M* Tris–HCl pH 8.5. Seeding further optimized the crystals, together with decreasing the protein concentration and the temperature. Improved crystals were immersed in cryoprotectant solution [20%(*w*/*v*) *meso*-erythritol, 240 m*M* $MgCl_2$, 30% PEG 3350, 120 m*M* Tris–HCl pH 8.5] and flash-cooled in liquid nitrogen. Data were collected to a resolution of 2.7 Å at the European Synchrotron Radiation Facility (ESRF). The structure was solved by molecular replacement with *MOLREP* (Vagin & Teplyakov, 2010) using the CENP-E structure (PDB entry 1t5c; Garcia-Saez *et al.*, 2004) as a search model. The asymmetric unit contained three copies of $Kif15_{19–375}$ with bound Mg^{2+}-ADP in the catalytic site positioned with *REFMAC*5 (Murshudov *et al.*, 2011) by rigid-body and restrained refinement. The structure model was improved using *Coot* (Emsley & Cowtan, 2004) and further refined using *PHENIX* (Adams *et al.*, 2010) with noncrystallographic symmetry (NCS) restraints.

2.9. *In vitro* assay for neuronal migration

We used a previously established *in vitro* culture system to study the migration of rat cerebellar granule neurons (Bix & Clark, 1998; Hirotsune *et al.*, 1998). Cerebella were isolated from 6–8-day-old rat pups, triturated to give a single-cell suspension and then transfected with either control or Kif15 siRNA and control EGFP plasmid using an Amaxa electroporator and plated on polylysine-coated plastic dishes in serum-containing medium. The next day, the cells were

released by treatment with trypsin and were allowed to stand in a solution overnight after removing the trypsin. During this period the cells formed aggregates, which were plated on glass cover slips coated with laminin in serum-free medium to stimulate migration. For time-lapse imaging, the cover slips were placed in an imaging station consisting of a Zeiss environmental chamber and a Zeiss Observer microscope. Serial images were captured every 2 min for a period of 4 h. To quantify cell movement, the total displacement exhibited by the cell body was measured using the *AxioVision* software and was divided by the time taken for the displacement.

3. Results and discussion

3.1. Biophysical characterization of mammalian Kif15 motor and tail domains

Human Kif15 is a protein of 1388 residues (Fig. 1*a*) with an N-terminal motor domain (19–375) followed by a long α-helical rod-shaped stalk predicted to form an interrupted coiled coil. A bar diagram of Eg5 is presented in Fig. 1(*b*). Kif15 does not contain the conventional C-terminal globular domain typical of many other kinesins (*e.g.* Eg5); it possesses a C-terminal leucine zipper, a common dimerization motif (residues 1359–1380). The C-terminal region has also been shown to contain binding sites for the forkhead-associated (FHA) domain of Ki-67 (Sueishi *et al.*, 2000; Vanneste *et al.*, 2009) and for the nuclear protein TPX2 (targeting protein for Xklp2; Tanenbaum *et al.*, 2009) (Fig. 1*a*). The internal region of Kif15 contains a putative myosin tail homology domain, which has been shown to enable Kif15 to co-localize with actin (Buster *et al.*, 2003).

We subcloned, expressed and purified the Kif15 motor ($Kif15_{19–375}$, coding for residues 19–357) and $Kif15_{1–375}$ including the first 18 residues that are thought to include the cover strand, a short nine-residue N-terminal region shown to interact with the C-terminal neck-linker region. These two regions have been shown to fold into the so-called neck-cover bundle by forming a small β-sheet and represent a force-generating element in several members of the kinesin superfamily (Hwang *et al.*, 2008; Khalil *et al.*, 2008). Finally, we cloned the C-terminal tail construct (named $Kif15_{1149–1388}$; Fig. 1*c*) using *Escherichia coli* codon-optimized cDNA. The identity of the purified proteins was verified by mass-spectrometric fingerprint analysis, with a sequence coverage of 65% for $Kif15_{19–375}$, 81% for $Kif15_{1–375}$ and 61% for $Kif15_{1149–1388}$. The molecular masses of $Kif15_{19–375}$ and $Kif15_{1–375}$ determined by gel filtration were 37 and 39 kDa close to their theoretical masses of 37 and 39 kDa, respectively, indicating that the Kif15 motor domain and the Kif15 motor including the cover-strand region are monomeric, in agreement with other kinesins. The gel-

Table 1
Data-collection and refinement statistics for the *H. sapiens* $Kif15_{19–375}$–Mg^{2+}-ADP binary complex.

Values in parentheses are for the highest resolution shell.

PDB entry	4bn2
Data-collection statistics	
Beamline	ID23-1, ESRF
Detector	ADSC Q315R
Resolution range	30–2.7
Space group	$P3_221$
Unit-cell parameters (Å, °)	$a = b = 90.2$, $c = 251.4$, $\alpha = \beta = 90$, $\gamma = 120$
Completeness (%)	89.7 (86.5)
R_{merge} (%)	9.8 (37.8)
Multiplicity	3.7 (3.5)
Mean $I/\sigma(I)$	8.6 (3.1)
Total No. of reflections	108223
No. of unique reflections	29592
No. of copies per asymmetric unit	3
Refinement statistics	
R_{work}/R_{free} (%)	21.2/26.3
No. of Mg^{2+}-ADP molecules	3
No. of water molecules	156
R.m.s.d. from ideal geometry	
Bond lengths (Å)	0.013
Bond angles (°)	1.60

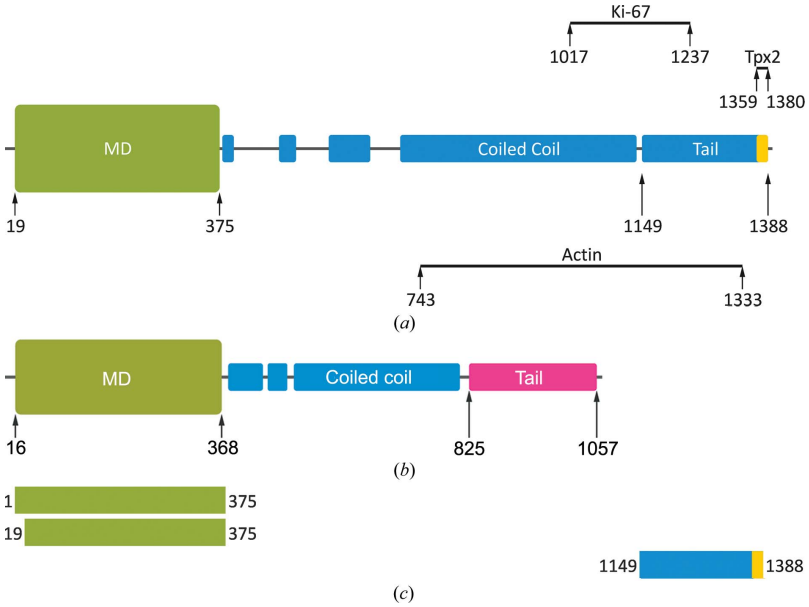

Figure 1
Schematic representation of human Kif15 and Eg5. (*a*) The Kif15 motor domain shown in green is followed by a discontinuous α-helical region predicted to form a coiled-coil stalk domain (coloured blue). The C-terminal leucine-zipper motif is shaded in yellow. The putative interacting regions for actin (residues 743–1333), Ki-67 (residues 1017–1237) and TPX2 (residues 1359–1380) in the C-terminal half of Kif15 are also indicated. (*b*) The Eg5 motor domain shown in green is followed by a discontinuous α-helical region forming a coiled-coil domain (coloured blue). The C-terminal globular tail is marked in pink. (*c*) Bar diagrams of the Kif15 constructs used in this study.

filtration profile for $Kif15_{1149–1388}$ was heterogeneous, indicating possible assembly into higher oligomers and/or partial aggregation.

3.2. Crystal structure of the binary $Kif15_{19–375}$–Mg^{2+}-ADP complex

The structure of the Kif15 motor domain was solved by molecular replacement and refined to a resolution of 2.7 Å. Data-collection and refinement statistics are shown in Table 1. $Kif15_{19–375}$ crystallized in space group $P3_221$ with three molecules in the asymmetric unit. The crystals have a Matthews parameter of 2.4 Å^3 Da^{-1} and a solvent content of 49.1%. The r.m.s. deviations from ideal geometry were 0.013 Å for bond lengths and 1.60° for bond angles for the refined structure. The final model contains residues 24–375 for molecules *A* and *B* and residues 24–372 for molecule *C*. Owing to missing or non-interpretable electron density, several smaller loops could not be built and are absent from the model. Side chains for which no density was observed were deleted from the C^{β} position onwards. The Ramachandran plot shows that 94.3% of the residues are in favoured regions, 5.5% are in additionally allowed regions and 0.2% are outliers. Since molecule *A* presented better defined electron density and a more complete model than molecules *B* and *C*, we subsequently use it for further descriptions of the structure.

The Kif15 motor domain shows the typical kinesin fold with an eight-stranded β-sheet surrounded by three major α-helices on each side (Fig. 2*a*). The crystallized Kif15 construct contains the neck linker, which aligns with the catalytic core, forming a small β-sheet. Although Mg^{2+}-ADP is bound in the catalytic site, Kif15 is in the so-called 'ATP-like' conformation. The switch II cluster (helix α4–loop L12–helix α5) is in the so-called 'upward' position, allowing the neck linker to dock to the motor domain (Fig. 2*a*). We subsequently compared the structure of the Kif15 motor with that of the functionally related Eg5 (Blangy *et al.*, 1995; Turner *et al.*, 2001), using the AMP-PNP-bound complex representing the 'ATP-like' state of Eg5 (Parke *et al.*, 2009). Sequence alignment of Kif15 and Eg5 shows their high similarity inside their motor domains, with 41.8% identical, 15.5% strongly similar and 12.8% weakly similar residues, which is also reflected by their structures (Fig. 2*b*). Outside their motor domains the primary sequence is at best only weakly conserved, with 20.3% identical, 20.2% strongly similar and 9.8% weakly similar residues. Kif15 has a deletion of two amino acids and a single insertion in the loop L1 region. In the case of Eg5 loop L1 is interrupted by helix α0, while in Kif15 loop L1 is longer. Loop L1 is part of the L1–L3–L5 cluster that together with loop L9 mediates the entrance of the nucleotide (Song *et al.*, 2001). In contrast to Eg5, three residues are missing in the Kif15 loop L2 region. Four residues are missing in loop L5, five in loop L8 (loop L8 is implicated in MT-stimulated ADP release; Fourniol & Moores, 2010) and a single residue is missing in the surface loop L10. There is a five-residue insertion in loop L6 of Kif15 which is believed to influence the nucleotide affinity (Kollmar & Glöckner, 2003). In Eg5, loop L5 is known to be important for inhibitor binding, and differences in the length of this motif in Kif15 (in Kif15 this loop is shorter) explain why Eg5-targeting inhibi-

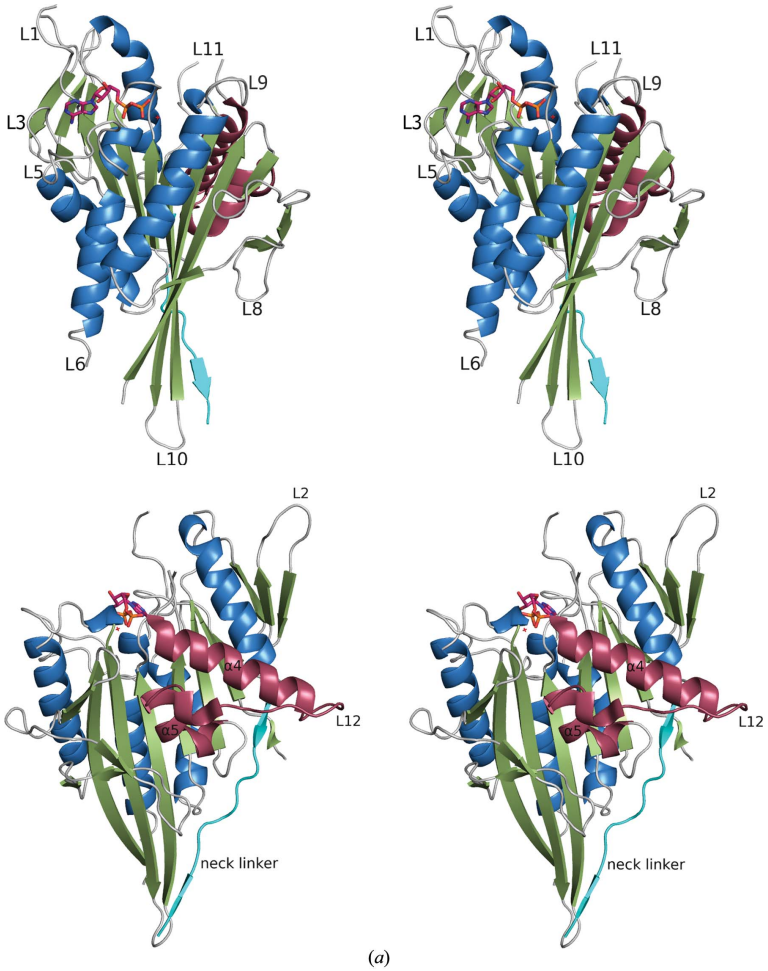

(*a*)

Figure 2
Overall structure of the binary $Kif15_{19–375}$–Mg^{2+}-ADP complex and comparison of the sequence/secondary structure of the Kif15 and Eg5 motor domains. (*a*) Stereo plots of the front and back view of the human Kif15 motor domain. α-Helices are coloured blue, β-strands green and loops/turns grey. The switch II cluster (α4–L12–α5) is highlighted in claret and the neck linker following the C-terminal helix α6 is shown in cyan. Mg^{2+}-ADP is shown as a ball-and-stick model.

tors do not inhibit Kif15 (Liu *et al.*, 2010). In addition, several other key residues involved in inhibitor binding in Eg5, such as Glu116, Arg119, Trp127 and Ala216, are not present in Kif15. Loop L11 is not visible in any of the three molecules in the asymmetric unit.

3.3. Steady-state ATPase activity

We subsequently measured the kinetic parameters for $Kif15_{19–375}$ and $Kif15_{1–375}$ (Fig. 3 and Table 2). To determine the optimal salt concentration, the rates of basal ATPase activity were measured on varying the NaCl concentration from 0 to 275 m*M*. The highest basal activity was measured at 75 m*M* NaCl for $Kif15_{19–375}$ and at 50 m*M* for $Kif15_{1–375}$ (Fig. 3*a*). The differences in activity were rather minor and only decreased slowly at higher salt concentrations. The basal ATPase activity was measured using ATP concentrations from 0 to 2 m*M*. The k_{cat} for the basal ATPase activity of $Kif15_{19–375}$ was 0.054 ± 0.001 s^{-1}, with a $K_{m,ATP}$ of 40.5 ± 5.4 µ*M* (Fig. 3*b*, red data points). The k_{cat} for the basal ATPase activity of $Kif15_{1–375}$ was 0.028 ± 0.0004 s^{-1}, about twofold lower, with a $K_{m,ATP}$ of 23.0 ± 1.9 µ*M* (Fig. 3*b*, blue data points), an almost twofold difference but still similar to the construct without the cover strand. Subsequently, the salt dependence of the MT-stimulated ATPase activity of $Kif15_{19–375}$ and $Kif15_{1–375}$ was determined by measuring the rates at MT concentrations from 0 to 10 µ*M* in the presence of 0, 50, 100 or 150 m*M* KCl for $Kif15_{19–375}$ and of 0 or 50 m*M* KCl for $Kif15_{1–375}$. With increasing salt concentrations the MT-stimulated ATPase activity for both Kif15 constructs decreased significantly (Fig. 3*c*). The k_{cat} for the MT-stimulated ATPase activity was 2.3 ± 0.1 s^{-1} with a $K_{0.5,MT}$ of 1.1 ± 0.1 µ*M* for $Kif15_{19–375}$, and k_{cat} was 2.1 ± 0.1 s^{-1} with a $K_{0.5,MT}$ of 3.1 ± 0.3 µ*M* for $Kif15_{1–375}$, indicating that there are no differences in the k_{cat} values between these two Kif15 constructs. Finally, the MT-stimulated ATPase activity in the presence of increasing ATP concentrations (from 0 to 2 m*M*) was determined (Fig. 3*d*). The $K_{m,ATP}$ values were 33 ± 3 µ*M* for $Kif15_{19–375}$ and 109 ± 20 µ*M* for $Kif15_{1–375}$. With the exception of a threefold difference in the $K_{0.5,MT}$ and $K_{m,ATP}$ values there was no significant difference between these two constructs, indicating that the presence or absence of the cover strand does not significantly change the ATPase characteristics.

Table 2
Kinetic parameters determined for $Kif15_{19–375}$ and $Kif15_{1–375}$.

	Basal ATPase activity		MT-stimulated ATPase activity		
	k_{cat} (s^{-1})	$K_{m,ATP}$ (µ*M*)	k_{cat} (s^{-1}) ([KCl], m*M*)	$K_{0.5,MT}$ (µ*M*)	$K_{m,ATP}$ (µ*M*)
$Kif15_{19–375}$	0.054 ± 0.001	40.5 ± 5.4	2.3 ± 0.1 (0) 0.5 ± 0.1 (50) 0.5 ± 0.1 (100) 0.4 ± 0.1 (150)	1.1 ± 0.1	33 ± 3
$Kif15_{1–375}$	0.028 ± 0.0004	23.0 ± 1.9	2.1 ± 0.1 (0) 0.05 ± 0.01 (50)	3.1 ± 0.3	109 ± 20

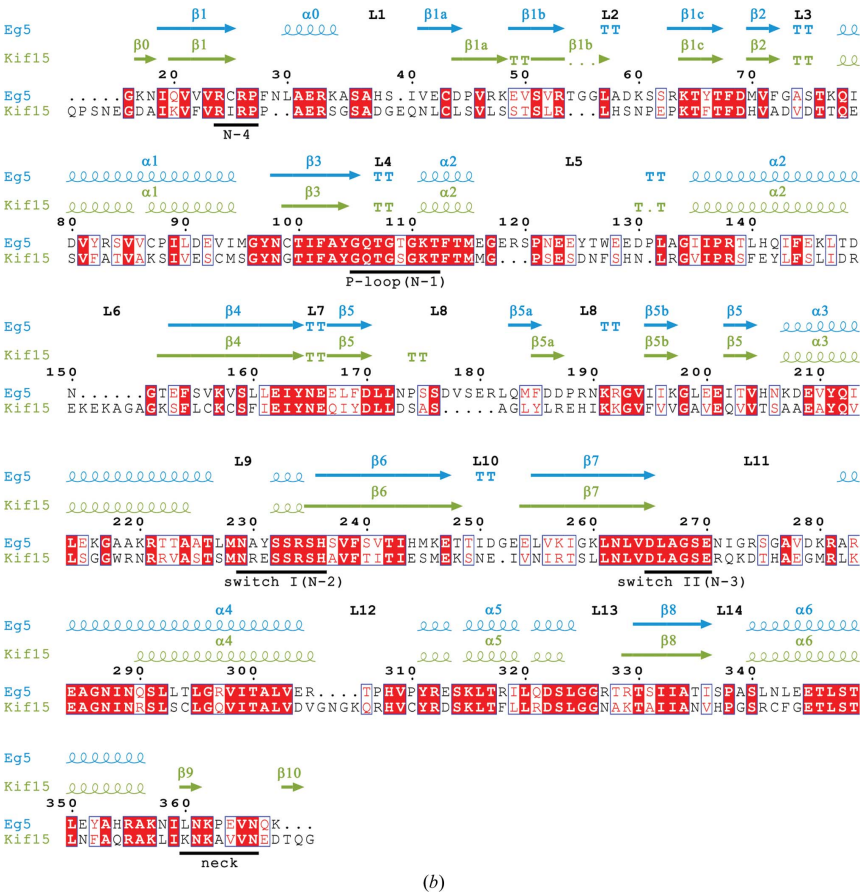

(*b*)

Figure 2 (continued)
(*b*) Structural and sequence alignment of the Eg5 (PDB entry 3hqd; Parke *et al.*, 2009) and Kif15 motor domains. Residue 16 of Eg5 is aligned with residue 24 of Kif15. Identical residues are coloured white on a red background and similar residues are shaded in red. The position of the ATP-binding pocket (N1–N4), the switch I and II regions and the position of the neck-linker regions are underlined in black.

3.4. Transient-state ATPase activity

Mant-ATP is a fluorescent analogue of ATP that for some

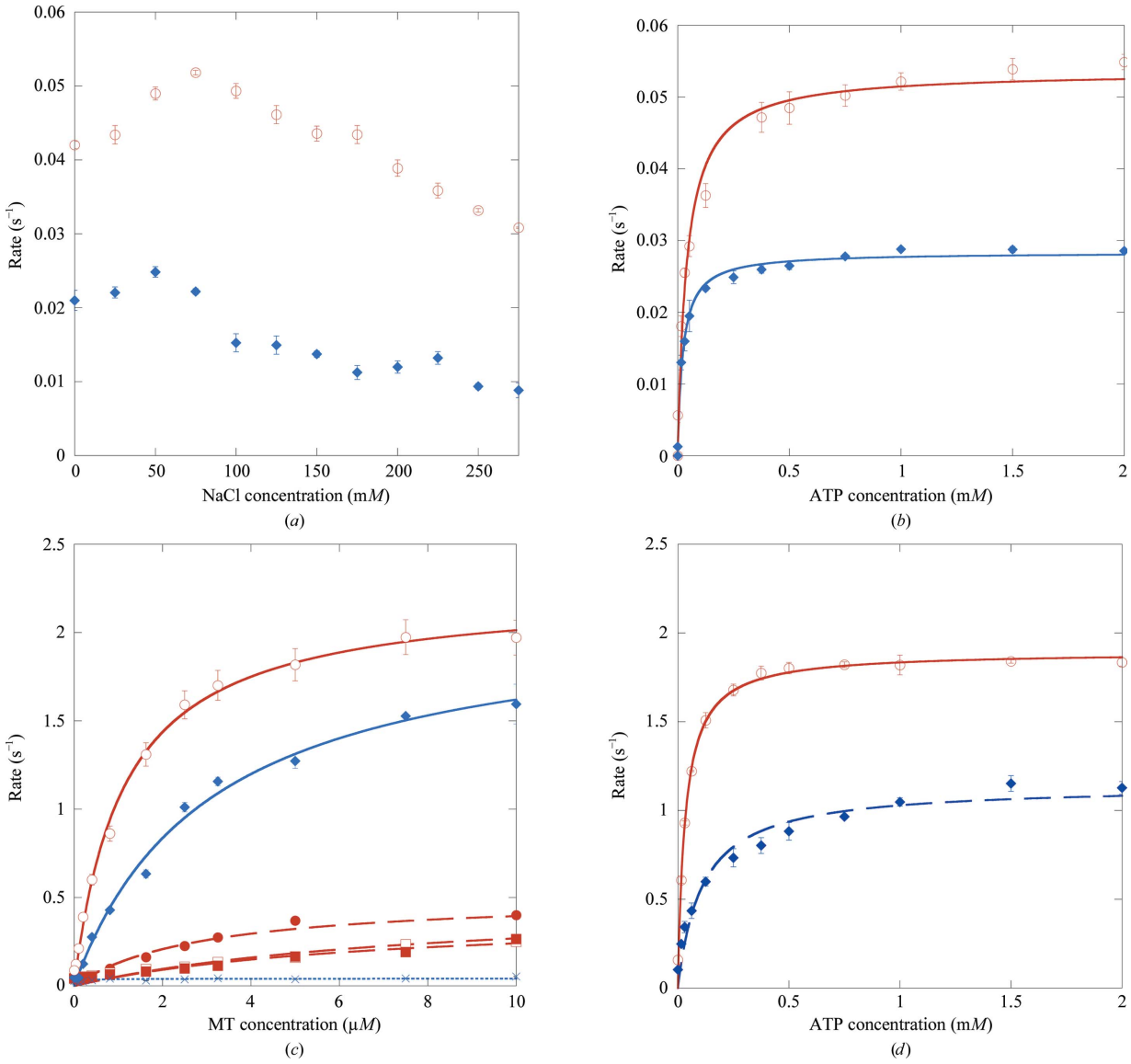

Figure 3
Characterization of the basal and MT-stimulated ATPase activities of Kif15$_{19–375}$ and Kif15$_{1–375}$. (*a*) Influence of the NaCl concentration on the basal ATPase activity of Kif15$_{19–375}$ (red) and Kif15$_{1–375}$ (blue) in the presence of 1 m*M* ATP. (*b*) Optimization of the basal ATPase activity in the presence of increasing ATP concentrations measured at 75 m*M* NaCl for Kif15$_{19–375}$ (red) and 50 m*M* NaCl for Kif15$_{1–375}$ (blue). (*c*) Salt dependence of the MT-stimulated Kif15$_{19–375}$ ATPase activity (red) in the absence (circles) and in the presence of 50 m*M* (filled circles), 100 m*M* (squares) and 150 m*M* (filled squares) KCl and salt dependence of the MT-stimulated Kif15$_{1–375}$ ATPase activity (blue) in the absence (filled diamonds) and the presence (squares) of 50 m*M* KCl. Data were measured at increasing MT concentrations ranging from 0 to 10 μ*M* in the presence of 1 m*M* ATP. (*d*) Optimization of the ATP concentration for the MT-stimulated ATPase activity of Kif15$_{19–375}$ (red) and Kif15$_{1–375}$ (blue) in the presence of increasing ATP concentrations, measured at 3 μ*M* MTs, in the absence of salt.

kinesins gives a fluorescent enhancement on binding at the motor active site. Initial slow transient-state turnover assays of Mant-ATP were performed by making manual additions to a fluorimeter cuvette (Supplementary Fig. S1*a*[1]). As can be seen in our crystal structure, Kif15, like other kinesins, purifies with Mg^{2+}-ADP in its active site (Fig. 2*a*). Addition of an excess of Mg^{2+}-Mant-ATP initiates replacement of this active-site Mg^{2+}-ADP with Mant-ADP at a rate limited by the basal rate constant of Mg^{2+}-ADP release from the Kif15 motor domain. We estimate this rate constant to be 0.017 s^{-1}. Once a plateau of enhanced fluorescence is reached, addition of a ‘chase’ of

[1] Supporting information has been deposited in the IUCr electronic archive (Reference: DW5063).

nonfluorescent Mg^{2+}-ATP (Supplementary Fig. S1*a*) initiates the opposite reaction, in which active-site Mg^{2+}-Mant-ADP is replaced with chasing Mg^{2+}-ADP. At 0.005 s^{-1}, the rate constant for Mant-ADP release is approximately threefold slower than that for Mg^{2+}-ADP release, indicating that Mant-ADP binds slightly tighter than Mg^{2+}-ADP but is nonetheless a reasonably faithful surrogate and reporter for Mg^{2+}-ADP release. Preliminary stopped-flow assays were performed to examine the MT activation of Mant-ADP release (Supplementary Fig. S1*b*). Kif15 was pre-incubated on ice to load the active site with Mant-ATP. The complex was then rapidly warmed to 25°C, loaded into the stopped flow and rapidly mixed with various concentrations of MTs in the presence of an excess of unlabelled chasing MgATP. The stopped-flow data are preliminary, but nonetheless show that MTs activate MgADP release from Kif15 motor domains ∼1000-fold. The

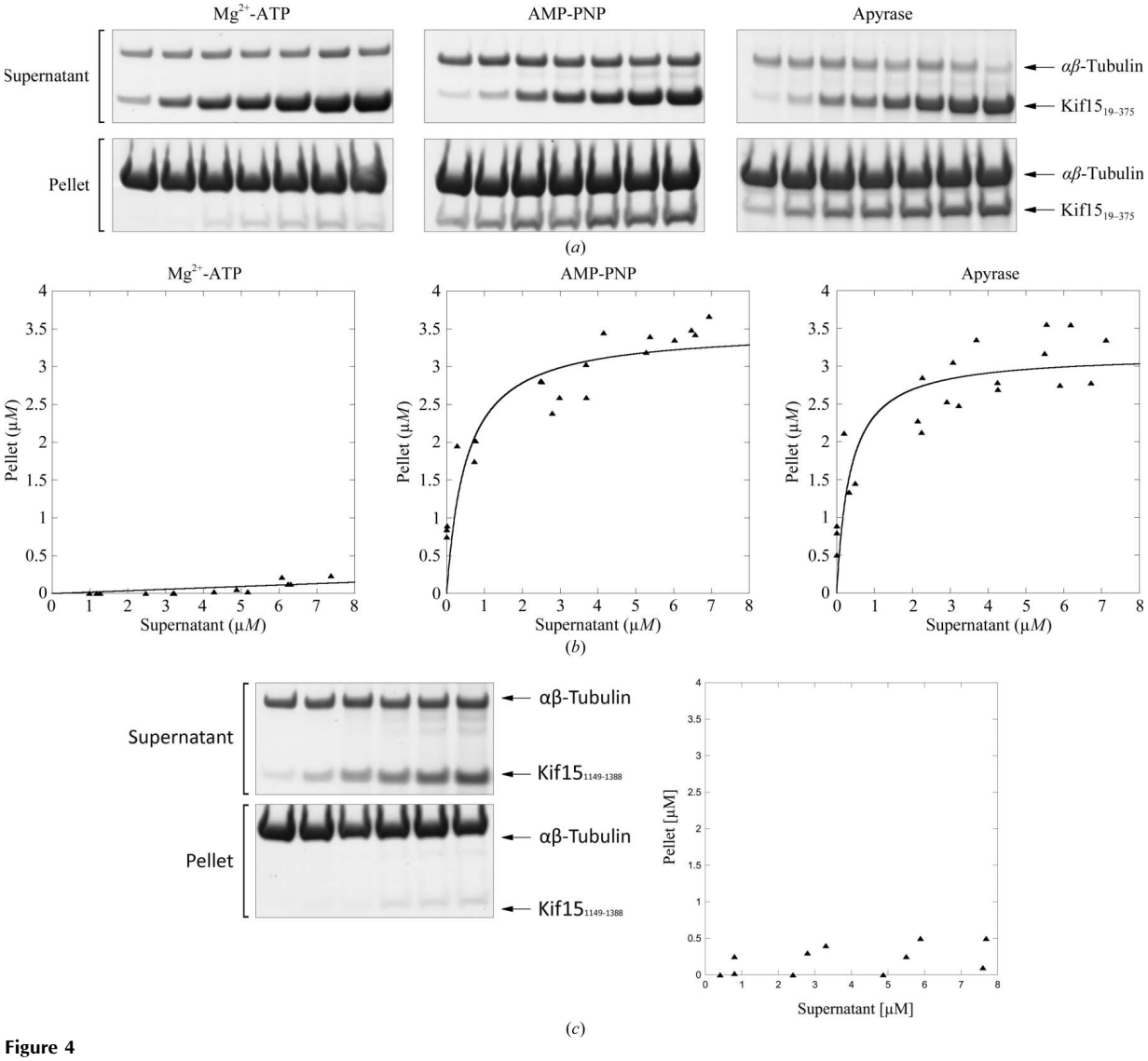

Figure 4
MT pelleting assays in the presence of Kif15 motor or tail domains. (*a*) MT pelleting assays of the Kif15 motor domain in the presence of various nucleotides. Increasing amounts of $Kif15_{19–375}$ (1–12 μ*M*) were incubated with MTs (5 μ*M*) in the presence of 2 m*M* Mg^{2+}-ATP, 2 m*M* AMP-PNP or 4 mU apyrase. Samples of supernatants and pellets were analysed by SDS–PAGE. (*b*) MT binding of $Kif15_{19–375}$ in the presence of 2 m*M* Mg^{2+}-ATP, 2 m*M* AMP-PNP or 4 mU apyrase. The plotted data relate to the amounts (μ*M*) of $Kif15_{19–375}$ recovered from supernatant and pellet (pelleted with MTs) fractions of reactions run in the presence of various nucleotides. Data were obtained by analysing the SDS–PAGE (*ImageJ* 143.u) presented in (*a*). (*c*) MT pelleting assays of the Kif15 tail domain. Increasing amounts of $Kif15_{1149–1388}$ (1–10 μ*M*) were incubated with MTs (5 μ*M*). Samples of supernatants and pellets were analysed by SDS–PAGE. The plotted data relate to the amounts (μ*M*) of $Kif15_{1149–1388}$ recovered from supernatant and pellet (pelleted with MTs) fractions. Data were obtained by analysing the SDS–PAGE (*ImageJ* 143.u) presented on the left side of the figure.

Table 3
Binding of the Kif15 motor domain to MTs in two different nucleotide states.

Dissociation constants (K_d) and the stoichiometry of binding of $Kif15_{19–375}$ to MTs measured in the presence of 20 m*M* NaCl. Values for Mg^{2+}-ATP were not determined.

	AMP-PNP	Apyrase
K_d (μ*M*)	0.5 ± 0.2	0.4 ± 0.2
Stoichiometry	1:1.1	1:1.3

apparent affinity for MTs in the presence of ATP was consistent with steady-state assays (Fig. 3*c*) and MT pull-down experiments (Figs. 4*a* and 4*b*).

Comparison of the steady-state ATPase kinetic parameters of Eg5 and Kif15 show that they exhibit optimal *in vitro* activity at higher salt concentrations (Eg5, 150 m*M*; Kif15, 50–75 m*M*). The two motors have similar K_m and k_{cat} values for their basal activity, but the MT-activated ATPase activity is higher in the case of Eg5 than of Kif15. The affinities of the motor domains for MTs vary similarly according to the type of bound nucleotide (Lockhart & Cross, 1996), but steady-state, transient-state and direct binding measurements all indicate that the $K_{0.5,MT}$ is considerably higher in the case of Kif15.

3.5. Kif15 contains a nucleotide-dependent MT-binding site in its motor domain, but not in its tail domain

We then determined the affinity of $Kif15_{19–375}$ for MTs in the presence of Mg^{2+}-ATP, AMP-PNP and apyrase (thus establishing the 'nucleotide-free' state) using the MT pelleting assay. The results for the Kif15 motor domain are shown in Fig. 4 and the K_d values as well as the stoichiometry of the Kif15–MT complex are summarized in Table 3. In the presence of the slowly hydrolysable ATP analogue AMP-PNP or apyrase, $Kif15_{19–375}$ shows comparable affinities for MTs, with K_d values of 0.5 ± 0.2 and 0.4 ± 0.2 μ*M*, respectively, and a stoichiometry close to one (1.1 and 1.3, respectively), indicating that one Kif15 motor domain binds to one $\alpha\beta$-tubulin heterodimer, in agreement with the results reported for other kinesins. Under the conditions tested the Kif15 motor domain shows no affinity for MTs in the presence of Mg^{2+}-ATP (in the presence of MTs ATP is rapidly hydrolysed to ADP, which is known to possess low affinity for MTs). In conclusion, human Kif15 contains a nucleotide-dependent MT-binding region in its motor domain.

We then investigated whether or not Kif15 contains a nucleotide-independent MT-binding region in its tail domain (Fig. 4*c*). A second MT-binding site has been identified in a variety of kinesin tail domains (Liao *et al.*, 1994; Germani *et al.*, 2000; Kuriyama *et al.*, 1994; Echard *et al.*, 1998; Chandra *et al.*, 1993; Karabay & Walker, 1999; Meluh & Rose, 1990; Narasimhulu & Reddy, 1998; Jiang *et al.*, 2007) and has been shown in some cases to be physiologically important for their biological functions. In our hands $Kif15_{1149–1388}$ does not bind to MTs in pelleting assays, indicating that the tail does not contain an MT-binding side. This in contrast to human Eg5, which has recently been shown to contain a nucleotide-independent MT-binding region in its tail which is implicated in MT cross-linking and sliding (Weinger *et al.*, 2011).

3.6. Functional comparison of Kif15 and Eg5 in a non-mitosis scenario

Given that the mitotic spindle is a rather unique MT apparatus, we wished to investigate whether these two different motors could accomplish similar functions in a non-mitosis scenario. It has previously been reported that Eg5 as well as Kif15 are both enriched in the populations of neurons undergoing migration in the developing brain (Ferhat, Kuriyama *et al.*, 1998; Buster *et al.*, 2003). A role for Eg5 in

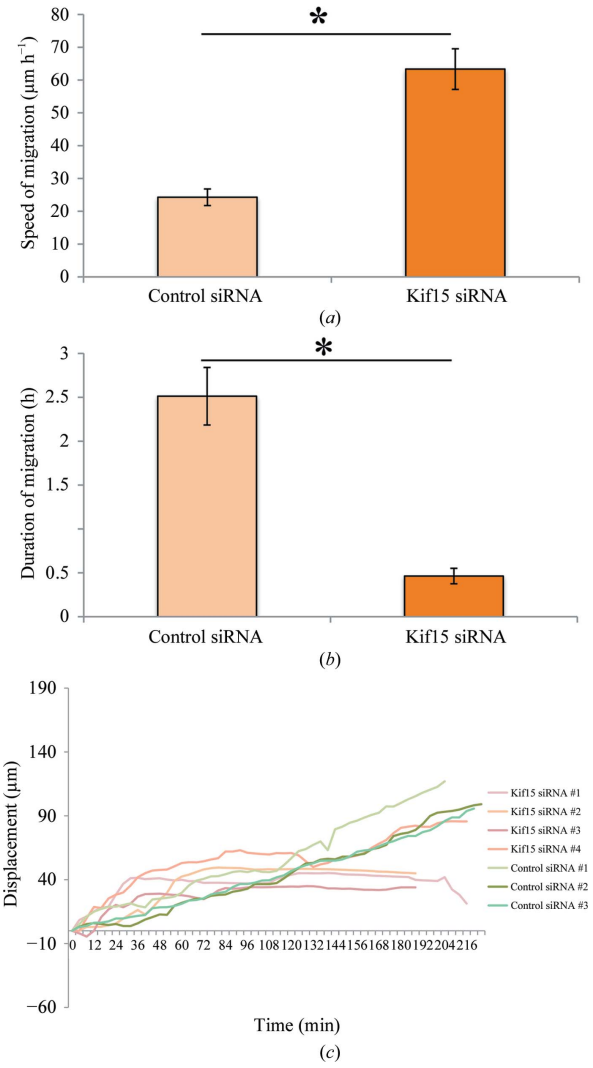

Figure 5
Depletion of Kif15 results in faster moving migratory neurons, which migrate less consistently. (*a*) Quantification of average speed of migration for control siRNA and Kif15 siRNA-treated cells (n = 11 and n = 12 cells, respectively). (*b*) Quantification of the time period for control siRNA and Kif15 siRNA-treated neurons, during which they exhibited consistent forward movement. (*c*) Tracing of movements of individual cell bodies.

regulating neuronal migration has already been documented such that depletion of Eg5 results in neurons that migrate faster (Falnikar *et al.*, 2011). Here, we tested whether Kif15 plays a similar role by depleting it from migrating cerebellar granule neurons using siRNA followed by time-lapse imaging. We found that neurons depleted of Kif15 typically migrated faster but less consistently, such that after a period of vigorous forward movement a cell either remained stationary or underwent a temporary stationary phase before restarting the next phase of forward movement. Quantification showed that the average displacement exhibited by neurons transfected with control siRNA was 24.3 $\pm$ 2.5 µm h^{-1}, whereas that for neurons transfected with Kif15 siRNA was 63.3 $\pm$ 6.1 µm h^{-1} ($p < 0.0001$; see Fig. 5*a*). The average time period during which neurons exhibited consistent forward movement was 2.5 $\pm$ 0.32 h for the control siRNA group, whereas that for the Kif15 siRNA group was 0.46 $\pm$ 0.09 h ($p < 0.0001$; see Fig. 5*b*). This phenotype differs from the Eg5-depletion phenotype in terms of the consistency of migration. For tracings of the movements of individual cell bodies, see Fig. 5(*c*). These observations are reminiscent of previous studies on axonal growth and guidance, in which depleting each of the two motors produced similar but not identical phenotypes (Liu *et al.*, 2010).

3.7. Kif15 and Eg5 in mitosis

The role of Kif15 during bipolar spindle formation in early prometaphase reveals that it may – under certain conditions – be a functional homologue of Eg5. Although their mechanism of action is clearly different (Fig. 6), both proteins are able to work redundantly to fulfill their similar roles. Homotetrameric Eg5 performs its function because of its unique quaternary structure that allows it to cross-link antiparallel MTs and, with its plus-ended directed motility, to slide them apart to form the bipolar spindle. It has recently been suggested that the mechanistics of Eg5 function are even more complex, with additional MT binding sites located in the tail domains (Weinger *et al.*, 2011). In contrast, Kif15 works as a dimer (Wittmann *et al.*, 1998) by crosslinking parallel kinetochore-MTs (Sturgill & Ohi, 2013) and we demonstrated that it does not contain an MT-binding site within its tail domain. The function of the MT linker is most likely carried out by TPX2 through the C-terminal leucine-zipper region of Kif15 (Wittmann *et al.*, 2000). Owing to their similar functions, Kif15 may be able to take over the role of Eg5 following anti-Eg5 chemotherapy by simply up-regulating protein-expression levels, at least in cell culture (Tanenbaum *et al.*, 2009). Such an interchange ability of the two motors, albeit not perfect, is supported by our observations on neurons, which are non-mitotic, suggesting a broadly applicable theme by which two structurally different motors can be made to work in very similar ways. If the scenario of a possible resistance mechanism were true for certain tumours, co-inhibition of both of motors, Eg5 and Kif15, could be a vital therapeutic approach.

This paper reports the crystal structure of human Kif15, which will be a valuable asset for structure-guided design. The comparison of both motors revealed that despite overall functional similarity, Kif15 and Eg5 have important differences, allowing Kif15 to be impervious to Eg5-targeting drugs.

We are grateful to Tobias Klar of the ESRF for assistance and support in using beamline ID29. This publication contains part of the doctoral thesis of MK. We thank Cancer Research UK (MK, VU and FK) and the NIH, USA (AF and PWB) for financial support.

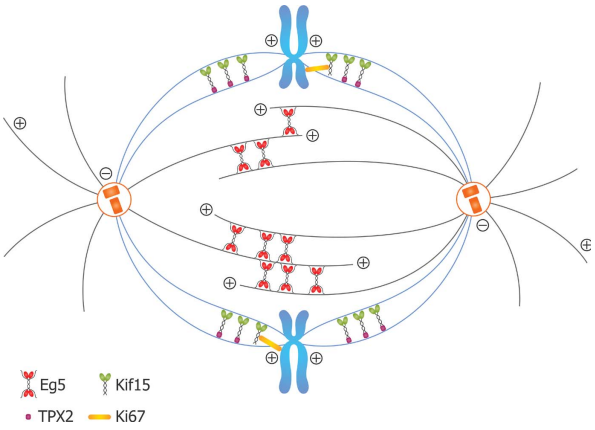

Figure 6
Comparison of current models for Eg5 and Kif15 MT crosslinking and function. Under physiological conditions homotetrameric Eg5 (blue) interacts with antiparallel MTs through two distinct binding sites in its motor and tail domains (two in the motor and two in the tail for each MT it crosslinks), and slides them apart (Weinger *et al.*, 2011). Dimeric Kif15 (green) works predominantly on K-fibres (Sturgill &Ki-67 and the Kif15–TPX2 complex is unknown.

References

Adams, P. D. *et al.* (2010). *Acta Cryst.* D**66**, 213–221.
Bix, G. J. & Clark, G. D. (1998). *J. Neurosci.* **18**, 307–318.
Blangy, A., Lane, H. A., d'Hérin, P., Harper, M., Kress, M. & Nigg, E. A. (1995). *Cell*, **83**, 1159–1169.
Boleti, H., Karsenti, E. & Vernos, I. (1996). *Cell*, **84**, 49–59.
Buster, D. W., Baird, D. H., Yu, W., Solowska, J. M., Chauvière, M., Mazurek, A., Kress, M. & Baas, P. W. (2003). *J. Neurocytol.* **32**, 79–96.
Castoldi, M. & Popov, A. V. (2003). *Protein Expr. Purif.* **32**, 83–88.
Chandra, R., Endow, S. A. & Salmon, E. D. (1993). *J. Cell Sci.* **104**, 899–906.
Echard, A., Jollivet, F., Martinez, O., Lacapère, J.-J., Rousselet, A., Janoueix-Lerosey, I. & Goud, B. (1998). *Science*, **279**, 580–585.
Emsley, P. & Cowtan, K. (2004). *Acta Cryst.* D**60**, 2126–2132.
Falnikar, A., Tole, S. & Baas, P. W. (2011). *Mol. Biol. Cell*, **22**, 1561–1574.
Ferhat, L., Cook, C., Chauviere, M., Harper, M., Kress, M., Lyons, G. E. & Baas, P. W. (1998). *J. Neurosci.* **18**, 7822–7835.
Ferhat, L., Kuriyama, R., Lyons, G. E., Micales, B. & Baas, P. W. (1998). *Eur. J. Neurosci.* **10**, 1383–1393.
Fourniol, F. & Moores, C. A. (2010). *Proc. Natl Acad. Sci. USA*, **107**, 3949–3950.
Ganem, N. J. & Compton, D. A. (2004). *J. Cell Biol.* **166**, 473–478.
Garcia-Saez, I., Yen, T., Wade, R. H. & Kozielski, F. (2004). *J. Mol. Biol.* **340**, 1107–1116.

Germani, A., Bruzzoni-Giovanelli, H., Fellous, A., Gisselbrecht, S., Varin-Blank, N. & Calvo, F. (2000). *Oncogene*, **19**, 5997–6006.
Hackney, D. D. & Jiang, W. (2001). *Methods Mol. Biol.* **164**, 65–71.
Hirokawa, N., Noda, Y., Tanaka, Y. & Niwa, S. (2009). *Nature Rev. Mol. Cell Biol.* **10**, 682–696.
Hirotsune, S., Fleck, M. W., Gambello, M. J., Bix, G. J., Chen, A., Clark, G. D., Ledbetter, D. H., McBain, C. J. & Wynshaw-Boris, A. (1998). *Nature Genet.* **19**, 333–339.
Huszar, D., Theoclitou, M. E., Skolnik, J. & Herbst, R. (2009). *Cancer Metastasis Rev.* **28**, 197–208.
Hwang, W., Lang, M. J. & Karplus, M. (2008). *Structure*, **16**, 62–71.
Jiang, S., Li, M., Xu, T., Ren, D. & Liu, G. (2007). *J. Biochem. Mol. Biol.* **40**, 44–52.
Karabay, A. & Walker, R. A. (1999). *Biochemistry*, **38**, 1838–1849.
Khalil, A. S., Appleyard, D. C., Labno, A. K., Georges, A., Karplus, M., Belcher, A. M., Hwang, W. & Lang, M. J. (2008). *Proc. Natl Acad. Sci. USA*, **105**, 19247–19252.
Kollmar, M. & Glöckner, G. (2003). *BMC Genomics*, **4**, 47.
Kuriyama, R., Dragas-Granoic, S., Maekawa, T., Vassilev, A., Khodjakov, A. & Kobayashi, H. (1994). *J. Cell Sci.* **107**, 3485–3499.
Liao, H., Li, G. & Yen, T. J. (1994). *Science*, **265**, 394–398.
Liu, M., Nadar, V. C., Kozielski, F., Kozlowska, M., Yu, W. & Baas, P. W. (2010). *J. Neurosci.* **30**, 14896–14906.
Lockhart, A. & Cross, R. A. (1996). *Biochemistry*, **35**, 2365–2373.
Mazumdar, M., Sundareshan, S. & Misteli, T. (2004). *J. Cell Biol.* **166**, 613–620.
McDonald, A., Bergnes, G. & Morgans, D. J. Jr (2004). US Patent WO2004026226.
Meluh, P. B. & Rose, M. D. (1990). *Cell*, **60**, 1029–1041.
Murshudov, G. N., Skubák, P., Lebedev, A. A., Pannu, N. S., Steiner, R. A., Nicholls, R. A., Winn, M. D., Long, F. & Vagin, A. A. (2011). *Acta Cryst.* D**67**, 355–367.
Narasimhulu, S. B. & Reddy, A. S. (1998). *Plant Cell*, **10**, 957–965.
Parke, C. L., Wojcik, E. J., Kim, S. & Worthylake, D. K. (2009). *J. Biol. Chem.* **285**, 5859–5867.
Rath, O. & Kozielski, F. (2012). *Nature Rev. Cancer*, **12**, 527–539.
Rogers, G. C., Chui, K. K., Lee, E. W., Wedaman, K. P., Sharp, D. J., Holland, G., Morris, R. L. & Scholey, J. M. (2000). *J. Cell Biol.* **150**, 499–512.
Segbert, C., Barkus, R., Powers, J., Strome, S., Saxton, W. M. & Bossinger, O. (2003). *Mol. Biol. Cell*, **14**, 4458–4469.
Song, Y.-H., Marx, A., Müller, J., Woehlke, G., Schliwa, M., Krebs, A., Hoenger, A. & Mandelkow, E. (2001). *EMBO J.* **20**, 6213–6225.
Sturgill, E. G. & Ohi, R. (2013). *Curr. Biol.* **23**, 1280–1290.
Sueishi, M., Takagi, M. & Yoneda, Y. (2000). *J. Biol. Chem.* **275**, 28888–28892.
Tanenbaum, M. E., Macůrek, L., Janssen, A., Geers, E. F., Alvarez-Fernández, M. & Medema, R. H. (2009). *Curr. Biol.* **19**, 1703–1711.
Tanenbaum, M. E. & Medema, R. H. (2010). *Dev. Cell*, **19**, 797–806.
Turner, J., Anderson, R., Guo, J., Beraud, C., Fletterick, R. & Sakowicz, R. (2001). *J. Biol. Chem.* **276**, 25496–25502.
Vagin, A. & Teplyakov, A. (2010). *Acta Cryst.* D**66**, 22–25.
Vaisberg, E. A., Koonce, M. P. & McIntosh, J. R. (1993). *J. Cell Biol.* **123**, 849–858.
Vanneste, D., Takagi, M., Imamoto, N. & Vernos, I. (2009). *Curr. Biol.* **19**, 1712–1717.
Weinger, J. S., Qiu, M., Yang, G. & Kapoor, T. M. (2011). *Curr. Biol.* **21**, 154–160.
Wilkins, M. R., Gasteiger, E., Bairoch, A., Sanchez, J. C., Williams, K. L., Appel, R. D. & Hochstrasser, D. F. (1999). *Methods Mol. Biol.* **112**, 531–552.
Wittmann, T., Boleti, H., Antony, C., Karsenti, E. & Vernos, I. (1998). *J. Cell Biol.* **143**, 673–685.
Wittmann, T., Wilm, M., Karsenti, E. & Vernos, I. (2000). *J. Cell Biol.* **149**, 1405–1418.
Wordeman, L. (2010). *Semin. Cell Dev. Biol.* **21**, 260–268.
Zhu, C. & Jiang, W. (2005). *Proc. Natl Acad. Sci. USA*, **102**, 343–348.
Zhu, C., Zhao, J., Bibikova, M., Leverson, J. D., Bossy-Wetzel, E., Fan, J.-B., Abraham, R. T. & Jiang, W. (2005). *Mol. Biol. Cell*, **16**, 3187–3199.

Acta Crystallographica Section D
Biological Crystallography
ISSN 0907-4449

Structural insights into human Kif7, a kinesin involved in Hedgehog signalling

Marta Klejnot* and Frank Kozielski*

The Beatson Institute for Cancer Research, Garscube Estate, Switchback Road, Glasgow G61 1BD, Scotland

Correspondence e-mail: m.klejnot@beatson.gla.ac.uk, f.kozielski@beatson.gla.ac.uk

Received 11 October 2011
Accepted 9 December 2011

PDB References: Kif7, native, 4a14; mutant, 2xt3.

Kif7, a member of the kinesin 4 superfamily, is implicated in a variety of diseases including Joubert, hydrolethalus and acrocallosal syndromes. It is also involved in primary cilium formation and the Hedgehog signalling pathway and may play a role in cancer. Its activity is crucial for embryonic development. Kif7 and Kif27, a closely related kinesin in the same subfamily, are orthologues of the *Drosophila melanogaster* kinesin-like protein Costal-2 (Cos2). In vertebrates, they work together to fulfil the role of the single Cos2 gene in *Drosophila*. Here, the high-resolution structure of the human Kif7 motor domain is reported and is compared with that of conventional kinesin, the founding member of the kinesin superfamily. These data are a first step towards structural characterization of a kinesin-4 family member and of this interesting molecular motor of medical significance.

1. Introduction

Members of the kinesin superfamily of motor proteins (Kifs) move unidirectionally along microtubules (MTs) in an ATP-dependent manner. They perform various functions and are best known for their role in neuronal transport (Hirokawa *et al.*, 2009) and mitosis/cytokinesis. Kinesins have been implicated in a range of diseases, usually related to their role in cellular transport, transport of pathogens and cell division (Mandelkow & Mandelkow, 2001).

Human Kif7 and Kif27, which are members of the kinesin-4 family (Katoh & Katoh, 2004*a*,*b*), are paralogues. They share 44% sequence identity overall and have even higher identity in the motor domain (61%). They possess an N-terminal globular motor domain that contains nucleotide-binding and MT-interacting regions, followed by a stalk domain predicted to form a discontinuous coiled coil and a globular C-terminal tail domain (Fig. 1).

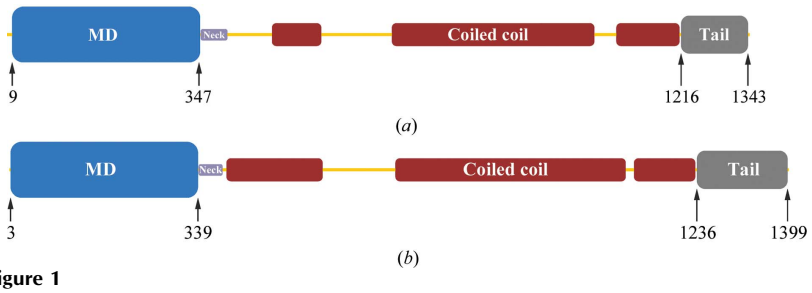

Figure 1
Bar diagrams of the human kinesin-4 family members (*a*) Kif7 and (*b*) Kif27. The globular motor domain (MD, blue) is followed by the short neck linker (Neck, violet), a stalk predicted to form a discontinuous coiled-coil region (red) and a C-terminal tail domain (grey).

Both proteins are orthologues of the *Drosophila melanogaster* kinesin-like protein called Costal-2 (Cos2) that plays a key role in Hedgehog (Hh) signalling. The Hedgehog ligands [Sonic hedgehog (SHh), Indian hedgehog (IHh) and Desert hedgehog (DHh)] are glycoproteins that play a crucial role during embryogenesis (Bijlsma *et al.*, 2004) and tumourigenesis (Magliano & Hebrok, 2003). Their signals are transduced through the transmembrane proteins Patched 1 (Ptch 1), Patched 2 (Ptch 2) and Smoothened (Smo). In the absence of Hh proteins, Ptch-family members suppress Smo activity, which becomes activated upon Hh ligand binding to the Ptch proteins. These events lead to the activation of the transcription factors Gli 1, Gli 2 and Gli 3. Direct interaction of the MT-bound protein Cos2 with Cubitus interruptus (Ci) in the cytoplasm is believed to be essential for its sequential phosphorylation by three distinct kinases, PKA, GSKβ and CK1, and subsequent proteosome-dependent cleavage. The generated fragment, CiR, diffuses into the nucleus, where it co-represses Hh target genes (Tay *et al.*, 2004; Wang *et al.*, 2000). Human Kif7 and Kif27, which are putative ciliary motors with roles in the primary cilia, a sensory organelle (Verhey *et al.*, 2011), have been shown to interact with Gli transcription factors and are believed to fulfil distinct functions in regulating Gli proteins. Kif7, a critical regulator of mammalian Hh signalling, acts as both a positive and negative regulator in the Hh signalling pathway but performs this role differently from Cos2 in that it does not interact with Smo or Fu (Endoh-Yamagami *et al.*, 2009). The current hypothesis suggests that Kif7, as a plus-end-directed motor, transports Gli 2 away from the cilium, thus preventing its activation (Goetz & Anderson, 2010). In contrast, Kif27 interacts with Fu, which takes part in the construction of the primary cilium (Wilson *et al.*, 2009). Kif7 and Kif27 seem to work together in vertebrates to fulfil the role of the single Cos2 gene in *D. melanogaster*.

There are several reports describing Kif7 mutant alleles in mouse embryos and their characterization has shown the critical role of Kif7 in primary cilia formation and Hh signalling (Karel *et al.*, 2009; Cheung *et al.*, 2009; Endoh-Yamagami *et al.*, 2009). One of these alleles carried a $Kif7_{L130P}$ mutation and caused death of mouse embryos at the end of gestation.

In humans, various Kif7 mutations have been linked to a range of neurodegenerative diseases, including Joubert (Dafinger *et al.*, 2011), hydrolethalus and acrocallosal syndromes (Putoux *et al.*, 2011). In addition, since inappropriate activation of Hh signalling can lead to the formation of medulloblastomas, rhabdomyosarcomas, basal carcinomas and other tumour types (Goetz & Anderson, 2010) and given the role of Kif7 in human primary cilia formation and Hh signalling (Karel *et al.*, 2009), Kif7 might also be linked to other diseases such as cancer.

In our effort to characterize human kinesins of medical interest, we report here the crystal structure of the human Kif7 motor domain to 1.6 Å resolution. We compare this crystal structure with that of the founding member of the kinesin superfamily, conventional kinesin (kinesin-1 family). This is the first step towards the structural characterization of a kinesin-4 family member.

2. Materials and methods

2.1. Cloning, protein expression and purification

Codon-optimized cDNAs for $Kif7_{8–361}$ and $Kif27_{1–341}$ were purchased from GenScript and cloned into a modified pET-M20 *Escherichia coli* expression vector carrying an N-terminal Trx-fusion protein, a His tag and a TEV (tobacco etch virus) cleavage site. The sequences were verified by DNA sequencing. Subsequently, we cloned shorter constructs using the following forward and reverse primers: $Kif7_{8–347}$, 5′-CGT GCC CAG *TAA** ATC CGC AAC CGC GCC AC-3′; $Kif27_{1–339}$, 5′-GCG AAC CGC GCG CGT *TAG** ATT CTC GAG TAA TCG-3′; $Kif27_{6–341}$, 5′-CT ATG GAA GCC ATG GCG GTG AAA GTT GCG-3′, 5′-GT GGT GCT CGA TTA CTC GAG AAT GTT ACG C-3′; $Kif27_{17–341}$, 5′-GT ATT CGT CCC ATG GTG TGC AAA GAA GCG-3′, 5′-GT GGT GCT CGA TTA CTC GAG AAT GTT ACG C-3′. The Kif7 single point mutation ($Kif7_{8–347}$L130P) was cloned employing the QuikChange Kit (Roche) with the following mutagenesis primer: 5′-C GAA GCC TTC AAA *CCG* ATC GAT GAA AAC GAC C-3′. All proteins were expressed in *E. coli* BL21 (DE3) pLysS expression cells (Novagen). Bacteria were grown in Terrific Broth (TB) medium (Sigma) at 310 K to an A_{600} of 0.7 and were subsequently induced with 0.5 m*M* isopropyl β-D-1-thiogalactopyranoside (IPTG; Sigma) at a temperature of 291 K. Overnight cultures were centrifuged (20 min, 277 K, 3300*g*) and resuspended in lysis buffer. Cells were lysed by sonication (eight cycles of 8 s on/off as 20 ml lysate fractions) and centrifuged (1 h, 277 K, 31 400*g*). Supernatants were pooled and the proteins were purified by affinity chromatography [1 ml HisTrap FF (GE Healthcare); buffer *A*, 50 m*M* piperazine-*N*,*N*′-bis(2-ethanesulfonic acid) (PIPES) pH 7.0, 250 m*M* NaCl, 2 m*M* $MgCl_2$, 40 m*M* imidazole (Sigma); buffer *B*, 50 m*M* PIPES pH 7.0, 250 m*M* NaCl, 2 m*M* $MgCl_2$, 500 m*M* imidazole], followed by overnight cleavage with TEV protease (0.05 mg TEV per milligram of protein). Prior to TEV cleavage, the buffer was exchanged to eliminate imidazole from the protein solution (HiPrep 26/10, GE Healthcare; 50 m*M* PIPES pH 7.0, 250 m*M* NaCl, 2 m*M* $MgCl_2$). Subsequently, His-tagged Trx and TEV were removed by a second run on a His-trap affinity column. The final step of purification consisted of gel filtration (Superose S75; GE Healthcare) in gel-filtration buffer [50 m*M* PIPES pH 7.0, 250 m*M* NaCl, 2 m*M* $MgCl_2$, 1 m*M* dithiothreitol (DTT; Sigma)].

2.2. Crystallization

All Kif7 and Kif27 constructs described above were used for crystallization trials at 10 mg ml^{-1} at 277 and 292 K in the presence and absence of 1 m*M* Mg^{2+}ATP. The crystallization screens used were ComPAS, JCSG+, PACT (all from Qiagen), Ammonium Sulfate Grid Screen, Sodium Malonate Grid Screen, MPD Grid Screen, Crystal Screen HT, Crystal Screen Lite, PEG/Ion, PEG 6000 and PEG LiCl (all from Hampton Research). $Kif7_{8–347}$ crystals grew in 20%(*w*/*v*) PEG 3350 in the presence of various salts (0.1 *M* magnesium formate dihydrate, 0.2 *M* lithium acetate, 0.2 *M* potassium sodium tartrate tetrahydrate, 0.1 *M* sodium acetate, 0.2 *M* ammonium

nitrate, 0.2 *M* sodium nitrate). However, the best crystals were obtained in the presence of lithium acetate. All other protein constructs did not yield crystals under the conditions tested.

2.3. Analytical gel filtration

Analytical gel filtration was performed to determine the oligomeric state of the proteins (Superose 12 10/300 GL, GE Healthcare; buffer 50 m*M* PIPES pH 7.0, 250 m*M* NaCl, 2 m*M* $MgCl_2$, 1 m*M* DTT). Experiments were conducted using a flow rate of 1 ml min^{-1} and an injection volume of 250 µl. Prior to running $Kif7_{8–347}$ and $Kif27_{1–341}$ constructs, the column was calibrated with proteins of known molecular mass (ribonuclease A, 16.7 kDa; carbonic anhydrase, 14.5 kDa; ovalbumin, 13.5 kDa; conalbumin, 13.0 kDa) and dextran blue. The K_{av} values were calculated for calibration proteins $[(V_e - V_0)/(V_c - V_0)$, where V_e is the elution volume, V_0 is the void volume and V_c is the column volume)] and plotted against the log of the molecular weights of the standards. The molecular masses of $Kif7_{8–347}$ and $Kif27_{1–341}$ were calculated from the resulting equation. The identities of the proteins were confirmed by mass spectrometry fingerprint analyses.

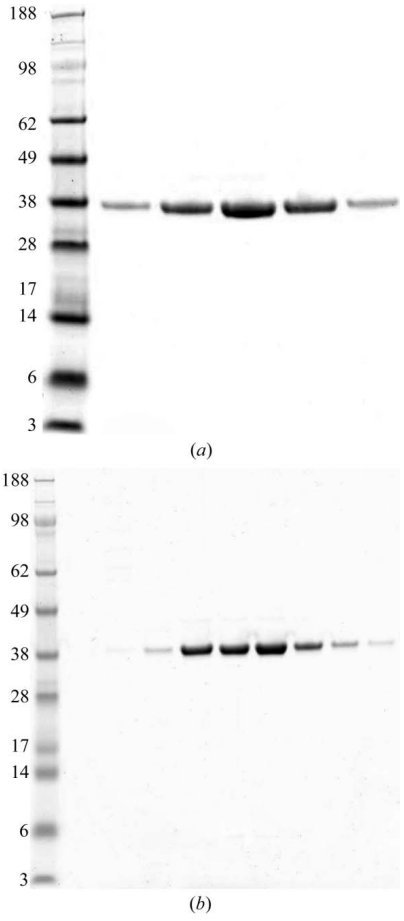

Figure 2
SDS–PAGE of gel-filtration profiles of (*a*) $Kif7_{8–347}$ and (*b*) $Kif27_{1–341}$. The left lane contains molecular-weight markers (labelled in kDa).

Table 1
Data-collection and refinement statistics for human $Kif7_{8–347}$.

Values in parentheses are for the highest resolution shell.

PDB entry	4a14
Beamline/detector	I04-1/Pilatus 2M
Resolution range (Å)	30–1.6
Space group	$P2_12_12_1$
Unit-cell parameters (Å, °)	a = 45.99, b = 79.80, c = 95.05, $\alpha = \beta = \gamma$ = 90.0
Completeness (%)	99.9 (100)
R_{merge} (%)	3.2 (43.1)
Multiplicity	7.5 (7.5)
Mean $I/\sigma(I)$	30.1 (4.4)
No. of unique reflections	46998 (6746)
No. of copies per asymmetric unit	1
Refinement statistics	
R_{work}/R_{free} (%)	18.25/20.67
No. of Mg^{2+}ADP/waters	1/328
R.m.s.d. from ideal geometry	
Bond lengths (Å)	0.011
Bond angles (°)	1.547
Average B factors (Å^2)	
Protein	27.6
Solvent	39.9
Ramachandran plot	
Residues in favoured regions (%)	98.7
Residues in allowed regions (%)	1.3
Outliers (%)	0.0

2.4. Data collection, structure determination and model refinement

$Kif7_{8–347}$ crystals grown in 0.2 *M* lithium acetate, 20%(*w*/*v*) PEG 3350 on a microscale in hanging drops consisting of a 1:1 ratio of protein and reservoir solutions were transferred to cryoprotectant solution [20%(*w*/*v*) *meso*-erythritol (Sigma), 0.24 *M* lithium acetate and 24%(*w*/*v*) PEG 3350, 0.06 *M* Pipes, 0.3 *M* NaCl, 2.4 m*M* $MgCl_2$, 1.2 m*M* DTT, 2.4 m*M* Mg^{2+}ATP] and flash-cooled in liquid nitrogen. Data were collected on beamline I04-1 at Diamond Light Source and were processed with *XDS* (Kabsch, 2010) to 1.6 Å resolution in space group $P2_12_12_1$. The structure was solved by molecular replacement with *MOLREP* (Vagin & Teplyakov, 2010) using the Kif3B structure (PDB entry 3b6v; Structural Genomics Consortium, unpublished work) as a search model. The asymmetric unit contained one copy of $Kif7_{8–347}$ with bound Mg^{2+}ADP positioned with *REFMAC*5 (Murshudov *et al.*, 2011) by rigid-body and restrained refinement. The model was subsequently improved with *Coot* (Emsley *et al.*, 2010) and further refined using *PHENIX* with TLS restraints (Zwart *et al.*, 2008).

2.5. Determination of protein concentrations

Protein concentrations were determined using the Beer–Lambert law with molar extinction coefficients (ε) of 10 430 mol cm^{-1} for $Kif7_{8–347}$ and 18 910 mol cm^{-1} for $Kif27_{8–347}$, taking bound ADP into account (ε_{ADP} = 2500 mol cm^{-1}), or by the Bradford method. Both methods yielded very similar protein concentrations, with differences of <10%.

2.6. Western blot

1 l cultures of native $Kif7_{8–347}$ and of $Kif7_{8–347}$L130P were grown, harvested and lysed as described previously. Subsequently, supernatants and pellets were analyzed separately. Supernatants were diluted tenfold. 200 µl of pellets was resuspended and boiled in 2 ml 6 *M* urea and diluted tenfold. SDS–PAGE was run with the following ratio: 10 µl sample, 8 µl loading buffer and 2 µl reducing agent. Proteins were then transferred onto nitrocellulose membrane (30 V, 400 mA, 1 h 20 min) in NuPAGE transfer buffer (Invitrogen) supplied with 20% methanol. The membrane was subsequently blocked overnight at 277 K using a solution of 5% milk powder in TBS-T (Tris-buffered saline/Tween-20). The blocking solution was washed out with three cycles of 5 min washes with TBS-T and the membrane was incubated in 1% milk solution containing the 6×His mAb-HRP conjugate (Clontech) for 1 h at room temperature. After incubation, the excess conjugate was removed by three washes with TBS-T (5 min each) and a final rinse (5 min) in water. Finally, the membrane was developed with BM Chemiluminescence Western Blotting Substrate (Roche).

3. Results and discussion

Human Kif7 and Kif27 possess an N-terminal motor domain that contains nucleotide-binding and MT-interacting regions followed by a discontinuous α-helical region predicted to form a coiled coil responsible for oligomerization and a C-terminal globular tail domain (Fig. 1). Mass spectrometry fingerprint analysis with coverage of 56 and 49% confirmed that the recombinantly expressed and purified proteins were in fact Kif7 and Kif27. Analytical gel filtration showed that both constructs were monomeric (38 and 36 kDa), as expected for kinesin motor domains. Both proteins were >95% pure as judged by SDS–PAGE (Fig. 2). Of the seven Kif7 and Kif27 constructs used for crystallization, only $Kif7_{8–347}$, which lacks the neck linker region, yielded crystals. $Kif7_{8–347}$ crystallized as a monomer with one molecule per asymmetric unit. Data were collected to 1.6 Å resolution and the structure thus belongs to a small group of kinesins solved to a higher resolution. Data-collection and refinement statistics are summarized in Table 1. The final structure included residues 12–347 (missing regions: 107–114, 207–211, 230–241, 260–273) with bound Mg^{2+}ADP (octahedrally coordinated) in the catalytic site and 328 water molecules. The refined structure contained 98.7% of residues in the most favourable region, 1.3% in allowed regions and no outliers. Fig. 3(*a*) presents the front and the back views of the overall structure of the Kif7 motor domain. Kif7 contains an eight-stranded β-sheet core with three major solvent-exposed α-helices on each side, displaying the characteristic arrowhead-like structure typical of all members of the kinesin superfamily solved to date (Kull *et al.*, 1996).

Subsequently, we compared the Kif7 structure with that of conventional

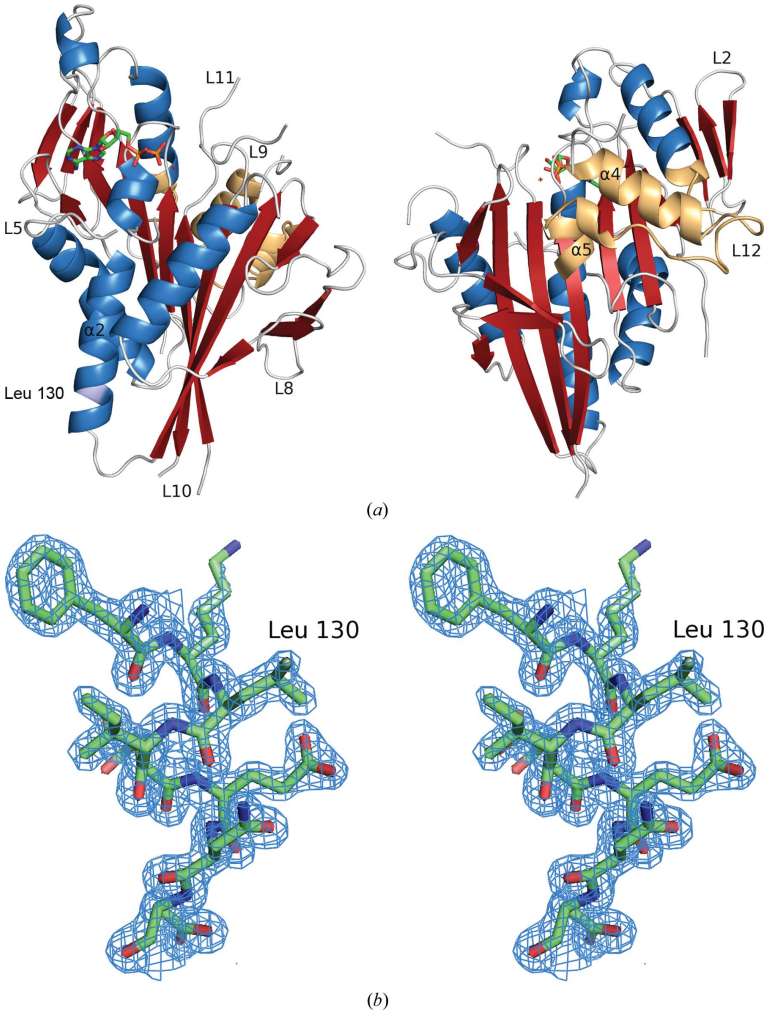

Figure 3
(*a*) Overall structure of $Kif7_{8–347}$ in complex with Mg^{2+}ADP (ball-and-stick model). α-Helices are shown in blue, β-strands are coloured red and loop regions are shaded in grey. The switch II cluster (helix α4/loop L12/helix α5) and the end of helix α6 preceding the neck linker region (not visible in this structure), which are thought to be pivotal for force generation in kinesins, are coloured orange. (*b*) Stereo-plot of helix α2 residues 128–132. The $2F_o - F_c$ map (coloured in blue) is contoured at 1σ. A single mutation in this region (L130P) causes embryonic lethality in mice.

kinesin, the founding member of the kinesin superfamily. Alignment of $Kif7_{8–347}$ with conventional kinesin (Kif5b) revealed their high structural similarity (Fig. 4). The sequence identity between the motor domains of Kif5b and Kif7 is 37%. There are two single insertions in the loop L2 region in the small three-stranded antiparallel β-sheet of Kif7. The P-loop or Walker motif (phosphate-binding region) is conserved in both proteins. In both structures, helix $\alpha2$ is interrupted by loop L5, a highly important region for inhibitor binding in the mitotic kinesin Eg5. Kif7 contains a three-residue insertion in this loop. Although we could see some electron density for loop L5, residues Ala107–Glu114 are missing owing to its increased length and higher flexibility. In Kif7, the end of the second part of helix $\alpha2$ has a single-residue deletion compared with Kif5b. Another two-residue insertion in Kif7 occurs in the loop L8 region, which is fully visible in the structure. Only residues Val159–Thr161 have an unclear density, which may suggest a dual conformation of this part of the loop. In Kif5b the switch I region (residues 199–205) consists of a small helix ($\alpha3a$), whereas in Kif7 it forms a loop (L9). In Kif7 there is an eight-residue long insertion in loop L10; this region is disordered and is not visible in our structure. Switch II (Asp251–Glu257), which is highly conserved in both proteins and typically disordered in kinesins, is not fully visible in our $Kif7_{9–349}$ structure. The switch II cluster (helix $\alpha4$/loop L12/helix $\alpha5$) is in the so-called 'down' or 'obstructive' position and one would expect the neck linker (Arg350–Asn356) to be either unstructured or structured but in an undocked position with respect to the motor domain. However, the neck linker is not included in our protein owing to the short length of the Kif7 construct used for crystallization. $Kif7_{8–361}$ contained the neck-linker region but did not crystallize, whereas $Kif7_{8–347}$ lacking the neck linker revealed that the C-terminal residue Gln347 shows crystal contacts indicating that there would not be space for a neck linker in this crystal form. This might explain why the longer Kif7 construct did not yield crystals. The loop L11 region (Leu260–Ile273) is missing as in most other kinesin structures. Kif7 contains a three-residue insertion in loop L12 which is fully visible.

We also solved a mutated Kif7 motor-domain structure (PDB entry 2xt3). Despite four point mutations ($Kif7_{E226K}$, $Kif7_{R268L}$, $Kif7_{L269R}$ and $Kif7_{H295N}$), the overall structure of the motor domain remained unchanged (data not shown). In summary, the structure of human Kif7 resembles that of human conventional kinesin.

As previously mentioned, mutations in Kif7 alleles can disturb Hh signalling, leading to death of mouse embryos. For example, in mouse models a single mutation in the Kif7 motor domain (L130P) caused early embryonic lethality at the gestation stage. This mutation was introduced through *N*-ethyl-*N*-nitrosourea induction in order to determine the impact on Hh signalling (Karel *et al.*, 2009). To understand how a single mutation in Kif7 can lead to such a dramatic event, we wanted to investigate the structure of the mutant. The construct carrying the mutation was expressed in *E. coli* but was insoluble (Fig. 5). Nevertheless, the structure of native Kif7 reveals that the L130P mutation would be situated at the end of the second half of the interrupted helix $\alpha2$ (Fig. 3*b*). We speculate that the mutation of leucine to proline, a known 'helix breaker', could cause a significant change to the secondary structure of the protein in this region. Another possibility could be that mutated Kif7 is degraded or aggregates *in vivo* owing to its misfolding. Also, there is one C—H—π interaction between Leu130 and Phe83 that is lost when leucine is mutated to proline.

In conclusion, we have provided structural insights into the human Kif7 motor domain, a kinesin that is potentially impli-

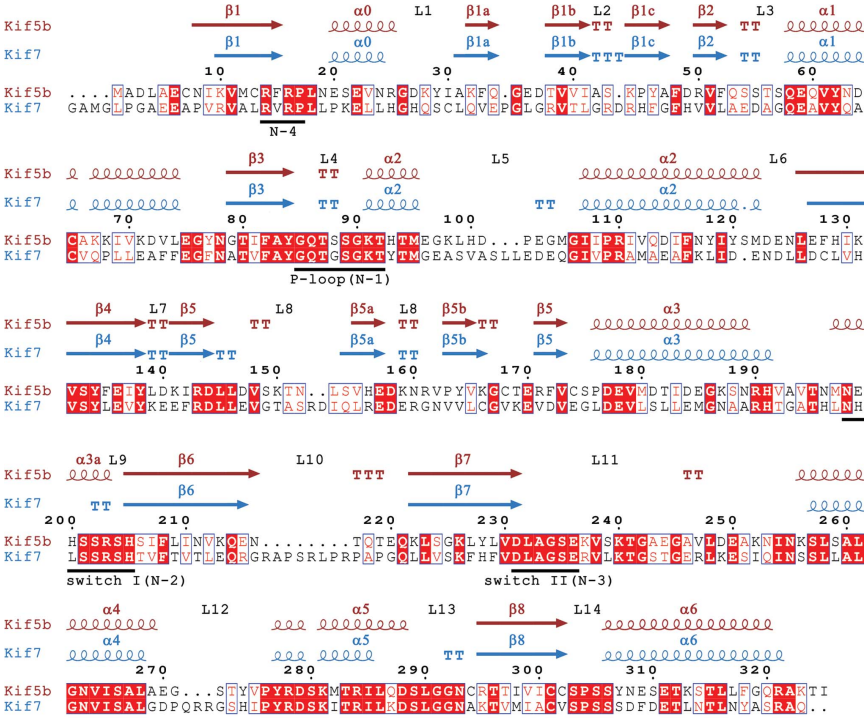

Figure 4
Sequence alignment and secondary-structure elements derived from the crystal structures of the Kif5b (conventional kinesin, kinesin-1; PDB entry 1bg2; Kull *et al.*, 1996) and Kif7 motor domains. The numbering relates to residues of Kif5b. Identical residues are coloured in white on a red background; similar residues are shaded in red. The ATP-binding pocket and the switch regions (N1–N4) are underlined in black.

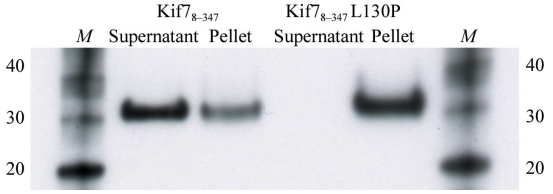

Figure 5
Western blot of soluble and insoluble fractions of Kif7$_{8–347}$ and Kif7$_{8–347}$L130P. Lanes *M* contain molecular-weight markers (labelled in kDa).

cated in several diseases. In the future, it will be interesting to determine whether Kif7 and its closely related paralogue Kif27 are proteins that are worth targeting in the Hedgehog signalling pathway (Sarangi *et al.*, 2009).

We are grateful to Agnieszka Koziol for help in the laboratory and Dr Jackie Beesley for insightful comments. We thank the Diamond Light Source for access to beamline I04-1 (native Kif7), which contributed to the results presented here. We thank D. Flot of the European Synchrotron Radiation Facility for assistance and support in using beamline ID14-4 (mutant Kif7). This publication contains part of the doctoral thesis of MK. We are grateful to Cancer Research UK for financial support.

References

Bijlsma, M. F., Spek, C. A. & Peppelenbosch, M. P. (2004). *Bioessays* **26**, 387–394.
Cheung, H. O.-L., Zhang, X., Ribeiro, A., Mo, R., Makino, S., Puviindran, V., Law, K. K. L., Briscoe, J. & Hui, C.-C. (2009). *Sci. Signal.* **2**, ra29.
Dafinger, C. *et al.* (2011). *J. Clin. Invest.* **121**, 2662–2667.
Emsley, P., Lohkamp, B., Scott, W. G. & Cowtan, K. (2010). *Acta Cryst.* D**66**, 486–501.
Endoh-Yamagami, S., Evangelista, M., Wilson, D., Wen, X., Theunissen, J. W., Phamluong, K., Davis, M., Scales, S. J., Solloway, M. J., de Sauvage, F. J. & Peterson, A. S. (2009). *Curr. Biol.* **19**, 1320–1326.
Goetz, S. C. & Anderson, K. V. (2010). *Nature Rev. Genet.* **11**, 331–344.
Hirokawa, N., Noda, Y., Tanaka, Y. & Niwa, S. (2009). *Nature Rev. Mol. Cell Biol.* **10**, 682–696.
Kabsch, W. (2010). *Acta Cryst.* D**66**, 125–132.
Karel, F., Liem, J., Hea, M., Ocbinaa, P. J. R. & Andersona, K. V. (2009). *Proc. Natl Acad. Sci. USA*, **106**, 13377–13382.
Katoh, Y. & Katoh, M. (2004*a*). *Int. J. Oncol.* **25**, 1875–1880.
Katoh, Y. & Katoh, M. (2004*b*). *Int. J. Oncol.* **25**, 1881–1886.
Kull, F. J., Sablin, E. P., Lau, R., Fletterick, R. J. & Vale, R. D. (1996). *Nature (London)*, **380**, 550–555.
Mandelkow, E. & Mandelkow, E.-M. (2001). *Trends Cell Biol.* **12**, 585–591.
Murshudov, G. N., Skubák, P., Lebedev, A. A., Pannu, N. S., Steiner, R. A., Nicholls, R. A., Winn, M. D., Long, F. & Vagin, A. A. (2011). *Acta Cryst.* D**67**, 355–367.
Pasca di Magliano, M. & Hebrok, M. (2003). *Nature Rev. Cancer*, **3**, 903–911.
Putoux, A. *et al.* (2011). *Nature Genet.* **43**, 601–606.
Sarangi, A., Valadez, J. G., Rush, S., Abel, T. W., Thompson, R. C. & Cooper, M. K. (2009). *Oncogene*, **28**, 3468–3476.
Tay, S. Y., Ingham, P. W. & Roy, S. (2004). *Development*, **132**, 625–634.
Vagin, A. & Teplyakov, A. (2010). *Acta Cryst.* D**66**, 22–25.
Verhey, K. J., Dishinger, J. & Kee, H. L. (2011). *Biochem. Soc. Trans.* **39**, 1120–1125.
Wang, G., Amanai, K., Wang, B. & Jiang, J. (2000). *Genes Dev.* **14**, 2893–2905.
Wilson, C. W., Nguyen, C. T., Chen, M.-H., Yang, J.-H., Gacayan, R., Huang, J., Chen, J.-N. & Chuang, P.-T. (2009). *Nature (London)*, **459**, 98–102.
Zwart, P. H., Afonine, P. V., Grosse-Kunstleve, R. W., Hung, L.-W., Ioerger, T. R., McCoy, A. J., McKee, E., Moriarty, N. W., Read, R. J., Sacchettini, J. C., Sauter, N. K., Storoni, L. C., Terwilliger, T. C. & Adams, P. D. (2008). *Methods Mol. Biol.* **426**, 419–435.